Modelling primeval galaxies in the JWST era

Marie Lecroq

Sorbonne Université

École doctorale 127: Astronomie et Astrophysique d'Île-de-France

Institut d'Astrophysique de Paris

Modelling primeval galaxies in the JWST era

Doctoral thesis in Astrophysics

Author:
Marie Lecroq

Supervisor:
Stéphane Charlot

Presented and publicly defended on June, 12th 2024
in front of the following jury

Benoît Semelin	Professor, LERMA, Observatoire de Paris	President
Jarle Brinchmann	Professor, Faculdade de Ciências, Universidad do Porto	Referee
Jérémy Blaizot	CNAP Astronomer, CRAL, Université Lyon 1	Referee
Véronique Buat	Professor, LAM, Aix-Marseille Université	Examiner
Nicole Nesvadba	Research Director, Laboratoire Lagrange, OCA	Examiner
Stéphane Charlot	Research Director, IAP, CNRS	Supervisor

Institut d'Astrophysique de Paris
Unité mixte de recherche 7095 CNRS - Sorbonne Université

Abstract

The James Webb Space Telescope, launched in December 2021, is heralded as the major observatory of the coming decade. While it will explore all phases of cosmic history, one of its main scientific goals is to reveal the first stars and galaxies formed in the darkness of the early Universe, which led to its reionisation before evolving into the population of galaxies observable today. To interpret the spectroscopic data collected by *JWST*, it is necessary to develop models which can effectively constrain the physics of primeval-galaxy emission. This approach can be guided by observations of nearby galaxies with properties similar to those expected of primeval galaxies, i.e. extremely metal-poor and actively star-forming. Such galaxies in the local Universe exhibit surprisingly hard radiation fields, resulting notably in intense high-ionization emission lines, which cannot be fully explained by any existing model. Recent studies point to the essential role that massive binary stars could play in this emission.

The aim of this thesis is to open up a new gap in the modelling of the emission from primeval galaxies, by exploring the spectral signatures of massive binary stars. To this end, I study the nebular emission of populations of young stars generated using the new GALSEVN model, combining the population synthesis code SEVN, which includes interactions between stars in binary systems, with the spectral evolution code GALAXEV. This approach confirms that interactions between stars in binary systems strongly influence the emission properties of young galaxies. In particular, I show that GALSEVN is able to account for the high He II/Hβ intensity ratios commonly observed in metal-poor galaxies with active stellar formation, which are difficult to reproduce with current models. I also demonstrate how successive bursts of star formation can improve agreement with observations, while the most extreme He II spectral features can be reproduced by stellar populations dominated by massive stars. GALSEVN also makes it possible to evaluate the emission from accretion discs of X-ray binaries and radiative shocks from stellar winds and supernovae in an innovative way, using a self-consistent approach built from the characteristics of the modelled stellar populations. This work shows that these contributions likely have little effect on ratios such as He II/Hβ, contrary to predictions from other models, which appear to overestimate the X-ray luminosities of nearby galaxies relative to the observed mean luminosity function of X-ray binaries. GALSEVN can also predict the emission of extremely metal-poor stellar populations, representative of the first generations of stars in our Universe. A study of different parameters characterising the emission of these stars supports the view that the first stars may have played a major role in the reionization of the Universe and the subsequent formation of the structures observed today.

Overall, the results presented in this thesis provide a solid basis for further investigation of the properties of early galaxies. By building a grid of models spanning a wide range of stellar and nebular properties, it is possible to apply statistical methods to interpret data collected by *JWST* in terms of constraints on the physical properties of the observed galaxies.

In conclusion, this thesis has led to the development and publication of new models enabling a novel interpretation of the physical properties of galaxies whose emission is dominated by young stellar populations.

Résumé court

Le télescope spatial James Webb, lancé en décembre 2021, est considéré comme l'observatoire majeur de la décennie en cours. S'il doit explorer toutes les phases de l'histoire cosmique, l'un de ses principaux buts scientifiques est de dévoiler les premières étoiles et galaxies formées dans l'obscurité de l'Univers primitif, qui ont conduit à sa réionisation avant d'évoluer vers la population de galaxies observable aujourd'hui. Pour interpréter les données spectroscopiques recueillies par le *JWST*, il est nécessaire de développer des modèles qui contraignent efficacement la physique de l'émission des galaxies primitives. Cette démarche peut être guidée par l'observation de galaxies proches aux propriétés similaires à celles attendues pour les galaxies primitives, c'est-à-dire extrêmement pauvres en métaux et formant activement des étoiles. De telles galaxies dans l'Univers local présentent des champs de rayonnement étonnamment durs, se traduisant notamment par d'intenses raies d'émission à haute ionisation, qui ne peuvent être pleinement expliquées par aucun modèle existant. De récentes études pointent vers le rôle essentiel que pourraient jouer les étoiles binaires massives dans cette émission.

Le but de cette thèse est d'abord d'ouvrir une nouvelle brèche dans la modélisation de l'émission des galaxies primitives, en explorant les signatures spectrales d'étoiles binaires massives. Pour cela, j'étudie l'émission nébulaire de populations d'étoiles jeunes générées grâce au nouveau modèle GALSEVN, qui combine le code de synthèse de population SEVN, qui inclut les interactions entre étoiles binaires, et le code d'évolution spectrale GALAXEV. Cette démarche confirme que les interactions entre les étoiles des systèmes binaires influencent fortement les propriétés d'émission des galaxies jeunes. Je montre en particulier que GALSEVN reproduit les rapports d'intensités He II/Hβ élevés communément observés dans les galaxies sous métalliques à formation stellaire active, difficiles à reproduire avec les modèles actuels. Je montre également comment la considération de sursauts de formation stellaire successifs peut améliorer l'accord avec les observations, tandis que les valeurs les plus extrêmes des caractéristiques spectrales de He II peuvent être reproduites par des populations stellaires dominées par les étoiles massives. GALSEVN m'a aussi permis de calculer de manière inédite l'émission des disques d'accrétion dans les binaires X et des chocs radiatifs issus des vents stellaires et des supernovae, en utilisant une approche auto-cohérente construite à partir des caractéristiques des populations stellaires. Ce travail montre que ces contributions n'affectent que peu les rapports tels que He II/Hβ, contrairement à ce qui a pu être prédit par d'autres modèles, qui semblent surestimer les luminosités X de galaxies proches par rapport à la fonction de luminosité moyenne observée pour les binaires X. GALSEVN peut également prédire l'émission de populations stellaires extrêmement sous-métalliques, représentatives des premières générations d'étoiles de notre Univers. L'étude de différents paramètres caractérisant l'émission de ces étoiles conforte l'idée que les premières étoiles ont pu jouer un rôle majeur dans la réionisation de l'Univers et la formation des structures observées aujourd'hui.

L'ensemble des résultats présentés dans cette thèse permettent finalement d'établir une solide base pour l'investigation plus poussée des propriétés des galaxies primitives. En construisant une grille étendue de modèles aux propriétés stellaires et nébulaires variées, il est possible d'appliquer des méthodes statistiques pour interpréter les données collectées par le *JWST* et contraindre les propriétés physiques des galaxies observées.

En conclusion, cette thèse a conduit au développement et à la publication de nouveaux modèles permettant une interprétation inédite des propriétés physiques de galaxies à l'émission dominée par leur jeune population stellaire.

Résumé détaillé

Cette thèse s'intéresse à la modélisation des propriétés physiques des galaxies primitives, c'est-à-dire les premières galaxies, qui se sont formées dans un Univers jeune, chaud, opaque et composé d'environ 75% d'hydrogène et 25% d'helium. Ces galaxies, qui se sont formées quelques centaines de milliers d'années après le Big Bang seulement, sont un ingrédient essentiel des transitions qui ont conduit l'Univers évoluer jusqu'à l'état physique dans lequel on peut l'observer aujourd'hui, même si leur contribution exacte est encore un sujet d'étude très actif. Le téléscope spatial James Webb (*JWST*), lancé en décembre 2021 et ayant déjà fourni à ce jour des observations d'objets de l'Univers très distant avec une résolution inégalée, est particulièrement adapté à l'observation de telles galaxies, grâce à la présence à son bord d'un imageur et d'un spectrographe (NIRCam et NIRSpec) dotés d'une résolution et d'une sensibilité sans précédent dans le proche infrarouge ($0.6 - 5\,\mu$m), qui permettront de sonder l'émission ultraviolette et visible dans le repère propre de galaxies très lointaines. Afin de pouvoir interpréter les données spectroscopiques collectées par le *JWST*, il est nécessaire de comprendre et de modéliser les processus à l'origine de l'émission dans ces galaxies primitives. Ainsi, le travail présenté dans le cadre de cette thèse a pour but de caractériser le spectre d'émission de ces galaxies, dans les longueurs d'onde allant du visible aux rayons X, afin de pouvoir contraindre à partir de leur spectre les paramètres physiques des sources responsables de l'émission des galaxies primordiales qui pourront être observées.

Ces galaxies se sont formées dans un Univers jeune encore pauvre en métaux (c'est-à-dire en éléments chimiques plus lourds que l'hydrogène et l'helium), évoluant rapidement, dans lequel les conditions physiques étaient très différentes de celles que l'on peut observer aujourd'hui dans l'Univers local. Une première partie de ce manuscrit (chapitre 1) sera donc consacrée à la description de l'histoire cosmique de cet Univers primordial et des propriétés qui résultent de cette évolution, en faisant notamment état des preuves observationnelles qui ont permis de contraindre ces propriétés précoces. A cause des conditions physiques reignant dans l'Univers primitif, les premières générations d'étoiles à s'être formées devraient aussi exhiber des propriétés très différentes des populations d'étoiles plus récentes, observées par exemple dans notre Galaxie. En particulier, l'absence d'éléments chimiques lourds au cours du processus de formation des premières étoiles a eu pour conséquence de former des étoiles très massives et chaudes. On s'attend à ce que de telles étoiles aient suivi au cours de leur vie une évolution particulière aux étoiles très massives, au cours de laquelle elles sont potentiellement passées par des phases pouvant produire des signatures observationnelles bien spécifiques. La présence d'étoiles si massives et chaudes dans une région de formation stellaire a également un impact significatif sur leur environnement proche : de telles étoiles forment autour d'elles de grandes régions complètement ionisées, appelées régions H II. Ces régions constituées de gaz ionisé sont caractérisées par la présence dans leur spectre d'intenses raies d'émission associées à l'ionisation des éléments chimiques présents, en conséquence du rayonnement fortement ionisant auquel ces éléments sont soumis. Je présenterai donc également dans une première partie les différentes caractéristiques d'émission attendues des étoiles présentes dans l'Univers jeune et des régions riches en gaz qui les entourent, qui nous serviront dans ce travail d'indicateurs principaux pour estimer les différentes propriétés physiques des populations stellaires à l'origine de l'émission dans les galaxies auxquelles nous nous intéressons.

Afin de pouvoir contraindre avec précision les propriétés physiques de ces jeunes galaxies à partir des données spectroscopiques collectées par le *JWST*, il est nécessaire de développer des modèles adaptés à l'interprétation des caractéristiques d'émission de tels objets. Les propriétés physiques de populations lointaines d'étoiles, qui sont le plus souvent non résolues, doivent donc être déduites de leur distribution spectrale d'énergie (SED), qui somme les contributions de toutes les sources de lumière en fonction de la longueur d'onde. L'interprétation de cette SED repose sur une compréhension poussée de l'évolution de toutes les étoiles au cours du temps, afin de pouvoir estimer leurs propriétés individuelles au sein d'une population stellaire, ainsi que sur l'utilisation de bibliothèques spectrales permettant de reproduire l'émission individuelle de chacune de ces étoiles selon leur état physique. Les possibilités inédites d'observation de galaxies à très haut redshift offertes par le *JWST* ont été confirmées par les détections récentes de galaxies très distantes, avec des redshifts supérieurs à 12. Ces perspectives ont récemment motivé le développement de nombreux codes de synthèse de population stellaire et d'évolution spectrale, qui permettent une telle interprétation. Ces codes peuvent dans un premier temps être mis à l'épreuve et calibrés par l'analyse de certaines galaxies de l'Univers proche, mieux caractérisées, qui présentent des propriétés similaires à celles attendues pour les galaxies primitives, c'est-à-dire extrêmement pauvres en métaux et formant activement des étoiles. De telles galaxies locales exhibent des champs de rayonnement étonnamment durs, qui ne peuvent être pleinement expliqués par aucun modèle existant. Ces champs de rayonnement pourraient être produits par de nombreux phénomènes, encore non décrits ou contraints de manière incertaine dans les modèles actuels : émission des étoiles supermassives, fusion d'étoiles binaires massives pauvres en métaux, accrétion de matière sur les trous noirs stellaires ou super-massifs... La détermination des sources à l'origine de cette émission très intense et énergétique aura des implications profondes pour la mise en évidence des processus physiques qui ont dominé la formation des premières étoiles, trous noirs et galaxies et qui ont fait émerger l'Univers des âges sombres. Des études récentes semblent pointer vers le rôle essentiel qu'ont pu jouer les étoiles binaires massives dans cette transition de phase. En effet, on attend de la plupart des étoiles massives qu'elles évoluent dans des systèmes binaires, à partir d'observations dans l'Univers local. Les interactions entre les deux étoiles de tels systèmes, et notamment l'échange de matière entre les deux astres, permet entre autres effets de stabiliser les étoiles les plus massives, responsables d'une intense émission dans l'ultraviolet, et qui normalement ont une durée de vie, très courte à l'échelle des galaxies, d'à peine quelques millions d'années. Les échanges de masse sont également responsables d'une production accrue de photons à haute énergie par des phénomènes spécifiques aux systèmes binaires, tels que la mise à nu des coeurs chauds des étoiles ayant perdu leur enveloppe externe, ou les changements de structure chimique des étoiles ayant reçu rapidement une masse importante de la part de leur compagnon. L'évolution tardive d'étoiles au sein de systèmes binaires est également à l'origine de la formation d'objets bien particuliers, comme les binaires X ou les systèmes binaires d'objets compact, qui peuvent exhiber des processus d'émission et des signatures observationnelles qui leurs sont propres.

Dans cette optique, le nouveau code de synthèse spectrale GALSEVN combine le code de synthèse de population SEVN, qui inclut les interactions entre étoiles binaires, et le code d'évolution spectrale GALAXEV. Les prédictions d'émission stellaire de GALSEVN doivent, pour rendre compte de l'interaction des étoiles avec les régions H II les environnant, être combinées avec le code de photo-ionisation CLOUDY. Ce code décrit le transfert radiatif du rayonnement stellaire à travers le nuage de gaz qui entoure les étoiles, en prenant en compte les absorptions de photons par les différents éléments chimiques qui le composent, mais aussi l'interaction de ce rayonnement avec la poussière interstellaire. Un grand nombre

de paramètres sont ajustables dans ces modèles, que ce soit dans les modèles de GALSEVN (paramètres stellaires) ou dans le calcul de CLOUDY (propriétés physiques du gas, dites nébulaires). Les prédictions de GALSEVN pour les caractéristiques de galaxies locales analogues aux galaxies primitives confirment que les interactions entre les étoiles des systèmes binaires influencent fortement les propriétés d'émission des galaxies jeunes (chapitre 2). Le travail mené lors de cette thèse révèle notamment que GALSEVN est capable de reproduire, de manière inédite, la dureté du rayonnement communément observée dans les galaxies sous métalliques à formation stellaire active, qui se traduit notamment par la forte intensité de ratios de luminosités de raies d'émissions telles que He II/Hβ, difficilement reproduite par les modèles actuels, et ce sans besoin d'inclure de processus d'émission supplémentaire pour la majorité des observations. Certains objets restent cependants inexplicables dans cette étude préliminaire et avec les paramètres standard des modèles..

La grande variété de paramètres physiques attendue dans les galaxies primitives, et observée dans leurs analogues proches, ainsi que l'existence d'objets à l'émission extrême difficilement explicable malgré les résultats inédits de GALSEVN, appelle à une exploration approfondie de l'impact des propriétés des populations stellaires et de leur environnement sur leur SED (chapitre 3). Ainsi, les abondances des différents éléments chimiques présents, les caractéristiques des régions H II englobant les zones de formation d'étoiles, mais aussi les distributions de masse des étoiles ou le rythme de formation stellaire doivent impacter de manière non négligeable les propriétés d'émission des populations stellaires modélisées. Il est important de quantifier cet impact pour pouvoir contraindre au mieux les propriétés des galaxies observées. En particulier, la fréquence et l'intensité des épisodes de formation stellaire joue un rôle majeur dans l'émission des galaxies jeunes, puisque l'émission stellaire est dominée par les étoiles très jeunes et chaudes ayant une durée de vie courte.

Par ailleurs, plusieurs phénomènes physiques additionnels sont fréquemment invoqués pour expliquer la dureté du rayonnement des galaxies locales sous-métalliques à formation active d'étoile, que la plupart des modèles de synthèse spectrale peinent à reproduire, y compris ceux qui incluent les interactions au sein des sytèmes d'étoiles binaires. Les sources supplémentaires de photons ionisants ainsi proposées dans la littérature sont variées : émission par les éléments chimiques chauffés dans les zones pré- et post-choc des chocs radiatifs issus des supernovæ ou des vents stellaires, émission X des disques d'accrétion d'objets compacts (trous noirs ou étoiles à neutrons) accrétant dans des systèmes binaires (aussi appelés binaires X, ou XRBs), étoiles super-massives ou soumises à une évolution inhabituelle due à leur très faible métallicité, émission des trous noirs super-massifs au centre des galaxies... Nous complétons donc, dans le chapitre 4, les prédictions présentées précédemment par des descriptions de ces phénomènes, construites de manière auto-cohérente à partir des caractéristiques des populations modélisées par GALSEVN. En particulier, nous proposons un modèle d'émission due aux chocs rapides causés par les supernovæ et les vents stellaires, qui prend en compte le taux précis de supernovæ et la perte de masse par vents se produisant dans la population étudiée. Nous construisons également un modèle d'émission due à l'accrétion dans les systèmes binaires X présents dans nos populations stellaires, dont nous vérifions l'accord avec la distribution de luminosités observée pour des binaires X de l'Univers local. L'inclusion de ces deux effets dans les prédictions de GALSEVN permet de montrer que ces contributions n'affectent probablement que peu la SED des galaxies que nous modélisons, aux âges jeunes auxquelles nous les observons. En revanche, ces phénomènes pourraient gagner en importance relative à mesure que les étoiles évoluent et meurent, et s'ils persistent, potentiellement contribuer au rayonnement de populations nées d'un épisode de formation stellaire ultérieur. Concernant l'émission due à

l'accrétion dans les binaires X, cette affirmation va à l'encontre de ce qui a pu être prédit par d'autres études récentes, qui semblent surestimer la luminosité X totale produite par ces systèmes et ainsi ne pas être en accord avec la fonction de luminosité moyenne observée pour les binaires X de galaxies proches.

La possibilité d'observer des galaxies à très haut redshift, et donc s'étant formées dans un Univers extrêmement jeune, motive également l'étude avec GALSEVN de prédictions concernant les caractéristiques de populations stellaires dites "Population III", c'est à dire les toutes premières générations d'étoiles à s'être formées, et qui ont donc une métallicité nulle ou quasi-nulle. On attend de ces étoiles, dont l'observation s'annonce extrêmement difficile, qu'elles aient des caractéristiques et des signatures spectrales encore plus extrêmes que celles mises en avant pour les populations sous-métalliques mentionnées précédemment, avec des masses pouvant atteindre jusqu'à mille fois celle de notre Soleil. Il est donc intéressant d'étudier les prédictions de GALSEVN, dont la justesse à basse métallicité est confortée par leur accord avec les observations de galaxies sous-métalliques locales, pour de telles populations à métallicité nulle (chapitre 5). A cause du peu d'espèces chimiques différentes présentes dans ces étoiles et dans le gaz les environnant, restreignant ainsi la variété de signatures spectrales sur lesquelles baser une telle étude, il est utile de compléter leur caractérisation spectrale, limitée principalement aux raies d'émission de l'hydrogène et de l'hélium, par l'étude de propriétés complémentaires. Ces propriétés, telle que les taux de production de photons ionisants, ou de photons capables de dissocier les premières molécules de l'Univers, ont des conséquences fondamentales sur les possibles scénarios décrivant l'évolution de l'Univers jeune. De telles population stellaires ont très probablement existé au sein des premières galaxies ; galaxies qui sont considérées comme principales responsables de la Réionisation de l'Univers (c'est-à dire la transition d'un Univers neutre et froid à un Univers principalement constitué de matière ionisée, tel qu'observé aujourd'hui) quelques centaines de milliers d'années après le Big-Bang. La description précise de l'émission et du pouvoir ionisant de ces étoiles de population III pourrait ainsi être un ingrédient important des simulations ayant pour but de contraindre les mécanismes à l'origine de la Réionisation. Les prédictions de GALSEVN pour ces populations stellaires permettent également de s'intéresser aux échelles de temps impliquées dans l'enrichissement chimique des galaxies primitives, qui conditionne le passage d'étoiles de population III aux étoiles de population II, moins extrêmes, moins chaudes, et moins massives. Il est également possible d'en déduire des informations concernant les différents types d'éléments chimiques produits sur ces échelles de temps, grâce au suivi individuel de l'évolution des étoiles et de leur explosion finale en différents types de supernovæ.

Enfin, afin de contourner la difficulté à obtenir des contraintes observationnelles directes pour de telles populations stellaires auxquelles comparer nos prédictions spectrales, il est utile de s'intéresser également à la possible existence d'indicateurs multi-messagers complémentaires. On peut notamment penser à l'émission d'ondes gravitationnelles par les objets les plus compacts et massifs de ces populations. De telles ondes gravitationnelles issues de la fusion de deux trous noirs, prédites par la relativité générale d'Einstein, ont pu être détectées pour la première fois le 14 septembre 2015 par l'interféromètre LIGO, et sont depuis des sources d'information très prisées concernant la présence, le nombre et les masses des trous noirs stellaires formés dans une population d'étoiles. De telles signatures gravitationnelles pourraient être observées jusqu'à des redshifts extrêmement élevés grâce à certains instruments qui devraient être mis en service dans les années à venir, comme le futur téléscope européen Einstein. Nous étudierons donc la détectabilité de telles signatures, pour les populations d'étoiles de population III simulées par GALSEVN.

Une fois les prédictions de GALSEVN confortées par leur accord inédit avec les galaxies locales aux propriétés analogues à celles attendues pour les galaxies primitives, il est intéressant d'appliquer ces modèles à la contrainte des propriétés physiques des galaxies primordiales, grâce aux observations récentes de galaxies très distantes. Pour cela, il est nécessaire de procéder à des régressions statistiques à partir des spectres observés pour ces galaxies, ou "SED fitting". Pour pouvoir mener à bien cette technique, il est fondamental de réaliser une bibliothèque de modèles calculés avec la plus grande variété de paramètres possible. L'algorithme ensuite utilisé, qui dans le cadre de ce travail sera l'outil d'analyse spectrale BEAGLE (chapitre 6), interpole ensuite cette grille de modèles et cherche à établir l'ensemble des valeurs des différents paramètres physiques qui permettent de reproduire au mieux le spectre observé pour chaque galaxie. Une telle approche permet de rendre compte de la grande diversité de paramètres physiques observés dans les régions de formation stellaire, et de laisser variables certains paramètres fondamentaux, comme le taux de formation d'étoiles, sur lesquels il peut être ardu d'imposer des contraintes a priori.

En conclusion, le travail de thèse exposé dans ce manuscrit a pour but de présenter en détail et de mettre en application le nouveau modèle de synthèse spectrale GALSEVN, très récemment publié, qui permet d'interpréter les propriétés physiques de galaxies sous-métalliques dont l'émission de photons très énergétiques n'avait jamais pu être expliquée jusqu'à présent grâce à l'incorporation des avancées les plus récentes des théories d'évolution stellaire. En particulier, je m'intéresse à l'étude de l'impact des différents paramètres ajustables de ce modèle sur les prédictions des signatures spectrales des étoiles massives sous-métalliques et du gas ionisé les environnant. Je présente également en détail la manière dont ont été construits et calibrés empiriquement les modèles complémentaires qui ont été combinés à GALSEVN pour prédire l'émission des processus additionnels se produisant au sein des zones de formation stellaire active, tels que l'accrétion dans les systèmes binaires X ou les chocs intenses dus aux vents stellaires et aux supernovæ. Je m'intéresse ensuite à l'application de ces modèles pour les diagnostics d'étoiles à métallicité quasi-nulle, ainsi qu'aux prédictions de différents observables caractérisant le pouvoir ionisant de ces populations fondamentales pour la compréhension de l'Univers primitif, ainsi que l'enrichissement chimique résultant de leur évolution. Je procède finalement à la construction d'une bibliothèque de modèles calculés avec une grande variété de paramètres stellaires et nébulaires, avec l'objectif final de pouvoir interpréter le spectre de galaxies observées à haut redshift en terme de propriétés physiques. Ceci s'inscrit dans le cadre d'observations de plus en plus fréquentes et précises du spectre de galaxies primitives grâce au *JWST*, exhibant pour certaines des signatures très surprenantes. Ce travail devrait par la suite permettre de mener de telles interprétations de manière plus étendue sur toute une population de galaxies à haut redshift, permettant ainsi d'étudier statistiquement les conditions et les processus physiques à l'oeuvre dans l'Univers primordial à l'époque de la Réionisation.

Acknowledgements

Je tiens tout d'abord à remercier énormément Stéphane, pour son accompagnement au quotidien, sa bienveillance et son soutien à toute épreuve, pour les longues heures de discussions scientifiques (et même non scientifiques) que nous avons pu avoir. Même si très tôt dans la thèse j'ai manifesté la volonté de ne pas forcément continuer dans la recherche comme activité principale, tu n'as jamais cessé de m'encourager sur tous les plans, professionnel comme personnel. Je n'en serais sûrement pas là aujourd'hui si je n'avais pas eu la chance de travailler et d'être encadrée par toi pour cette thèse.

I would also like to thank all the people who provided a great scientific environment for this thesis work : Gustavo, and our collaborators from SEVN and BEAGLE of course, for their invaluable help and explanations on different subjects, and also Stephane's former PhD students Alba, Adèle and Julia, who helped me get to grips with all the necessary tools for this work. At IAP, I would like to particularly thank Clotilde for her kindness and her regular check-ups, as well as being my "marraine de thèse" ; Florence, who constituted with Clotilde my "comité de suivi" and followed and supported me during these 3 years ; Frédéric, who took the time not only to help me with all the doctoral procedures, but also to discuss certain scientific aspects of my work ; the mezzanine people, who welcomed me even if I was not at all working on exoplanets, and who often came to the rescue with chocolate and kindness ; and in particular, my office neighbour Clément, who always lends an attentive ear to everybody's problems, and spent hours helping me with many things including my applications for my next job, and with invaluable advice on how to handle various administrative procedures (thanks partly to his unfailing knowledge of the intricacies of the Education Nationale and the Rectorat de Paris). A special though for Romain also, who acted as a bridge between IAP and the Paris Observatory, and taught me all about reionisation and simulations.

J'aimerais aussi remercier toutes les personnes qui, ici à l'IAP, m'ont beaucoup aidée sur le plan administratif; toute l'équipe administrative de l'IAP qui est toujours très réactive et d'une grande aide, Valérie, Chantal qui a pris du temps pour tout m'expliquer sur les missions au CNRS et sans qui je n'aurais pas pu organiser ma soutenance, Sandy qui m'a également beaucoup aidée pour toute la logistique, Christophe pour son aide avec tous les petits problèmes du quotidien, et toustes les autres. Et enfin également la direction de l'école doctorale, qui a toujours su répondre à mes interrogations et problèmes très rapidement et efficacement.

I would also like to thank all the members of my thesis Jury, for their precious feedback on my work, the interesting discussions that followed, and their responsiveness and flexibility throughout the whole submission and defense process.

Academic research has proven to be a challenging field, on many points. I quickly realized it was not made for me, and I have never been able to reconcile my personal convictions with the way academic research works today. I tried to help as best as I could during these three years on the subjects which were partly up to me, but it took quite a lot of energy and not always good interactions on a daily basis. I truly hope that the people at IAP who share the same feelings as me will be able to face the many challenges

of the years to come, and I would also like to thank them for working on addressing these challenges.

IAP has its challenges, but it also has great strengths. I have always been very impressed by the cohesion and the friendship between IAP PhD students, which is an invaluable support when things become tough. During my years there, we have had to face difficult times, and knowing that all of you were there has always been of great help. I would like in particular to thank all the people who were very friendly and welcoming when I arrived at IAP, and all the PhD students who were already there 3 years ago, who were from the same year as me, or in the following year. Unfortunately, this year has been quite busy for me, so I have not had time to get to know this year PhD students as well as I would have hoped, but you always were very friendly despite this, so I thank you. I could mention so many nice things you all do, the memories of the karaokes, the picnics, the yoga sessions, the knitting and stitching group, the Friday night beers, the card games, the morning or afternoon teas... so many of these things, which are really making the daily life better, so huge thanks to you all !

Je vais aussi évidemment remercier tous mes copaines qui avez toujours été là au quotidien, en particulier les anciens de l'ENS et Spammens. Les discussions quotidiennes sur tout et rien, lorsqu'il fallait évacuer la frustration sur un sujet ou un autre, les soirées et sorties régulières, les vacances annuelles, les sessions de jeux pour couper du monde réel pour quelques heures, tout ce qu'on a pu faire régulièrement et qui rendait la vie plus belle. La liste est très longue et je ne peux donc pas tout écrire, mais je vous aime toustes très fort, et merci d'avoir toujours été là.

Je voulais aussi remercier particulièrement Hugo, Dread, Louis et Adrien : pendant pas loin de 2 ans, on a quand même réussi à se libérer du temps quasiment toutes les semaines pour faire de la musique ensemble, malgré nos emplois du temps parfois chargés, et je vous en suis extrêmement reconnaissante. C'est probablement ce qui m'a permis de donner le plus de rythme à ma thèse, c'était la seule constante, que ça aille bien ou pas, le moment hebdomadaire où il était "obligatoire" de se changer les idées, mais sans jamais aucune pression, toujours dans la bonne humeur. Ces moments ont toujours été très agréables et importants pour moi. Vous avez quand même réussi à me faire aimer et attendre avec impatience les dimanches soirs, et ça, c'était loin d'être gagné ! Je voulais donc vous remercier tout particulièrement pour ces moments incroyables, sincères et très bienvenus à chaque fois, et d'avoir été une part si importante de ma vie ces dernières années.

Enfin, je tiens évidemment à remercier ma famille, pour leur accompagnement de tous les jours. Mes parents, pour m'avoir toujours poussée, encouragée et accompagnée, pour m'avoir appris toutes ces choses, appris à aimer apprendre mais aussi à avoir un esprit pratique, et pour m'avoir aussi remis les pieds sur terre (ce qui n'est pas mal quand on a la tête dans les étoiles). Même si je voyais bien que vous ne compreniez pas forcément tout lorsque j'essayais de vous expliquer le détail de ce que je faisais, vous m'avez souvent donné des idées nouvelles en me forçant à réfléchir à certaines choses sous un autre angle, ce qui est toujours important. Ca y est, je quitte enfin le monde des études pour passer de l'autre côté de la salle de classe, et je n'y serai pas arrivée sans tout ce que vous m'avez apporté et appris. Chloé aussi, qui a toujours été là, et qui a finalement passé une bonne partie de ma thèse à vivre chez nous, pour mon plus grand plaisir ! Merci pour tous ces moments de partage et d'échange, et pour m'aider à avoir une autre perspective sur ma vie au quotidien.

Et pour finir Adrien : je ne vais pas pouvoir me lancer maintenant dans des remerciements détaillés, ce serait bien trop long. Je veux quand même souligner à quel point je

t'admire et te remercie pour avoir supporté au quotidien mon stress, mes humeurs, mes plaintes et mon sel, ou encore ma manie de faire des listes pour tout et n'importe quoi, surtout quand je suis stressée. Je vais juste te dire que savoir que j'allais rentrer le soir pour te retrouver chez nous me permettait rentrer avec le sourire, malgré tout ce qui avait pu se passer dans la journée. C'est aussi une grande part de ce qui m'a permis de si bien vivre ces dernières années, et je ne t'en remercierai jamais assez.

Je m'étais promis de ne pas faire trop long pour ces remerciements, mais j'aurais encore énormément de choses à dire. J'aurais aimé pouvoir remercier chacun-e pour tout ce que vous m'avez apporté, et j'espère que vous êtes toustes conscient-es de l'importance que vous avez eue pour moi au cours de ces dernières années.

Contents

Acronyms

AGB	Asymptotic Giant Branch
AGN	Active Galactic Nucleus
BBH	Binary Black Hole
BH	Black Hole
CDM	Cold Dark Matter
CE	Common Envelope
CMB	Cosmological Microwave Background
CM	Center of Mass
CSP	Composite Stellar Population
DCBH	Direct-Collapse Black Hole
EMPG	Extremely Metal-Poor Galaxy
EoR	Era of Reionisation
EW	Equivalent Width
GRB	Gamma-Ray Burst
GW	Gravitational Wave
HMXB	High-Mass X-ray Binary
HRD	Hertzsprung-Russell Diagram
IGM	Intergalactic Medium
IMF	Initial Mass Function
IMXB	Intermediate-Mass X-ray Binary
ISM	Interstellar Medium
LAE	Lyman-α Emitter
LMXB	Low-Mass X-ray Binary
LW	Lyman-Werner
MCMC	Markov Chain Monte-Carlo
MS	Main Sequence
NS	Neutron Star
pAGB	Post AGB
PDF	Probability Density Function
PISN	Pair-Instability Supernova
QHE	Quasi-Homogeneous Evolution
SED	Spectral Energy Density
SFH	Star-Formation History
SFR	Star-Formation Rate
SNR	Signal-to-Noise Ratio
SN	Supernova
SPS	Stellar Population Synthesis
TP	Thermal Pulses
UV	Ultraviolet
WC	C-rich Wolf-Rayet star
WD	White Dwarf
WNE	Early-type WN
WNL	Late-type WN
WN	N-rich Wolf-Rayet star
WO	O-rich Wolf-Rayet star
WR	Wolf-Rayet
XLF	X-ray Luminosity Function
XRB	X-Ray Binary
ZAMS	Zero-Age Main Sequence

Chapter 1

Introduction

Contents

This thesis focuses on modelling the physical properties of primeval galaxies and characterizing their emission spectrum in wavelengths ranging from the visible to the X-ray bands. These galaxies, formed in a young metal-poor Universe, are thought to be among the main drivers of reionization through their very energetic emission. Due to having formed in a metal-poor and gas-rich environment, they exhibit peculiar stellar populations and interstellar-medium (ISM) properties, which are expected to produce characteristic spectral features. These galaxies therefore provide important insight into the physical conditions in the early Universe and the processes that led to reionization.

This chapter provides an introduction to the physics of the early Universe, and to the specific properties of stellar populations and the ISM in young, metal-poor star-forming galaxies.

1.1 The primordial Universe

All that is known about the early Universe is heavily dependent on the cosmological assumptions made to derive these results from observations. In this section, I briefly describe the general cosmological framework of this thesis.

1.1.1 The Standard Cosmological Model

The standard cosmological model rests on the fundamental principle that the Universe is homogeneous – it looks the same in any position – and isotropic – it looks the same in all directions – on large enough scales. This cosmological principle has so far been observationally confirmed by the isotropy of the cosmic microwave background (CMB; Planck Collaboration et al., 2020b) and the homogeneity and isotropy of the large scale distribution of galaxies (e.g., Maddox et al., 1990; Gregory and Condon, 1991).

Another important property of the Universe in the Standard Model is that it is expanding in an accelerated way. This expansion, first measured and formalised by Lemaître (1927) and Hubble (1929) for nearby galaxies, can be described by the Hubble-Lemaître law:

$$\vec{v}(t) = H_0 \, \vec{D}(t) \,, \tag{1.1}$$

where $v(t)$ and $D(t)$ are the recession velocity and proper distance of the considered object relative to the observer, and the Hubble constant H_0 is the value of the Hubble parameter

$$H(t) \equiv \frac{\dot{a}(t)}{a(t)}, \tag{1.2}$$

measured at the present time t_0. In this expression, $a(t)$ is a dimensionless time-dependent function called the scale factor, which describes the expansion of the Universe and is usually normalized so that $a(t_0) = 1$. The value of H_0 is subject to a tension between local – using standard candles as Cepheid stars and type-Ia supernovae – and CMB-based measurements, which both give precise but distinct results. The most recent measurements based on Planck CMB maps and assuming the Standard Model favor the value $H_0 \approx 67.4 \pm 0.5 \,\mathrm{km\,s^{-1}\,Mpc^{-1}}$ (Planck Collaboration et al., 2020a).

Our expanding, spatially homogeneous and isotropic Universe can be described in General Relativity by the Friedman-Robertson-Walker metric. The Einstein field equations written with this metric yield the Friedman equation, which relates the expansion of the Universe to its matter-energy content. The Standard Model thus provides expressions for the equations of state of the different fluids that form the Universe based on this equation. Various observational constraints, such as galaxy rotation curves (notably exposed by Rubin et al., 1980), galaxy-cluster dynamics, large-scale structure in the Universe and gravitational lensing, suggest the existence of a substantial amount of unseen mass, or dark matter, in addition to the classical baryonic matter and relativistic (i.e. radiation) components of the Universe. Another additional and indirectly detectable component must be introduced to explain the accelerated expansion of the Universe, observationally supported by indicators such as the distance-redshift relation and the absence of any detectable global curvature in the Universe : dark energy. In the so-called ΛCDM Standard Model, which assumes a flat Universe, this dark energy is considered equivalent to vacuum energy and can be linked to the cosmological constant Λ in Einstein's equations.

The work presented this thesis was carried out in the theoretical framework of the ΛCDM model. In this framework, the standard cosmological parameters correspond to a Universe composed of ~ 72 per cent dark energy, ~ 23 per cent dark matter and ~ 5 per cent baryonic matter.[1]

[1]The canonical values we adopt in this thesis are the matter and dark energy density parameters $\Omega_m = 0.315$ and $\Omega_\Lambda = 0.6847$, and the value $H_0 = 67.4 \,\mathrm{km\,s^{-1}\,Mpc^{-1}}$ for the Hubble constant (Planck Collaboration et al., 2020a).

1.1.2 Cosmological redshift

In this context of an expanding Universe, the light emitted by distant objects is affected by the expansion by relativistic Doppler effect. By definition of the scale factor, a photon of rest wavelength λ_0 emitted at time t_{em} and observed at time t_{obs} is observed with a dilated wavelength λ_{obs} such that:

$$\frac{\lambda_{obs}}{\lambda_0} = \frac{a(t_{obs})}{a(t_{em})}, \tag{1.3}$$

as the space has expanded by a factor $a(t_{obs})/a(t_{em})$.

For a photon observed at the present time, $a(t_{obs}) = 1$, and the *redshift* z is defined as:

$$z = \frac{\lambda_{obs} - \lambda_0}{\lambda_0} = \frac{1}{a(t_{em})} - 1. \tag{1.4}$$

It follows that

$$a = \frac{1}{1+z} \tag{1.5}$$

Consequently, the redshift, which can be estimated from observed spectra, provides a measurable way to label both cosmic time and cosmic distance. At present, $a(t_0) = 1$ and $z = 0$, and as the cosmic time decreases, z increases. The longer ago a photon was emitted by a distant galaxy, the higher the redshift.

1.1.3 Cosmological epochs

To understand the conditions in which primeval galaxies formed, it is necessary to consider the physical properties and the state of the baryonic matter in the Universe after the Big Bang. In this section, I describe the successive states the early Universe is thought to have gone through in the early epochs before reaching the fully ionized state we can observe today. Figure 1.1 illustrates the different epochs and their main characteristics.

A few thousand years after the Big Bang, the Universe was a fully-ionized, high-temperature plasma composed of protons, electrons, and the atomic nuclei of He, Li and traces of the other primordial nucleosynthesis products. During this phase, the plasma was totally opaque, because photons had a very short free path limited by their scattering off electrons. This tight coupling between radiation and matter also prevented gravitational interaction between baryons.[2] As the Universe progressively expanded, this plasma cooled until the temperature was no longer sufficient to maintain a fully-ionized state. At this point, electrons and protons combined to form mainly atoms of neutral hydrogen. This first decoupling phase is called *recombination*. It left the Universe fully neutral, and fully transparent as the atoms were unable to scatter photons as the electrons had done. It was only after this event that the photons were able to travel freely, the first of which constituting the photons of the CMB, which is therefore an image of the last scattering elements of the primordial plasma.

Since the gas constituting the Universe after recombination was neutral, and stars did not yet exist, the only radiation emitted after recombination was the 21 cm hydrogen line, which does not require incident radiation to be emitted.[3] This obscure phase is called the *Dark Ages*. Analysis of the CMB shows that this pristine gas was originally distributed nearly homogeneously and isotropically. As the Universe expanded, this now-decoupled gas cooled adiabatically and began to accrete onto the dark matter overdensities, or mini-haloes, which had formed before recombination. In these accreting clouds, the gas was subject to competition between two opposite interactions: gravitation, which tended to contract a cloud as its mass increased, and internal pressure. The equilibrium was determined by the cloud mass and the gas temperature: if the gas reached high-enough mass and low-enough temperature,

[2] This is not the case for dark matter, which has no coupling with electromagnetic radiation.

[3] This line results from a spin flip transition in the hyperfine levels of isolated, neutral H atoms. Although it is highly forbidden with an extremely low transition rate, the hydrogen density and the length of cosmic history actually make this line observable.

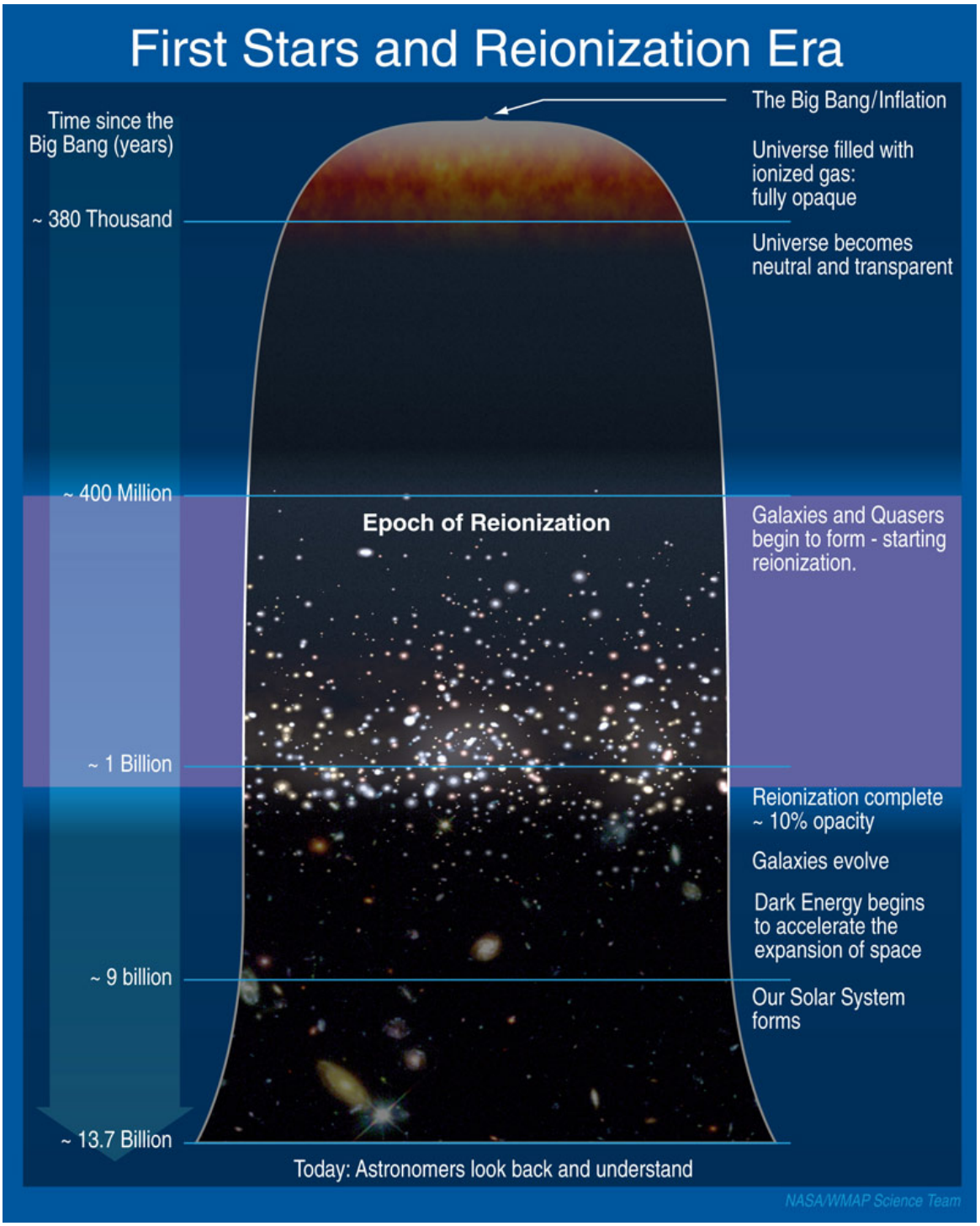

Figure 1.1: State of the Universe through the different cosmological epochs, from the Big Bang to the present day. The designation "primeval Universe" refers to times from the Big Bang to roughly 1 billion years afterwards, once the reionization is complete. In terms of redshift, the recombination of the plasma electrons and protons into neutral hydrogen occurred around $z \sim 1100$, and was followed by the so-called Dark Ages which extended then until $z \sim 10$–20. At this point, the formation of the first galaxies coincided with the beginning of reionization, which was complete around $z \sim 6$. *Credit: NASA/WMAP Science Team.*

gravity would overcome internal pressure and the cloud would collapse to form a protostar (Jeans instability). This is why understanding the cooling processes at work in this phase of the primordial Universe is essential for understanding the formation of the first population of stars. Very little cooling could occur in this pristine gas, neutral hydrogen being a very inefficient coolant in low-mass star-forming regions;[4] it has been suggested that this cooling occurred through rotational and vibrational transitions of the few simple molecules (mostly H_2, with trace amounts of helium hydride HeH^+ and lithium hydride LiH) that had formed at this time (see, e.g., Oh and Haiman, 2002; Wiklind et al., 2013). Around $z \sim 20$–30, the molecular clouds were finally cool enough to fully collapse and initiate the Cosmic Dawn: the first stars were born.

As the cooling of protostellar clouds was so inefficient in such a metal-poor environment, the first generations of stars to form, called *Population III* (hereafter simply Pop III) stars, are thought to have been very hot and massive stars composed of ~ 75 per cent of hydrogen and ~ 25 per cent of helium (by mass) with trace amounts of lithium. Chemical composition can be characterized by the metallicity, Z, defined as the fraction by mass of all elements heavier than helium (*metals*), i.e.,

$$Z = \frac{\sum\limits_{Z_i \geq 3} n_i A_i}{\sum\limits_{Z_i \geq 1} n_i A_i} \tag{1.6}$$

where Z_i , n_i and A_i are, respectively, the atomic number, number density and atomic mass of element i (with $n_1 = n_{\rm H}$). For a star to be classified as Pop III, it is generally considered that its metallicity Z must be lower than $10^{-4}\,Z_\odot$. In fact, models have predicted that stars formed in such conditions could reach $10^5\,M_\odot$ (Boekholt et al., 2018; Klessen and Glover, 2023). For a typical Pop III star of mass around 100 $M_\odot$, the surface temperature is expected to average 10^5 K and the luminosity to reach $10^6\,L_\odot$ (see Bromm, 2013, for more details). Due to their high masses and luminosities, such stars have very short lifetimes, typically estimated at around 1 Myr. After this short time, the star explodes as a supernova (SN), whose exact type and mechanism depend on its mass. This event was particularly crucial for the first generation of stars, as it marked the beginning of the ISM enrichment by successive generations of massive-star explosions, mainly with carbon, nitrogen, oxygen and traces of other α elements (neon, magnesium, silicon, nickel, etc.). The short cycle of this process implies that after only a few million years, the stars formed from such polluted gas could no longer be qualified as Pop III but transitioned to population II (Pop II) stars, corresponding to higher metallicities.

The details of the formation of the first galaxies, which emerged from the initial Pop III stars around $z \sim 10$–20, remain to be fully understood. This period marks the end of the Dark Ages, as the ultraviolet (UV) emission from the first stars, first galaxies and potentially hot accretion discs around early black holes progressively ionized the ambient neutral gas in the now intergalactic medium (IGM). As the number of ionizing sources rose, the fraction of ionized gas in the Universe increased until hydrogen became fully ionized, at $z \sim 6$ (Planck Collaboration et al., 2016). This last transition from a fully neutral to an ionized Universe, called the *Epoch of Reionization* (EoR), represents a major milestone in understanding the primordial Universe. Indeed, these newly formed object have specific emission features, which can be observed and interpreted in terms of physical conditions. It is also the transition between a Universe dominated by the gravity of dark matter to a Universe where baryonic gas becomes prominent in the formation and evolution of structures. The mechanisms at work during the EoR, and the contribution from the different types of sources to the radiation responsible for reionization, have yet to be clarified. The main sources responsible for powering reionization are believed to be the emergent population of metal-poor, low-mass, actively star-forming galaxies (e.g., Bouwens et al., 2015), with a minor contribution from accretion discs around early black holes. These may include massive black holes hosted in galaxies (i.e., active galactic nuclei, hereafter AGNs; see, e.g., Hassan et al. 2017; Parsa et al. 2018; Torres-Albà et al. 2020), low-mass quasars (e.g., Wang et al. 2010) and direct-collapse black holes (e.g., Begelman et al., 2006b). Interactions between dark-matter

[4] Atomic cooling, via Lyα emission from excited H atoms, has been shown to be efficient in dark-matter haloes with masses higher than $10^8\,M_\odot$, which have virial temperatures greater than 10^4 K (Oh and Haiman, 2002).

particles have also been recently considered (e.g., Kaurov et al., 2016). The scarcity of observational constraints at $z \gtrsim 6$ makes it difficult to tightly constrain ionizing-source properties and so to determine the precise contribution from metal-poor stars to reionization. This makes the characterization of galactic properties at this epoch crucial for understanding structure formation in the early Universe.

1.1.4 Early galaxies and chemical enrichment

As mentioned above, the first galaxies are believed to have formed at redshifts as high as $z \sim 10$–20 (Hashimoto et al., 2018; Laporte et al., 2021), very soon after the first stars. It is not as yet clear which properties were required for dark-matter haloes hosting star formation (hereafter simply star-forming haloes) to form galaxies. If galaxies are defined as structures capable of maintaining active star formation despite stellar feedback, it has been shown (see Wiklind et al., 2013) that a halo probably needs to have a mass around 10^7–$10^8\,\mathrm{M}_\odot$ for its gas not to be completely cleared out by the radiation and SN-driven shocks from Pop III stars, and thus become a primordial galaxy. This assumption, supported by simulation, implies that in the scenario where the first generation of Pop III stars are thought to have formed in haloes with $M \sim 10^5$–$10^6\,\mathrm{M}_\odot$, these stars may not have been the precursor of the first galaxies (see e.g., Kitayama and Yoshida, 2005). However, the lack in observational constraints to support simulations leaves the exact steps and conditions of the formation of the first galaxies a widely unresolved issue.

The stellar feedback from Pop III stars also played a major role in the enrichment of the primordial ISM and IGM. As mentioned in 1.1.3, these massive stars had very short lifetimes, at the end of which they underwent various types of SNe depending on their masses. These explosive events very quickly released both high amounts of energy, of order 10^{51}–10^{52} erg per SN (e.g., Klessen and Glover, 2023), and heavy elements issued from their thermonuclear burning chain (mainly C, N and α elements[5]). It is estimated that the formation haloes could have been enriched up to one thousandth of the solar metallicity ($Z \sim 10^{-3}\,\mathrm{Z}_\odot$) in only a few million years (Wiklind et al., 2013). Part of the metal-enriched gas was then expulsed into the low-density IGM by SN blast waves, and mixed with it, enriching it in turn. While the mixing with the IGM can be well described and is expected to have been efficient, it is not yet clear whether these SNe had enough energy to also enrich nearby, denser star-forming haloes. To determine the extent to which this mixing may have taken place, simulations need to be carried out to determine the velocity of the ejecta. The simulations by Greif et al. (2010) challenge the possibility of an efficient mixing with star-forming haloes, thus calling into question the rapidity of halo enrichment, and hence the timescale of the transition to Pop II stars. Other processes, such as hydrodynamical instabilities and small-scale diffusion, may have played a major role in accelerating halo enrichment by neighbouring SNe. Moreover, another issue which must be considered when studying the enrichment of star-forming haloes is that the very energetic light emitted by young, massive, hot stars may quench star formation in the closest surrounding haloes. Indeed, the few molecules enabling the gas to cool more efficiently in low-mass collapsing clouds, and especially H_2, are easily dissociated by ultraviolet photons of moderate energy, in the so-called *Lyman-Werner* band (11.2 to 13.6 eV). In this case, if the amount of ionizing photons produced by stars in a given halo is high enough, such low-mass collapsing clouds may not be able to cool enough to form stars near that halo, resulting in an isolation of star-forming regions, which makes it more difficult to enrich star-forming haloes with elements from SNe in other haloes.

Be that as it may, the fraction of metals in the primordial IGM and star-forming haloes increased over time until the stars formed could no longer be considered Pop III stars. These newly formed Pop II stars were born from molecular clouds where cooling was rendered much more efficient by the presence of metals such as carbon, oxygen, iron and silicon. As a result, they were less massive and luminous than Pop III stars, and therefore enjoyed much longer lifetimes, so that some of them can still be observed today.

[5]The most abundant of which are O, Ne, Mg, Si, S, Fe and Ni.

1.1.5 Observing primordial galaxies

To settle whether stellar feedback quenched Pop III star formation before the formation of the first galaxies, to determine the properties of the precursors to these galaxies, and to estimate their contribution to reionization, it is critical to predict and to search for signatures of Pop III stars in high redshift star-forming regions. These signatures arise from the high masses and temperatures of these stars and the highly energetic ionizing radiation they produce, which is absorbed by the surrounding dense gas and re-emitted mainly through H and He recombination lines (notably He II λ4686 and He II λ1640 if $h\nu \geq 54.4\,\mathrm{eV}$) in such an extremely metal-poor environment.

It will be extremely difficult to detect individual Pop III stars of reasonable mass ($M \lesssim 1000\ \mathrm{M}_\odot$, see e.g., Schauer et al., 2020), unless perhaps they are exceptionally magnified by gravitational lensing in cluster-caustic transits (Zackrisson et al., 2023). Indirect detection seems more likely. Catastrophic end-of-life events, such as supernovæ and mergers of compact remnants, have been suggested as potential tracers of Pop III stars, due to the colossal amounts of energy they can release. For example, the highest peak luminosities for core-collapse supernovæ are expected to exceed single-star luminosities by a factor $\sim 10^4$ (Whalen et al., 2013b). Gamma-ray detection of supernovæ afterglows and gravitational-wave signature of remnant mergers could also provide a useful multi-messenger counterpart to direct detections of Pop III stars. However, the probabilities of detecting such transient phenomena remain extremely low (see Klessen and Glover, 2023, for a more detailed review of the models, constraints and limitations of direct and indirect observations). From a spectroscopic perspective, a large helium-to-hydrogen line-intensity ratio is a key feature for identifying primordial-star formation at high redshift (e.g., Raiter et al., 2010) associated with near-zero metallicities. As the ISM is progressively enriched by successive generations of stars, emission lines of relatively abundant metals (C, O) begin to appear in the spectra.

High-redshift galaxies also exhibit specific spectral and photometric signatures, which help to identify and characterize them. As these young star-forming galaxies contain very little dust, they are expected to display a blue continuum spectrum, peaking in the UV, mainly powered by very massive stars. This spectrum is truncated below 912 Å, as radiation at wavelengths below this threshold is absorbed by the neutral hydrogen contained in the star-forming region and the IGM. This lower limit to the wavelength of the spectra is called the Lyman break, and is a very useful tool to directly identify distant galaxies. Indeed, observing the object in different filters, and identifying the wavelength range in which the image disappears as all the emitted radiation is absorbed by neutral hydrogen in the surrounding medium, provides a rough estimate of its redshift. Once the galaxy has been identified as being at high redshift, more precise measurements can than be made to confirm its detection if its magnitude is not too faint. This Lyman-Break selection method has proved effective to identify distant galaxies at redshifts up to $z \sim 9$–11 for bright enough galaxies, whose detection has then been confirmed spectroscopically. The detection of intense Lyman-α line has also been considered for many years (Partridge and Peebles, 1967) as another observational clue to identify distant galaxies as Lyman-α emitters (LAEs). Although such detection poses many observational challenges, this technique has enabled spectroscopic confirmation of the detection of distant galaxies out to redshifts $z \sim 7.3$, and the identification of primeval-galaxy candidates out to $z \sim 9$. Other observables, such as gamma-ray-burst (GRB) afterglows at very high redshifts, have also been recently suggested and used as promising selection methods. A more detailed review on primeval-galaxy signatures and emission features can be found in Stark (2016).

The observation of galaxies and star-forming regions at high redshift is extremely challenging due to their faintness, which often falls below detection thresholds. Moreover, most of the UV emission from young, hot massive stars at $z \gtrsim 6$ is redshifted towards infrared wavelengths, outside of the high-sensibility wavelength range of most existing facilities before the launch of the *James Webb Space Telescope* (*JWST*). However, thanks in part to the gravitational lensing of some sources, recent observations with the near-infrared WFC3/IR imager on board the *Hubble Space Telescope* (*HST*), the Suprime-Cam and FOCAS instruments at Subaru, the *Spitzer Space Telescope* at mid-infrared wave-

lengths, the ISAAC/Hawk-I imager and FORS2 spectrometer at the Very Large Telescope (VLT) and the red-sensitive optical spectrometer DEIMOS at Keck have provided photometric and spectroscopic data of galaxies out to $z \sim 11$ (Oesch et al., 2016). In the absence of precise spectroscopic coverage for high-redshift objects, their spectral energy distributions (SED) can be fitted to that predicted by modelled spectra to infer their physical properties. These sparse observations can also be supplemented and confronted with observations of nearby extremely metal-poor galaxies (EMPGs) to calibrate simulations and extrapolate the expected properties of Reionization-era star-forming regions. Many efforts have been made recently to identify nearby galaxies with properties close to what might be expected for primeval galaxies (see, e.g., Berg et al., 2016; Izotov et al., 2017b; Senchyna et al., 2017), in order to calibrate the models used to identify and analyse high-redshift galaxy observations. In fact, it is mostly this category of observations, based on a sample constructed by Plat et al. (2019) and presented in section 2.3, that I will use to test the models introduced in chapter 2 and to prepare the analysis of *JWST* observations.

The *James Webb Space Telescope* (*JWST*), successfully launched in December 2021 and whose first image was released in July 2022, carries instruments specifically designed to observe the rest-frame ultraviolet and optical emission of primeval galaxies, with various capabilities. In particular, the near-infrared camera NIRCam and the near-infrared spectrograph NIRSpec, which can observe at wavelengths between 0.6 and 5 μm (with resolving power of up to $R \sim 2700$ for NIRSpec), allow the detection of a wide variety of photometric and spectral features in the emission of high-redshift galaxies, which should provide considerable and unprecedented insight into the properties of pristine gas and early star formation. Thanks to these unrivaled characteristics, several teams, including the *JWST* Advanced Deep Extragalactic Survey (JADES) team, have already observed and confirmed observations of extremely distant galaxies, out to $z = 13.2$ (Curtis-Lake et al., 2023), the highest-redshift object spectroscopically confirmed at the time of this writing.

1.2 Stars in primeval galaxies

The emission from young, metal- and dust-poor, star-forming primeval galaxies is dominated by that of the stars they enclose. More precisely, at early ages, this emission is dominated by the most massive stars, type-O and B stars, which produce enormous amounts of highly-ionizing photons able to completely ionize their surrounding medium. A small change in the assumed physics of the models of these extreme stars can therefore dramatically alter the global emission predictions of these models. It is thus critical to understand and model as accurately as possible the time evolution of such stars. In the following section, I present a quick overview of the evolutionary stages intermediate- and high-mass stars undergo through their lifetime. I detail the specificities due to their initial masses, and the important phenomena that need to be modelled to describe with sufficient accuracy the radiation emitted by these stars along their lives.

An extremely useful tool for describing stellar evolution, which I will use in the following sections, is the *Hertzsprung-Russell (HR) diagram*. This diagram shows stellar bolometric luminosity L as a function of effective temperature $T_{\rm eff}$, that is, the temperature of the black-body that would emit the same total bolometric luminosity as the star. The intrinsic relations between L and $T_{\rm eff}$ are manifested in this diagram by evolutionary sequences, which allow identification of the different stages of stellar evolution through the positions of stars in the HRD.

1.2.1 Evolution of massive stars

From the initial collapse of the molecular cloud resulting in the protostar formation to the final steps of stellar evolution, accurately modelling stellar evolution represents a substantial challenge. Indeed, numerous phenomena influence increasingly complicated models whose equations are often not analytically solvable. In this section, I briefly describe the main stages in the evolution of intermediate- and high-mass single stars. The modelling for these different stages has been extensively presented in Chapters 26 to 36 of Kippenhahn et al. (2013).

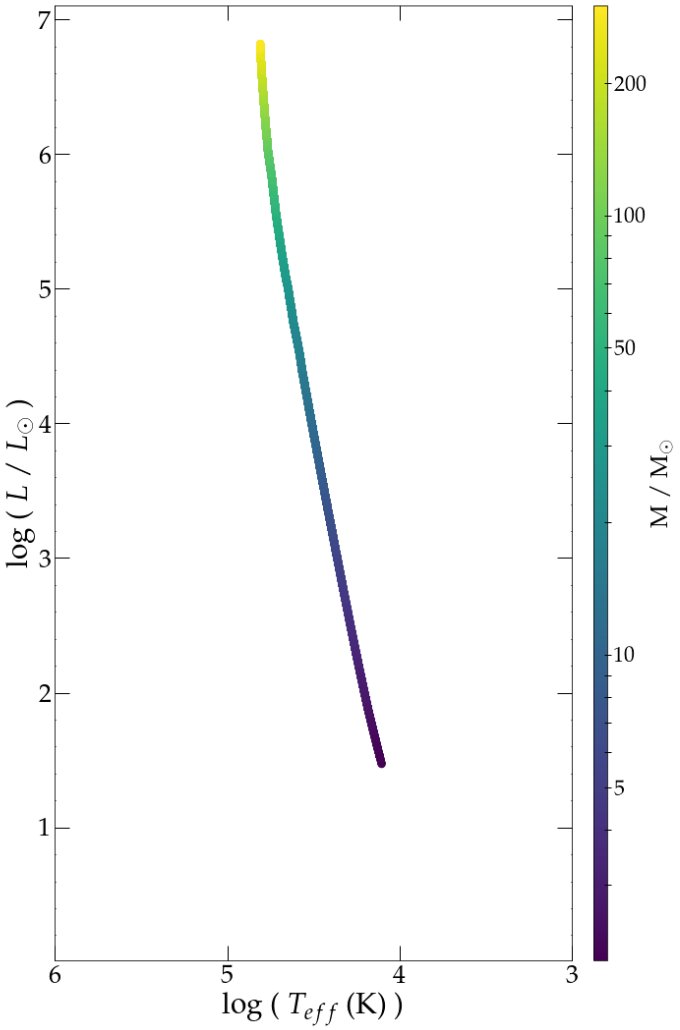

Figure 1.2: Zero-age Main Sequence (ZAMS) for single stars of metallicity $Z = 0.001$. The colour bar represents increasing stellar masses. The evolutionary tracks introduced in this section start burning hydrogen from this ZAMS. The tracks were computed using SEVN, as described in section 2.1.

We can consider the starting point of stellar evolution as the time at which a star begins to burn hydrogen in its core to produce helium. At this point, the physical properties of the star depend primarily on its mass. In the HR diagram, this defines a line on which stars of different masses lie, called the *zero-age main sequence* (ZAMS), with increasing L and $T_{\rm eff}$ towards higher masses. This ZAMS is represented in an HR diagram on Figure 1.2.

The details of star formation to reach this ZAMS involve complex interactions between forces in competition to support gravity, or on the contrary stabilize the clouds, and an accurate description of the fragmentation process in molecular clouds, which requires characterizing the different instabilities at play. Accurate descriptions of the phenomena at work in collapsing clouds and reviews of modelling work on the subject have been proposed by Zinnecker and Yorke (2007) and McKee and Ostriker (2007) for massive stars. I simply mention here that recent models have shown that star formation can be roughly described by 4 successive stages:

– a first stage during which the turbulent molecular gas is cold and dense and begins to collapse as gravity overcomes internal pressure, turbulence and other additional repulsive effects such as magnetic forces or rotation;

– a second stage where the gas at the core of the collapsing cloud becomes dense enough to gradually turn optically thick, resulting in the heating of the core by the release of trapped gravitational energy;

– a third stage where the collapse of the central region has stopped due to the core having reached quasi-hydrostatic equilibrium, its internal pressure being able to balance gravity on a dynamical timescale. This core continues to accrete from the outer regions of the cloud, which are still collapsing through an accretion disc, and as it continues to slowly contract, the central temperature eventually reaches the temperature and density of hydrogen ignition;

– a final stage before reaching the ZAMS, where the newly-ignited star has already begun to burn hydrogen and photoionizes and dissipates its accretion disc, eventually reaching its final mass and meeting the ZAMS. During this stage, massive stars can expel considerable matter from their envelopes through winds, thus reaching well below their initial masses.

The duration and characteristics of the last two stages are expected to be heavily mass-dependent. Some massive stars therefore burn hydrogen for quite some time during their pre-MS evolution, which somewhat calls into question the definition of the ZAMS given above.

All stars, both massive and non massive, then follow a quieter evolution as they burn their hydrogen fuel and form a growing helium core, during which they remain in thermal equilibrium. This hydrogen burning can take place through different nuclear channels, and for a vast majority of stars, several channels occur simultaneously. The main burning channel for low-mass stars is generally the so-called proton-proton (p-p) process, which combines H nuclei to produce first deuterium, and then helium. This process is relatively insensitive to temperature. For stars more massive than the Sun, H-burning is dominated by the CNO cycle, a catalytic cycle using the naturally present nuclei of N, C and O as intermediates to produce He. The very strong temperature dependence of the catalytic cycle makes this process a good thermostat to regulate central burning, even in stars with low trace amounts of C, N and O nuclei. During this phase, called the *main sequence* (MS), most stars are divided between an inner convective and an outer radiative zones, and their chemical composition is expected to be highly inhomogeneous. The exact description of transport equations in stellar interiors is beyond the scope of this manuscript, but can be found in Kippenhahn et al. (2013). In the case of massive stars, this description is rendered even more challenging by the increased importance of the convective zone and hence the complications created by the poorly-constrained physics in the transition zone between the convective and radiative parts of the star, called the overshooting zone. Massive stars are also expected to have high-enough rotational velocities to alter the mixing of chemical elements in the stellar interiors. More importantly, massive stars, during their MS evolution, are subject to important mass losses due to radiation-supported winds, arising from the very high energy released through radiation in the hottest and most massive stars (e.g., Vink, 2012). These winds are responsible for important mass variations in MS massive stars at intermediate metallicities.

In the HR diagram, the main sequence is very similar for stars with convective cores, that is, stars of intermediate and high masses. During this phase, the stellar luminosity increases, as the mean molecular weight in the star rises due to helium enrichment, and the temperature globally drops as the radius of the star increases moderately. Towards the end of the hydrogen-burning phase, there is generally a slight increase in $T_{\rm eff}$ due to rearrangements in the convective/radiative structure of the star as a result of the small amount of central hydrogen fuel available. This main sequence evolution is shown in Figure 1.3, between the points labelled A and B. These tracks show the increase in luminosity, especially for the low masses, and the decrease in $T_{\rm eff}$, especially for high masses, as well as the "hydrogen beak" at the end of the MS. Stellar winds do not play a major role in MS evolution for stars with a metallicity as low as that shown in Figure 1.3.

The lifetime of stars on the main sequence mostly depends on their mass. It can be estimated as

$$\tau_{\rm H} \sim \frac{E_{\rm H}}{L} \tag{1.7}$$

where $E_{\rm H}$ is the nuclear energy content that can be released by central hydrogen fusion. This variable is directly linked to the hydrogen mass of the star, and therefore to its mass. Moreover, if the mass-

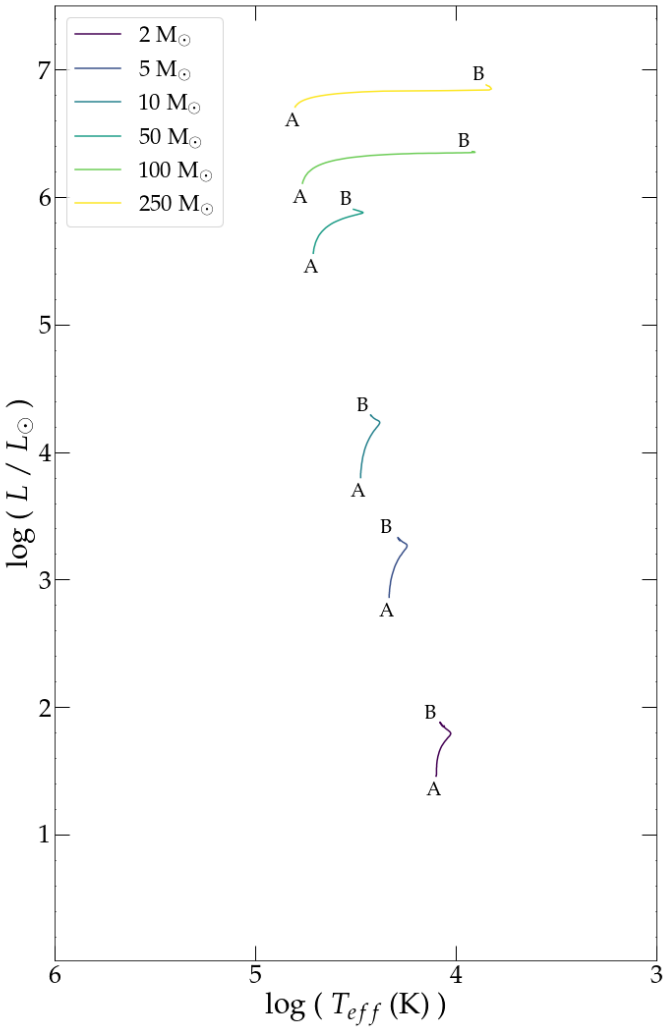

Figure 1.3: Main Sequence (MS) evolution of stars of various masses (2, 5, 10, 50, 100 and 250 $M_\odot$), colour-coded as in Figure 1.2. These tracks are for stars with metallicity $Z = 0.001$.

luminosity relation of the ZAMS is assumed, $L \propto M^\eta$ with $\eta \approx 3.5$,[6] and equation (1.7) becomes

$$\tau_{\rm H} \sim M^{1-\eta} \approx M^{-2.5} \tag{1.8}$$

This relation indeed shows a sharp decrease in $\tau_{\rm H}$ with increasing mass. In fact, a 40 $M_\odot$ O-type star is expected to remain on the main sequence for approximately 5 Myr only.

When the central hydrogen has been exhausted by the star, its core is composed of inert helium, and hydrogen burning continues on a shell of growing radius. As the shell burns, the mass of the helium core continues to increase, this time without nuclear reactions to counteract the effect of gravity. The central core then quickly contracts, and to maintain equilibrium, the radius of the star has to grow rapidly.[7] The star then enters a *red giant phase*, going in the HR diagram through the Hertzprung gap between the main sequence and the giant branch, as the probability of observing stars in this brief evolutionary stage is extremely low. During this phase, $T_{\rm eff}$ and, to a lesser extent, L both drop, due respectively to the sudden increase in stellar radius and the drop in available nuclear energy. This phase is represented between the points labelled B and C in the left panel of Figure 1.4. A consequence

[6] This relation is in principle strictly valid only for intermediate-mass MS stars, with masses between 2 and 55 $M_\odot$. For higher masses, the relation flattens progressively until it becomes linear ($L \propto M$) for almost fully-convective stars.

[7] This is called the "mirror effect", as the burning shell acts like a mirror between the envelope and the core: to maintain thermal equilibrium, the temperature of the burning shell has to remain constant (implying a constant radius). Therefore, as the inner core contracts, the pressure in the burning shell has to decrease so that it does not contract, and the outer envelope has to expand to reduce the overlying pressure.

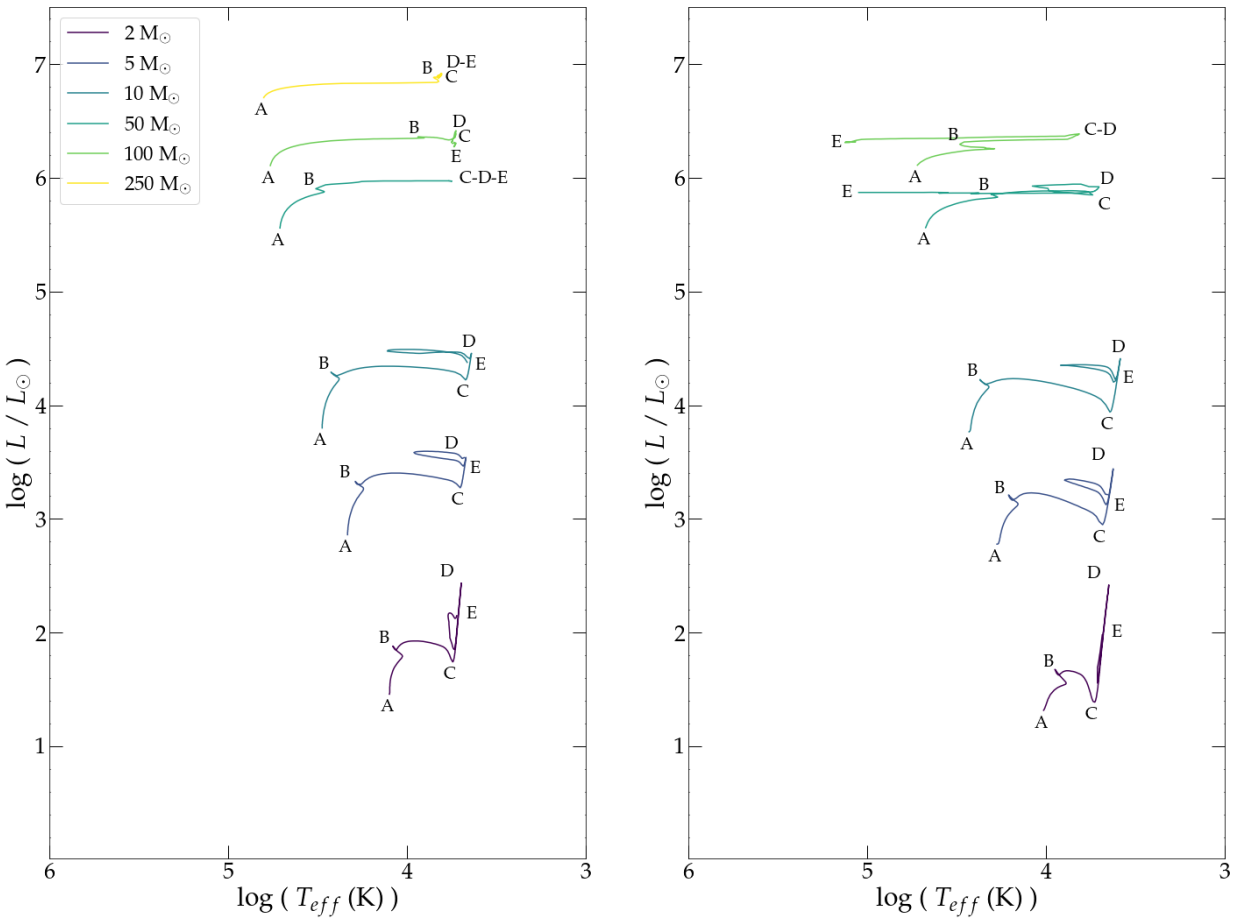

Figure 1.4: Left panel: Stellar evolution following the $Z = 0.001$ MS shown in Figure 1.3 (between A and B). The region between the points labelled B and C is the Hertzprung gap, when the helium core is contracting while the outer envelope is expanding. Helium burning begins at C, and occurs until E. D is the point where the luminosity decreases as the stellar radius contracts, first evolving downwards the Hayashi line before the evolutionary track leaves it to loop due to the transition to a radiative-transport dominated phase.
Right panel: Stellar evolution at the higher metallicity $Z = 0.008$. For the highest masses, above $10\,M_\odot$, the hydrogen envelope is stripped towards the end of the He-burning sequence, causing these WR stars to veer towards much higher temperatures (D-E).

of this contraction is that the core reaches the high temperature required to ignite helium. The star then undergoes another, quieter phase of equilibrium burning, with a burning core of helium producing carbon and a burning shell of hydrogen supplying the core with helium. In this case, central He burning globally enriches the star in C and O. This causes the dominant fusion process in the outer H-burning shell to be the CNO cycle. This catalytic cycle requires the presence of C and O isotopes supplied by central He burning, and all the elements other than H are supposed to be regenerated at the end of the cycle (hence the term catalytic). However, due to nitrogen reaction rates, if the shell temperature is not high enough, most of the C and O atoms initially present transform and remain in the form of ^{14}N, at the slowest step of the cycle, resulting in a nitrogen-enriched H-burning shell. This phenomenon is called the "nitrogen bottleneck" (see, e.g., Kippenhahn et al., 2013).
The core-helium burning phase usually lasts around 20 per cent of the time spent by the star on the main sequence; for the most massive of the stars, it can be extremely brief. During this phase, for convection-dominated stars, the effective temperature initially remains almost constant whereas the luminosity increases sharply thanks to the resurgence of nuclear fuels and the creation of new heavy elements. This rapid phase can be seen as an almost vertical line in the HR diagram, close to what is known as the Hayashi line (which is in fact the track for full convective stars). This phase can be observed between the points C and E in the left panel of Figure 1.4. During this helium-burning phase, and after equilibrium core-burning has settled again (corresponding to point D in the diagram), stars

can experience increases in $T_{\rm eff}$, which show up as loops in the HR diagram (D–E in the left panel of Figure 1.4). These increases in $T_{\rm eff}$ and drops in luminosity are due to internal convective/radiative-structure rearrangements, as the stellar radius contracts under the effect of steady He-core and H-shell burning, always to satisfy the thermal-equilibrium condition (as the burning core begins to expand again under the effect of a renewed energy input, the mirror principle causes the outer radius of the envelope to decrease).[8] This contraction progressively leads to an increase in the radius of the radiative part of the star, which then leaves the "pure-convective" Hayashi line and whose effective temperature increases due to changes in the energy-transport mechanisms. Nuclear burning later slows down, acting once again as a thermostat as the central He fuel progressively thins out, and the radius of the star progressively increases again to remain at thermal equilibrium until it rejoins its Hayashi line while the envelope becomes convective again until the end of core-He burning. As shown in Figure 1.4, the behaviour of the star in this He-burning phase and the characteristics of the loops depend strongly on its mass, with larger L and $T_{\rm eff}$ variations for lower-mass stars, because their convective envelope is thinner. These giant helium-burning stars can therefore be observed in different states and populate the giant-branch region of the HR diagram. These looped parts of the evolutionary tracks are more challenging to constrain and their exact shape strongly depends on chemical composition and the transport and mixing models adopted, especially for massive stars.

As strong stellar winds are driven by high radiative pressures and therefore high luminosities and effective temperatures, massive stars can be subjected to intense mass loss by winds in this phase too. Such winds can even completely strip the stars of their outer envelope, leaving their extremely hot helium cores exposed: such stars are then called Wolf-Rayet (WR) stars. These changes in mass and chemical composition can dramatically alter the amount of ionizing photons emitted by a star and must therefore be taken into account when modelling massive stars (see section 2.3 to see the impact such stars can have on spectral signatures).

If the mass loss is sufficiently important, the winds can expose the different nuclear-processed layers that compose the star, creating different types of WR stars:

- first, an outer layer with a high abundance of nitrogen, corresponding to the hydrogen-burning shell where the CNO process could take place due to global C and O enrichment from helium burning : such an N-rich WR star is referred to as WN. Two distinctions are made for WN stars: if the outer layer is still rich enough in hydrogen (up to ~ 60 per cent), the star is said to be of WN-late (WNL) type. If all of the surface hydrogen has been swept by stellar winds, the star is said to be of WN-early (WNE) type.
- for stronger winds which completely sweep away the hydrogen layer before the CNO cycle can produce a significant amount of N, helium-rich layers with a high abundance of produced carbon and sometimes oxygen are exposed, creating C-rich WR stars designated as WC, and O-rich WR (WO) stars exhibiting the most extreme oxygen abundances.

As the nuclear-burning shells are exposed, these stars are quite compact and extremely hot, with surface temperatures ranging from $25,000$ to over $200,000\,$K, and high metal abundances which create unique features (broad N, C and even O wind emission lines) in their stellar spectra. The tracks of such stars therefore turn away from the giant branch in the HR diagram to evolve towards higher temperatures. Some examples are shown in the right panel of Figure 1.4. These tracks are for a higher metallicity of $Z = 0.008$, as stellar winds are not strong enough at $Z = 0.001$ to produce WR stars. The tracks for the highest masses of 50 and 100 $M_\odot$ exhibit a clear bifurcation towards much higher temperatures (WR zone of the HR diagram) in their late He-burning phase (between the points labelled D and E).

When the helium fuel in the core is completely exhausted, the situation becomes similar to that at the end of the main sequence. However, this time the structure of shell burning is more complicated than before, due to the presence of two shells: a helium-burning and an outer hydrogen-burning one, around an inert core composed mainly of carbon and oxygen. For intermediate-mass stars (up to

[8] This behaviour is different from that during MS H-core burning, when core expansion meant radius expansion, because of the presence of an H-burning shell in this He-core burning phase.

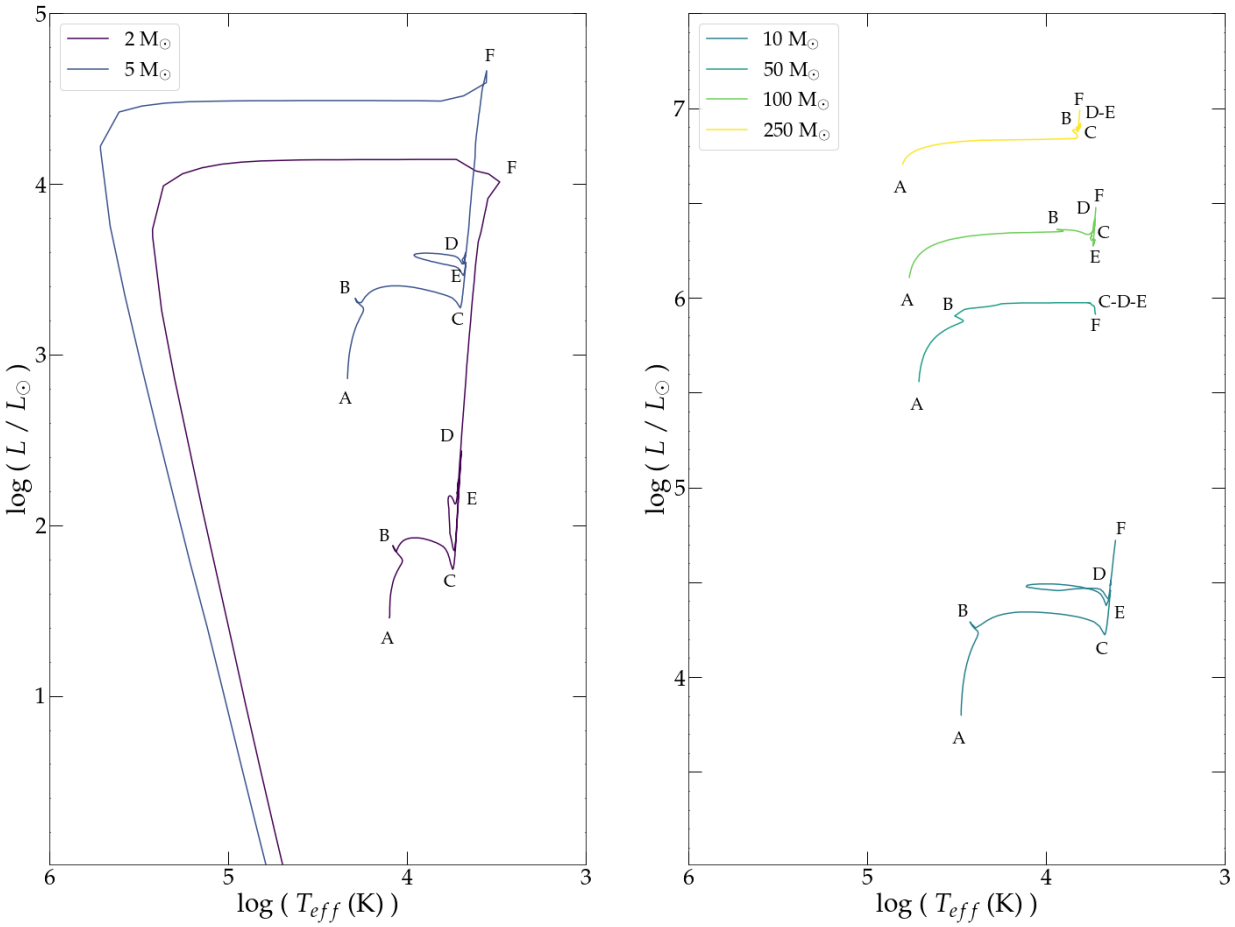

Figure 1.5: Left panel: Stellar evolution of intermediate-mass stars following the red giant phase shown in Figure 1.4. The AGB phase is represented between points E and F, while the planetary-nebula nucleus phase is nearly horizontal and brings the star to the white-dwarf region in the lower left part of the diagram.
Right panel: High-mass star evolution after the He-burning phase (ending at point E). The carbon-burning phase that follows ends at the point labelled F, and the core-burning phases that follow are too rapid to be visible on the HR diagram.

$\sim 8\,\mathrm{M}_\odot$), this phase is characterized by luminosity and temperature fluctuations due to the intermittent extinction of the outer hydrogen-burning shell, which expands in response to flashes from the helium shell below (after a period of accumulation of helium from the hydrogen-burning shell above it). The reignition of hydrogen burning follows these thermal pulses in the underlying, hotter helium shell. This phase, called *asymptotic giant branch* (AGB), is generally characterized by a higher mean luminosity and lower mean temperature, and these cyclic variations in radius, L and T_{eff} are called thermal pulses (TP). This AGB phase is shown in the left panel of Figure 1.5, between the points labelled E (end of He burning) and F. This phase progressively disrupts and expels the outer hydrogen envelope, creating a planetary nebula around the star and leaving a bare C-O core, which contracts and becomes degenerate as the star transitions into a white dwarf (post-AGB evolution). The tracks of such stars thus bifurcate towards much lower luminosities and higher temperatures as the hydrogen envelope disappears, populating the lower-left part of the HR diagram. The post-AGB phase is also represented in the left panel of Figure 1.5, and white dwarfs populate the HR diagram at luminosities below $\sim \mathrm{L}_\odot$ and temperatures above $\sim 25,000\,\mathrm{K}$.

For more massive stars, when helium in the core is exhausted, the contracting core reaches extremely high temperatures able to ignite carbon burning. The core evolution of such stars is thus a succession of cycles of nuclear burning, fuel exhaustion, contraction and ignition of more massive elements. Each burning cycle will leave shells which are still burning when fusion stops in the core: these stars have a highly layered structure of burning shells of elements of increasing mass. Figure 1.6 shows a simplified, schematic structure of this type of star. Each fusion cycle is also shorter than the previous one, due

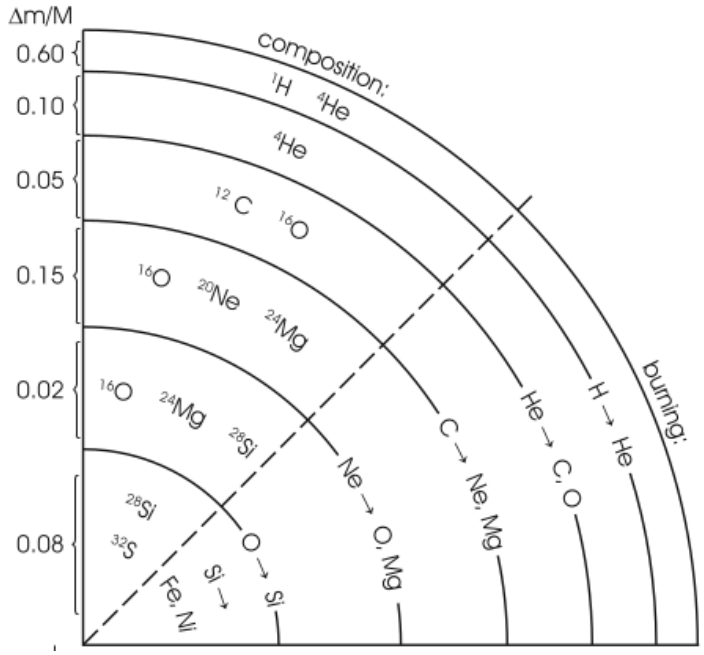

Figure 1.6: Schematic representation of the core structure of a shell-burning massive star. Δm/M represents the quantity of stellar mass inside of the shell, and is roughly representative of the radius to the centre of the star. *Credit: Kippenhahn et al. (2013).*

to the decrease in available nuclear energy: heavier elements have lower binding energies and therefore release less nuclear energy via fusion. This phase of stellar evolution therefore represent a very brief period in the star lifetime, which is mostly dominated by the MS. The stellar tracks of such stars until the end of carbon burning are shown in the right panel of Figure 1.5, where the point labelled E marks the end of He burning. Carbon burning then occurs in a quasi-vertical sequence, similar to He burning, but over a much shorter time span, and this succession of phases is repeated with increasingly heavy elements.

When the star reaches a stage where it can no longer ignite the heaviest element in its core, or for the most massive stars when the core is composed of nickel and iron and can no longer be ignited in exothermic fusion reactions, it eventually collapses. Depending on its mass, it may go through different explosive phases, eventually leaving a highly compact remnant, that is, a neutron star (NS) or a black hole (BH). The physical conditions reached during this collapse phase (core degeneracy, opacities, velocity of the resulting shocks, etc.) depend on the previous evolution of the star, its mass and chemical composition, as well as its structure, and can result in different types of type-II supernovæ (SNe). While most massive stars undergo a typical *core-collapse supernova*, intermediate mass stars initially weighting around $10\,\mathrm{M}_\odot$ can develop degenerate Mg, Ne or O cores in which electron capture becomes dominant and slows down the collapse, resulting in a relatively low-energy ($\sim 10^{50}$ erg) *electron-capture supernova*. On the other hand, the heavy cores of extremely massive, metal-poor stars (initially in the range 130–250 $\mathrm{M}_\odot$, with variations in these threshold values with metallicity) can produce photons energetic enough ($h\nu \geq 2m_e c^2$) to create electron-positron pairs at the surface of the collapsing core. The annihilation of these pairs creates a sudden violent thermonuclear explosion which can release up to $\sim 10^{53}$ erg for the most massive progenitors (Heger and Woosley, 2002) and completely disrupts the stellar remnant in what is called a *pair-instability supernova* (PISN).

As for low-mass stars, they follow a different evolution after the exhaustion of their core hydrogen fuel. This is due partly to their different structure, as they show very small or no convective cores compared to massive stars, resulting in a smooth transition from central- to shell-H burning and significant degeneracy in the stellar core. This degeneracy results in much longer timescales for the central ignition of helium burning, and in the absence of the very rapid phases seen in the evolution

of more massive stars, such as the Hertzsprung gap. These stars however still evolve towards a red giant phase similar to that of more massive stars, the main difference being the very deep convective envelope of low-mass stars, which results in this evolutionary phase closely following the Hayashi line. This evolution is then followed by an AGB phase resulting in the formation of a white dwarf. We do not detail more here the evolution of low-mass stars, whose contribution to the ionizing spectrum is expected to be negligible compared to that of more massive stars until very late ages. A more detailed discussion, especially on the evolution of their internal structure after the MS, can be found in chapter 33 of Kippenhahn et al. (2013).

Hot massive stars generally dominate the production of high-energy photons in a young stellar population. However, the more massive they are, the shorter their lifetime. This can lead to discrepancies when attempting to reproduce observations of the light emitted by metal-poor stellar populations, which often exhibit stronger signatures of high-ionization emission lines and larger populations of WR-like stars than can presumably be produced by the standard evolution of single massive stars (e.g., Eldridge and Stanway, 2009). That is where a fundamental parameter comes into play, which we have not yet mentioned: the multiplicity of stellar systems, and especially of massive stars. In the following section, I briefly describe how interactions between stars coexisting in a binary system can affect the evolution described above and the stellar emission associated with these interactions.

1.2.2 Stellar interactions in binary systems

Recent observations have revealed that most massive stars within our Galaxy – at least 70 per cent, (see, e.g., Sana et al., 2012; Moe and Di Stefano, 2017) – evolve in binary systems. The main effect of interactions in binary systems is the exchange of stellar matter between the two companions, which occurs on much shorter timescales than classical stellar winds in single massive stars and tends to stabilize the most massive stars, allowing them to slow down their evolution. In this manuscript, unless specifically mentioned, I refer to the most massive and rapidly evolving star in a binary system as the *primary* star, and to its companion star as the *secondary* star.

Mass transfer in binary systems can occur through two main channels: stellar winds and Roche-lobe overflow (e.g., Hurley et al., 2002). The accretion through winds is highly non-conservative, as angular momentum is lost by the mass-losing star, and the mass accreted onto the secondary can be estimated by the Bondi and Hoyle (1944) formula for wind accretion, which links it to the primary mass-loss rate, the velocity of the wind, and the characteristics (eccentricity, mass ratio and semi-major axis) of the binary system. In a close binary system, mass transfer preferably occurs through *Roche-lobe overflow*. The Roche lobe is defined as the region around the star of a binary system where matter is gravitationally attached to that star. It is mathematically defined in the barycentric frame as the equipotential critical curve of a fictive potential accounting for the gravitational potential of both companions and the non-inertial centrifugal forces at play in the binary system. The radius of the Roche-lobe around a star mainly depends on the mass-ratio q between the two stars: for $q \sim 1$, both Roche lobes have roughly the same radius, whereas for low q, the radius of the primary Roche lobe increases while that of the secondary one decreases. The Roche lobes of both stars meet at the Lagrange point L1, the lowest-potential equilibrium point in the system. The shape of the Roche lobes in a binary system with $q = 0.25$ is shown in Figure 1.7. In semi-detached systems, one of the stars fills its Roche lobe as a result of stellar evolution, and some of its matter passes into the Roche lobe of the other star through the Lagrange point L1 to be accreted. This mass transfer generally occurs at higher mass-transfer rates than wind accretion. This mass transfer can also be non conservative. It can be or become unstable on a dynamical timescale: in this case, the two stars merge or enter a phase of coevolution called *common envelope* (CE), which can also be reached if both stars fill their Roche lobes. In this scenario, both cores, engulfed in a unique stellar envelope, spiral towards one another and their separation decreases; depending on the amount of gravitational energy consequently released, the system may separate again or finally merge. Stellar mergers are one of the main phenomena responsible for the presence of high-mass stars at ages greater than $\sim 1\,\mathrm{Myr}$.

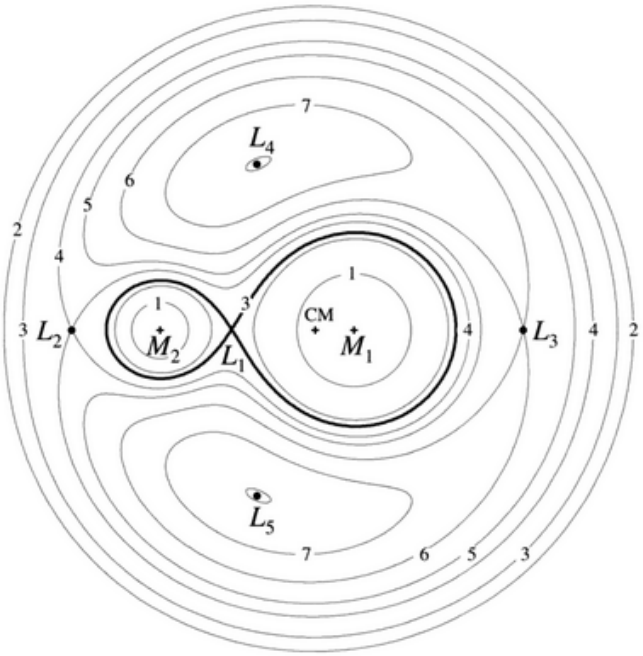

Figure 1.7: Equipotential curves for a binary system with mass ratio $q = 0.25$. The Lagrange points L1 to L5 are represented, as well as the centre of mass (CM) of the system. As expected, the radius of the secondary Roche lobe is smaller than that of the primary, for $q < 1$.*Credit: Frank et al. (2002).*

For massive stars in interacting binary systems, even outside a CE phase, mass transfer can profoundly affect their evolution beyond extending their lifetimes with mass loss and the creation of more massive stars through mergers. These mass transfers can completely strip the donor star of its outer envelope (*envelope stripping*), leaving its core exposed as a WR star. This stripping channel for WR star formation may explain the missing WR stars in the discrepancy between observed populations and those expected to arise from a population of single stars, especially at low metallicities where wind ejection is less efficient.
The wind-stripped, helium-dominated, hydrogen-free WNE stars line up in a sequence parallel to the MS, with higher temperatures, sometimes called the "helium main sequence". In this phase, their behaviour is similar to that of MS star burning their helium, but with a pure-He envelope and an inert carbon core.

The other main process affecting the production of ionizing radiation by massive stars pertains to the secondary star: when a large amount of mass (at least 5 per cent of the secondary mass) is transferred from the primary, the secondary is spun up so that its layers become almost completely mixed. This phenomenon is called *quasi-homogeneous evolution* (QHE) (e.g., Eldridge and Stanway, 2012). In this phase, the star becomes a homogeneous mix of hydrogen and helium, and therefore appears hotter and brighter than it would with a hydrogen envelope, because the mean surface molecular weight increases. These stars continue to burn their hydrogen and evolve into WNL stars as their hydrogen mass diminishes in favour of He.

The changes in stellar evolutionary tracks induced by these binary interactions can easily be visualized in HR diagrams similar to those introduced in section 1.2.1. Figure 1.8 shows such diagrams, comparing single and binary stars, again for stellar populations with $Z = 0.001$. Unlike the diagrams showed in the previous section, where a star of a given mass was followed with increasing age, these diagrams show the positions of all the stars in the stellar population at a fixed age (also called an *isochrone*). At the chosen age of 4 Myr, most of the low- and intermediate-mass stars are still in their hydrogen-burning phase (and therefore appear as aligned MS stars). The diagram on the right, showing the positions of single stars at this fixed age of 4 Myr, serves as a reference to identify the

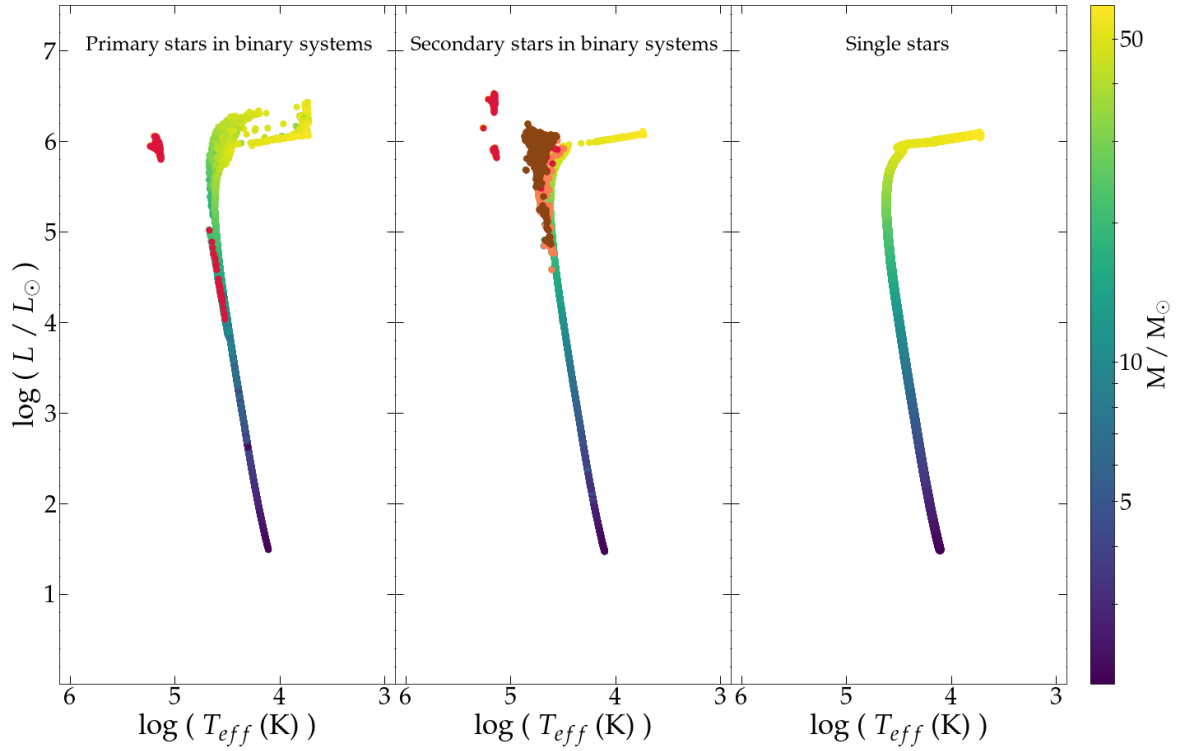

Figure 1.8: Position in the HR diagram of all the stars of a 4-Myr old stellar population with metallicity $Z = 0.001$, colour-coded by mass. The left and middle panel show the properties of primary and secondary stars in binary systems, respectively, and the right panel shows the properties of single stars for comparison. The orange dots represent stars in a QHE phase, and the red dots WR stars. Stars undergoing a QHE phase which have become WNL stars are highlighted in brown.

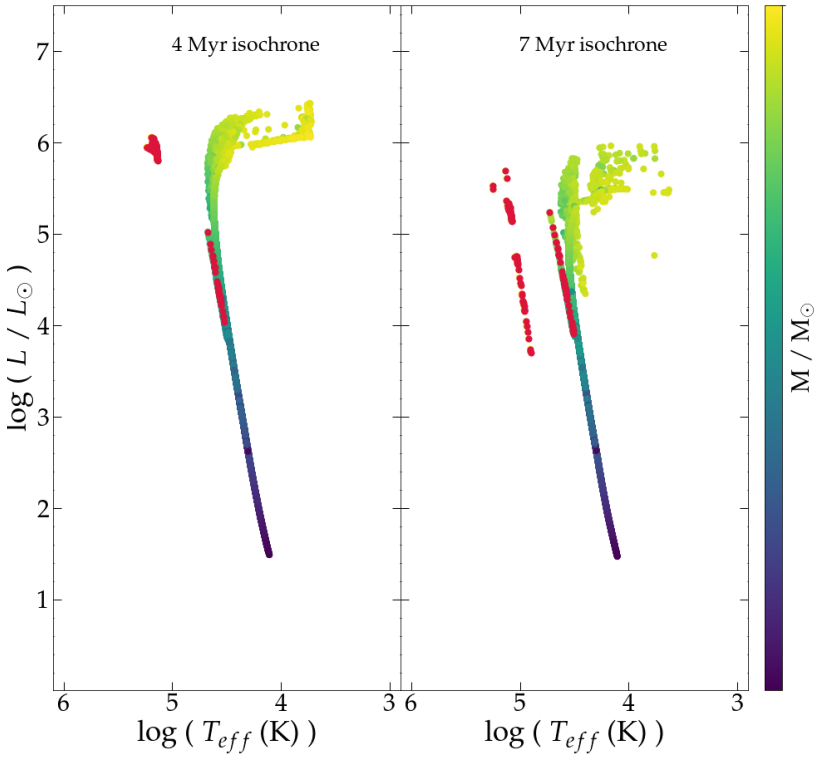

Figure 1.9: Isochrones for primary stars of metallicity $Z = 0.001$, at ages of 4 (left panel) and 7 Myr (right panel). As before, the red dots show WR stars. Some of the WNL stars which were located on the branch close to the MS at 4 Myr have evolved to become WNE stars and form the hydrogen-poor stars of the He main sequence at 7 Myr.

features linked to binary interactions for primary (left panel) and secondary (middle panel) stars in binary systems. The first notable change in the left panel is the broadening of the massive-star sequence for primaries, due to stellar mergers making stars jump towards the tracks of more massive stars. Moreover, new regions of the diagram are populated. WR stars (highlighted as red dots) exist at higher temperatures than MS and giant stars, with a difference in behaviour and properties between WNL stars, which occupy the part slightly branching to the left of the MS, and WNE stars, which have much higher temperatures and lie to the far left of the MS. Secondary stars undergoing a QHE phase (orange dots), which increases both their luminosity and temperature due to global mixing, are located in the upper left part of the MS. As mentioned above, as QHE stars continue to burn their hydrogen, they evolve into WNL stars. WNL stars which are still in their QHE phase are shown in the middle panel by brown points.

At later ages, some of the wind-stripped primary stars which still had a significant surface abundance of hydrogen have burnt this hydrogen and completely detached from the MS to form the He main sequence mentioned above. This late evolution is shown in Figure 1.9 at 7 Myr, in comparison to the previous diagram at 4 Myr.

A clearer picture of the evolution of metal-poor, massive stars throughout their lifetime emerges from the elements described in sections 1.2.1 and 1.2.2. This evolution will be manifested in models and observations by very specific emission features in the spectra of a metal-poor stellar population, which I outline in the next section.

1.2.3 Spectral signatures of massive stars

The bluest part of the spectrum of a stellar population is dominated by the light emitted by the most massive stars. This emission, similar to that of a black body, peaks in the UV for O-, B- and A-type stars. The peak of the spectrum rapidly shifts redwards with increasing age, as the most massive, dominant stars have a short lifetime.

As for characteristic emission lines, the spectral features of massive stars have long been identified and observed. Beals (1929) first identified broadenings in certain lines of stellar spectra which were associated with massive, hot O-type and WR stars. These so-called *P-Cygni profiles*, named after the blue variable giant star P-Cygni in whose spectrum this line profile was first observed, are characterized by the presence of both absorption and emission in the profile of the same spectral line. This profile can be observed in several resonant[9] lines, such as Hα, N V λ1240 or C IV λ1549 (Prinja et al., 1991), and is indicative of strong stellar winds. The emission part of this profile is caused by heating of the stellar envelope due to intense winds, whereas the blueshifted absorption originates from a rapidly expanding shell of ejected matter moving towards the observer and absorbing stellar light. Another commonly observed broadening, originating from the dense and highly-ionized stellar winds of some WR and O-type stars, is that of He II λ4686.[10]
Such spectral features are visible in the Senchyna et al. (2017) spectra of nearby metal-poor star-forming regions shown in Figure 1.10. As explained in the previous section, metallicity puts an important constraint on stellar winds, as for extremely-low metallicities, the opacity of massive-star envelopes is not high enough to sustain this type of winds. Figure 1.10 illustrates two regimes distinguished by metallicity: star-forming regions with $12 + \log(\mathrm{O/H}) \lesssim 8.1$[11] do not show wind-related spectral features, and exhibit only intense nebular emission lines (as will be discussed in section 1.3.3), whereas

[9] An emission line is said to be resonant when it is a non-forbidden transition between the ($n = 2$) and ($n = 1$) levels. In the case of C IV λ1549, for instance, the emission is due to the change of electronic orbitals of the excited outer electron of C^{3+}, which drops from the fundamental 2p level to the fundamental 2s level (ignoring the hyperfine structure of the orbitals).

[10] He II is non-resonant, so the P-Cygni profile for this line is extremely weak, but can sometimes be observed in addition to the aforementioned broadening originating from stellar winds.

[11] According to Gutkin et al. (2016), $12 + \log(\mathrm{O/H}) \approx 8.1$ is equivalent to a metallicity $Z \approx 0.004$, that is, about 25 per cent of solar. For reference, $12 + \log(\mathrm{O/H})_\odot \approx 8.7$.

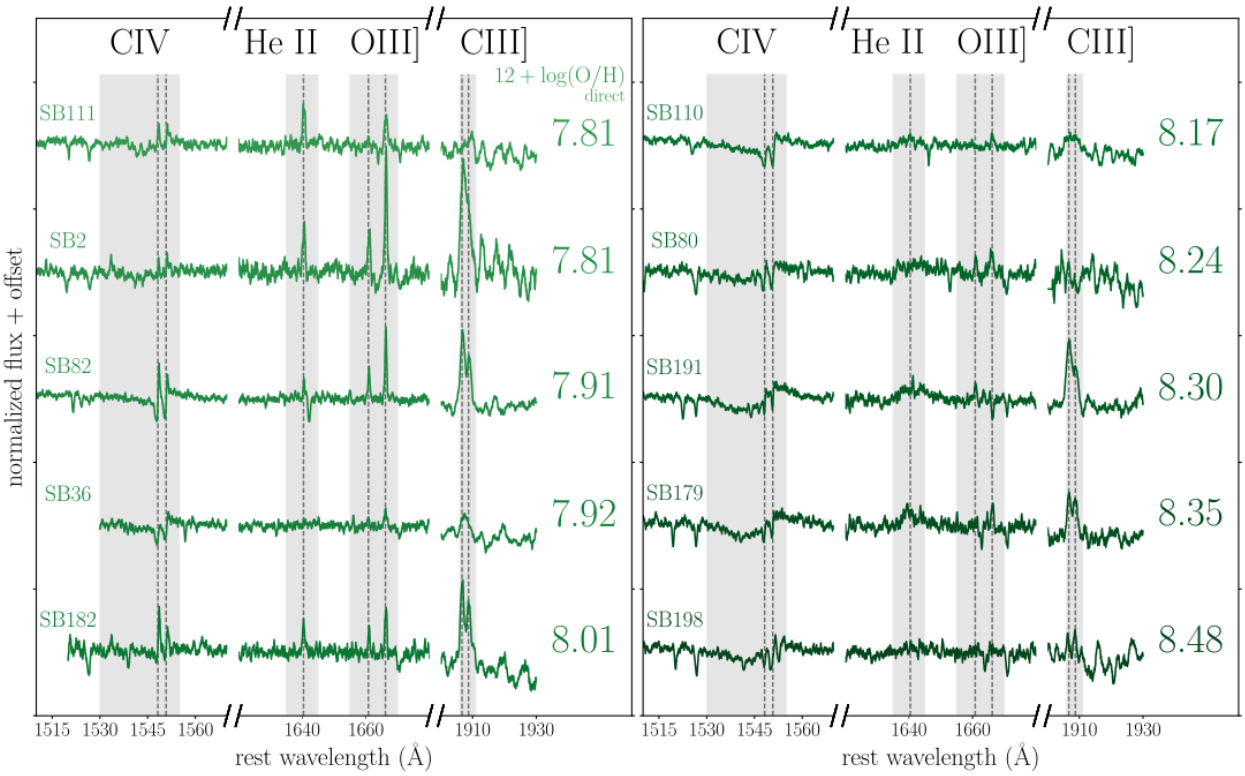

Figure 1.10: *HST*/COS normalized and offset-corrected spectra of 10 nearby metal-poor star-forming regions, classified by gas-phase oxygen abundance (equivalent to metallicity). The spectra are truncated in order to show a few spectral lines of particular interest for massive stars signatures. *Credit: Senchyna et al. (2017)*

at higher metallicities, stellar emission dominates the spectrum and C IV λ1549 P-Cygni profile and He II λ4686 broadenings, highlighted by the grey shaded areas, can easily be observed.

A much more detailed discussion on massive-star diagnostics and multi-messenger emission can be found in Vink (2022).

In general, for the models that I will present in this thesis and from chapter 3 onwards, I will focus on metallicities of at most $Z = 0.004$. Therefore, I do not expect the above spectral features to be dominant in my spectra, and will therefore focus on nebular emission, as presented in section 1.3.

1.2.4 Feedback from stellar remnants: the case of X-ray binaries

During the evolution of the bound stars, and especially during the explosive phases at the end of nuclear burning, binary systems can be disrupted by the ejection of one of the stars (supernova kick). If a binary system resists this late evolution, often thanks to the companion being relatively massive, it can remain bound and continue to evolve with at least one compact stellar remnant, that is, a neutron star or a black hole. This requires the two stars to be separated enough to avoid a common-envelope phase during their evolution, but close enough that after the SN explosion of the primary, mass transfer is still possible. In such a case, the compact object will eventually accrete matter from its companion and form an accretion disc. The emission of these systems is known to peak at X-ray energies (e.g., Mitsuda et al., 1984; Fragos et al., 2013; Mirocha, 2014; Senchyna et al., 2019), hence their name *X-ray binaries* (XRBs). In such systems, mass transfer from the primary creates a geometrically thin and optically thick accretion disc around the compact object, composed of gas dominated by gas pressure or, in the inner parts, by radiation pressure. The viscosity of this disc allows matter to transfer angular momentum to its outer parts and thus to accrete onto the primary. It is this transfer that releases energy in the form of radiation emitted from the surface of the disc. X-rays are mainly emitted from the inner part of the disc, where the gas is hottest (e.g., Grimm, 2003). For matter to keep infalling stably onto the compact object, radiation pressure has to remain dominated by the gravitational attraction

of the compact object. This sets a theoretical limit to the maximum luminosity emitted by the disc at equilibrium: the Eddington luminosity, defined as the ratio between the gravitational and radiative forces, given by

$$L_{\mathrm{Edd}} = 1.26 \times 10^{38} \left(\frac{2}{1+\mathrm{X}}\right) \left(\frac{m_{\mathrm{c}}}{\mathrm{M}_{\odot}}\right) \mathrm{erg\,s^{-1}} \tag{1.9}$$

where m_{c} is the mass of the compact object and X the hydrogen mass fraction in the accretion disc.

XRBs can be classified into two main types: high-mass X-ray binaries (HMXBs), in which the companion star is massive; and low-mass X-ray binaries (LMXBs). The mass limit is usually taken around $5\,\mathrm{M}_{\odot}$ and can vary between authors; sometimes a third category, intermediate-mass X-ray binaries (IMXBs), is introduced if the companion star weighs between around 5 and $20\,\mathrm{M}_{\odot}$. In theory, in actively star-forming, extremely metal-poor galaxies, HMXBs are expected to be dominant because of the predominance of massive stars. This classification on companion mass roughly separates "long-lived" from "short-lived" XRBs, as the lifetimes of HMXBs companions can be shorter by a factor ~ 100. As a result, HMXBs are generally considered as good tracers of recent star-formation episodes in galaxies.
Due to the fundamental differences between neutron-star and black-hole physics, the nature of the primary is also expected to have an impact on the observed properties of XRB systems, although these trends are more subtle and harder to confirm observationally. The intense magnetic field and hard surfaces of neutron stars should produce a somewhat harder emission from accretion, and intensify the variability of the system emission, compared systems driven by black holes (e.g., Sunyaev and Revnivtsev, 2000).

Accretion rates in such systems depend on the evolutionary stage and chemical evolution of the donor star, the mass ratio between the donor and the compact object and their orbital separation. As in ordinary binary-star system, accretion can theoretically occur through two channels: Roche-lobe overflow or stellar winds from the secondary. In accordance with what was described in the previous sections concerning stellar winds, this accretion channel should potentially occur only in HMXBs, winds being predominant for massive stars with sufficiently high metallicities; its efficiency should also depend on the nature of the compact object, as the capture radius of the accreting matter depends on the gravitational field produced by the primary. While the physics of accretion processes in such systems is still relatively poorly constrained, it has been observed that XRBs can reach extremely high accretion rates, and even exceed the Eddington limit for stable accretion in a disc at hydrostatic equilibrium (e.g., Rees, 1988; Begelman, 2002; Bachetti et al., 2014; Pinto et al., 2016; Rodríguez Castillo et al., 2020). As a consequence, they are believed to be an important ingredient of stellar population modelling to explain observations of very high-ionization emission lines (Schaerer et al., 2019; Umeda et al., 2022; Katz et al., 2023). As most galaxies exhibit significant X-ray emission, possibly due to their XRB populations, the total X-ray luminosity produced in a stellar population should certainly be constrained in stellar populations models, and may prove to be an interesting tracer of the star-formation history (SFH) in distant galaxies.

A more detailed overview of how XRB models have been combined with stellar population synthesis codes and on the impact such object can have on the spectra of star-forming regions will be the subject of section 4.1.

1.3 Nebular emission in primeval galaxies

In the previous section, I gave an overview of the characteristics of the stellar radiation produced by a population of young metal-poor, massive stars. However, it would be inaccurate to consider stellar emission without examining its interaction with the surrounding gas-rich medium. As mentioned before, such young stellar populations are capable of generating extremely high-energy photons, which ionize part of the stellar birth cloud, giving rise to intense emission lines from the chemical elements present in these clouds. In the next section, I present the basic properties of these ionized regions,

Figure 1.11: *JWST* NIRCam images of the Orion nebula (M42) on the left, and of the Eagle nebula (M16) on the right zoomed on the star-forming region called the Pillars of Creation. The different colours are tracers of the different chemical elements present in the photoionized region. The darker clouds illustrate the absorption by dust. *Credit: ESA, NASA/STScI.*

called *H* II *regions*, and highlight the main emission processes involved and the features arising in the spectra of the corresponding star-forming region.

1.3.1 A brief overview of H II regions

The UV emission from young massive stars is capable of completely photoionizing H (and to a lower extent He) atoms present in the gas-rich birth cloud surrounding these stars, which is initially composed mainly of molecular hydrogen. These interstellar regions are maintained at equilibrium by the radiation from young stars. For reference, an O-type star with an effective temperature of $T_{\rm eff} \sim 35,000\,{\rm K}$ emits 32 per cent of its photons above the hydrogen ionization threshold of 13.6 eV during its MS evolution (Draine, 2011b). These regions can vary in density (typically $n_{\rm H} \sim 10$–$10^4\,{\rm cm}^{-3}$), temperature (7,000–15,000 K) and radius (from $\sim 0.1\,{\rm pc}$ for the ultra-dense regions to a few hundred parsecs for the most diffuse ones), depending on the properties of their progenitor molecular cloud and their ionizing stars. Two famous examples of H II regions are the Orion nebula, and the Eagle nebula around the young stars forming in the "Pillars of Creation". *JWST* images of these regions are shown in Figure 1.11.

As these regions are home to numerous excitation and deexcitation processes, and are enriched in metals through the different evolution phases of their stars, they are responsible for the production of numerous spectral emission lines. To accurately characterize and model these emission lines, it is important to understand the composition and state of the interstellar gas in and near H II regions. The Strömgren (1939) formalism can be adopted to describe an ideal, spherical, fully ionized and uniformly dense H II region (or *Strömgren sphere*) maintained at equilibrium by the absorption of photoionizing photons from a hot luminous central star. In this case, it is possible to determine the radius of the ionization front as a function of the rate of ionizing photons Q_0 and hydrogen density $n_{\rm H}$ of the region (Draine and McKee, 1993), as

$$R_{\rm Ström} \equiv \left(\frac{3Q_0}{4\pi {n_{\rm H}}^2 \alpha_{\rm B}} \right)^{1/3} \tag{1.10}$$

for a pure-H nebula, where α_B is the case-B hydrogen recombination coefficient (see section 1.3.3) which mainly depends on the temperature of the gas. Outside this Strömgren radius, all the ionizing photons have been absorbed by the atoms of the H II region, and the interstellar gas remains neutral. As a result, such a region is referred to as *ionization bounded*. If the Strömgren radius extends beyond the H II-region physical radius, the region is called *density bounded*, and hydrogen-ionizing photons can escape from the region without being absorbed. The amount of escaped hydrogen-ionizing photons is usually referred to as f_{esc} in terms of observables.

This description of H II regions is very simplified: they usually contain elements other than H, and in truth the ionization state of hydrogen is not as simple as completely ionized for $r < R_{Ström}$ and neutral for $r > R_{Ström}$. For reference, Draine (2011b) provides more detail on the H-ionization profile in H II regions in their Chapter 15. However, the Strömgren model provides an accurate enough estimation of the quantities involved in H II-region emission.

Even metal-poor stellar birth clouds contain not only H but also a certain fraction of He. If the ionizing photons have energies above the helium first-ionization threshold of 24.6 eV, as is the case for the hottest O-type stars, there may be another Strömgren radius for the helium-ionized region, which is expected to be shorter than the hydrogen-related Strömgren radius. In this case, the H II region will be composed of an inner part where both He and H are ionized, and an outer part where only H is.

If the gas-phase metallicity of the birth cloud is high enough, the H II region may also contain a significant fraction of more complex molecules and dust grains. These dust grains are likely to be partly photo-dissociated by energetic stellar radiation, thus absorbing some of the ionizing photons. Dust grains can also act as catalysts for some photo-induced chemical reactions, thus interfering with the chemical composition of the region.

All these factors result in complicated spectra from H II regions. I therefore provide more details on the mechanisms at play for both the continuum and emission-line components of H II-regions spectra in the next section.

1.3.2 Continuum emission and dust in ionized regions

H II regions emit continuum radiation across the whole electromagnetic spectrum due various electronic processes, as electrons are released by photoionization. The main two processes at play are *free-free* and *free-bound interactions*.

Free-free interaction, or Brehmsstrahlung (literally "braking radiation"), occurs when free electrons interact with ions of the medium without being captured. This interaction results in a scattering of the electrons, and a braking which releases an energy continuum ranging from radio to near-thermal energies. This effect is schematically illustrated in Figure 1.12. This emission results from a transition between two kinetic energy states of the free electrons. In H II regions, it usually peaks at low energies and represents the main source of radio emission. At low frequencies, free-free absorption can also be observed, where an electron is accelerated to a higher kinetic energy-level by the absorption of a low-energy photon (Draine, 2011b).

Free-bound emission involves the capture of an electron by an ion of the surrounding medium. The emitted photon then comes from the transition between a free state and a specific bound energy level. This is the inverse process to photoionization, where an electron is ejected from a bound level of an atom under the effect of an incoming photon. This process of electron capture is also called radiative recombination, so free-bound emission is more frequently referred to as the *recombination continuum*. This continuum exhibits a very specific spectrum shape, with steep steps corresponding to the energies of the different ionization thresholds of the atom (H and He in H II regions), followed by a continuum due to the electron initially spanning a whole range of energies. An example of such spectrum is shown in Figure 1.13. For the hydrogen continuum, the different discontinuities correspond to the familiar series of recombination lines: the Lyman-break for recombination to the level $n = 1$, the Balmer-break for recombination to $n = 2$, the Paschen-break for recombination to $n = 3$, and so on.

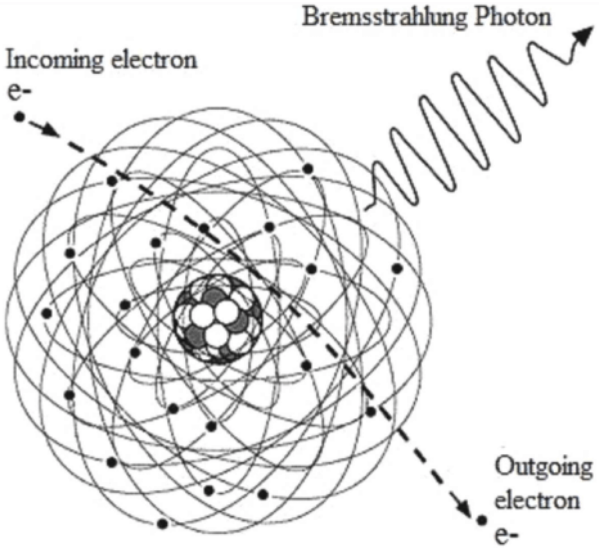

Figure 1.12: Schematic representation of a free electron being scattered and slowed down by its interaction with an stationary ion, and of the resulting Brehmsstrahlung emission. *Credit: Tekin et al. (2017).*

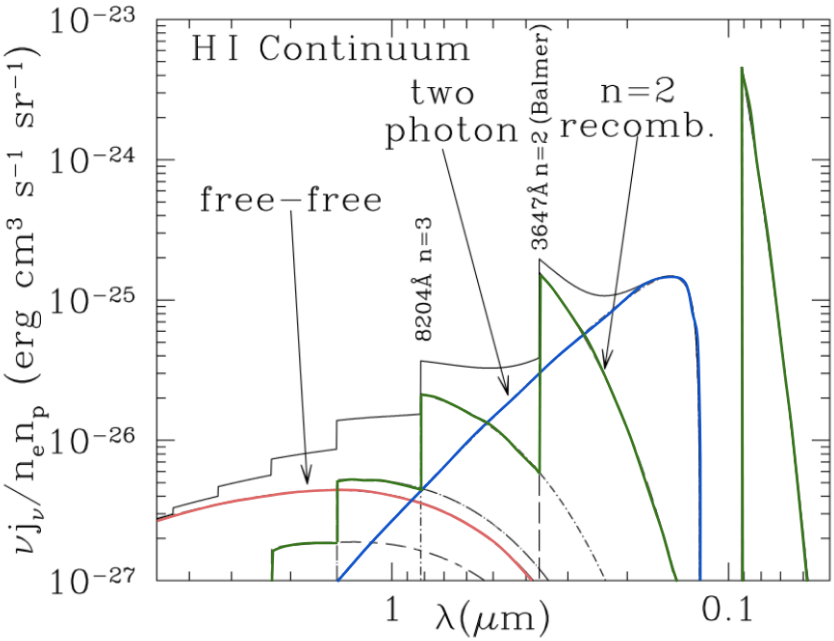

Figure 1.13: Various contributions to the continuum spectrum (emission lines are not shown) of a hydrogen plasma at $T \sim 8000$ K. The y-axis represents the specific emissivity, normalized by the electron and H^+ number densities. The red curve represents Brehmsstrahlung emission, the blue curve two-photon emission, and the green curve the hydrogen recombination continuum. The two-photon contribution represented here fades at densities $n_H \gtrsim 10^3$ cm^{-3}. *Credit: Original image from Draine (2011b).*

Figure 1.13 shows an additional process contributing to the continuum in the UV range: the *two-photon process*. This emission comes from a spontaneous transition between the two first energy levels of an atom, when the creation of a virtual level causes the emission of two photons of lower energies instead of a single one.[12] As this decay is strongly forbidden (e.g., Draine, 2011b), this emission has a low probability, but in low-density regions where collisions are rare it is not negligible. Indeed, in the case of neutral hydrogen, it is the only radiative transition from the metastable $2s^2$ excited state to the ground state, so in cases where the atom cannot de-excite collisionnally, it is the main channel for $2s \rightarrow 1s$ transitions. A similar process can also occur in neutral helium gas. This continuum emission can therefore become important at UV wavelengths in low-density cases.

Dust present in the H II regions (particularly at high metallicities) interacts with stellar radiation and the surrounding gas. Dust grains preferentially absorb radiation at UV wavelengths (including ionizing photons with energies greater than 13.6 eV). This absorption has the effect of heating the dust and re-emitting a thermal continuum at infrared wavelengths. The loss of energy between the absorbed and re-emitted photons is due to vibrational and molecular transitions in the dust molecules, resulting in inelastic scattering. In fact, dust emission generally dominates the spectrum at wavelengths between 5 and 600 μm. This alters the overall shape of the spectrum by changing the energies of the absorbed photons. When considering the impact of dust, the standard terminology (e.g., Meurer et al., 1999; Calzetti, 2001) reserves the term *extinction* for the combination of absorption and scattering of photons off individual lines of sight, whereas *attenuation* represents the combination of absorption and scattering into and out of the line of sight due to local and global geometric effects. Dust attenuation models generally distinguish between several dust components: dust in the ionized interiors of stellar birth clouds; dust in the outer neutral envelopes of these clouds; and dust in the diffuse ISM (e.g., Charlot and Fall, 2000; Calzetti, 2001).

Dust emission can also have an impact on the physical properties of the H II region: the additional radiation pressure from the emitted IR photons has to be compensated for, and the amount of ionizing photons is reduced. The result is a shortening of the radius of the region and a rearrangement of the gas leading to an inhomogeneous gas density within the region, with less ionized gas near the star and increased density at the edges of the region (see, e.g., Petrosian et al., 1972; Draine, 2011a, for a detailed formalism for the impact of dust on H II regions properties). In addition, ions in the H II region can interact with dust grains, exchanging electrons with them (leading to a decrease in the fraction of ionized gas), or be condensed onto dust grains in a phenomenon called *depletion*, leading to changes in gas abundance. These complex interactions reveal the need to accurately model dust-related processes in the H II regions in spectral modelling of stellar populations. However, it is important to keep in mind, when studying the primordial Universe, that these processes are described for dust grains composed mainly of metals such as O, Si, C, Mg and Fe (e.g., Draine, 2003; De Cia et al., 2016), so the importance of these interactions should be less for metal-poor star-forming regions.

1.3.3 Emission lines and photoionization

In the previous section, I provided a brief overview of the physical processes involved in continuum emission from H II regions. However, the spectra of such regions are also characterized by intense emission lines resulting from the photoionization by hot stars, whose emission mechanisms I discuss in the present section.

As described in section 1.3.2, radiative recombination between a free electron and a photoionized H^+ ion generates a continuum due to the range of energies these electrons can carry prior to interaction. Once the electron has been captured on one of the energy levels of the hydrogen atom, if it is at higher energies than the ground state, it progressively de-excites and cascades down to lower energy levels until it reaches the ground state. This results in transitions with given energy differences, which create not continuum radiation, but emission lines at these very specific energies. These lines are called recombination lines, and are named based on the transition levels, just like the breaks for the continuum

[12] In this case, the sum of the energies of the two photons has to be equal to the energy difference between the first and ground states.

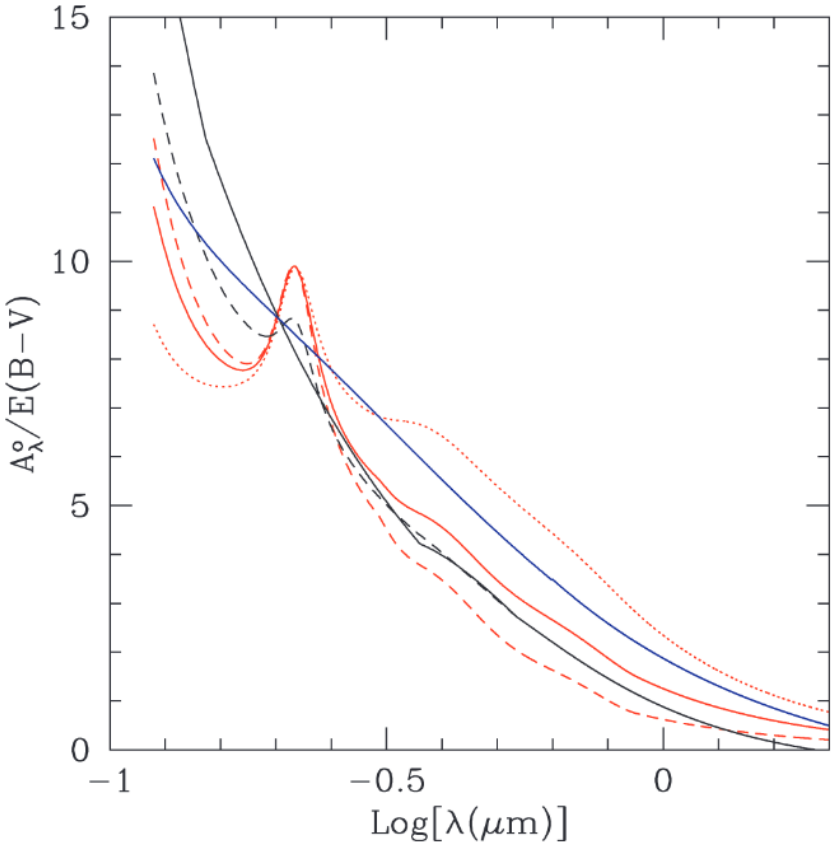

Figure 1.14: Examples of extinction curves in local galaxies. The orange curves represent different empirical models of the Milky-Way extinction curve, reflecting the expected variation in the properties of interstellar dust along different lines of sight. The solid and dashed black curves represent the extinction curves of the Small and Large Magellanic Clouds, respectively. The dark-blue curve represents a mean attenuation curve for starburst galaxies, constructed by Calzetti (2001) on the basis of local observations. *Credit: Calzetti (2001).*

emission: the Lyman series for transitions to the ground level, the Balmer series for transitions to $n = 2$, the Paschen series for transitions to $n = 3$, etc. To fully characterize the transition, a Greek letter is added to indicate the number of levels the electron has passed during the transition: α for 1 level, β for two, and so on. The overall recombination lines are therefore called Lyman-α ($n = 2 \rightarrow n = 1$), Lyman-β ($n = 3 \rightarrow n = 1$), Balmer-α ($n = 3 \rightarrow n = 2$), Balmer-β ($n = 4 \rightarrow n = 2$), and so on. These transitions for hydrogen are represented in Figure 1.15. The strongest recombination lines for hydrogen are Lyman-α (Lyα, at 1216 Å) in the UV range, and Balmer-α (Hα, at 6562 Å) and Balmer-β (Hβ, at 4861 Å) in the optical range. In the regions where the ionization field is intense enough to produce a significant amount of ionizing photons with extreme energies greater than 54.4 eV, He is doubly ionized and intense helium recombination lines can be observed, such as He II λ1640 and He II λ4686 (or He I λ3889, He I λ6678, He I λ7065 for lower-ionization regions, where He is only singly ionized). Following the same process, radiative recombination lines can also be observed for metals, although they are much weaker than H and He lines.

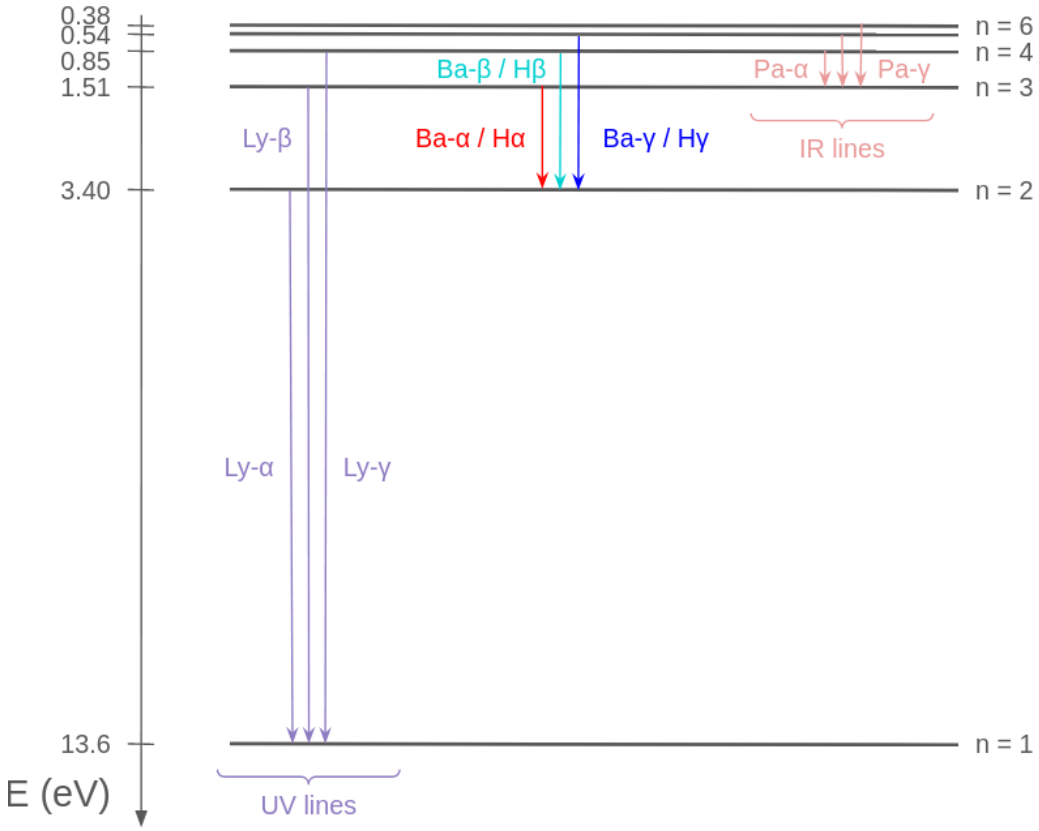

Figure 1.15: First series of recombination transitions for hydrogen. The colour of a transition indicates the wavelength of the resulting recombination line.

As far as radiative recombination is concerned, it is useful to separate star-forming regions into two categories: the optically thin ones, where all Lyman-series photons produced by recombination can escape the nebula without being recaptured by other neutral atoms; and the optically thick ones, where all Lyman-series photons are recaptured and all electrons finally cascade down to the $n = 2$ level, before finally producing only Ly-α photons (or decaying through the two-photon process in cases of low-enough densities; see section 1.3.2). These cases are respectively named *case-A* and *case-B recombination*, the latter being the most frequent at the typical densities of H II regions ($\sim 10^2$–$10^3\,\mathrm{cm}^{-3}$), where Lyman-series photons are likely to be reabsorbed. In case B, as all electrons are expected to reach the $n = 2$ level before their final decay, each ionization results in the production of a Balmer-series photon: this makes the number of Balmer photons a reliable indicator of the production rate of ionizing photons by the central source of the region. In the remainder of this work, I will consider only case-B recombination for H and He.

In general, H II-regions spectra also show intense collisionally-excited lines of metals. Heavier elements, whether photoionized or neutral, can enter an excited state following collisions with thermal electrons accelerated by photoionization. In such a case, one of the electrons bound to the atom moves to a higher energy level due to the absorption of some energy from the incident thermal electron. These metastable states should have long lifetimes, and these excitations should not normally result in radiative decay, as the probability of spontaneous radiative decay is much lower than that of collisional de-excitation under classical conditions for these states. Such emission lines are therefore qualified as forbidden, or semi-forbidden, depending on how low the probability of radiative decay is.[13] At the typical densities of H II regions, however, the probability of collisional de-excitation is low, and these states can decay radiatively. This gives rise to several forbidden or semi-forbidden lines in H II-regions spectra, whose intensities depend on the abundances of the different metals and the density of the region. Some of the most frequently observed lines are, for example, C III] λ1908, the oxygen doublets [O II]$\lambda\lambda$3726, 3729, O III]$\lambda\lambda$1661, 1666 and O III $\lambda\lambda$4959, 5007, and [N II] λ6584. Because of their sensitivity to temperature, density and abundance, these collisionally-excited lines can provide important insight into the physical conditions of H II regions.

In short, the very hot young stars at the centre of H II regions emit intense and energetic radiation which can at least partially ionize their environment. Such an ionized H II region absorbs part of the stellar emission through its dust and interactions with its gas, but reemits a continuum emission and some additional emission lines (called *nebular* emission lines) specific to the elements contained in the gas through the various mechanisms introduced in sections 1.3.2 and 1.3.3. An example of spectrum emerging from such a region is shown in Figure 1.16. The study of such a spectrum can provide valuable information to infer the physical conditions of the gas within the H II region, and the sources of the ionizing radiation. In the next section, I present the main diagnostics that can be constructed from H II-regions spectra and what they can tell us about the properties of star-forming regions.

1.4 Emission-line diagnostics

Nebular emission lines can provide valuable constraints on the sources of ionizing photons and the physical conditions in the ISM of observed galaxies. These spectral constraints can be derived from two types of indicators: emission-lines ratios, i.e. ratios between the intensities of two emission lines, which can be from the same or different species and at the same or different ionization levels; and equivalent widths, defined as

$$W_\lambda = \int_0^\infty \mathrm{d}\lambda \left(\frac{L_\lambda}{L_{\mathrm{cont}}} - 1 \right) . \tag{1.11}$$

where L_λ and L_{cont} are, respectively, the total (line+continuum) and pure-continuum spectra (in units of luminosity per unit wavelength). While line ratios can indicate the ionization levels and abundances of elements in the gas, equivalent widths provide information about the strength of an emission line relative to the continuum around a given wavelength. To be a useful probe for spectral analysis, a species has to be sufficiently abundant, and exhibit radiative transitions probable enough and in the right energy ranges.

A first, useful diagnostic of emission lines is that the presence of high-ionization lines requiring high ionization energies (such as He II, C III], C IV, O III] and Ne III lines) indicates a very hot source capable of producing highly energetic photons. The following paragraphs give more quantitative details on the methods to better quantify thermodynamic quantities (section 1.4.1), abundances (section 1.4.2) and source properties (section 1.4.3) using spectral analysis. To clarify the notation adopted here, the transition wavelengths given in the following section and the rest of this thesis are rest-frame wavelengths, in units of Å.

[13] Forbidden emission lines are distinguished by being written in square brackets, whereas semi-forbidden lines are written with a single bracket.

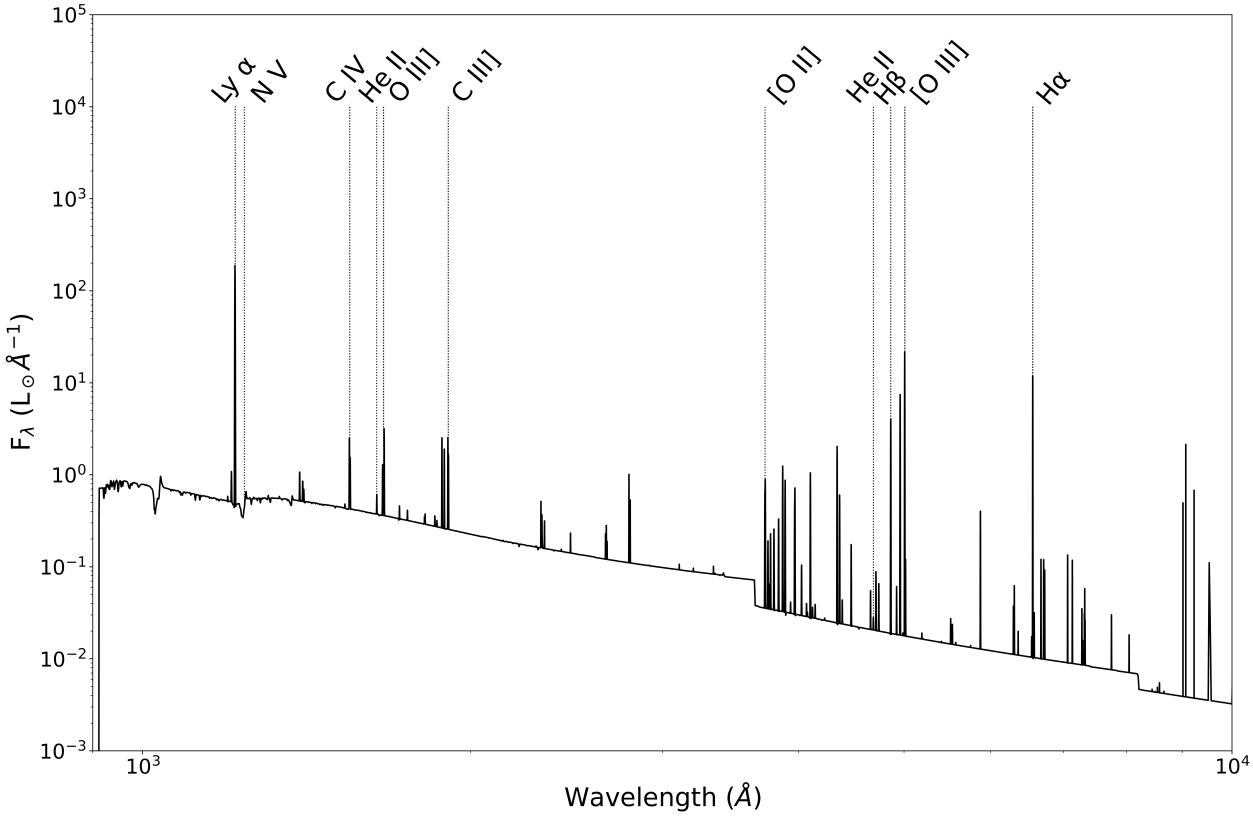

Figure 1.16: Modelled rest-frame spectrum of an H II region of gas-phase metallicity Z = 0.001, surrounding a generation of stars of the same metallicity with an age of 1 Myr. This spectrum shows the peak in stellar emission at UV wavelengths (on the left of the plot), different breaks in the continuum, including the Balmer and Paschen recombinaton breaks and the Lyman break (below which all photons are absorbed by neutral hydrogen, and cannot be observed), and some recombination and collisionally-excited lines of the most abundant elements.

1.4.1 Constraints on the thermodynamics of the gas

The first thermodynamic quantity that can be constrained through line ratios in the ionized gas is the electronic temperature T_e. At a given density, if the two excited levels involved in two transitions of a same atom or ion have an energy difference around $k_\mathrm{B}T$, and because in this case the probability of populating both levels is directly linked to T_e, the intensity ratio will probe the difference in atomic-level population, and hence the electronic temperature. Draine (2011b) shows[14] that, in the low-density limit ($\sim$ 1–$10^3\,\mathrm{cm}^{-3}$), the emissivity ratio between ($n = 4 \rightarrow n = 3$) and ($n = 3 \rightarrow n = 2$) collisionally-excited transitions depends only on fixed atomic quantities and an $\exp(-k_\mathrm{B}T_\mathrm{e})$ term for np^2 and np^4 ions,[15] that is, mainly O III] and [N II] at low metallicity (and to a lesser extent [S III] and Ne III for more metal-rich H II regions). This makes the line ratios [O III]λ4363/λ5007, [N II]λ5755/λ6584 and [S III]λ6312/λ9532 the best estimators of the electronic temperature. Such a measurement based on the direct comparison of nebular emission lines is called the *direct-T_e* method, and is generally considered to be the most accurate method to derive the thermodynamic state of the gas. The top panels of Figure 1.17 show the strong dependence of these line ratios on temperature at fixed density.

The electron density n_e can be determined in a similar fashion. This time, the two excited levels involved in the two transitions should have similar energies, making the transition probability weakly sensitive to temperature, as the difference in the probability of populating both levels will not depend on T_e. In this configuration, the emissivity ratios in the low-density and high-density cases will exhibit two different behaviours, which will provide an estimate of the density (or at least an upper limit). The

[14] See their Chapter 18.1 for the detailed atomic calculations and electronic diagrams.

[15] In practice, the sufficient-abundance constraint limits these considerations to the $2p^2$, $2p^4$, $3p^2$ and $3p^4$ ions at most.

bottom panel of Figure 1.17 shows the dependence of two such emissivity ratios on n_e. If the measured intensity ratio is on the low- or high-density plateau, this method will only be able to give an upper or lower limit for n_e values, but in the intermediate regime, it will provide an accurate estimate of n_e. Atomic calculations and atomic-configuration diagrams in Draine (2011b, see their Chapters 18.2 and 18.3) show that this is the case for [O II] and [S II]. This makes [O II]λ3729/λ3726 and [S II]λ6717/λ6731 good estimators of the electron density in H II regions.

It is important to keep in mind that this approach provides only mean estimates of the electronic temperature and density. Indeed, temperatures are expected to be largely inhomogeneous in H II regions, and line ratios such as [O III]λ4363/λ5007 can only give access to the temperature in the O III] ionization zone. Recent work (see e.g., Cameron et al., 2023a) has suggested alternative ways of estimating an integrated temperature, to better account for the homogeneity of temperatures in H II regions.

1.4.2 Abundance determinations

If the radiation emitted by the central source of an H II region is energetic enough to ionize He, the abundance of He relative to H can be determined directly by comparing the intensities of H and He radiative recombination lines, as the rates of radiative recombination for He and H have a very similar dependence on T_e and n_e.

For heavier elements, it is possible to estimate the abundance of a given metal relative to H by comparing the intensity of one of its collisionally-excited transition lines to some H radiative-recombination lines, as a function of T_e and n_e. For example, for doubly-ionized oxygen, it is possible to derive (see Draine, 2011b, for the complete calculation)

$$\frac{[O^{2+}]}{[H^+]} = C\frac{I([O\,III]\,\lambda5007)}{I(H\beta)} f(T_e, n_e)\,, \tag{1.12}$$

where $f(T_e, n_e)$ depends only on transition rates and energies and atomic coefficients which can be determined theoretically. The total oxygen abundance relative to H can then be determined as

$$\frac{[O]}{[H]} = \frac{[O^0]}{[H^+]} + \frac{[O^+]}{[H^+]} + \frac{[O^{2+}]}{[H^+]}\,, \tag{1.13}$$

assuming that H is fully ionized in the H II region. One subtlety is that the electron temperature in the H II region generally differs between the O^+ and O^{2+} emission zones[16] (the neutral oxygen abundance being negligible), and so the equivalent of equation (1.12) must be used to constrain $[O^+]/[H^+]$, usually on the basis of the ratio between the intensities of the auroral ($\lambda\lambda$7320, 7330) and nebular ($\lambda\lambda$3726, 3729) [O II] lines.

Therefore, accurate measurements of T_e and n_e, and the detection of Hβ and emission lines of transitions at different ionization levels of the metal of interest, allow its abundance in the gas phase to be estimated theoretically.

Photoionization models offer an alternative way of estimating the total abundance of an element through the fitting of even a limited number of lines, since they account for the temperature structure of an H II region, and hence, the relative abundances of all the different ionic species of that element. Clearly, the results of such an approach depend sensitively on the adopted model. Therefore, the choice of model parameters is crucial in these measurements, and typical parameters derived from studies of local H II regions may not be appropriate to investigate the pristine environment of primeval galaxies. These limitations, and more sophisticated models able to circumvent the issues they raise, are explored in Gutkin et al. (2016).

[16] H II regions are generally stratified in ionization structure, with O^{2+} zones lying closer to the ionizing source than O^+ zones.

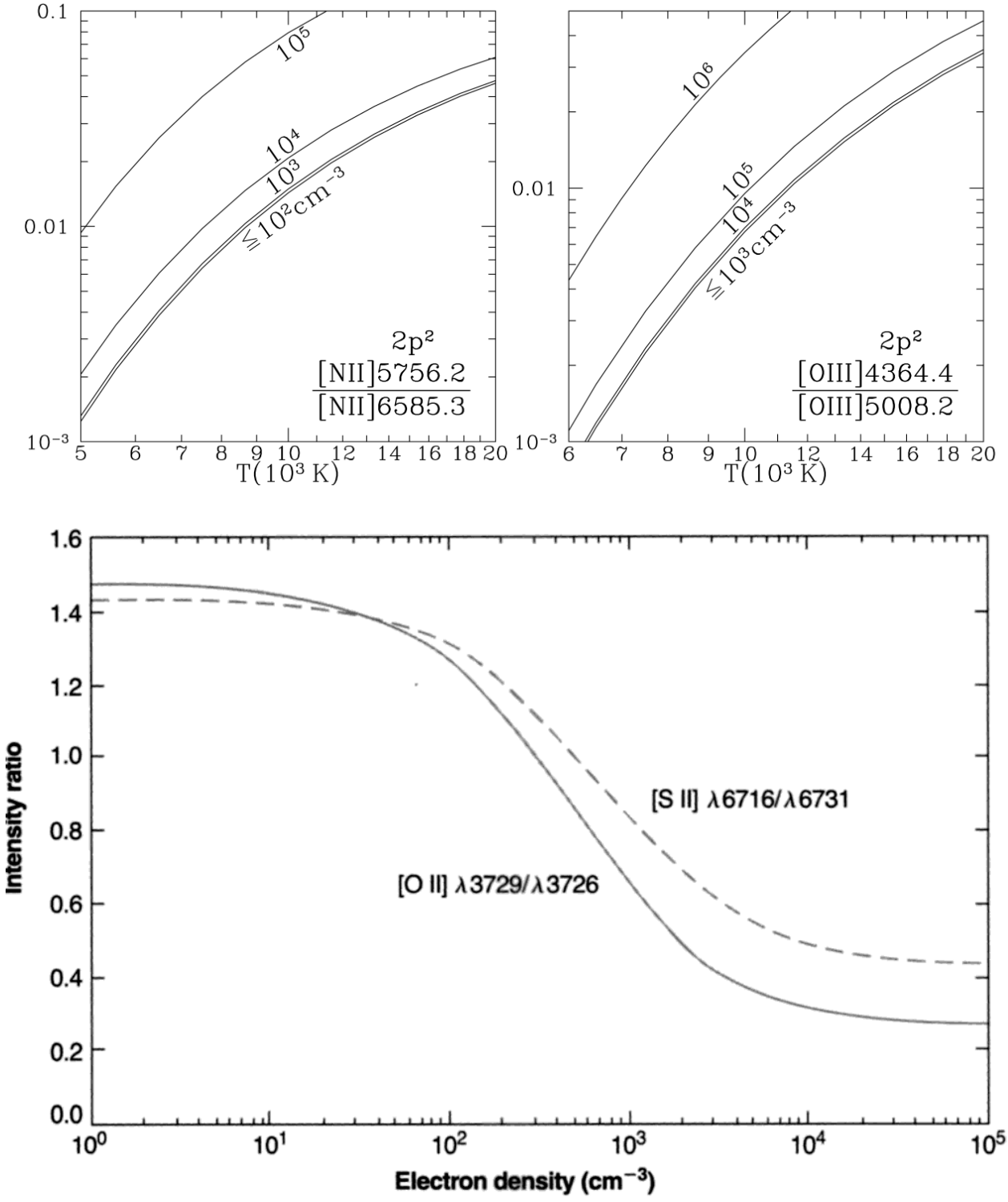

Figure 1.17: Top panel: Intensity ratios of [N II]λ5755/λ6584 and [O III]λ4363/λ5007 as a function of temperature, for different densities. The strong temperature dependence of these ratios makes them good probes for T_e. Bottom panel: Intensity ratios of [O II]λ3729/λ3726 and [S II]λ6717/λ6731 as a function of electron density, for T = 10^4 K ($n_e/\sqrt{T/10^4 K}$). The shapes of these curves make these line ratios good estimators of n_e. *Credit: Draine (2011b) and Osterbrock and Ferland (2006)*

As the high-ionization lines used to reliably measure T_e and n_e are often weak and not always detected in galactic spectra, especially at low metallicities, other statistical approaches have been developed to estimate element abundances. These are generally called *strong-line* methods, and although they are less accurate because of being statistical methods, they can be used to roughly estimate metallicity and abundances when the direct-T_e method is not applicable to measure T_e. In these methods, first proposed by Pagel et al. (1979), element abundances are inferred from intensity ratios of strong collisionally-excited lines to H recombination lines, based on predictions of photoionization models. For example, Kewley and Dopita (2002) establish calibrations between $R_{23} = ([\mathrm{O\,II}]\lambda3727 + \mathrm{O\,III}\,\lambda\lambda4959,5007)/\mathrm{H}\beta$ and [O/H] for different photoionization parameters. These calibrations show complex behaviour of such ratios with nebular parameters, which requires the complementary use of other lines to settle the choice of suitable nebular parameters. These methods rely on the underlying assumptions of the chosen photoionization model,[17] and these line-intensity ratios can also be affected by other physical parameters, such as cooling mechanisms, gas properties, and the rate of ionizing photons produced by the central source.

Other nebular parameters can be estimated using line ratios, in what are called emission-line diagnostic diagrams. For instance, higher-to-lower ionization ratios for a same element (e.g., $[\mathrm{O\,III}]\,\lambda5007/[\mathrm{O\,II}]\lambda3727$ or $\mathrm{C\,IV}\,\lambda1549/\mathrm{C\,III}]\,\lambda1908$) tend to increase as the volume-averaged ionization parameter increases. Also, ratios of metals-to-H and metals-to-He lines tend to first increase with metallicity, then decrease when the amount of efficiently-cooling species becomes high enough in the interstellar gas. The joint study of several diagrams of this kind, to try to account for degeneracies in the dependence of line ratios on the different nebular parameters, can provide valuable information on the physical conditions in star-forming regions and will be studied in more detail in chapter 3.

1.4.3 Insight into the radiation sources

The emission-line diagrams described in the previous paragraph can also help to discriminate between different potential origins of the ionizing radiation from an observed spectrum. Outside star-forming regions, strong emission lines in an observed galactic spectrum may result from the ionization of interstellar gas by intense radiative shocks, an active galactic nucleus (AGN), very hot isolated stars, etc., making it difficult to draw direct conclusions as to which lines might be characteristic of such emission. Baldwin et al. (1981) were the first to introduce this type of diagnostic diagram and used them to show that some specific ratios could highlight specific regimes characteristic of one or other possible source of radiation. The most widely used such diagram, now called *BPT* diagram after these authors, represents $[\mathrm{O\,III}]\,\lambda5007/\mathrm{H}\beta$ as a function of $[\mathrm{N\,II}]\,\lambda6584/\mathrm{H}\alpha$, and is shown in Figure 1.18. These emission lines have the great advantage to be strong even for metal-poor star-forming galaxies. Other lines, much fainter and rarely observed in distant galaxies, are considered to be characteristic of some of these potential sources and may complement this diagnostic if they are observed. For instance, strong $[\mathrm{Ne\,V}]\,\lambda3426$ emission is suggested to be closely linked to strong radiative shocks (e.g., Izotov et al., 2012), whereas $\mathrm{N\,V}\,\lambda1240$ emission is often expected in the narrow-line regions of AGNs (e.g., Feltre et al., 2016).

Other spectral features can be used to estimate various characteristics of star-forming regions. For example, the *star-formation rate* (SFR) can been estimated from the luminosities of emission lines (particularly Hα) and the continuum. Indeed, Kennicutt (1998, see also Kennicutt and Evans 2012) proposed widely-used formulæ to estimate the SFR directly from the observed spectra, such as

$$\begin{aligned}\mathrm{SFR}\,(\mathrm{M_\odot\,yr^{-1}}) &= 7.9\times10^{-42}\,L(\mathrm{H}\alpha)\,(\mathrm{erg\,s^{-1}})\\ &= 1.08\times10^{-53}\,Q(H^0)\,(\mathrm{s^{-1}})\end{aligned} \tag{1.14}$$

where $L(\mathrm{H}\alpha)$ is the luminosity of the Hα line and $Q(H^0)$ the rate of H-ionizing photons produced by newly-born stars (which is linked to the assumed IMF), and

$$\mathrm{SFR}\,(\mathrm{M_\odot\,yr^{-1}}) = 1.4\times10^{-28}\,L_{1500\text{Å}}\,(\mathrm{erg\,s^{-1}\,Hz^{-1}}) \tag{1.15}$$

[17] It is important to keep in mind that this is often also the case for direct-T_e determinations.

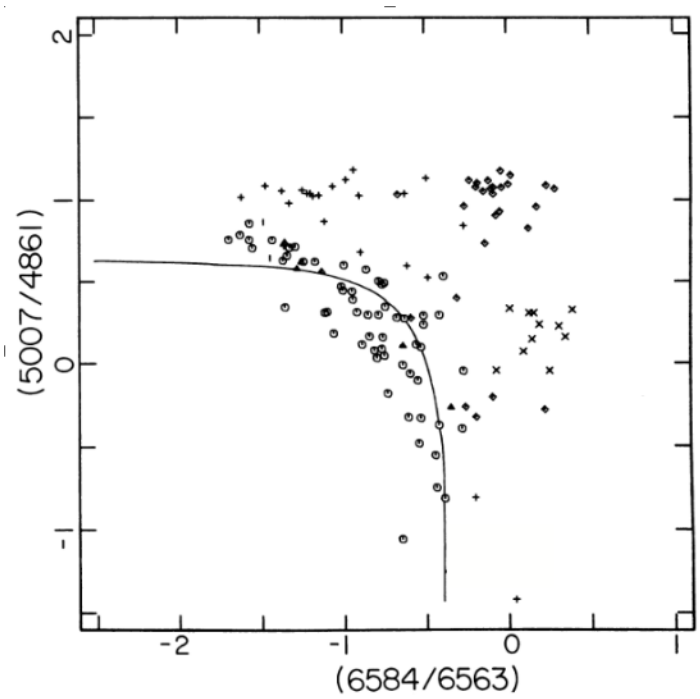

Figure 1.18: Original BPT diagram published by Baldwin et al. (1981), showing $\log([\mathrm{O\,III}]\,\lambda5007/\mathrm{H}\beta)$ as a function of $\log([\mathrm{N\,II}]\,\lambda6584/\mathrm{H}\alpha)$. The different symbols correspond to different sources of ionizing radiation: circles for classical H II regions, triangles for extragalactic H II regions, +'s for planetary nebulæ, ×'s for shock-heated regions, and diamonds for sources with a power-law SED. The different types of sources are grouped into reasonably well-separated regions, enabling a rapid estimate of the mechanism at work in the ionizing emission of an observed object. The solid line shows the limit between classical H II regions and other sources.

where $L_{1500\text{Å}}$ is the continuum luminosity in the range 1500-2800 Å. These formulæ are approximate and are those used in the work of Umeda et al. (2022) and Katz et al. (2023) discussed in section 4.1.3.

Equivalent widths are another useful spectral feature, allowing us to probe emission-line strengths relative to the continuum. For lines such as Hα and Hβ, this gives direct insight into the star-formation history, as the line luminosities depend on the production of ionizing photons by newly-born stars, while the continuum emission is dominated by cool evolved stars. However, such tracers should be treated with caution, as for example binary interaction may give rise to late production of ionizing photons. This will be discussed in more detail in chapter 2.

Other uses of spectral features to infer the properties of star-forming regions go beyond the main focus of this thesis. For the sake of completeness, it is important to mention that in cases where emission lines can be resolved, the study of line profiles and relative redshifts can provide valuable information about the mechanisms responsible for the broadening and shifting these lines, that is, gas kinematics (see, e.g., Mink and Wyatt, 1995; Steidel et al., 2010; Carniani et al., 2015; Übler et al., 2023). Finally, spectral energy distributions can be used to measure the redshift of distant galaxies, either by using the break-detection methods mentioned in section 1.1.5, or by identifying strong lines and directly estimating their redshift.

1.5 Outline

In this thesis, I present the new GALSEVN model for the spectral characterisation of primeval galaxies and their analogues, which takes into account the theoretical elements of the evolution of massive and binary stars discussed above. I therefore detail, in chapter 2, the codes used in this work to model stellar populations and photoionization, after giving a brief overview of the different methods and models that can be used to describe the emission of stellar populations.

I show that the models we use achieve unprecedented accuracy in reproducing the spectra of metal-poor star-forming galaxies, before focusing in chapter 3 on exploring the impact of model parameters on the agreement with observed data of primeval-galaxy analogues. I then complement these models, in chapter 4, with additional modelling of two specific processes which may be important in describing the emission spectrum of primeval galaxies: emission lines originating from regions heated by shocks driven by stellar winds and supernovæ; and continuum emission arising from accretion discs in X-ray binaries. Chapters 2, 3 and 4 are mainly based on the work presented in Lecroq et al. (2024), although with some more detail given to the general context and model description.

After confirming the agreement of the model with most observational constraints for stellar populations with metallicities of a few per cent of solar, I focus, in chapter 5, on predictions at extremely-low metallicities, which may be encountered in Reionization-Era galaxies. I supplement the somewhat restricted spectral predictions for such stellar populations, limited by the presence in their environment of hydrogen and helium only, with additional predictions for observables characterising their ionizing power. Finally, I explore the possibility of detecting gravitational waves from remnants of such extreme populations, which are extremely difficult to observe directly. The work presented in this chapter is the subject of a study in progress which will be submitted for publication.

Lastly, in chapter 6, I present the approach that can be used to constrain properties of stars and the ISM from observations of high-redshift galaxies, based on Bayesian in inference using the GALSEVN model library. This final chapter paves the way for promising future work on SED fitting for high-redshift and Reionization-Era observations, which will be able to provide unprecedented insight into the physical conditions in the early Universe.

Chapter 2

Modelling spectra of stellar populations

Contents

The *James Webb Space Telescope* (*JWST*) has opened a new window on the rest-frame ultraviolet and optical emission of young galaxies at the Epoch of Reionization. The emission-line signatures of such galaxies should contain valuable information about the sources that potentially contributed to reionizing the Universe. Over the past several years, numerous studies have been conducted at various redshifts to characterize and analyse the ultraviolet and optical spectra of metal-poor, actively star-forming galaxies approaching the properties of these Reionization-era galaxies (e.g., Stark et al., 2014; Steidel et al., 2016; Amorín et al., 2017; Senchyna et al., 2017; Nakajima et al., 2018; Berg et al., 2022). These observations have put a heavy strain on models designed to interpret the nebular emission from young galaxies, as some emission lines requiring highly energetic photons, such as He II-recombination lines, occasionally exhibit intensities so high that they cannot be reproduced by standard models fitting lower-ionization lines (e.g., Shirazi and Brinchmann, 2012; Nanayakkara et al., 2019; Stanway and Eldridge, 2019; Plat et al., 2019; Schaerer et al., 2019; Olivier et al., 2022).

In the first part of this thesis, I explore the emission-line properties of interstellar gas photoionized by young binary-star populations computed using a new spectral-synthesis model, built by combining the SEVN (Iorio et al., 2023) and GALAXEV (Bruzual and Charlot, 2003) population-synthesis codes, coupled with the CLOUDY photoionization code (Ferland et al., 2017). This spectral-synthesis model, called GALSEVN, enables us to compute, for the first time in a physically consistent way, the emission from stars, accretion discs of X-ray binaries and radiative shocks driven by stellar winds and supernova explosions in young, metal-poor galaxies.

In this chapter, after a brief overview of the principles of stellar population modelling, I describe the models we used to compute the stellar and nebular emission from young galaxies. Following the

approach of Charlot and Longhetti (2001, see also Gutkin et al. 2016), the luminosity per unit frequency ν emitted at time t by a star-forming galaxy can be expressed as

$$L_\nu(t) = \int_0^t \mathrm{d}t' \, \psi(t - t') \, S_\nu[t', Z(t - t')] \, T_\nu(t, t') \, , \tag{2.1}$$

where $\psi(t - t')$ is the star formation rate at time $t - t'$, $S_\nu[t', Z(t - t')]$ the luminosity produced per unit frequency per unit mass by a single generation of stars of age t' and metallicity $Z(t - t')$, and $T_\nu(t, t')$ the transmission function of the interstellar medium (ISM). We compute S_ν for populations of single and binary stars using a combination of the SEVN (Iorio et al., 2023) and GALAXEV (Bruzual and Charlot, 2003) population-synthesis codes, as described in section 2.1.2, and T_ν using the CLOUDY photoionization code (Ferland et al., 2017) in the way presented in section 2.2.1.

2.1 Stellar population modelling

2.1.1 Generalities on population synthesis codes

The physical properties of distant, unresolved stellar populations are mainly estimated from their integrated light, that is, their *spectral energy distribution* (SED). Such properties range from the distribution of stellar masses to the star-formation histories, to element abundances and physical conditions in the ISM. Models are necessary to link these fundamental properties with observational constraints. Translating observed SEDs into physical constraints relies on an understanding of the physics and evolution of stars, on calibrated spectral libraries to emulate the light they emit, and on some assumptions about the stellar initial mass function (IMF) and element abundances. Models which combine all these components to predict the global spectrum emitted by a star-forming region or galaxy are called *stellar population synthesis* (SPS) models, and have been extensively investigated since the pioneering work of Tinsley and Gunn (1976). An exhaustive list of such works can be found in Conroy and Gunn (2010). Charlot and Bruzual (1991) first introduced the now widely used *isochrone synthesis* method, which allows a coeval population of stars born at the same age, called *simple stellar population* (SSP), to be studied throughout their evolution by following their interpolated evolutionary tracks.[1]

For a given set of stellar evolutionary tracks, the most decisive parameter of the stellar population will be its IMF, which dictates how the stars will be distributed on the ZAMS before they evolve. Canonical IMFs are often power laws of the form $\phi(m) \propto \mathrm{d}N/\mathrm{d}m \propto m^{-(1+x)}$. Most works adopt the value $x = 1.3$ close to that of 1.35 first proposed by Salpeter (1955), with different refinements to account for the turnover at masses below $1\,\mathrm{M}_\odot$ (see, e.g., Kroupa, 2001; Chabrier, 2003). Some of the most commonly used IMFs are represented in Figure 2.1. In primeval galaxies, the metal-poor stars to form are expected to be more massive than in local galaxies due to the absence of efficient metallic coolants in the star-forming gas clouds. Therefore, IMFs which favour more massive stars, or *top-heavy* IMFs, have been suggested (e.g., Wise et al., 2012; Goswami et al., 2022) to account for such stellar populations. The impact of such top-heavy IMFs on stellar emission will be discussed in section 3.2.2. To account for more realistic star-formation histories (SFH), SSPs can be combined into composite stellar populations (CSPs). Such combination requires a description of the time evolution of the star-formation rate. A constant SFR is often considered for simplicity, although any time evolution may be adopted. This parametrization of the SFH is important, as stars in different phases dominate different parts of the spectral energy distribution. SFH shapes and estimates will be discussed in more detail in section 3.2.1.

Recent progress in stellar-evolution theory has given rise to a wide variety of SPS models, each with different approaches to address the remaining issues and uncertainties pertaining to population synthesis: the detailed treatment of stellar structure; the competing effects of the dependence on

[1] An isochrone is the region populated by all stars of the same age in the HR diagram, typically a line for stars of different initial mass with fixed metallicity. This differs from the evolutionary tracks of stars with fixed initial mass.

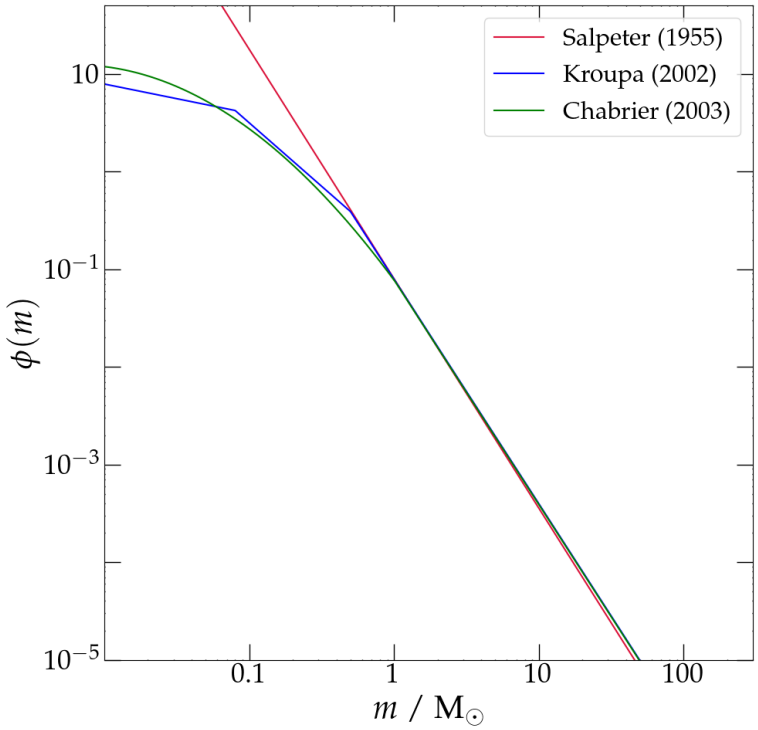

Figure 2.1: Most commonly used IMFs: the Salpeter (1955) single power-law IMF, with $x = 1.35$; the Kroupa (2001) broken power-law IMF, with $x = 1.3$ for $m > 0.5\,M_\odot$, $x = 0.3$ for $0.08 < m < 0.5\,M_\odot$, and $x = -0.7$ for $m < 0.08\,M_\odot$; and the Chabrier (2003) log-normal IMF.

age and metallicity, especially for massive stars; the treatment of variable stars, notably the TP-AGB phase; the choice of track libraries for the most extreme (giant, AGB, WR) stars and/or at largely sub-solar metallicities; the effects of multiplicity in stellar systems; the effects of high rotational velocities on massive-star evolution; non-solar abundance ratios; and ISM feedback on star formation. SPS predictions will also depend on the choice of spectral libraries: these can be theoretical or empirical, both having complementary strengths and weaknesses. Semi-empirical libraries have been constructed to overcome the shortcomings of both categories. In the next paragraphs, I provide a brief overview and comparison of some widely-used SPS codes, in order to set the context for the description of GALSEVN. Many variants of these SPS codes have been developed over the past 30 years, and the following overview is not intended to be exhaustive.

Among the most widely used SPS codes are the STARBURST99 (Leitherer et al., 1999, 2014), GALAXEV (Bruzual and Charlot, 2003; Plat et al., 2019) and Flexible SPS (FSPS; Conroy et al., 2009; Byler et al., 2018) codes. All three codes rely on interpolating the evolution of single stars over a grid of evolution tracks. They differ mainly in the theoretical prescriptions for these tracks, and much less in their adopted libraries of stellar spectra. Since these codes are constantly updated and improved, I mention here only their main distinguishing characteristics.

STARBURST99 relies on two sets of stellar evolutionary tracks, which include or not the effect of rotation on the evolution of massive stars, for a few metallicities (from the Geneva-group calculations of Ekström et al., 2012; Georgy et al., 2013). The code includes tracks for stars up to $120\,M_\odot$, but is specifically designed for the study of young stellar populations and is not suitable to describe the spectral evolution at ages above 100 Myr. The most recent version of GALAXEV incorporates evolutionary tracks, for single non-rotating stars only, from the PARSEC (PAdova and TRieste Stellar Evolution Code) library for stars with masses over the full range from 0.1 to $600\,M_\odot$ and metallicities in the range $10^{-11} \leq Z \leq 0.04$ (Bressan et al., 2012; Chen et al., 2015; Costa et al., 2019, 2023; Nguyen et al., 2022; Santoliquido et al., 2023). This code can be used to describe the spectral evolution of stellar populations over the full range of ages. Lastly, FSPS incorporates tracks for single-rotating and non-rotating stars of masses 0.1–300,$M_\odot$ over a full ranges of metallicities from the MESA (Modules for

Experiments in Stellar Astrophysics) library (Paxton et al., 2015). These three codes all rely on widely overlapping libraries for the spectral properties of massive stars of particular interest to us, namely, model spectra computed with the WM-BASIC code (Pauldrach et al., 2001) for massive O stars, and the Potsdam-WR (PoWR; Hamann and Gräfener, 2004; Sander et al., 2012; Todt et al., 2015; Hainich et al., 2019) and CMFGEN (Hillier and Lanz, 2001) codes for WR stars. These codes follow the evolution of a mono-metallic coeval SSP, and allow the user to adjust stellar-population parameters such as IMF and SFH.

The SLUG (Stochastically Light Up Galaxies; da Silva et al., 2012, 2014) code uses the same stellar-track libraries as STARBURST99, with updated Geneva and Padova stellar-evolution tracks. However, it relies on a stochastic scheme to generate stellar-population properties, rather than on a smooth, IMF-weighted sampling of isochrones. For each run, it randomly generates a star-forming cluster mass, fills this cluster with stars drawn from the chosen IMF, which are then evolved along the selected evolutionary tracks up to the maximum simulation time. This is repeated until the mass of the integrated SFH is reached by the galaxy. While this code accounts for the effects of stochasticity in star-forming regions, apparent through the observed Hα emission and other spectral features characteristic of short-lived evolutionary phases, this method also introduces a dispersion in the predicted properties. A detailed comparison between SLUG and STARBURST99 is explored in da Silva et al. (2012).

A more recent code including stellar rotation is POSYDON (Fragos et al., 2023). This code also includes interactions between stars in binary systems, using a grid of MESA (Paxton et al., 2015) stellar evolution tracks to predict stellar-population properties following the isochrone synthesis technique. However, POSYDON is a pure stellar-population synthesis code, which does not include spectral modelling. This makes a direct comparison with other recent SPS codes more complex.

On the other hand, the Binary Population and Spectral Synthesis (BPASS; Eldridge and Stanway, 2012; Eldridge et al., 2017) code, which was the first to include binary interactions in SPS modelling, combines both population and spectral synthesis. Unlike most of the SPS codes mentioned above, it does not rely on the interpolation of stellar evolution onto a grid of stellar tracks. Instead, it follows the method developed in the Cambridge STARS code (Eggleton, 1971) and solves, for each star or binary system, the detailed stellar structure and properties. To optimise these calculations, it uses an adaptive spatial and temporal mesh to precisely track stellar evolution. It then assigns a spectrum to each star throughout its evolution, using similar prescriptions to the STARBURST99, GALAXEV and FSPS codes above for hot massive O-type (WM-BASIC) and WR-type (PoWR) stars.

As with the modelling approach described in this thesis, BPASS takes binary interactions into account, but neglects the effects of rotation on the stars. It has proved remarkably effective, partly thanks to the inclusion of binary interactions, to reproduce spectral features of recent observations, with the exception of the most intense high-ionization lines such as He II (Stanway and Eldridge, 2019). As a consequence, we will focus on comparing the predictions of our SPS model GALSEVN, presented in more detail in the next section, with the most recent BPASS predictions for single and binary stellar populations. This detailed comparison will be carried out in section 2.3.3.

2.1.2 Stellar population synthesis using GALSEVN

To describe the emission from populations of single and binary stars, we appeal to a combination of the SEVN population-synthesis code (Spera et al., 2015; Spera and Mapelli, 2017; Spera et al., 2019; Mapelli et al., 2020; Iorio et al., 2023) with the GALAXEV code for the spectral evolution of stellar populations (Bruzual and Charlot, 2003). We briefly recall the main features of these codes in the following paragraph, referring the reader to the original studies for more details.

SEVN (Stellar EVolution for N-body) is an open-source binary population-synthesis code,[2] based on the interpolation of stellar properties (e.g., mass, radius, luminosity, core mass, core radius) from interchangeable libraries of pre-computed evolutionary tracks to describe the temporal evolution of stellar populations including binary-evolution processes. In this work, we adopt the PARSEC (PAdova and

[2] https://gitlab.com/sevncodes/sevn. The SEVN version used in this work is the release *Iorio22* (https://gitlab.com/sevncodes/sevn/-/releases/iorio22).

TRieste Stellar Evolution Code) library of evolutionary tracks (including pre-main sequence evolution) for stars with initial masses between 2 and 600 $M_\odot$ and metallicities in the range $10^{-11} \leq Z \leq 0.04$ (Bressan et al., 2012; Chen et al., 2015; Costa et al., 2019, 2023; Nguyen et al., 2022; Santoliquido et al., 2023). These tracks account for all stellar evolution phases mentioned in section 1.2.1, from pre-MS stars to stellar remnants, including AGB and TP-AGB stars, and heavy elements burning phases for massive stars.

The binary-evolution processes incorporated in SEVN include, most notably, mass transfer driven by winds and Roche-lobe overflow, common envelope evolution, removal of stellar angular-momentum by magnetic braking, the effect of stellar tides on orbital motions, orbital decay through gravitational-wave emission and stellar mergers. These are described in depth in section 2.3 of Iorio et al. (2023). I only provide here a short summary describing how SEVN handles binary-evolution products using the PARSEC tracks adopted in this study.

The SEVN code evolves stars in a binary system by interpolating from a set of precomputed single-star tracks from the PARSEC library. The evolution of a star involves interpolation from four tracks bracketing its mass and metallicity (see Iorio et al. 2023 for details). However, binary processes, such as wind mass transfer, Roche-Lobe overflow and stellar mergers, can significantly alter the properties of a star. In such cases, SEVN searches for new tracks to interpolate from to better match the current stellar properties. This is achieved through different strategies tailored to specific situations, as follows.

- Mass loss/accretion: for main-sequence stars, SEVN checks whether the net cumulative mass variations due to binary processes exceed 1 per cent of the current stellar mass. In such cases, SEVN searches for new interpolating tracks providing a better match to the total mass of the star at the same percentage of stellar life. The evolution of stars with decoupled He and CO cores is driven by core properties (Hurley et al., 2002). For this reason, we do not allow stars outside the main sequence to change stellar tracks unless the core mass has changed (e.g., during stellar mergers) or the star has completely lost its envelope.

- Envelope stripping: if a star completely loses its envelope, SEVN switches to pure-He stellar-evolution tables, selecting the pure-He interpolating tracks that best match the mass of the bare He core at the same percentage of stellar life. In this work, we use the PARSEC pure-He stellar-evolution tables described in Iorio et al. (2023). When a pure-He star loses its He envelope, SEVN models the bare CO core as a remnant: if the core is massive enough to produce a black hole or neutron star, its properties remain constant until remnant formation, otherwise it immediately becomes a white dwarf.

- Stellar merger: depending on the properties of the merging stars, SEVN employs different strategies to select the interpolating tracks for the merger product. If two main-sequence stars merge, SEVN changes stellar evolution tracks similarly to cases of mass loss or accretion. Instead, if at least one of the merging stars is evolved, SEVN searches for new interpolating tracks by matching the core mass at the same percentage of stellar life. For mergers between a 'standard' star and a stripped, pure-He star, SEVN searches for new interpolating tracks in the H-rich tables matching the new core mass. We assume that mergers between stars and remnants (white dwarfs, neutron stars, black holes and bare-CO cores) completely destroy the star, leaving only the remnant, and no mass is accreted on to the remnant.

Additional details about the strategy for selecting interpolating tracks of binary-evolution products in SEVN can be found in Iorio et al. (2023).

In the simulations presented in this thesis, mass transfer is assumed to be always stable for donor stars on the main sequence and in the Hertzsprung gap. For other stars, mass transfer stability depends on the binary mass ratio and the evolutionary stage of the donor star (following option 'QCRS' in table 3 of Iorio et al., 2023). Also, we set here the adjustable fraction of orbital energy converted into kinetic energy during common-envelope evolution to $\alpha_{\rm CE} = 3$ (section 2.3.3 of Iorio et al., 2023, see also Hurley et al. 2002).

Finally, in this work, we adopt the formalism of quasi-homogeneous evolution introduced by Eldridge et al. (2011, see section 2.3.2 of Iorio et al. 2023). According to this formalism, a low-metallicity, main-sequence star spun up by accretion of substantial material via stable Roche-lobe overflow mass transfer sees its core replenished with fresh hydrogen through rotational mixing and remains fully mixed until it burns all its hydrogen into helium (ending as a pure-He star), at nearly constant radius. Following Eldridge et al. (2011, see also Eldridge and Stanway 2012), we include this evolution for stars with metallicity $Z \leq 0.004$ (which have weak-enough winds to prevent strong loss of angular momentum) accreting at least 5 per cent of their mass and with post-accretion masses greater than $10\,\mathrm{M}_\odot$. Stars meeting these criteria brighten and see their temperature increase as they burn hydrogen at nearly constant radius during quasi-homogeneous evolution (e.g., Eldridge and Stanway, 2012). Their inclusion augments the population of compact, hot luminous stars, which has important implications for the results presented in this thesis.

For stars ending their lives as supernovae (SNe), SEVN includes several prescriptions to compute the compact-remnant (neutron star or black hole) mass and natal kick depending on SN type, i.e., electron-capture (Giacobbo and Mapelli, 2019), core-collapse (Fryer et al., 2012) or pair-instability (Mapelli et al., 2020) SNe. We adopt here the delayed SN model, which predicts a smooth transition between maximum neutron star mass and minimum black hole mass. We generate natal kicks as described by Giacobbo and Mapelli (2020), in agreement with the proper-motion distribution of young Galactic pulsars (Hobbs et al., 2005), and with reduced kick magnitude for stripped and ultra-stripped SNe (Tauris et al., 2017).

We set the initial conditions as follows. For a given metallicity Z, we produce with SEVN a stochastic population of 10^6 evolving binary pairs,[3] with initial primary-star masses in the range $2 \leq m \leq 300\,\mathrm{M}_\odot$ drawn from a power-law IMF $\phi(m) \propto m^{-1.3}$ (where $\phi(m)dm$ is the number of stars created with masses between m and $m + dm$). For each pair, we draw the ratio of initial secondary-star mass to initial primary-star mass (q), the orbital period (P) and the eccentricity (e) from the corresponding probability density functions (PDFs) adopted in Sana et al. (2012): $\mathrm{PDF}(q) \propto q^{-0.1}$ with $q \in [0.1, 1.0]$; $\mathrm{PDF}(\mathcal{P}) \propto \mathcal{P}^{-0.55}$ with $\mathcal{P} = \log(P/\mathrm{day}) \in [0.15, 5.5]$; and $\mathrm{PDF}(e) \propto e^{-0.42}$ with $e \in [0, 0.9]$.[4] The adopted primary-star IMF produces a larger proportion of massive stars than the standard Galactic-disc IMF, which has $\phi(m) \propto m^{-2.3}$ for $m \geq 1\,\mathrm{M}_\odot$ (e.g., Kroupa, 2001; Chabrier, 2003). We make this choice to appropriately sample the high-mass end of the IMF among this base collection of one million pairs, from which we can then extract populations with different IMFs (including Chabrier, 2003).

To compute the spectral evolution of stellar populations obtained this way, we adopt an approach similar to that in the GALAXEV code (Bruzual and Charlot, 2003). Specifically, we assign a spectrum to each SEVN star by selecting among the different stellar libraries listed in appendix A of Sánchez et al. (2022), supplemented by WM-BASIC model atmospheres computed by Chen et al. (2015) for stars hotter than 50,000 K. For a given metallicity, these models are interpolated at the mass-loss rate, effective temperature ($\log T_{\mathrm{eff}}$) and gravity ($\log g$) of the considered star. The spectra of stars hotter than the hottest Chen et al. (2015) model (i.e., with $T_{\mathrm{eff}} > 10^5\,\mathrm{K}$) are approximated by black bodies. We identify Wolf-Rayet (WR) stars of different types (WNL, WNE, WC and WO) in the populations generated with the SEVN code following the procedure outlined in section 3.2 of Chen et al. (2015), based on the H, C, N and O surface abundances of stars hotter than 25,000 K. We appeal to the high-resolution version of the Potsdam-WR (PoWR) models to describe the spectra of these stars (Hamann and Gräfener, 2004; Sander et al., 2012; Todt et al., 2015; Hainich et al., 2019). For each WR star, we select the PoWR model with closest parameters in a way similar to that outlined in appendix A of Plat et al. (2019), with the refinement that we also match the surface hydrogen fraction of WNL-type stars. For core-He burning stars less massive than $8\,\mathrm{M}_\odot$ and hotter than 20,000 K, we adopt CMFGEN spectral models of stripped-envelope stars by Götberg et al. (2018). All stellar spectra are re-sampled

[3] While we experimented with samples of up to 3×10^6 binary pairs, populations of 10^6 pairs were found sufficient to provide stable evolution of the nebular properties of young galaxies.

[4] Since the tables of PARSEC tracks implemented in SEVN for this work do not include the evolution of stars less massive than $2\,\mathrm{M}_\odot$, we redraw a new pair if a secondary star is found below this limit.

on a common wavelength scale ranging from 5.6 Å to 360 μm in 16,902 steps using the SpectRes tool (Carnall, 2017).

In the course of this procedure, we record cases of neutron stars and black holes accreting mass from a companion, where the accretion disc can produce X-ray emission (which will be discussed in section 4.1). Also, we record rates of pair-instability supernovae (PISNe), exploding (i.e., non-failed; Spera et al., 2015) core-collapse SNe and type-Ia SNe, which can lead to shock-driven nebular emission (see section 4.2).

In the remainder of this thesis, I refer to the combined SEVN and GALAXEV spectral evolution model as simply 'GALSEVN'. More details on the coupling between SEVN and GALAXEV will be published (Bruzual et al., in preparation), as well as predictions for the spectral evolution S_ν (Charlot et al., in preparation).

2.2 Photoionization modelling

As mentioned in section 1.3, most prominent spectral features, whether emission lines or continuum, are produced by the photoionized H II region surrounding the young population of stars. To model the emergent spectrum, it is therefore necessary to combine SPS predictions (S_ν in equation 2.1) with a photoionization code capable of reproducing the processes at work in such H II regions subjected to intense radiation fields, and estimate how stellar radiation is transmitted through the surrounding gas (T_ν in equation 2.1). In this work, I use the popular code CLOUDY (Ferland et al., 2013, 2017), which I briefly describe in section 2.2.1. Then, in section 2.2.2, I focus on the stellar spectra produced by GALSEVN, which are taken as input by CLOUDY and form the link between the population-synthesis and the photoionization steps of our modelling procedure.

2.2.1 Photoionization modelling using CLOUDY

Photoionization codes aim to model the physical conditions and ionization structures of photoionized regions. They usually take into account the continuum- and line-emission processes mentioned in section 1.3, that is, free-free interaction, recombination, photoionization, collisional excitation and ionization, and ionic interactions with dust grains. Such codes solve numerically the thermal and ionization structures of the ionized cloud by solving radiative-transfer and energy-conservation equations, often assuming thermal and ionization equilibrium, and sometimes adding hydrodynamical effects. Photoionization codes differ in the assumptions made to compute radiative transfer through the cloud: direction of transmission (inward and outward radiative transfer based on iterative resolution, or outward-only calculations), geometry (plane-parallel, spherical, or even 3D algorithms), static or non-static, and numerical approach (classical, iterative, Monte-Carlo, etc.). The most widely-used photoionization code is CLOUDY (Ferland et al., 2013, 2017), an open-source, microphysics plasma-simulation code, able to self-consistently compute the physical conditions (distributions of temperature, density, ionization, level populations, molecular state) of a cloud subjected to external heating (constrained by the input SED) over a wide range of temperatures, densities and adjustable parameters. Figure 2.2 shows in the left panel the two geometries that can be chosen for CLOUDY calculations. The right panel indicates the different radiation fields involved in CLOUDY calculations, with the input SED corresponding to the incident radiation, and the output spectrum to the transmitted radiation. In this diagram, the diffuse radiation field refers to all the scattering and reemission processes by atoms and dust grains, which can be considered nearly isotropic and participate in the diffusion of energy within the ionized region. To compute the spectrum emerging from an ionized region, CLOUDY divides the region into concentric shells (in spherical geometry), thin enough for physical properties to be quasi-static and homogeneous, over which it solves the radiative-transfer, statistic- and thermal-equilibrium equations. In our calculations, we always assume a closed spherical geometry and ionization-bounded regions (spherical H II regions surrounded by a shell of neutral hydrogen). More details on the numerical methods implemented in CLOUDY and on the atomic databases used for light-matter interaction calculations can be found in Ferland et al. (2017).

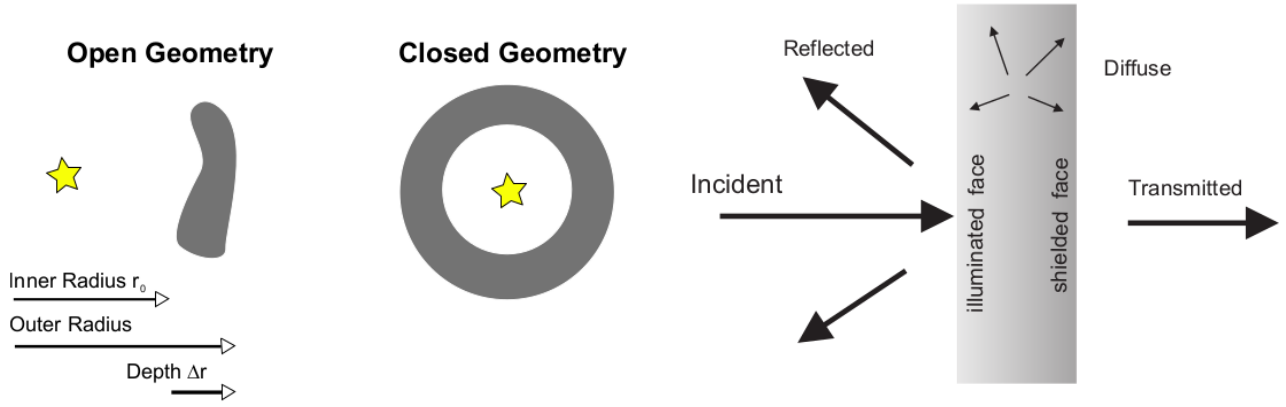

Figure 2.2: Left panel: Schematic representation of the open and closed geometries in CLOUDY. Right panel: Different radiation fields considered by CLOUDY. The input of CLOUDY is the incident radiation; the calculations take into account the reflected, absorbed and diffuse radiation fields, and give the transmitted radiation in the output CLOUDY. *Credit: CLOUDY/HAZY documentation, from www.nublado.org .*

The transmission function $T_\nu(t, t')$ of the ISM in equation (2.1) incorporates the absorption of stellar radiation by gas and dust in different phases of the ISM (ionized interiors and neutral envelopes of stellar-birth clouds, but also diffuse inter-cloud medium), as well as the production of nebular line-plus-continuum emission and dust emission (e.g., Charlot and Longhetti, 2001; da Cunha et al., 2008; Vidal-García et al., 2017). Here, we are primarily interested in young star-forming galaxies with age close to the typical timescale for dissipation of giant molecular clouds ($\sim 10\,\mathrm{Myr}$; e.g., Murray et al., 2010; Murray, 2011). In this case, we can write $T_\nu(t, t') \equiv T_\nu^+(t')$, where $T_\nu^+(t')$ is the transmission function of the ionized gas (Gutkin et al., 2016).

We compute $T_\nu^+(t')$ using version C17.00 of the CLOUDY photoionization code (Ferland et al., 2017). Following Charlot and Longhetti (2001), we assume for simplicity that galaxies are ionization-bounded and that the transfer of radiation through ionized gas can be described galaxy-wide by means of 'effective' parameters, the main ones being (Gutkin et al., 2016, see also section 2.1 of Plat et al. 2019):

– The hydrogen gas density, n_H.

– The gas-phase metallicity, which unless otherwise specified is taken to be equal to that of the ionizing stars, $Z_\mathrm{ISM} = Z$.

– The carbon-to-oxygen abundance ratio, C/O.

– The dust-to-metal mass ratio reflecting the depletion of heavy elements on to dust grains, ξ_d.

– The zero-age, volume-averaged ionization parameter, $\langle U \rangle \equiv \langle U \rangle(t' = 0)$. In spherical geometry, $\langle U \rangle(t')$ can be expressed in terms of the rate of ionizing photons produced by the evolving stellar population, $\dot{N}_\mathrm{H}(t')$, the volume-filling factor of the gas (i.e., the ratio of the volume-averaged hydrogen density to n_H), ϵ, and the case-B hydrogen recombination coefficient, α_B, as (e.g., Panuzzo et al., 2003):

$$\langle U \rangle(t') = \frac{3\alpha_B^{2/3}}{4c} \left[\frac{3\dot{N}_\mathrm{H}(t')\epsilon^2 n_\mathrm{H}}{4\pi} \right]^{1/3} . \tag{2.2}$$

We stop the photoionization calculations at the outer edge of the H II region, when the electron density falls below 1 per cent of n_H (we adopt a default inner radius of 0.1 pc). We adopt the prescription

of Gutkin et al. (2016) for the abundances and depletions of interstellar elements, as well as for scaling the total (primary+secondary) nitrogen abundance with that of oxygen. These abundances are summarised in Appendix A for convenience. In this framework, the present-day solar (photospheric) metallicity is $Z_\odot = 0.01524$, corresponding to a proto-solar metallicity $Z_\odot^0 = 0.01774$ (Bressan et al., 2012).

The choice of values used in this work for the nebular parameters described above will be detailed in section 2.3.2, in relation to the observationally constrained properties of the sample described in section 2.3.1. In the next section, I comment on GALSEVN generated SEDs that are input in CLOUDY.

2.2.2 GALSEVN ionizing spectra

For a given set of nebular parameters, CLOUDY output spectra highly depend on the shape of the ionizing spectrum, and on the properties of the stellar population generated by GALSEVN. As mentioned in section 2.1.1, the properties of the stellar population depend on the chosen stellar metallicity, IMF and SFH. However, as this work focuses on the contribution from binary stars to the amount of high energy photons produced by metal-poor stellar populations, the fraction of binary systems in our population is another crucial parameter of our models. The role of stellar composition, SFH and IMF in our predictions will be investigated in chapter 3.

With this in mind, it is of interest to examine how $\dot{N}_{\rm H}(t')$ depends on the fraction of binary stars in a stellar population according to the models presented in section 2.1 (see also section 2.4.1 of Eldridge et al., 2017). This is shown in the top panel of Figure 2.3 for an instantaneous-burst, 'simple stellar population' [SSP; corresponding to $\psi(t') = \delta(t')$ in equation (2.1)], for the typical metallicity $Z = 0.001$ (i.e., about 6 per cent of solar) of galaxies in the sample of section 2.3.1. The middle and lower panels show the equivalent plots for He I- and He II-ionizing photons. In each panel, the different curves correspond to different zero-age binary fractions, $f_{\rm bin} \equiv f_{\rm bin}(t' = 0)$, defined as $f_{\rm bin} = {\rm B}/({\rm S} + {\rm B})$, where B is the number of binary pairs and S the number of single stars at $t' = 0$. To isolate the effects of binary interactions, the IMF is taken to be exactly the same for binary and single stars. This is achieved by drawing single stars as binary systems whose member stars never interact, i.e., assuming a Chabrier (2003) IMF for primary stars and a Sana et al. (2012) distribution of secondary-to-primary mass ratios (see section 2.1), with orbital parameters (large semi-major axes and circular orbits) such that primary and secondary stars never interact. For reference, the total IMF (including primary and secondary stars) drawn in this way has an effective near-Salpeter (1955) slope, i.e., roughly $\phi(m) \propto m^{-2.35}$, at $m > 10\,{\rm M}_\odot$. All models are normalized to a total initial mass in stars of $1\,{\rm M}_\odot$ between 0.1 and $300\,{\rm M}_\odot$.[5]

Figure 2.3 shows that, at ages younger than 1 Myr, models with $f_{\rm bin} > 0$ produce slightly larger $\dot{N}_{\rm H}$, $\dot{N}_{\rm He\,I}$ and $\dot{N}_{\rm He\,II}$ than single-star models, due to the presence of merged stars with masses up to $\sim 600\,{\rm M}_\odot$ on the upper main sequence. Then, when the most massive stars leave the main sequence, all three quantities start to drop. The rate of He II-ionizing photons rises sharply again after 2 Myr in models with $f_{\rm bin} > 0$. This is caused by the appearance of the hot ($> 10^5$ K), pure-He (WNE-like) products of the first massive stars to lose their H-rich envelope, either by dumping mass on their companion through Roche-lobe overflow, or by being driven to quasi-homogeneous evolution and burning all of their H to He after receiving mass from their companion, or through common-envelope ejection (see, e.g., Spera et al., 2019; Iorio et al., 2023). These stars have a comparatively weak influence on the rates of He I- and H-ionizing photons, which remain dominated by the much more numerous

[5]This normalization is performed by drawing primary-star masses from a Chabrier (2003) IMF (and the associated secondary stars from a Sana et al. 2012 distribution) over the full range 0.1–300 $\rm M_\odot$, even though only pairs with both primary- and secondary-star masses greater than $2\,{\rm M}_\odot$ are retained (the pairs drawn with both primary- and secondary-star masses greater than $2\,{\rm M}_\odot$ are matched to those in the base collection of section 2.1). This has no influence on the predicted $\dot{N}_{\rm H}$, $\dot{N}_{\rm He\,I}$ and $\dot{N}_{\rm He\,II}$, since main-sequence stars less massive than $2\,{\rm M}_\odot$ are cooler than $\sim 14,000$ K at any metallicity and do not produce significant ionizing radiation. Also, rejecting binaries with primary mass above $2\,{\rm M}_\odot$ and secondary mass below this limit has a negligible impact on ionizing fluxes: artificially including such draws by assigning them the light of pairs with same primary mass and a secondary mass of $2\,{\rm M}_\odot$ would increase $\dot{N}_{\rm H}$, $\dot{N}_{\rm He\,I}$ and $\dot{N}_{\rm He\,II}$ by less than one per cent at ages below 40 Myr in Figure 2.3.

H-burning stars on the upper main sequence, at least until ages of several million years. Then, as the He-burning main sequence continues to develop, stellar mergers conspire to maintain the tip of the H-burning main sequence at a brighter and hotter point in binary-star models than in single-star models, leading to significantly larger $\dot{N}_{\rm H}$, $\dot{N}_{\rm He\,I}$ and $\dot{N}_{\rm He\,II}$. After a few tens of million years, the difference between models with $f_{\rm bin} > 0$ and $f_{\rm bin} = 0$ declines, especially for $\dot{N}_{\rm He\,II}$ after the disappearance of the brightest and hottest WNE-like stars (around 40 Myr). The faintest of these stars, together with stellar mergers and stars undergoing quasi-homogeneous evolution, contribute to maintain $\dot{N}_{\rm H}$ and $\dot{N}_{\rm He\,I}$ relatively strong in binary-star models relative to single-star models. The rise of $\dot{N}_{\rm He\,I}$ and $\dot{N}_{\rm He\,II}$ at ages around 30 Myr in single-star models is due to the development of the white-dwarf cooling sequence. From about 50 to 90 Myr, the hot ionizing radiation from the most massive of these stars leads to slightly higher $\dot{N}_{\rm He\,II}$ than in binary-star models, where their population is reduced through binary-star interactions (their progenitors avoiding white-dwarf evolution through mass gain, or being driven to fainter evolution through mass loss).

A notable feature of Figure 2.3 is that even small fractions of binary stars can have a major impact on the predicted rates of highly energetic photons. At an age of 3 Myr, for example, the ratio of He II- to H-ionizing photons, $\dot{N}_{\rm He\,II}/\dot{N}_{\rm H}$, which is 2700 times larger in models with $f_{\rm bin} = 1$ than in those with $f_{\rm bin} = 0$, is already 54, 480 and 1300 times larger for $f_{\rm bin} = 0.01$, 0.1 and 0.3, respectively. It is 2200 times larger for $f_{\rm bin} = 0.7$, often adopted as typical of massive-star populations (e.g., Sana et al., 2012).

In Figure 2.4, we compare in more detail the ionizing spectra $S_\nu(t')$ of SSPs with pure binary stars ($f_{\rm bin} = 1$, solid lines) and pure single stars ($f_{\rm bin} = 0$, dotted lines) at ages between 1 and 10 Myr, for a metallicity $Z = 0.001$. As expected from Figure 2.3, at an age of 1 Myr, the spectra of both models nearly overlap, while at older ages, the model with binary stars exhibits an excess of energetic photons relative to that with single stars. Populations of binary stars will therefore boost the production of highly-ionized species in the gas they irradiate (we indicate for reference the ionization energies of some common species in Figure 2.4). In fact, Figure 2.4 shows that at ages $t' \geq 3$ Myr in the binary-star model, the shape of $S_\nu(t')$ at ionizing energies up to $\gtrsim 50$ eV is similar to that of hard ionizing spectra of AGNs, $S_\nu \propto \nu^{\alpha_{\rm AGN}}$ with $-2.0 \leq \alpha_{\rm AGN} \leq -1.2$ (e.g., Feltre et al., 2016, grey shaded area).

2.3 Exploration of model predictions

Before investigating the effects of changing the different adjustable parameters of the model, it is important to assess whether our GALSEVN + CLOUDY predictions are able to reproduce observations of young metal-poor star-forming regions. In this section, I therefore compare the predictions of the models presented in sections 2.1 and 2.2 with observations of ultraviolet and optical emission lines in metal-poor star-forming galaxies, described in section 2.3.1, after setting standard model parameters based on the mean properties of this sample. These parameters, which we will then consider as standard parameters in the remainder of this study, are presented in section 2.3.2. Finally, I examine in section 2.3.3 how the predictions of our model compare with observed properties of analogues of primeval galaxies, and with the predictions of other spectral-synthesis codes.

2.3.1 Observed analogues of primeval galaxies

As mentioned in section 1.1.5, observations of primeval galaxies at high redshift are challenging (although less so since the advent of *JWST*), and when spectroscopic data are available, detailed spectral features are often difficult to detect. We therefore need to test our model using a sample of lower-redshift galaxies which exhibit what we expect to be primeval-like properties. For the sake of completeness, it is important to include as many different objects as possible in this sample. In this context, it is possible to classify the objects in our sample in three categories: classical star-forming galaxies; Lyman-continuum (LyC) leakers (compact galaxies exhibiting an important leakage in ionizing photons and characterized by the $f_{\rm esc}$ parameter); and galaxies hosting an AGN or a candidate AGN.

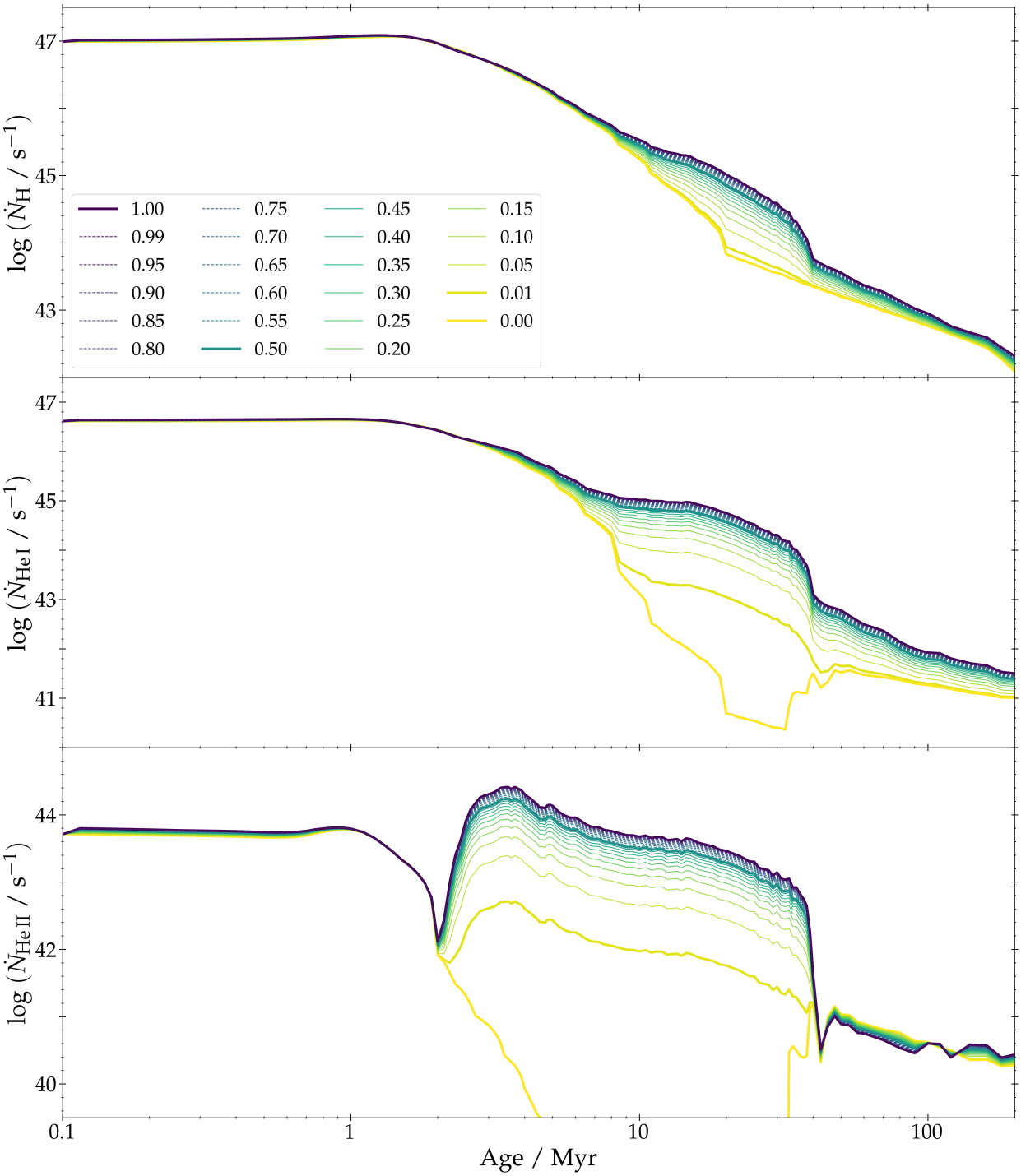

Figure 2.3: Rates of H- (top), He I- (middle) and He II- (bottom) ionizing photons as a function of age for 'simple' (i.e., instantaneous-burst) stellar populations (SSPs) with different fractions of binary stars, $f_{\rm bin}$ (colour-coded as indicated), for a metallicity $Z = 0.001$. The models assume a Chabrier (2003) IMF for primary stars and a Sana et al. (2012) distribution of secondary-to-primary mass ratios at age zero (single stars being modelled as non-interacting binaries) and are normalized to a total initial stellar mass of $1\,{\rm M}_\odot$ integrated over 0.1–300 $\rm M_\odot$ (see text for details).

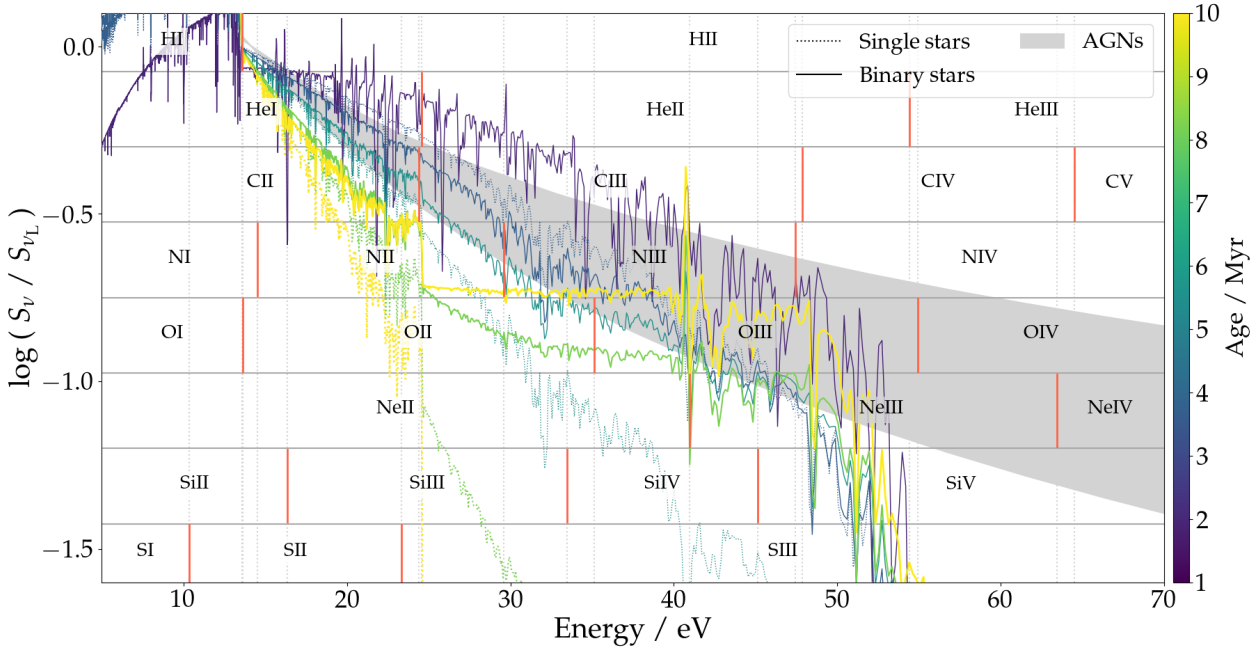

Figure 2.4: Spectral energy distribution S_ν entering equation (2.1) (in units of the luminosity per unit frequency at the Lyman limit) for the SSP models of Figure 2.3 with pure binary stars ($f_{\rm bin} = 1$, solid lines) and pure single stars ($f_{\rm bin} = 0$, dotted lines) at the ages $t' = 1$, 3, 5, 8 and 10 Myr (colour-coded as indicated on the right-hand side). Also shown in grey is the area sampled by ionizing spectra of AGNs with power-law indices between $\alpha_{\rm AGN} = -2.0$ (bottom edge) and -1.2 (top edge; Feltre et al. 2016). The ionization energies of some common species are indicated for reference.

We appeal to the compilation of emission-line measurements of star-forming galaxies by Plat et al. (2019, based on the samples of Fosbury et al. 2003; Erb et al. 2010; Jaskot and Oey 2013; Stark et al. 2014; Berg et al. 2016, 2018, 2019; Izotov et al. 2016b,a, 2017b, 2018a,b; Nakajima et al. 2016; Vanzella et al. 2016, 2017; Amorín et al. 2017; Chisholm et al. 2017; Schmidt et al. 2017; Senchyna et al. 2017, 2019; Nanayakkara et al. 2019). From this data set, we select all metal-poor galaxies with confident gas-phase oxygen abundances (i.e., determined using the direct-$T_{\rm e}$ or the strong-lines methods) less than $12 + \log({\rm O/H}) \approx 8.2$, corresponding to $Z \lesssim 0.004$ (see, e.g., table 2 of Gutkin et al., 2016, , which is reproduced in Appendix A). With this selection, we retain 102 galaxies, of which 20 are classified as LyC leakers, with fractions of escaping LyC photons up to ~ 0.6. The galaxies in this sample span wide ranges in redshift, $0 \lesssim z \lesssim 7$, ionization parameter, $-3.6 \lesssim \log\langle U\rangle \lesssim -1.0$, C/O abundance ratio, $0.1 \lesssim ({\rm C/O})/({\rm C/O})_\odot \lesssim 1.2$ and specific star formation rate, $1 \lesssim \psi/M \lesssim 1,000\,{\rm Gyr}^{-1}$ (where M denotes the galaxy mass). For reference, we also consider the emission-line properties of 84 AGNs and candidate AGNs from Diaz et al. (1988); Kraemer et al. (1994); Dors et al. (2014); Stark et al. (2015); Nakajima et al. (2018). We refer the reader to section 3 and tables 1 and 2 of Plat et al. (2019) for more details about this sample.

We complement this data set with recent emission-line measurements for a few more local analogues to primeval galaxies, including the extremely metal-poor ($Z < 0.1\,Z_\odot$) starburst-dwarf galaxies SBS 0335-052E (Wofford et al., 2021), J1631+4426, J104457 and I Zw 18 NW (Umeda et al., 2022), 7 extremely metal-poor galaxy candidates from Kojima et al. (2021) and 6 C IV emitters from Senchyna et al. (2022).

In our study, we compare the predictions of our model with the observed intensity ratios and equivalent widths (EWs) of selected ultraviolet (C IV λ1549, He II λ1640, O III] λ1664 and C III] λ1908) and optical ([O III] λ5007, [O II]λ3727, [O I] λ6300, He II λ4686, Hβ, Hα and [N II] λ6584) emission lines commonly observed in metal-poor star-forming galaxies. We will pay particular attention to the He II lines, which require ionization energies above 54.4 eV and represent a challenge for current models.

Table 2.1: Nebular parameters of the 'standard' models of section 2.3.

Parameter	Value	Description
$Z_{\rm ISM}$	0.001	Interstellar metallicity
$n_{\rm H}$	100 cm^{-3}	Hydrogen density
C/O	0.17	Carbon-to-oxygen abundance ratio
$\log\langle U\rangle$	-2.0	Volume-averaged ionization parameter at age $t'=0$
$\xi_{\rm d}$	0.3	Dust-to-metal mass ratio

2.3.2 Choice of adjustable parameters

We start by exploring how models with 'standard' parameters compare with the observations described above.

As in section 2.2, we consider stellar populations with metallicity $Z = 0.001$ (~ 7 per cent of solar), typical of the observational sample. For the photoionized gas, we adopt the same metallicity ($Z_{\rm ISM} = 0.001$) and a density ($n_{\rm H} = 100\,{\rm cm}^{-3}$), ionization parameter ($\log\langle U\rangle = -2.0$) and dust-to-metal mass ratio ($\xi_{\rm d} = 0.3$) typical of metal-poor star-forming galaxies (e.g., Berg et al., 2016; Gutkin et al., 2016; Mingozzi et al., 2022).

These choices of $Z_{\rm ISM}$ and $\xi_{\rm d}$ imply a gas-phase oxygen abundance $12 + \log({\rm O/H}) \approx 7.53$ (see Table A.2, or table 2 of Gutkin et al., 2016), which according to Figure 6 of Berg et al. (2016) corresponds to a typical carbon-to-oxygen abundance ratio C/O ≈ 0.17, i.e., about 40 per cent of the solar ratio $({\rm C/O})_\odot = 0.44$ (Gutkin et al., 2016). This is close to the typical value C/O ≈ 0.18 reported by Izotov et al. (2023) in low-redshift LyC-leaking galaxies with $12 + \log({\rm O/H}) \lesssim 8.1$. Yet, given that galaxies in the observational sample of section 2.3.1 exhibit C/O values up to 120 per cent of solar, we expect some of these galaxies to show stronger carbon lines than predicted by our standard models. We report the above standard nebular parameters in Table 2.1.

We perform the photoionization calculations for a single generation of stars (SSP) at stellar-population ages up to 10 Myr, i.e., roughly the timescale of dissipation of giant molecular clouds in star-forming galaxies (Murray, 2011; Ma et al., 2015).

Finally, we adopt for now a zero-age Chabrier (2003) IMF for primaries, as in Figure 2.3. The mass of the secondary is then sampled as explained in section 2.1.2.

2.3.3 Initial GALSEVN predictions

In this section, I provide a first comparison between the spectral features observed in the sample of primeval-galaxy analogues of section 2.3.1, the predictions of the GALSEVN model, and the predictions of the widely-used BPASS model of single and binary stars. All models were run using the set of standard parameters presented in the previous section. We also compare our predictions to the previous release of single-stars GALAXEV models presented in Plat et al. (2019), noted here as C&B.

In Figure 2.5, we show the intensity ratios and equivalent widths of emission lines predicted by the SSP models of Figure 2.3 with pure binary stars ($f_{\rm bin} = 1$, labelled 'GALSEVN') and pure single stars ($f_{\rm bin} = 0$, 'GALSEVN single') at ages up to 10 Myr (colour-coded as indicated on the right). It is instructive to start by examining the behaviour of these models in the He II λ4686/Hβ-versus-EW(Hβ) diagram (Figure 2.5(b)), where observations are traditionally challenging to reproduce with photoionization models powered by young stellar populations (e.g., Plat et al., 2019; Schaerer et al., 2019). All models start at high EW(Hβ) on the right-hand side of the diagram. As massive stars leave the main sequence and the first red super-giant stars appear in the single-star GALSEVN model, $\dot{N}_{\rm H}$ and $\dot{N}_{\rm He\,II}$ decrease while the continuum at Hβ increases, causing both EW(Hβ) and He II λ4686/Hβ to drop without ever reaching the area of the diagram occupied by the observations.

Remarkably, in the binary-star GALSEVN model, the rise in $\dot{N}_{\rm He\,II}$ triggered by the appearance of hot WNE-like stars with blue spectra around 3 Myr (Figure 2.3) makes both He II λ4686/Hβ and

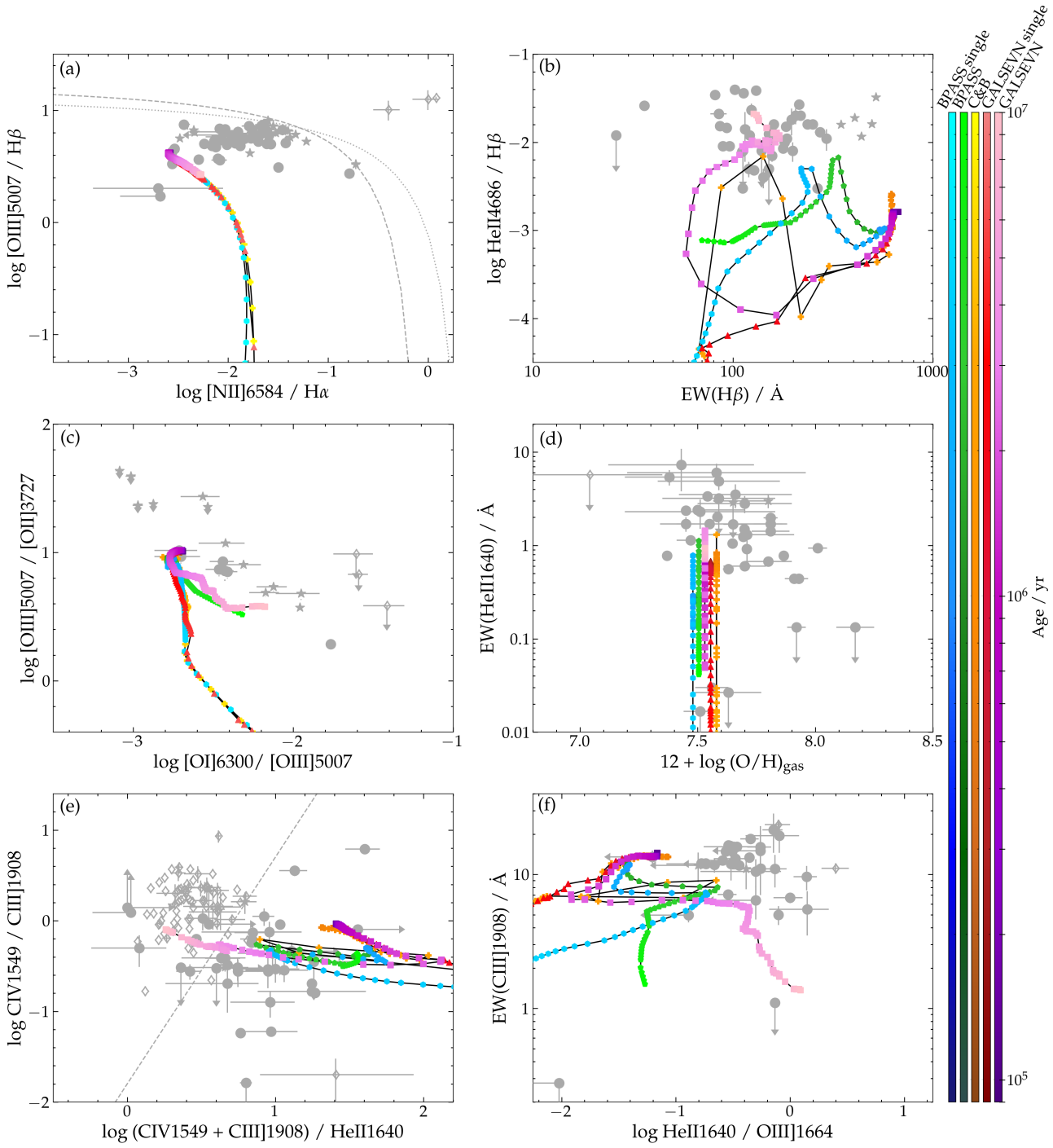

Figure 2.5: Optical and ultraviolet emission-line properties of the reference observational sample of star-forming galaxies (filled grey circles: non LyC leakers; filled grey stars: LyC leakers) and AGNs (open grey diamonds) described in section 2.3. The diagrams show different combinations of equivalent widths and ratios of the C IV λ1549, He II λ1640, O III] λ1664 and C III] λ1908, [O III] λ5007, [O II]λ3727, [O I] λ6300, He II λ4686, Hβ, Hα and [N II] λ6584 nebular emission lines, and the gas-phase oxygen abundance in (d). All line fluxes are corrected for attenuation by dust, as prescribed in the original studies (arrows show 1σ upper limits). In (a), the dotted and dashed lines show the criteria of Kewley et al. (2001) and Kauffmann et al. (2003), respectively, to separate AGN-dominated from star-forming galaxies, while in (e), the dashed line shows the equivalent criterion proposed by Nakajima et al. (2018). The curves interspersed with filled squares, triangles, pentagons, hexagons and crosses show the predictions of the GALSEVN binary- and single-star models, the BPASS binary- and single-star models and the C&B single-star model, respectively, colour-coded with age as indicated on the right (the BPASS models, available only at ages above 1 Myr, do not sample the youngest ages in the colour bars). In (d), the models are shown for clarity at slightly different abscissæ, although all have 12 + log(O/H) = 7.53. In all models, the ionizing stellar population is an SSP with metallicity $Z = 0.001$ and the same zero-age Chabrier (2003) IMF as in Figure 2.3, while the parameters of the photoionized gas are those listed in Table 2.1.

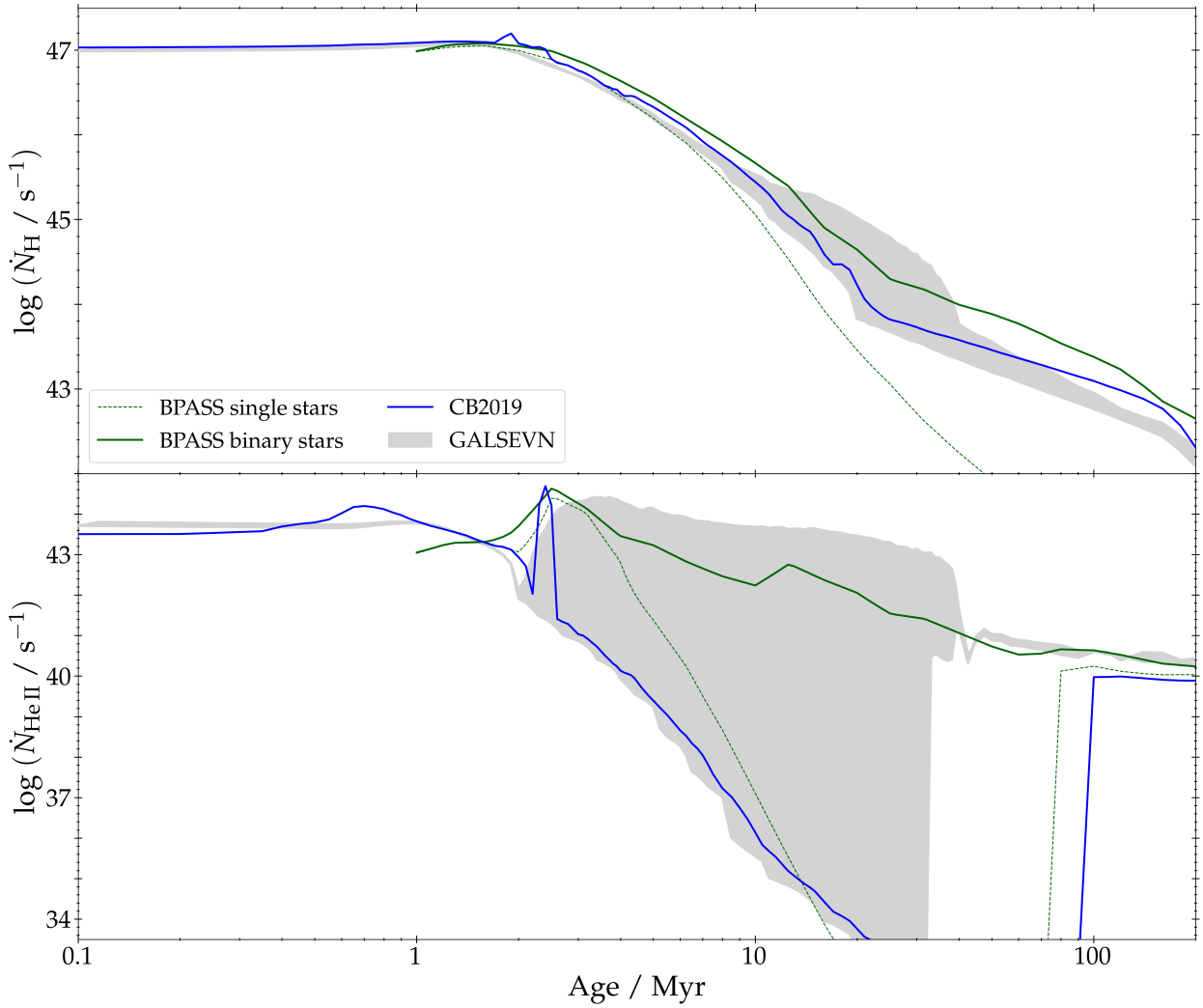

Figure 2.6: Rates of H- (top) and He II- (bottom) ionizing photons as a function of age for SSPs of metallicity $Z = 0.001$ computed with different models, as indicated (the BPASS models are available only at ages above 1 Myr). In each panel, the grey shaded area shows the area covered by the GALSEVN models with different fractions of binary stars from Figure 2.3. All models have the same zero-age Chabrier (2003) IMF normalized to a total initial stellar mass of 1 $M_\odot$ integrated over 0.1–300 $M_\odot$ as in Figure 2.3.

EW(Hβ) rise in such a way that the models spend all the time thereafter up to 10 Myr in the same location as the observations. It is worth recalling that, as shown by Figure 2.3, similar results would be obtained with models containing only a minor fraction of binary stars ($f_{\rm bin} \gtrsim 0.3$).

Also shown for comparison in Figure 2.5(b) are photoionization calculations performed using the BPASS v2.2.1 models of Stanway and Eldridge (2018) for single and binary stars, as well as the C&B single-star model used by Plat et al. (2019, based on an updated version of the Bruzual and Charlot 2003 GALAXEV code), for a metallicity $Z = 0.001$ and the same nebular parameters as in Table 2.1. The CLOUDY calculations for these models were conducted similarly to those for the GALSEVN models as part of the present study. We note the striking difference between the C&B and GALSEVN single-star models at ages around 2 Myr, when the brief ($\sim$ 0.2 Myr) WR phase that makes He II λ4686/Hβ rise up to the observed range in the C&B model is absent from the GALSEVN model. This can also be seen in the evolution of $\dot{N}_{\rm H}$ and $\dot{N}_{\rm He\,II}$ shown in Figure 2.6. Both models being based on the same library of stellar spectra (described in section 2.1), this difference originates from recent updates (in particular in the opacities) of the PARSEC-track library of Bressan et al. (2012) and Chen et al. (2015), leading to reduced mass loss, and hence fewer WR stars at low metallicity (Costa et al., 2021; Nguyen et al., 2022).

The brief WR phase at early ages is also present (although to a lesser extent) in the BPASS models for both single and binary stars, which are based on the Cambridge STARS code (Eggleton, 1971; Eldridge et al., 2008, see also Figure 2.6). After this phase and the disappearance of the most massive stars, EW(Hβ) and He II λ4686/Hβ both drop rapidly in the single-star model, as in the GALSEVN and C&B single-star models. Instead, in the BPASS binary-star model, He II λ4686/Hβ is maintained at a fairly high level by the appearance of envelope-stripped and spun-up stars, still without reaching the region of the diagram probed by the observations. Given that in GALSEVN, $\dot{N}_{\mathrm{He\,II}}$ is dominated by WNE stars after a few Myr, the discrepancy between the GALSEVN and BPASS binary-star models in Figure 2.5(b) can likely be attributed to a distinct population of these stars in BPASS, particularly as both models use similar spectra for them (from the PoWR library).

The behaviour of the models in the other diagrams of Figure 2.5 follows from the same arguments. In the classical Baldwin et al. (1981, hereafter BTP) diagram to distinguish AGNs from star-forming galaxies (Figure 2.5(a)), at early ages, all models lie at the high-[O III] λ5007/Hβ, low-[N II] λ6584/Hα end characteristic of low metallicity and high ionization parameter (see, e.g., Figure2 of Gutkin et al., 2016). The GALSEVN and BPASS binary-star models stay in this area at ages up to 10 Myr, while the [O III] λ5007/Hβ ratio of single-star models rapidly drops after the disappearance of photons more energetic than ~ 35.1 eV capable of ionizing O^{2+}. The implied drop in [O III] λ5007 luminosity is also the reason for the difference between binary- and single-star models in the [O III] λ5007/[O II]λ3727-versus-[O I] λ6300/[O III] λ5007 diagram (Figure 2.5(c)). In Figure 2.5(d), none of the models (plotted for clarity at slightly different abscissæ even though all have $12 + \log(\mathrm{O/H}) = 7.53$) reaches the highest observed EW(He II λ1640) $\sim$ 2–8 Å. In this diagram, only the GALSEVN binary-star models maintains EW(He II λ1640) > 0.5 Å at ages $t' \gtrsim 3$ Myr, while the BPASS binary-star model declines to EW(He II λ1640) ≈ 0.03 Å and all single-star models to EW(He II λ1640) ≈ 0.

The difference between the GALSEVN binary-star model and all other models is more striking in Figure 2.5(e), where GALSEVN is the only model able to account for the properties of star-forming galaxies similar to those of AGNs at low (C IV λ1549 +C III] λ1908)/He II λ1640 and high C IV λ1549/C III] λ1908. Again, albeit without certainty, the difference between the GALSEVN and BPASS binary-star models likely arises from distinct populations of WNE stars, which dominate the production of He II-ionizing photons. Similarly, in Figure 2.5(f), this model at ages $t' \gtrsim 2$ Myr is closest to the observational sequence at He II λ1640/O III] λ1664 > 0.3, although it does not appear to reach sufficiently high EW(C III] λ1908) at a given He II λ1640/O III] λ1664.

On the whole, Figure 2.5 shows the need to include binary stars and their inherent physical processes in modelling the emission-line properties of metal-poor, star-forming galaxies. It also validates reasonable agreement between GALSEVN binary-star models and (non-extreme) observations of such galaxies in our sample, although discrepancies between some observed and modelled spectral features remain to be explored. With this goal in mind, it is interesting to investigate how varying model parameters can influence our predictions and their agreement with observational constraints. This study will be presented in the next chapter.

Chapter 3

Influence of adjustable model parameters

Contents

In this chapter, I present a brief investigation of the impact of changing model parameters when modelling stellar and nebular emission with GALSEVN and CLOUDY. To assess with greater certainty the effects of a change in a given parameter, I vary a single parameter at a time. In section 3.1, I focus on the implications of changing gas chemistry – via the adjustment of nebular parameters and gas and stellar abundances – on the agreement with observations from the sample described in the previous chapter. In this study, I do not seek to create a detailed grid of parameters to reproduce precisely and infer the physical properties of given observations, but rather to roughly explore the parameter space and assess the ability of the models to account for the observations. A complementary approach, aimed at recovering the physical properties of observed star-forming region through SED fitting, will be developed later in chapter 6. I then examine, in section 3.2, the impact of the choices of IMF and SFH on SPS predictions.

3.1 Abundances and nebular parameters

So far, we have considered only models with metallicity $Z = 0.001$ and nebular parameters fixed at the standard values of table 2.1. Given the diversity of objects in the observational sample described in section 2.3.1, it is relevant to explore the effect of varying the values taken by these parameters. Here, we focus in turn on the influence of metallicity, volume-averaged ionization parameter and carbon-to-oxygen abundance ratio. We do not explore changes in $n_{\rm H}$ and $\xi_{\rm d}$, which have been shown by Plat et al. (2019) to have a minimal impact on the emission-line ratios presented in Figure 2.5. Unless specified otherwise, we adopt the same Chabrier (2003) IMF as in the standard models.

3.1.1 Metallicity

At first sight, a change in stellar metallicity is expected to change the amount of ionizing photons created by the stellar population: at lower metallicities, for a given IMF, the ionizing spectrum of the stellar population is harder due to the shift of the main sequence towards higher temperatures.

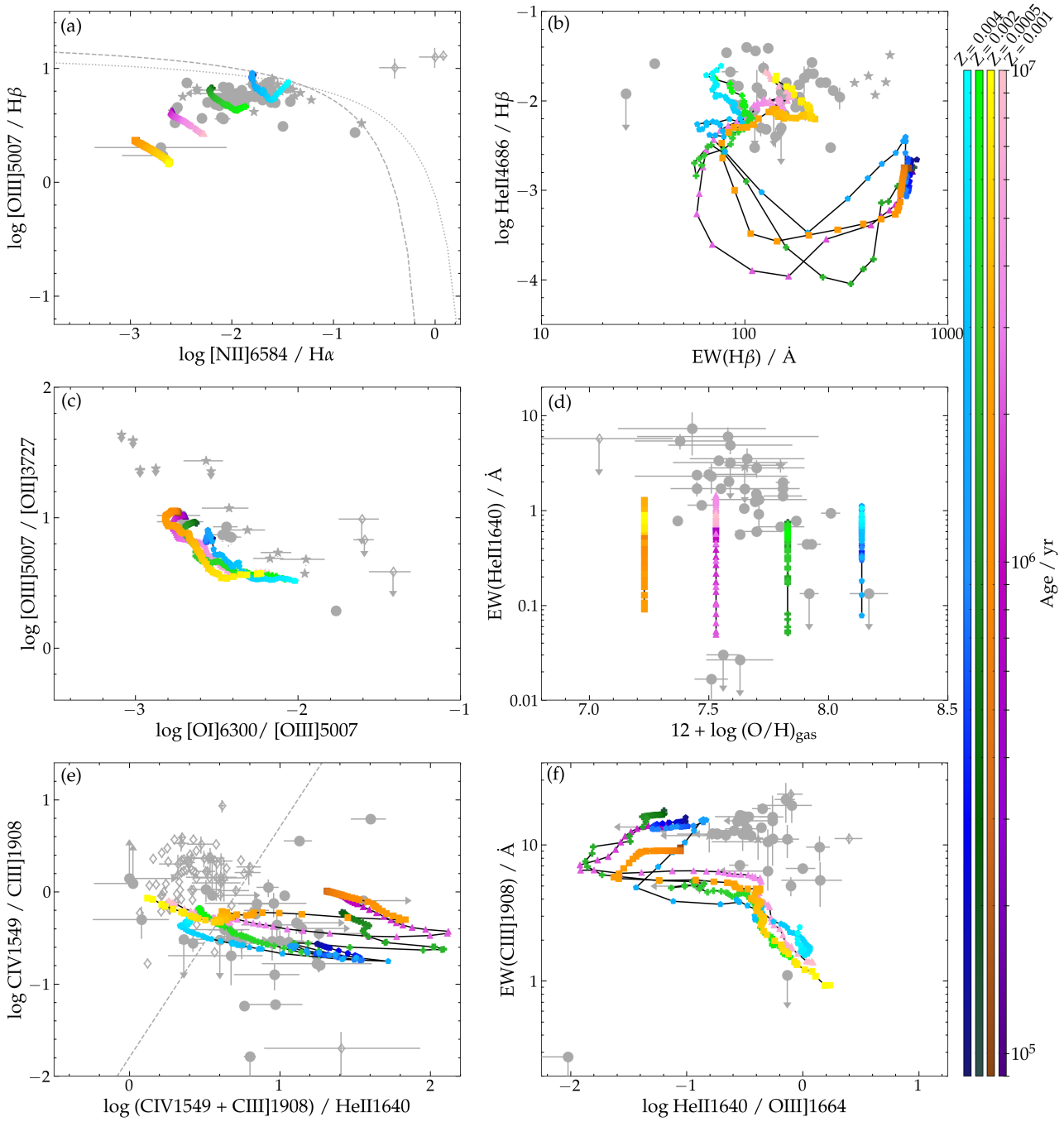

Figure 3.1: Same as Figure 2.5, but for GALSEVN binary-star models with different metallicities, as indicated at the tip of the colour bars. The curves interspersed with filled squares, triangles, crosses and pentagons refer to the metallicities $Z = 0.0005$, 0.001, 0.002 and 0.004, respectively.

As for the gas-phase metallicity, it influences the cooling mechanisms available in the gas, driven by metallic coolants, affecting the amount of photons released by radiative deexcitation – especially in the case of forbidden and semi-forbidden lines, which collisional deexcitation rates are affected by the gas temperature and metallicity. Moreover, more metals in the ISM means more atoms to be photoionized, therefore influencing the emission line intensities. I discuss these effect in more depth in this section, and illustrate them with GALSEVN models at different metallicities (keeping $Z = Z_{\rm ISM}$).

Figure 3.1 shows the evolution of GALSEVN binary-star models with metallicities $Z = Z_{\rm ISM} =$ 0.0005, 0.001, 0.002 and 0.004 – that is respectively $\sim$ 3.5, 7, 13.5 and 27 per cent of $Z_\odot$ – in the same diagrams as in Figure 2.5, with all other parameters fixed at their values in table 2.1.

An increase in metallicity makes cooling through collisionally-excited metal transitions more efficient, which reduces the electronic temperature $T_{\rm e}$. This causes the luminosity ratios of metal lines to H and He lines to rise and the ratios of high- to low-ionization lines to drop. Figures 3.1(a), (c), (e) and (f) illustrate well this evolution. The increase of [N II] λ6584/Hα with Z in Figure 3.1(a) is further enhanced by the inclusion of secondary nitrogen enrichment in the nebular-emission models (section 2.2). At $Z = 0.004$, we note the emergence of classical WR stars at early ages following the increased mass loss of evolved massive stars with metal-rich envelopes, which causes a brief excursion of the model at high He II λ4686/Hβ and He II λ1640/O III] λ1664 in Figures 3.1(b) and (f).

As Figure 3.1(d) shows, while metallicities in the range $0.0005 \leq Z \leq 0.004$ can fully describe the range of 12 + log(O/H) probed by the observational sample, metallicity has little influence on the maximum EW(He II λ1640) achievable with the GALSEVN binary-star model.

3.1.2 Ionization parameter and C/O abundance ratio

In Figure 3.2, we compare the standard GALSEVN binary-star model of Figure 2.5 with two GALSEVN binary-star models: one with ionization parameter $\log\langle U\rangle = -1$ instead of -2; and one with C/O = $(\mathrm{C/O})_\odot = 0.44$ instead of 0.17. All models have metallicity $Z = 0.001$.

As the ionization parameter evaluates the ionization level in the H II region, it is expected to influence the high-to-low ionization emission lines as the amount of high-to-low ionization species varies with it. As for the carbon-to-oxygen ration, one can straightforwadly expect it to influence the intensity of carbon and oxygen emission lines.

The effect of increasing $\log\langle U\rangle$ is to increase the probability of multiple ionizations, and hence to strengthen high-ionization lines (see equivalent widths of He II λ1640 and C III] λ1908 in Figures 3.2(d) and (f)) and increase ratios of high-to-low ionization lines (e.g., C IV/C III] and O III]/[O II]; Figures 3.2(c) and (e)). In Figure 3.2(a), the drop in [N II]/Hα as $\log\langle U\rangle$ increases results from the conversion of N^+ into N^{2+}. In Figure 3.2(b), the drop in EW(Hβ) is caused by the increase in H-column density, and hence in the absorption of H-ionizing photons by dust at fixed Z and $\xi_{\rm d}$, as the Strömgren radius increases (e.g., Plat et al., 2019). Overall, Figure 3.2 shows that enhancing the ionization parameter does not significantly improve the agreement between GALSEVN binary-star models and the observations considered here. We note that, while ionization parameters as high $\log\langle U\rangle = -1$ have been favoured for only a few objects in this observational sample (see table 1 of Plat et al., 2019), such parameters may be more common in young star-forming galaxies near the Epoch of Reionization (e.g., Cameron et al., 2023b).

Increasing the C/O abundance ratio at fixed metallicity means raising the abundance of carbon while reducing that of all other metals (e.g., Gutkin et al., 2016). This results in a strengthening of C lines and a slight weakening of O lines, with negligible effect on H and He lines, as Figure 3.2 shows. Interestingly, the adoption of solar C/O in place of the standard value in table 2.1 (favoured by the trend with 12 + log(O/H) in Figure 6 of Berg et al., 2016) appears to provide better agreement with the data in Figure 3.2(f). Such high C/O ratio at low metallicity is in agreement with the measured properties of some metal-poor galaxies in our sample, particularly those in the subsamples from Berg et al. (2016, 2019), Amorín et al. (2017) and Stark et al. (2014). Recently, D'Eugenio et al. (2023) also

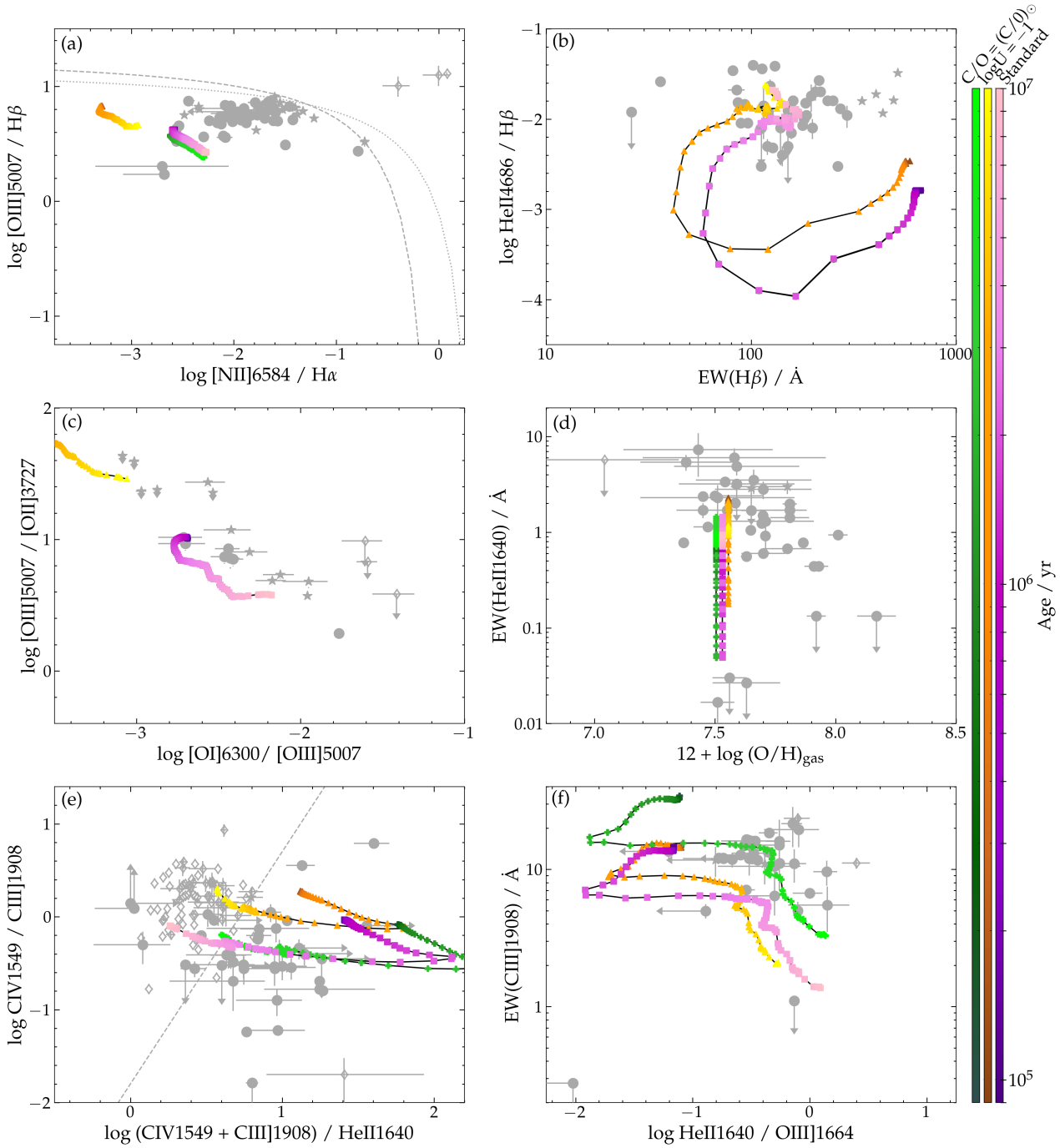

Figure 3.2: Same as Figure 2.5, for three GALSEVN binary-star models with metallicity $Z = 0.001$: a model with the standard parameters of table 2.1 ($\log\langle U\rangle = -2$, C/O = 0.17; filled squares), one with enhanced ionization parameter ($\log\langle U\rangle = -1$, C/O = 0.17; filled triangles), and one with enhanced C/O abundance ratio ($\log\langle U\rangle = -2$, C/O = $(\mathrm{C/O})_\odot = 0.44$; nearly overlapping with the standard model in (b) and (c); filled crosses), as indicated on the right.

reported the existence of a metal-poor star-forming galaxy with strong C III] emission corresponding to slightly super-solar C/O ratio at redshift $z \approx 12.5$.

3.1.3 O/Fe abundance ratio

Several recent studies have found evidence for super-solar ratios of α to iron-peak elements (e.g., O/Fe) in metal-poor star-forming galaxies at various redshifts, as expected for chemically young objects enriched by core-collapse SNe (e.g., Steidel et al., 2016; Strom et al., 2018; Topping et al., 2020; Cullen et al., 2021; Senchyna et al., 2022). Since Fe dominates the opacity of stellar ultraviolet spectra (which is relatively insensitive to O/H), while O, the most abundant heavy element in H II regions, dominates gas-phase metallicity (interstellar iron being almost entirely depleted on to dust grains), line emission of gas with super-solar O/Fe photoionized by metal-poor stars may be explored using models with fixed O/Fe, but adopting a lower total metallicity for the stars than for the gas (e.g., Steidel et al., 2016).

In this case, it is expected that H and He II lines, which do not depend strongly on gas-phase metallicity, should be similar to those of models with $Z = Z_{\rm ISM} = 0.0001$. On the other hand, metallic lines should be affected by both the harder spectrum from low-metallicity stellar population and the increased amount of metals in the interstellar gas.

In Figure 3.3, we compare the standard GALSEVN binary-star model of Figure 2.5 (with $Z = Z_{\rm ISM} = 0.001$) with two new GALSEVN binary-star models: one exploring the influence of super-solar O/Fe by setting the stellar metallicity to 10 per cent of the ISM metallicity (i.e., $Z = 0.0001$ versus $Z_{\rm ISM} = 0.001$) and the other investigating the impact of a global reduction of metallicity, with $Z = Z_{\rm ISM} = 0.0001$.

At fixed $Z_{\rm ISM} = 0.001$, lowering the stellar metallicity from $Z = 0.001$ to 0.0001 implies bluer stellar-population spectra and harder ionizing radiation, since stars evolve at higher effective temperature (e.g., Bressan et al., 2012; Plat et al., 2019). The Hβ equivalent width increases significantly in Figure 3.3(b) (due to both higher $\dot{N}_{\rm H}$ and fainter 4861-Å continuum), as does the He II λ4686/Hβ ratio at ages until ~ 3 Myr, when the ionizing radiation becomes dominated by pure-He, WNE-type stars at both metallicities. A similar effect is seen at early ages in the (C IV λ1549 +C III] λ1908)/He II λ1640 (Figure 3.3(e)) and He II λ1640/O III] λ1664 ratios (Figure 3.3(f)).

The model with $Z = Z_{\rm ISM} = 0.0001$ in Figure 3.3 produces a luminosity ratio and equivalent widths of Hβ and He II λ1640 comparable to those in the model with the same $Z = 0.0001$ but higher $Z_{\rm ISM} = 0.001$ (Figures 3.3(b) and (d)). This is because these emission lines are primarily sensitive to the shape of the stellar-population spectrum. Instead, as expected from Figure 3.1, the ratios of metal-to-H and He lines decrease significantly when $Z_{\rm ISM}$ is reduced from 0.0001 to 0.001 (Figures 3.3(a), (e) and (f)).

On the whole, Figure 3.3 shows that adopting super-solar O/Fe significantly affects the predicted emission-line properties of metal-poor star-forming galaxies, although we note that the impact on the equivalent width of He II λ1640 is relatively modest in Figure 3.3(d).

3.2 Parameters pertaining to the stellar population

In the previous section, we have explored the effects of stellar and several ISM parameters (ionization parameter, C/O and O/Fe abundance ratios) on the predicted emission-line properties of binary-star SSPs computed with the GALSEVN code. We showed that, while these models produce significantly more energetic radiation than previous single- and binary-star models, they do not appear to reach the largest observed equivalent widths of lines with high ionization energies, such as He II λ1640 and C III] λ1908. In the following paragraphs, we consider additional effects associated with the evolution of stellar populations, which could potentially influence these observables. Unless otherwise specified, for all models presented in the next section, we consider binary-star populations with $Z = 0.001$ and the standard nebular parameters listed in table 2.1.

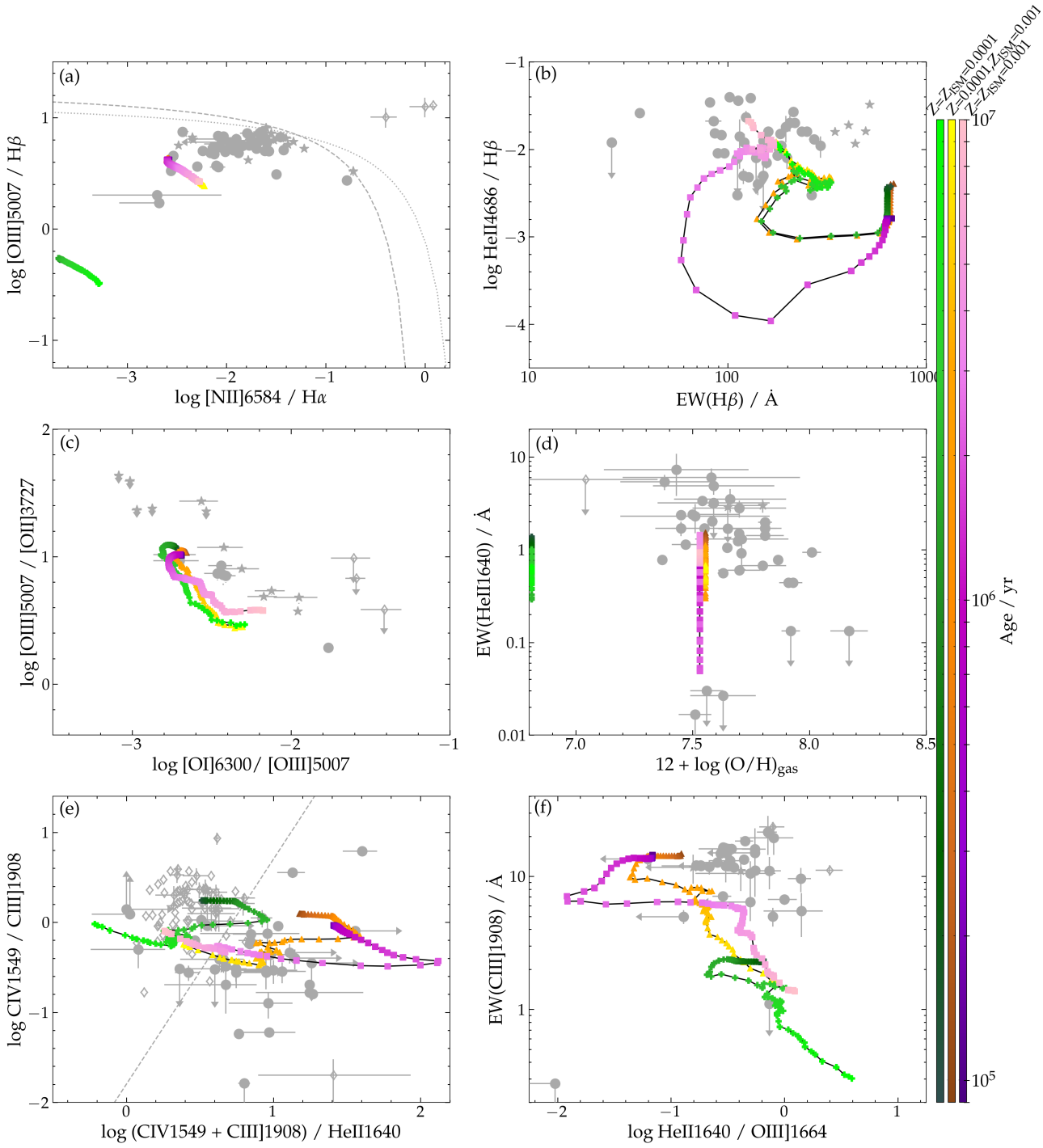

Figure 3.3: Same as Figure 2.5, for three GALSEVN binary-star models: a model with the standard parameters of table 2.1 (with $Z = Z_{\rm ISM} = 0.001$; filled squares), one exploring the influence of super-solar O/Fe (with $Z = 0.0001$ and $Z_{\rm ISM} = 0.001$; filled triangles), and one investigating the impact of a global reduction of metallicity (with $Z = Z_{\rm ISM} = 0.0001$; filled crosses). See main text for details. In (d), the model with $Z_{\rm ISM} = 0.0001$, which corresponds to $12 + \log({\rm O/H}) = 6.53$, is shown at the plot limit of $12 + \log({\rm O/H}) = 6.80$ to retain the same scale as in Figure 2.5.

3.2.1 Multiple bursts of star formation

So far, we have considered the emission-line properties of SSPs only, while even the most metal-poor nearby star-forming galaxies show evidence of several episodes of star formation (e.g., Izotov and Thuan, 2004; Tolstoy et al., 2009; Senchyna et al., 2019). In Figure 3.4, we show the effect of adding, at the age of 3 Myr, a second burst of star formation of the same amplitude as the first one to the evolution of an SSP. The sudden input of massive main-sequence stars boosts the rate of ionizing photons at that age, leading to a temporary rise in not only EW(Hβ), but also C IV λ1549/C III] λ1908 and EW(C III] λ1908) (see the difference between the orange and purple curves in Figures 3.4(b), (e) and (f)). As a result, the model probes a different region of the observational space than sampled by a pure SSP, the effect being less noticeable in the other diagrams of Figure 3.4.

We can explore more realistic histories of star formation for metal-poor galaxies by appealing to the SPHINX suite of cosmological (radiation-hydrodynamical) simulations of young galaxies in the Epoch of Reionization (Rosdahl et al., 2022). The green curve in Figure 3.4 shows the emission-line properties obtained for a typical galaxy experiencing several bursts of different amplitudes at ages up to 10 Myr in these simulations. The effects of three major bursts following the onset of star formation are clearly distinguishable through the associated boosts in EW(Hβ), C IV λ1549/C III] λ1908 and EW(C III] λ1908). This enables the model to probe new regions of the observational space not sampled by the SSP and two-burst models.

To illustrate the observational space sampled by models spanning a wider range of parameters, we show in Figure 3.5 the emission-line properties of 800 models computed using the star formation histories or 100 SPHINX galaxies, combined alternatively with four metallicities ($Z = Z_{\rm ISM} = 0.0005$, 0.001, 0.002 and 0.004) and two C/O abundance ratios (C/O =0.17 and 0.44), at ages between 2 and 10 Myr. The aim here is not to fully nor uniformly explore the space of adjustable parameters, but rather to provide global insight into the influence of star formation history, metallicity and C/O ratio on the observables of interest to us. The two (yellow) peaks of the model density distributions appearing in almost all diagrams of Figure 3.5 correspond to the two values of C/O sampled (see Figure 3.2).

Figure 3.5 shows that the restricted set of models considered here samples quite widely the observational space. In particular, it is worth emphasizing that the area of the He II λ4686/Hβ-versus-EW(Hβ) diagram with the highest density of models coincides with that where the bulk of observations lie, which was out of reach of previous models (Figure 2.5). Yet, some areas remained out of reach of these models, most notably those populated by galaxies with both largest He II λ4686/Hβ and EW(Hβ) (the most extreme of which being classified as LyC leakers; Figure 3.5(b)), He II λ1640 equivalent widths in excess of $\sim$ 1.5 Å (Figure 3.5(d)), largest C IV λ1549/C III] λ1908 (Figure 3.5(e)) and both largest EW(C III] λ1908) and He II λ1640/O III] λ1664 (Figure 3.5(f)).

3.2.2 Top-heavy IMF

Since the ionizing radiation of a young galaxy is controlled by massive stars, the upper part of the IMF could have a significant impact on the predicted emission-line properties of the models. So far, we have adopted in all models the standard Chabrier (2003) IMF truncated at 0.1 and 300 $M_\odot$, which can lead in binary-star populations to the presence of merged stars with masses up to $\sim$ 600 $M_\odot$ (section 2.2). To explore the influence of a top-heavy IMF, we adopt the generalised Rosin-Rammler distribution function (e.g., Chabrier, 2003; Wise et al., 2012; Goswami et al., 2022),

$$\phi(m) \propto m^{-2.3} \exp\left[-\left(\frac{m_{\rm char}}{m}\right)^{1.6}\right], \tag{3.1}$$

which approaches the standard Chabrier (2003) IMF at large m but is exponentially cut off at $m < m_{\rm char}$. Wise et al. (2012) used this function with $m_{\rm char} = 40\,M_\odot$ to explore the formation of Population III stars in early dwarf galaxies, while Goswami et al. (2022) adopted $200 \leq m_{\rm char} \leq 300\,M_\odot$

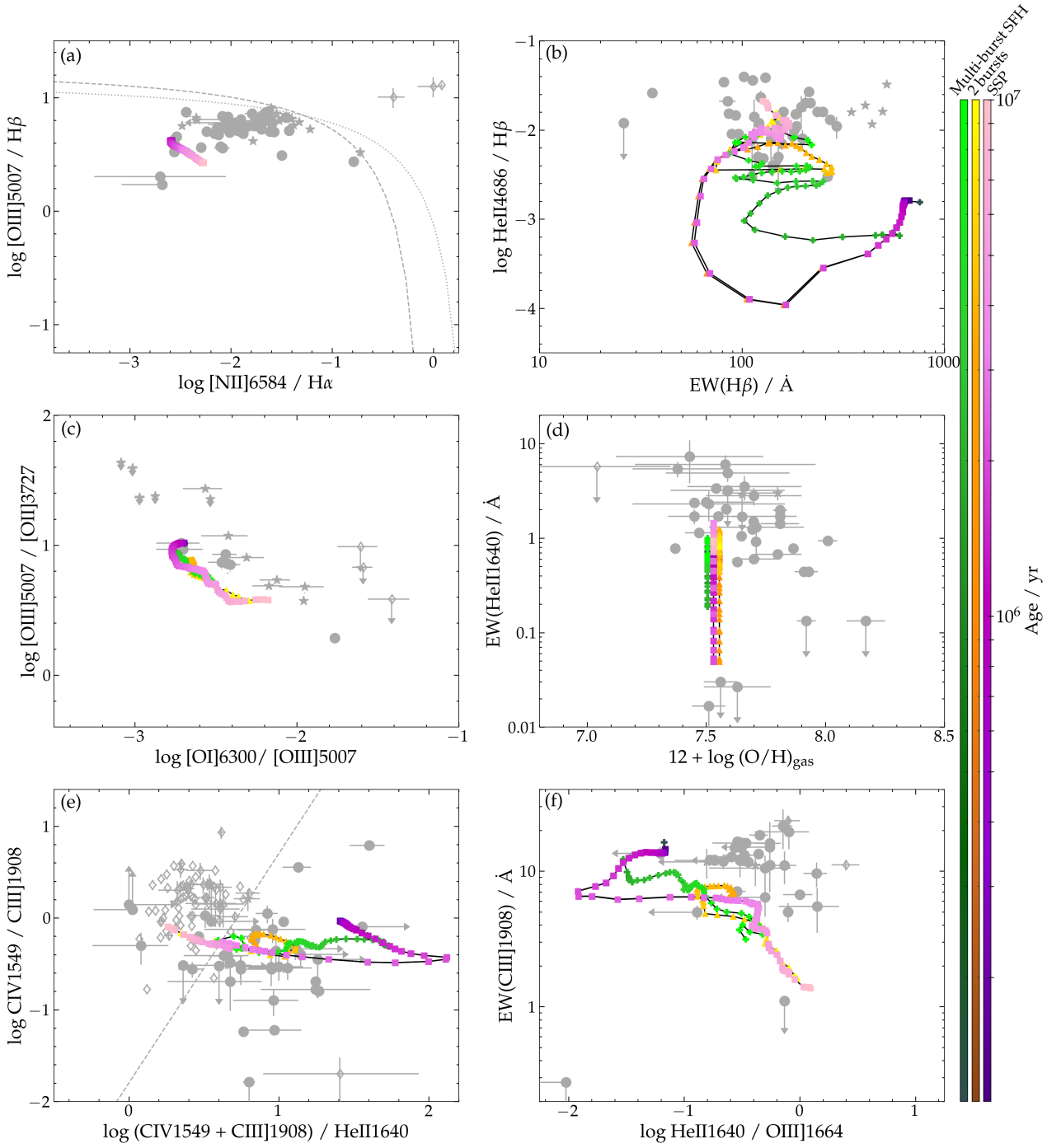

Figure 3.4: Same as Figure 2.5, for three GALSEVN binary-star models with metallicity $Z = 0.001$ and the standard nebular parameters of table 2.1: a plain SSP model (in green, with filled squares); one with a second burst of star formation of same amplitude as the first one added at the age of 3 Myr (in orange, with filled triangles); and one with the star formation history of a typical galaxy experiencing several bursts of different amplitudes at ages up to 10 Myr in the SPHINX cosmological simulations of Rosdahl et al. (2022, in green, with filled crosses; see text for details).

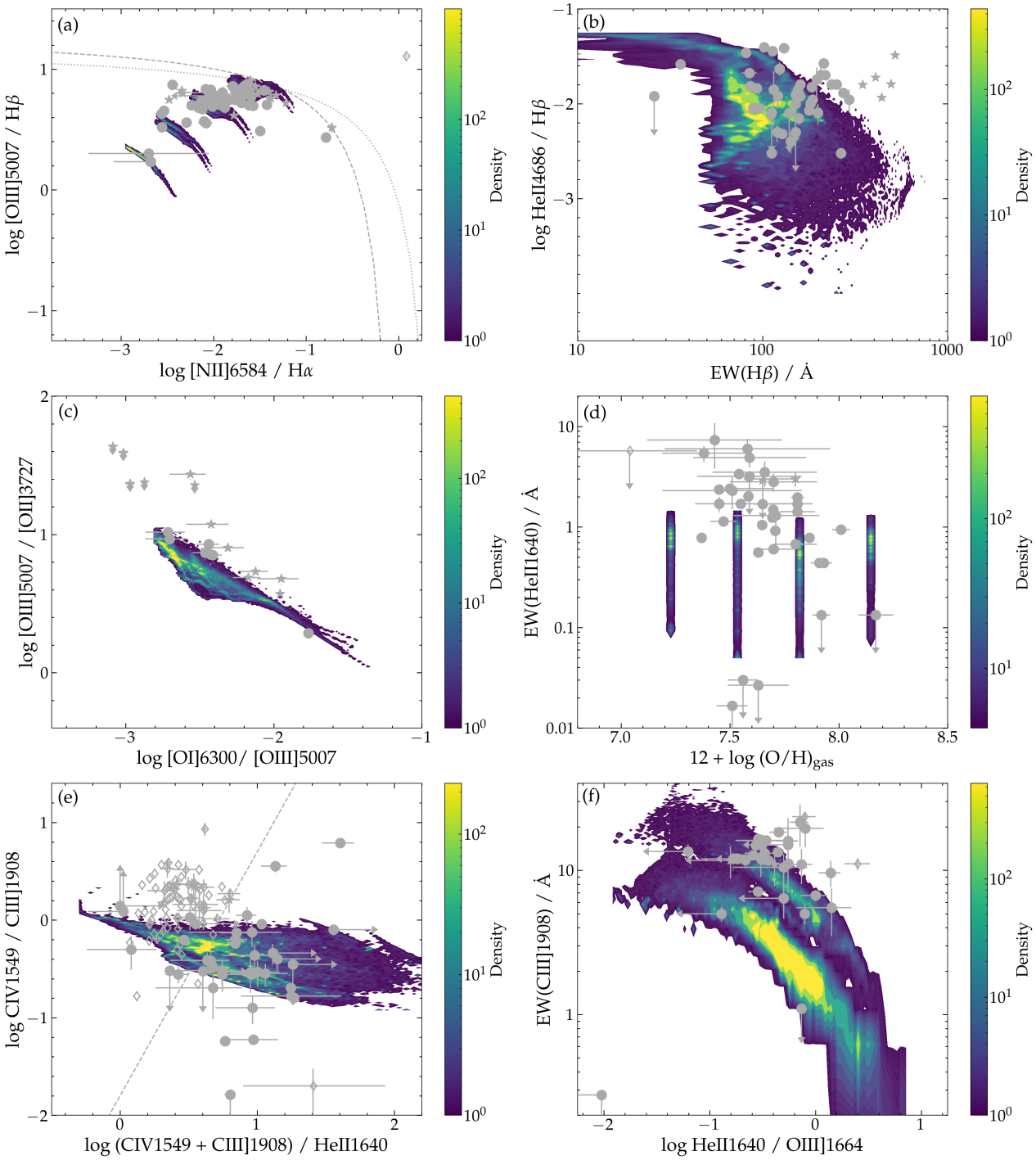

Figure 3.5: Same as Figure 2.5, but for 800 GALSEVN models computed using the star formation histories of 100 SPHINX galaxies from Rosdahl et al. (2022), combined alternatively with four metallicities ($Z = Z_{\rm ISM}$ = 0.0005, 0.001, 0.002 and 0.004) and two C/O abundance ratios (C/O =0.17 and 0.44), at ages between 2 and 10 Myr (younger models are not shown to avoid the artificial peak in model properties at early ages). The 2-dimensional histograms of models are colour-coded according to the density scale shown on the right.

to explore chemical enrichment by PISNe in extremely metal-poor galaxies. Here, we consider values of $m_{\rm char}$ in the range 50–100 $\mathrm{M}_\odot$ to explore the emission-line signatures of stellar populations strongly dominated by massive stars.

The upper panel of Figure 3.6 shows two versions of the top-heavy IMF of equation (3.1), for $m_{\rm char} = 50\,\mathrm{M}_\odot$ and $100\,\mathrm{M}_\odot$, compared to the standard Chabrier (2003) IMF. In the lower panel, we show the evolution of the absolute AB magnitude at 1500 Å, $M_{\rm UV}$, of GALSEVN binary-star models computed with these three IMFs, assuming a total initial mass in stars of $10^6\,\mathrm{M}_\odot$, metallicity $Z = 0.001$ and the standard nebular parameters of table 2.1. Since most of the mass in the models with top-heavy IMFs is concentrated in massive stars with low mass-to-light ratios, at fixed total initial stellar mass, these models are about 2 mag brighter in $M_{\rm UV}$ than that with a standard Chabrier (2003) IMF at early ages. The brightening in all models at ages before 2 Myr arises in part from stellar evolution on the main sequence, and in part from stellar mergers. Then, once the bulk of stars in the top-heavy IMF models leave the main sequence and complete their evolution, the population fades rapidly. Instead, the ultraviolet luminosity decreases more gradually in the model with standard Chabrier (2003) IMF, as stars of lower and lower mass progressively leave the main sequence.

In Figure 3.7, we present the emission-line properties of the three models shown in the lower panel of Figure 3.6. To avoid cluttering the diagrams, we do not show the properties of models fainter than $M_{\rm UV} = -14$ mag (limit marked by a cyan star), corresponding roughly to the typical luminosity of nearby, extremely metal-poor star-forming galaxies (see, e.g., table 1 of Senchyna et al., 2019). At early ages, when massive stars on the upper main sequence dominate the emission, the three models overlap in all diagrams. Once the bulk of stars in the top-heavy IMF models leave the main sequence to become red super-giant stars, at ages around 2 Myr, the implied strong drop in ionizing-photon rate and rise in 4861-Å continuum emission make the Hβ equivalent width decline more abruptly than in the standard model (Figure 3.7(b)). Meanwhile, after reaching a minimum, the He II λ4686/Hβ ratio (Figure 3.7(b)) and He II λ1640 equivalent width (Figure 3.7(d)) promptly rise again due to the emergence of hot, pure-He products of massive stars (section 2.2). In Figure 3.7(f), the C III] λ1908 equivalent width shows similar behaviour to EW(He II λ1640) relative to the standard model. EW(Hβ) takes longer than EW(He II λ1640) and EW(C III] λ1908) to increase again (Figure 3.7(b)), as red super-giant stars have stronger continuum emission at 4861 Å than at ultraviolet wavelengths.

Remarkably, Figure 3.7 shows that, in diagrams involving ultraviolet lines, the two GALSEVN binary-star SSP models with top-heavy IMFs, fixed metallicity $Z = 0.001$ and C/O = 0.17 investigated here reach regions of the observational space not sampled by the more complete grid of models with standard Chabrier (2003) IMF considered in Figure 3.5 (up to He II λ1640 equivalent withs of ~ 10 Å; Figure 3.7(b)). Although these SSP models spend less than a few Myr with such extreme emission-line properties, they can potentially be combined with more complex star formation histories. In fact, they could represent a transient phase in the evolution of a galaxy, when a cluster of massive stars happens to form and dominates the light for a while.

Overall, this parametric study has shown that adapting the nebular parameters and the properties of the stellar population can help the models reach reasonable agreement with most observations in the considered sample. To explore this agreement in more detail, to check whether the most extreme objects can be reproduced under very specific conditions, and to constrain the physical properties of these local analogues of primeval galaxies, the next step would be to generate a more detailed model grid, and to run statistical methods to fit the spectral energy distribution of a given object more precisely. This approach would also have the benefit of assessing whether GALSEVN models with well-chosen parameters are able to consistently reproduce all observed emission lines of a given object – this aspect being difficult to evaluate with the diagram-based approach presented in the previous chapter. This will be the subject of chapter 6.

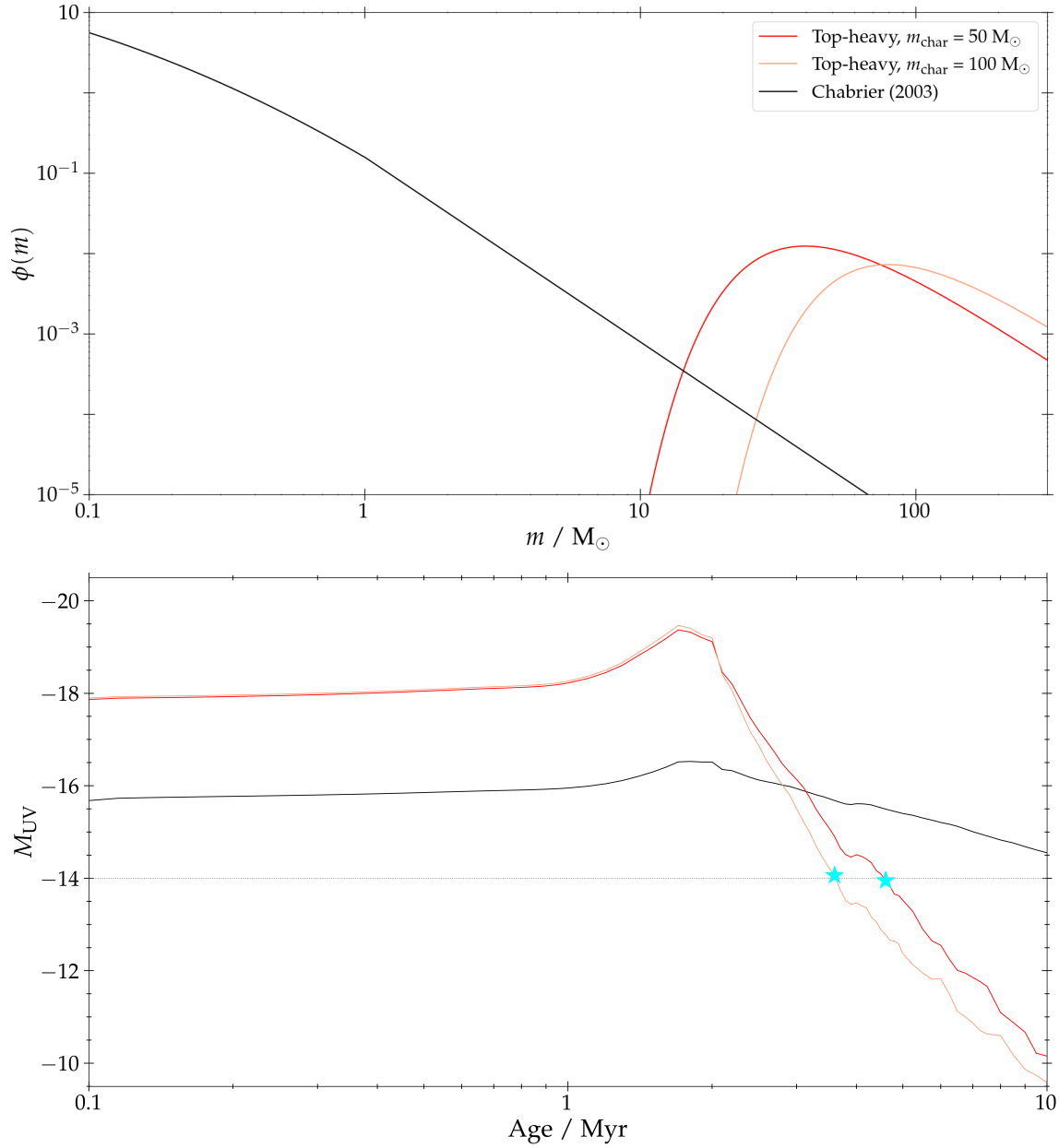

Figure 3.6: Top: top-heavy IMFs computed using equation (3.1) for two values of $m_{\rm char}$ (red: 50 $\mathrm{M}_\odot$; salmon: 100 $\mathrm{M}_\odot$), compared to the standard Chabrier (2003) IMF (in black). All IMFs are normalized to a total mass in stars of 1 $\mathrm{M}_\odot$. Bottom: absolute ultraviolet AB magnitude at 1500 Å, $M_{\rm UV}$, plotted against age for three GALSEVN binary-star models computed with the three IMFs shown in the top panel, assuming a total initial mass in stars of 10^6 $\mathrm{M}_\odot$, metallicity $Z = 0.001$ and the standard nebular parameters of table 2.1. For reference, the dotted horizontal line marks the magnitude $M_{\rm UV} = -14$ mag typical of nearby, extremely metal-poor star-forming galaxies (reached by the top-heavy-IMF models at the ages marked by the cyan stars).

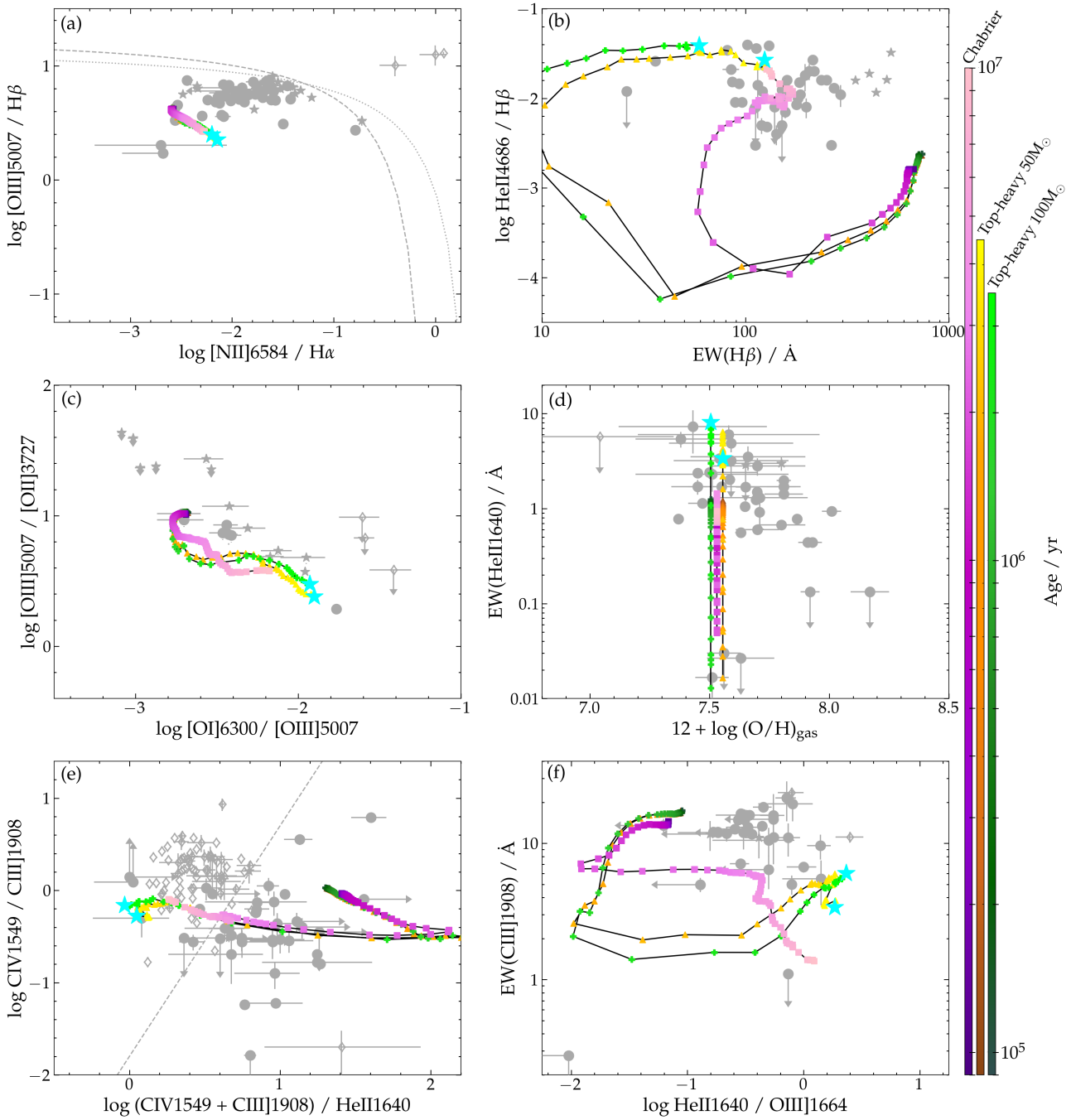

Figure 3.7: Same as Figure 2.5, for the three GALSEVN binary-star models with different IMFs shown in the lower panel of Figure 3.6 (colour-coded as indicated on the right). The curves interspersed with filled squares, triangles and crosses refer to the models with a Chabrier (2003) IMF and two top-heavy IMFs (equation 3.1) with characteristic masses of $m_{\rm char} = 50$ and $100\,{\rm M}_\odot$, respectively. Cyan stars mark the points beyond which the models with top-heavy IMFs become fainter than $M_{\rm UV} = -14$ mag and are not shown (see text and Figure 3.6 for details).

Before constructing this model grid, it is of interest to explore whether other sources of ionizing photons might be responsible for the missing high energy photons (e.g., the photons responsible for high He II-equivalent widths in the previous diagrams). Should this prove to be the case, it would be necessary to include additional modelling of this emission in spectral synthesis. These potential sources of ionizing photons are explored in the next chapter.

Chapter 4

Self-consistent modelling of additional ionizing processes

Contents

As mentioned in the previous chapters, most spectral synthesis models struggle to reproduce the highest observed equivalent widths of high-ionization emission lines such as He II λ1640, He II λ4686 and C IV λ1549. Although the previous chapter demonstrated that GALSEVN models with well-chosen parameters and assumptions (notably a top-heavy IMF) may lead to a reasonable agreement with most of these spectral features, the amount of highly ionizing photons produced in the most extreme objects of the considered sample remains hardly explained. If further exploration of the parameter space does not lead to satisfactory agreement for these objects, it will be necessary to consider other sources of high-energy photons.

Several production mechanisms have been suggested for these missing energetic photons. A most natural one is the hard radiation from hot, nearly pure-He stars produced through processes induced by binary interactions (such as envelope stripping, quasi-homogeneous evolution, and common-envelope ejection), often neglected in stellar population synthesis models (e.g., Eldridge and Stanway, 2012; Eldridge et al., 2017; Götberg et al., 2020). This possibility is all the more compelling in that ~ 70 per cent of massive stars in nearby stellar populations are thought to be part of binary systems (e.g., Sana et al., 2012; Moe and Di Stefano, 2017). Yet, the BPASS models of Stanway and Eldridge (2018), which incorporate the above processes, do not appear to produce enough energetic radiation to account for the observations (Stanway and Eldridge, 2019). Other proposed origins of the surprisingly strong high-ionization lines in some metal-poor star-forming galaxies include fast radiative shocks, accretion on to compact objects and active galactic nuclei (AGNs; e.g., Izotov et al., 2012; Nakajima et al., 2018; Plat et al., 2019; Schaerer et al., 2019; Umeda et al., 2022; Katz et al., 2023). Such components are typically modelled independently of the stellar population and then scaled to reproduce the data under consideration. While insightful, this approach suffers from the weakness of not guaranteeing physical consistency between the different spectral components involved.

4.1 Accretion discs of X-ray binaries

Several recent studies have suggested that the unusually strong He II λ1640 emission observed in the spectra of many metal-poor star-forming galaxies may originate from accretion discs of X-ray binaries, where a compact object (neutron star or stellar-mass black hole) accretes material from a companion (e.g., Schaerer et al., 2019; Umeda et al., 2022; Katz et al., 2023). Emission from the hot accretion discs of these systems peaks at X-ray energies (e.g., Mitsuda et al., 1984; Fragos et al., 2013; Mirocha, 2014; Senchyna et al., 2019). In detail, the accretion rate depends on the evolutionary stage and chemical evolution of the donor (or *companion*) star, the mass ratio between the donor and the compact object and their orbital separation.

In this context, the GALSEVN model, which follows the evolution of the physical properties and the emission from stars in binary systems, provides an ideal framework to compute in a self-consistent way the contribution by accretion discs of XRBs to the integrated light of stellar populations. In fact, in the next section, we present a simple model to compute the spectral energy distribution of XRB accretion discs in GALSEVN binary-star populations, based on a library of multicolour-disc spectra including potential Compton upward scattering of soft disc photons by energetic coronal electrons (Mirocha, 2014; Steiner et al., 2009). This model, which also accounts for X-ray variability (e.g., Tanaka and Shibazaki, 1996; Chen et al., 1997), provides good agreement with the observed X-ray luminosities of various samples of nearby, metal-poor star-forming galaxies (Douna et al., 2015; Brorby et al., 2016; Lehmer et al., 2019), as well as with the average X-ray luminosity function of XRBs in the five most metal-poor star-forming galaxies observed by Lehmer et al. (2019).

4.1.1 Modelling and calibration of accretion-disc emission in XRBs

We identify X-ray binaries among a population of evolving binary pairs generated with the SEVN code described in section 2.1.2 by searching for black holes and neutron stars whose masses increase with time, i.e., with positive mass accretion rate across a dynamical time step, $\dot{m}_{\rm acc} > 0$. For spherical infall, the maximum luminosity that can theoretically be produced by an accretion disc in hydrostatic equilibrium is the Eddington luminosity corresponding to the balance between radiation pressure and gravity (Cameron and Mock, 1967, see also Hurley et al. 2002). For accretion of fully-ionized H+He material, with hydrogen mass fraction X, on to a compact object of mass $m_{\rm c}$, this limit can be expressed as

$$L_{\rm Edd} \approx 1.26 \times 10^{38} \left(\frac{2}{1+{\rm X}}\right) \left(\frac{m_c}{{\rm M}_\odot}\right) \ {\rm erg\ s^{-1}}\,. \tag{4.1}$$

The Eddington luminosity is related to an Eddington accretion rate, $\dot{m}_{\rm Edd}$, through the formula (e.g., Shakura and Sunyaev, 1973)

$$L_{\rm Edd} = \eta \dot{m}_{\rm Edd} c^2\,, \tag{4.2}$$

where η is the radiative efficiency (i.e. the fraction of binding energy radiated away by the accretion flow) and c the speed of light.

Observationally, accretion on to compact objects is known to occasionally produce luminosities in excess of the theoretical Eddington limit, perhaps as a result of radiation-driven inhomogeneities (e.g., Begelman, 2002). Examples include tidal disruption events (e.g., Rees, 1988) and ultra-luminous X-ray sources (e.g., Bachetti et al., 2014; Pinto et al., 2016; Rodríguez Castillo et al., 2020), while some evidence suggests that most low-mass XRBs may have undergone a phase of super-Eddington accretion (Kalogera and Webbink, 1998). For super-Eddington accretion, corresponding to $\dot{m}_{\rm acc} > \dot{m}_{\rm Edd}$, the total accretion luminosity, noted $L_{\rm acc}$, can exceed the Eddington luminosity by a logarithmic factor $\sim \ln(\dot{m}_{\rm acc}/\dot{m}_{\rm Edd})$ (see Shakura and Sunyaev, 1973; Begelman et al., 2006a). We adopt here the convenient approximation (Watarai, 2006, see also Lapi et al. 2014)

$$L_{\rm acc} \approx 2 \ln\left(1 + \frac{\dot{m}_{\rm acc}}{2\dot{m}_{\rm Edd}}\right) L_{\rm Edd}\,, \tag{4.3}$$

which, for sub-Eddington accretion ($\dot{m}_{\rm acc} \leq \dot{m}_{\rm Edd}$), reduces to

$$L_{\rm acc} \approx \eta \dot{m}_{\rm acc} c^2 \,. \tag{4.4}$$

For super-Eddington accretion, the weaker-than-linear increase of $L_{\rm acc}$ with $\dot{m}_{\rm acc}$ in equation (4.3) (illustrated by figure 7 of Watarai, 2006) reflects how the accreting gas becomes optically too thick to radiate away all the dissipated energy, causing some radiation to be trapped and advected inward. For simplicity, we fix here the radiative efficiency to the standard value $\eta \approx 0.1$ corresponding to the fraction of energy liberated by a gas particle falling from far away on to the innermost stable circular orbit of a stationary (non-spinning) black hole (e.g., Shakura and Sunyaev, 1973).

In SEVN, the maximum rate at which a compact object can accrete mass is $\dot{m}_{\rm acc}^{\rm max} = f_{\rm Edd} \dot{m}_{\rm Edd}$, where $f_{\rm Edd}$ is an adjustable factor (Spera et al., 2019; Iorio et al., 2023).[1] This factor can be set to a value greater than unity to account for super-Eddington accretion. In practice, we compute the mass accretion rate as $\dot{m}_{\rm c}/(1-\eta)$, where $\dot{m}_{\rm c}$ is the mass-growth rate of the compact object recorded in SEVN. In the setup of the code used here, the mass lost by the donor that is not accreted by the compact object (if $\dot{m}_{\rm acc} > \dot{m}_{\rm acc}^{\rm max}$) is assumed to be lost from the system (other options are described in Iorio et al., 2023).

Observations of X-ray binaries show that these stars commonly undergo X-ray outbursts, during which their luminosity can exceed that in the quiescent state by up to several orders of magnitude (e.g., Tanaka and Shibazaki, 1996; Chen et al., 1997). While this transience phenomenon is often discussed in the context of low-mass XRBs, where the donor star is typically less massive than a few $M_\odot$ (e.g., Yan and Yu, 2015), it is also observed in high-mass XRBs (e.g., Martin et al., 2014; van den Eijnden et al., 2022). Even high-mass XRBs classified as 'persistent' (i.e., non-transient sources emitting X-rays continuously over long periods) exhibit variability accompanied by (sometimes giant) X-ray flares (e.g., Hertz et al., 1992; Pottschmidt et al., 2003; Fürst et al., 2010). Such X-ray outbursts appear to be correlated with variability at all wavelengths from ultraviolet to infrared (e.g., Hynes et al., 2003; Sonbas et al., 2019; López-Navas et al., 2020; Yang et al., 2022).

The physical origin of X-ray variability is unclear. For several decades, the so-called disc-instability model has been put forward, according to which, as material falls on to the disc, a thermal-viscous instability develops, leading to recurrent burst-accretion events (e.g., Meyer and Meyer-Hofmeister, 1981; Faulkner et al., 1983; van Paradijs, 1996; Hameury and Lasota, 2020, see the reviews by Lasota 2001; Hameury 2020). While the realistic incorporation of thermodynamics and the ability to reproduce fairly well observations of X-ray outbursts have made this model popular, it does suffer from several weaknesses and shortcomings, notably with regard to angular-momentum transport and the inclusion of several poorly-constrained parameters (see Hameury 2020 for details). Hence, any attempt to implement the disc-instability model in SEVN would be highly uncertain.

In this context, we prefer to adopt here a more empirical approach to account for variability when modelling the spectral properties of XRB accretion discs. We assume that any accretion event spreads over two phases: a quiescent phase during which accretion proceeds at the rate provided by SEVN, $\dot{m}_{\rm c}/(1-\eta)$, and an outburst phase during which it is boosted by a factor $f_{\rm A}$. We assume that a fraction $\epsilon_{\rm A}$ of the mass is accreted during the outburst phase. For the accreted mass $\delta m_{\rm c}$ to be conserved over the time interval $\delta t'$, we thus write

$$\dot{m}_{\rm acc}(t') = \begin{cases} \frac{1}{1-\eta}\frac{\delta m_{\rm c}}{\delta t'} & \text{during} \quad (1-\epsilon_{\rm A})\delta t' \,, \\ \\ \frac{f_{\rm A}}{1-\eta}\frac{\delta m_{\rm c}}{\delta t'} & \text{during} \quad \frac{\epsilon_{\rm A}}{f_{\rm A}}\delta t' \,, \end{cases} \tag{4.5}$$

where $\delta m_{\rm c}$ is the mass growth of the compact object in a time interval $\delta t'$ of the evolution of an SSP (adopting the same notation as in equation 2.1 of chapter 2). For reference, $\delta m_{\rm c}$ represents at most a few percent of $m_{\rm c}$.

[1] The quantity $f_{\rm Edd}$ is noted $\eta_{\rm Edd}$ in Iorio et al. (2023).

We describe the spectral distribution of the power $L_{\rm acc}\ (t')$ produced by the hot accretion disc at time t' (equation 4.3) by means of a multicolour-disc model (Mitsuda et al., 1984), i.e., a modified blackbody spectrum reflecting the gas-temperature distribution in the disc. To this end, we use the ARES[2] code of Mirocha (2014) and compute a comprehensive library of multicolour disc models for compact objects accreting at the Eddington limit, parametrized in terms of the accreting-object mass, $m_{\rm ARES}$, and the maximum radius of the accretion disc, $R_{\rm max}$. Following Senchyna et al. (2020), we fix $R_{\rm max}$ to 10^4 gravitational radii (we find that decreasing or increasing $R_{\rm max}$ by an order of magnitude would, respectively, lower by about 20 per cent or increase negligibly the X-ray luminosities and rates of He II-ionizing photons predicted by our models). By design, each spectrum is normalized to the Eddington luminosity given by equation (4.1) for $m_{\rm c} = m_{\rm ARES}$, for a pure-H gas (X = 1).

XRB spectra also often present a high-energy tail component, whose strength can vary over time, and which is thought to arise from Compton upward scattering of soft disc photons by energetic coronal electrons (e.g., Remillard and McClintock, 2006; Steiner et al., 2009). Based on the analysis of 20 XRBs with multi-epoch X-ray luminosities in the range ~ 0.5–$50 \times 10^{39}\,{\rm erg\,s^{-1}}$, Sutton et al. (2013) conclude that the spectra of sources with sub-Eddington accretion rates may be well represented by multi-colour discs, while those of sources with super-Eddington accretion rates tend to exhibit 'hard-luminous' and 'soft-luminous' components (in roughly equal proportions among the sample), presumably depending on inclination. For each $m_{\rm ARES}$, we therefore compute both a spectrum including Comptonization of disc photons (implemented in ARES using the SIMPL model by Steiner et al., 2009) and a spectrum not including it. If accretion is sub-Eddington, i.e. for $L_{\rm acc}(t') \leq L_{\rm Edd}$, we adopt the pure multi-colour-disc spectrum. Otherwise, we randomly draw between the pure multi-colour-disc and the Comptonized spectra.[3] We note that the results presented in this work about the X-ray luminosities and He II-ionizing photon rates of star-forming galaxies do not depend sensitively on this refinement of spectral modelling at the highest energies.

The above approach allows us to compute the spectrum of every hot accretion disc of XRB in a GALSEVN binary-star SSP of age t', from which we extract the disc luminosity in the 0.5–8 keV energy band, noted $L_{\rm X}$. For reference, the quantity $L_{\rm X}$ amounts to typically between 30 and 90 per cent of $L_{\rm acc}$. Figure 4.1 shows X-ray luminosity functions (XLFs) of XRBs obtained in this way for populations with binary-star fraction $f_{\rm bin} = 0.7$ (typical of massive-star populations; e.g., Sana et al., 2012), assuming 100 Myr of constant star formation, for different choices of the parameters $f_{\rm A}$ and $\epsilon_{\rm A}$ in equation (4.5). All models have the metallicity $Z = 0.008$, corresponding to the metallicity of the five most metal-poor star-forming galaxies observed with *Chandra* for which Lehmer et al. (2019) derived the average, completeness-corrected XLF of XRBs shown by the black data points with error bars (normalized per unit star formation rate in the same way as the models). The black dotted line shows an empirical model, incorporating also potential contamination by background point sources from the cosmic X-ray background, whose contribution to the XLF is however estimated to be minor, decreasing from about 20 per cent at $L_{\rm X} = 10^{37}\,{\rm erg\,s^{-1}}$ to about 3 per cent at $L_{\rm X} = 10^{40}\,{\rm erg\,s^{-1}}$ (for details, see Lehmer et al., 2019). We therefore ignore this component in our model. Furthermore, we adopt here $f_{\rm Edd} = 100$ to set the maximum allowed accretion rate in SEVN, as significantly lower values do not produce enough high-luminosity sources, while adopting higher values negligibly affects the predicted XLFs, indicating that only a few systems can potentially have $\dot{m}_{\rm acc} > 100\dot{m}_{\rm Edd}$.

We find that the predicted XLF depends in a somewhat degenerate way on the parameters $f_{\rm A}$ and $\epsilon_{\rm A}$ of the two-phase model, the main requirement for reproducing the observations being that the bulk of mass be accreted during outbursts. This is illustrated by the three models shown in Figure 4.1, accreting, during transient outbursts, fractions $\epsilon_{\rm A} = 1.00$, 0.99 and 0.95 of the mass at $f_{\rm A} = 100$, 100 and 1000 times the quiescent rate, respectively. In the first model, the entire mass is accreted during outbursts, while in the second model, outburst- and quiescent-accretion phases have similar durations, and in the third model, outburst accretion lasts less than $1/50^{\rm th}$ of quiescent accretion. All

[2] https://ares.readthedocs.io/en/latest/

[3] Since the ARES spectral library pertains to objects accreting at the Eddington rate, in practice, for a given $L_{\rm acc}$, we adopt the spectrum corresponding to the ARES model for a compact object accreting at the Eddington luminosity $L_{\rm Edd} = L_{\rm acc}$ given by equation (4.1) for a pure-H gas, i.e., $m_{\rm ARES} = L_{\rm acc}/(1.26 \times 10^{38}{\rm erg\ s^{-1}})\,{\rm M_\odot}$.

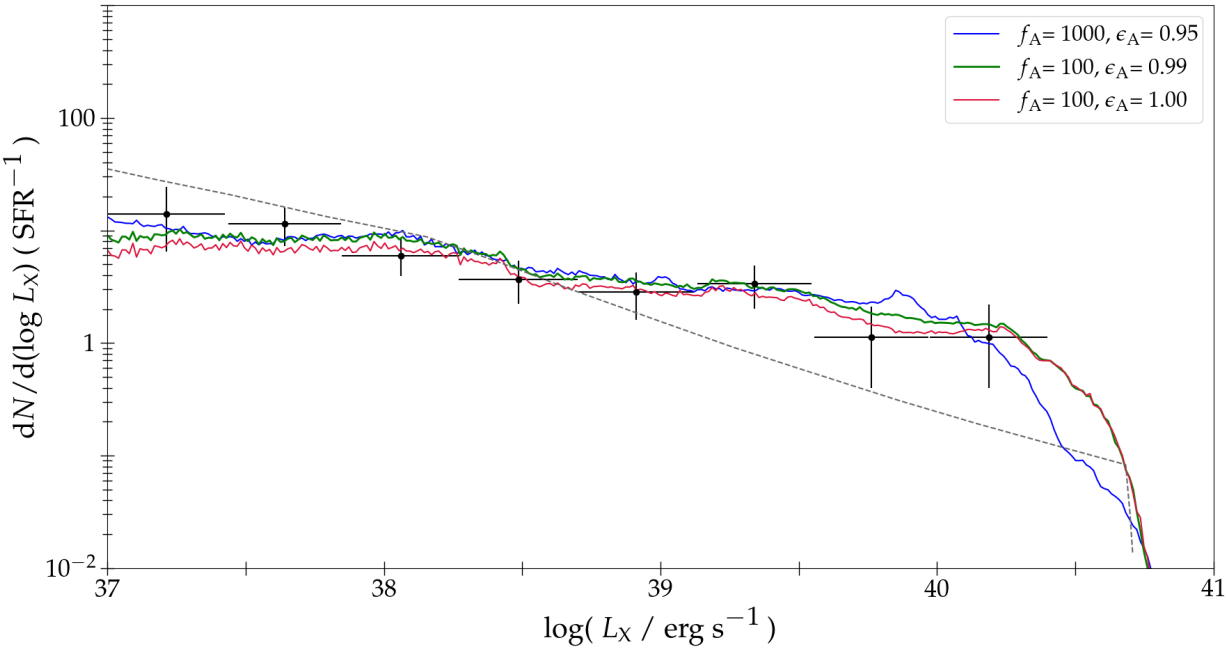

Figure 4.1: X-ray luminosity functions of XRBs for GALSEVN populations with binary fraction $f_{\rm bin} = 0.7$, assuming 100 Myr of constant star formation at the rate $\psi = 1 {\rm M}_\odot\,{\rm yr}^{-1}$. Accretion is taken to proceed according to the two-phase model of equation (4.5), for different choices of the fraction $\epsilon_{\rm A}$ of mass accreted while the rate is boosted by a factor $f_{\rm A}$, as indicated. All models have the metallicity $Z = 0.008$, corresponding to the metallicity of the five most metal-poor star-forming galaxies observed with *Chandra* for which Lehmer et al. (2019) derived the average, completeness-corrected luminosity function shown by the black data points with error bars. The black dotted line shows an empirical model proposed by these authors (see text for details).

three models provide roughly similar agreement with the observed XLF of XRBs compiled by Lehmer et al. (2019) in Figure 4.1. The maximum effective accretion rate for these models is $f_{\rm A} f_{\rm Edd} = 10^4$–$10^5$ times the Eddington rate $\dot{m}_{\rm Edd}$, corresponding to a maximum accretion luminosity $L_{\rm acc} \approx 17$–$22 L_{\rm Edd}$ (equation 4.3), compatible with the 10–$100 L_{\rm Edd}$ obtainable from radiation-driven inhomogeneities in accretion discs (e.g., Begelman, 2002). We note that about a third of XRBs exhibit super-Eddington accretion rates during the phase of standard accretion, compared to three quarters during the phase of enhanced accretion (for $f_{\rm A} = 100$).

The model with a single phase of enhanced accretion is the simplest conceptually. The one with $\epsilon_{\rm A} = 0.99$ and $f_{\rm A} = 100$ provides formally the best fit (mininum χ^2) to the data, while the one with quisecent accretion ~ 50 times longer than enhanced accretion is the closest conceptually to that proposed by, e.g., Li (2012) for the growth of supermassive black holes in quasars. Since all three models reproduce the observed XLF of XRBs measured by Lehmer et al. (2019) in nearby metal-poor galaxies, they predict similar contributions of XRB accretion discs to the ionizing-radiation budget of a star-forming galaxy modelled with the GALSEVN code. Here, we adopt the model with $\epsilon_{\rm A} = 0.99$ and $f_{\rm A} = 100$, which provides the best fit to the observations in Figure 4.1. Any of the other two models would provide similar results on the emission from XRB accretion discs presented in this work.

In Figure 4.2, we show the XLFs obtained at fixed $f_{\rm A} = 100$ and $\epsilon_{\rm A} = 0.99$, for GALSEVN binary-star populations of different metallicities in the range $0.0001 \leq Z \leq 0.02$. Remarkably, all XLFs remain compatible with the observational determination of Lehmer et al. (2019). This is because the XLF is largely dominated by systems composed of low-mass compact objects with relatively low-mass companions: nearly 80 per cent of overall accretion occurs in systems composed of a compact object lighter than $20\,{\rm M}_\odot$ (with progenitor main-sequence mass typically smaller than $30\,{\rm M}_\odot$; e.g., Spera et al., 2015) and a companion lighter than $25\,{\rm M}_\odot$. Since the evolution of stars lighter than $30\,{\rm M}_\odot$ is not significantly affected by line-driven stellar winds, we do not expect a strong dependence of XRB properties on metallicity. The main metallicity-dependent effect comes from the reduced population

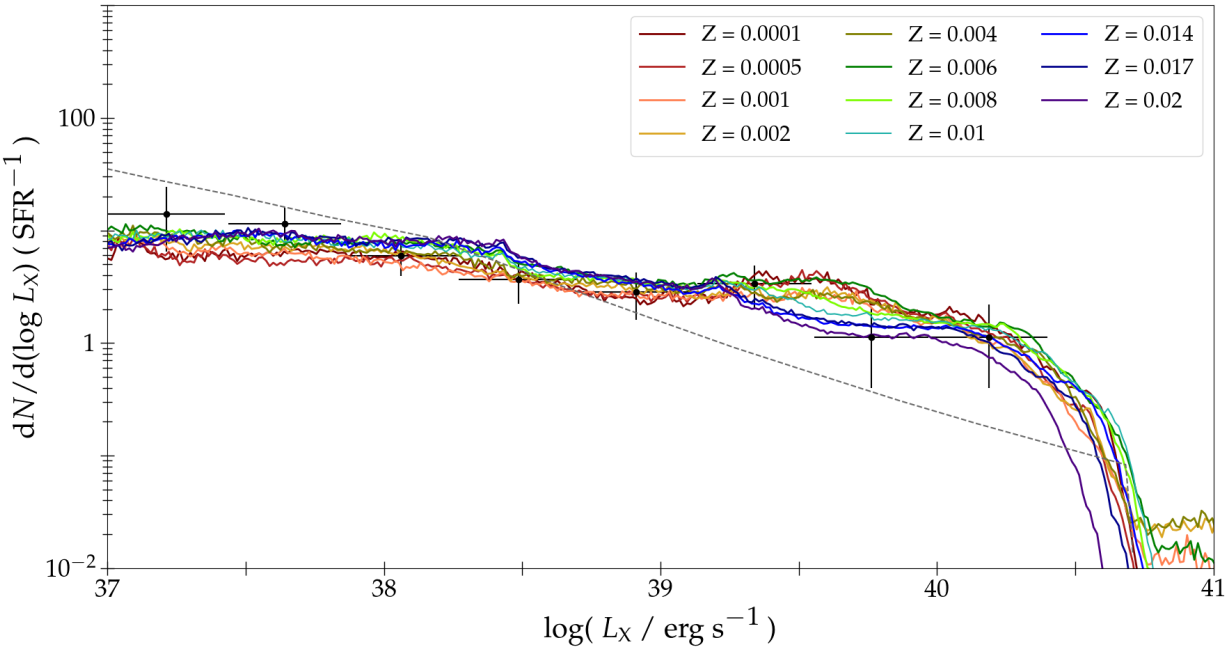

Figure 4.2: Same as Figure 4.1, for GALSEVN binary-star populations of different metallicities in the range $0.0001 \leq Z \leq 0.02$, as indicated. In all models, accretion is taken to proceed according to the two-phase model described by equation (4.5), with $f_{\rm A} = 100$ and $\epsilon_{\rm A} = 0.99$.

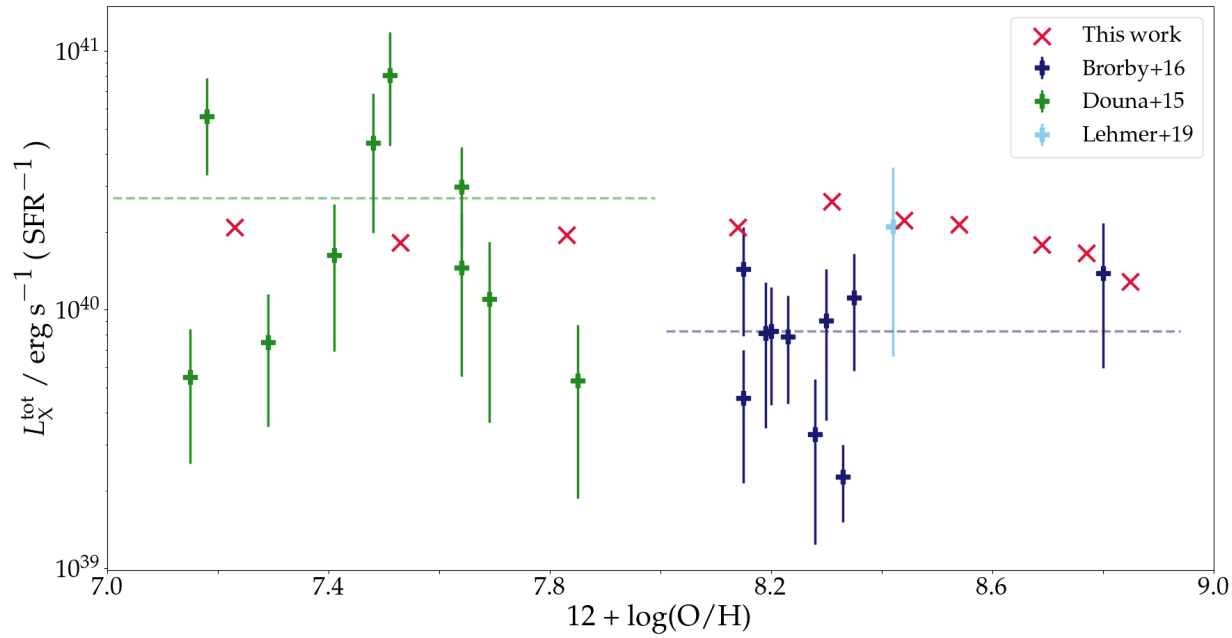

Figure 4.3: Total X-ray luminosity $L_{\rm X}^{\rm tot}$ (per unit star formation rate) obtained by integrating the luminosity functions of Figure 4.2, for metallicities in the range $0.0005 \leq Z \leq 0.02$ (red crosses). The data are from *Chandra* observations of a sample of 10 nearby star-forming galaxies with 12 + log(O/H) < 8.0 compiled by Douna et al. (2015, green points; see also Brorby et al. 2014) and a sample of nearby analogues of distant Lyman-break galaxies compiled by Brorby et al. (2016, dark blue points). The light-blue point (and error bars) at 12 + log(O/H) $\approx$ 8.4 shows the mean $L_{\rm X}^{\rm tot}$/SFR (and associated standard deviation) of the five metal-poor star-forming galaxies used by Lehmer et al. (2019) to derive the average XLF of Figure 4.1. Dotted horizontal green and blue lines represent the mean $L_{\rm X}^{\rm tot}$/SFR of galaxies in the Douna et al. (2015) and Brorby et al. (2016) samples, respectively. Brorby et al. (2016) estimate the typical uncertainty on 12 + log(O/H) at 0.14.

of massive compact objects at high metallicity (e.g., Dray, 2006; Mapelli et al., 2013), apparent in the slight decline in the XLF at the highest X-ray luminosities in Figure 4.2, while agreement with the observed luminosity function is maintained.

In Figure 4.3, we compare the total X-ray luminosities per unit star formation rate, $L_{\rm X}^{\rm tot}/{\rm SFR}$, obtained by integrating the XLFs of the binary-star models with different metallicities (converted to gas-phase O abundances using table 2 of Gutkin et al. 2016 for $\xi_{\rm d} = 0.3$) of Figure 4.2 with those of the sample of 10 nearby star-forming galaxies with $12 + \log({\rm O/H}) < 8.0$ compiled by Douna et al. (2015, green points; see also Brorby et al. 2014) and the sample of nearby analogues of distant Lyman-break galaxies compiled by Brorby et al. (2016). Also shown is the mean $L_{\rm X}^{\rm tot}/{\rm SFR}$ (and associated standard deviation) of the five metal-poor star-forming galaxies used by Lehmer et al. (2019) to derive the average XLF in Figure 4.1.[4] As expected from Figure 4.1, the model with $Z = 0.008$ (corresponding to $12 + \log({\rm O/H}) \approx 8.4$) lies near this mean value. More generally, Figure 4.3 shows that the total X-ray luminosity per unit star formation rate predicted by our models is well within the ranges found by Douna et al. (2015, green points) and Lehmer et al. (2019, light blue points) and near the upper end of that reported by Brorby et al. (2016, dark blue points).

We consider the reasonable agreement between GALSEVN models of binary-star populations and X-ray observations of nearby, metal-poor star-forming galaxies and analogues of distant Lyman-break galaxies in Figures 4.2–4.3 as support for our simple approach to model the emission from accretion discs of X-ray binaries consistently with the spectral modelling of stars.

4.1.2 Impact on emission lines

As shown in the previous section, such agreement with observations can be obtained with models in which most of the mass is accreted during episodes of X-ray outbursts, at a much higher rate than during the quiescent phase, the actual strength and duration of outbursts being degenerate. Figure 4.4 shows the X-ray luminosity function of XRBs computed assuming that 99 per cent of the mass is accreted by the compact object during outbursts at a rate 100 greater than in the quiescent phase, for a GALSEVN binary-star population corresponding to 100 Myr of constant star formation at the rate $\psi = 1{\rm M}_\odot\,{\rm yr}^{-1}$. The model has a binary-star fraction $f_{\rm bin} = 0.7$ (typical of massive-star populations; e.g., Sana et al., 2012) and the metallicity $Z = 0.008$, close to the typical metallicity of the five metal-poor galaxies for which Lehmer et al. (2019) derived the average luminosity function shown by the black data points with error bars, which is well reproduced by the model. In the previous section, we further highlighted that metallicity has only a minor influence on the predicted X-ray luminosity function (Figure 4.2).

In Figure 4.5, we show the contribution by XRB accretion discs to the total Hβ and He II λ4686 luminosities predicted by such a model for a GALSEVN binary-star population of standard metallicity $Z = 0.001$. The population of XRBs grows with time, as black holes and neutron stars form. Yet, the contribution by ionizing radiation from XRB accretion discs to the total line luminosities remains negligible, reaching at most a few percent at ages greater than about 30 Myr. We conclude that, based on the XRB luminosity function observed in nearby galaxies, XRB accretion discs are unlikely to contribute significantly to the strong He II emission from metal-poor star-forming galaxies in the sample of section 2.3.1.

4.1.3 Comparative discussion of previous models

In chapters 2 and 3 above, we have seen that the new GALSEVN spectral-evolution model of binary-star populations presented in section 2.1 predicts significantly harder ionizing radiation than previous models of single- and binary-star populations, making it possible to reproduce, in particular, the high He II λ4686/Hβ ratios and large Hβ equivalent widths commonly observed in metal-poor star-forming

[4] For each galaxy, $L_{\rm X}^{\rm tot}/{\rm SFR}$ was obtained by integrating the observed individual luminosity function in figure 3 of Lehmer et al. (2019) and then dividing by the star formation rate in their table 1.

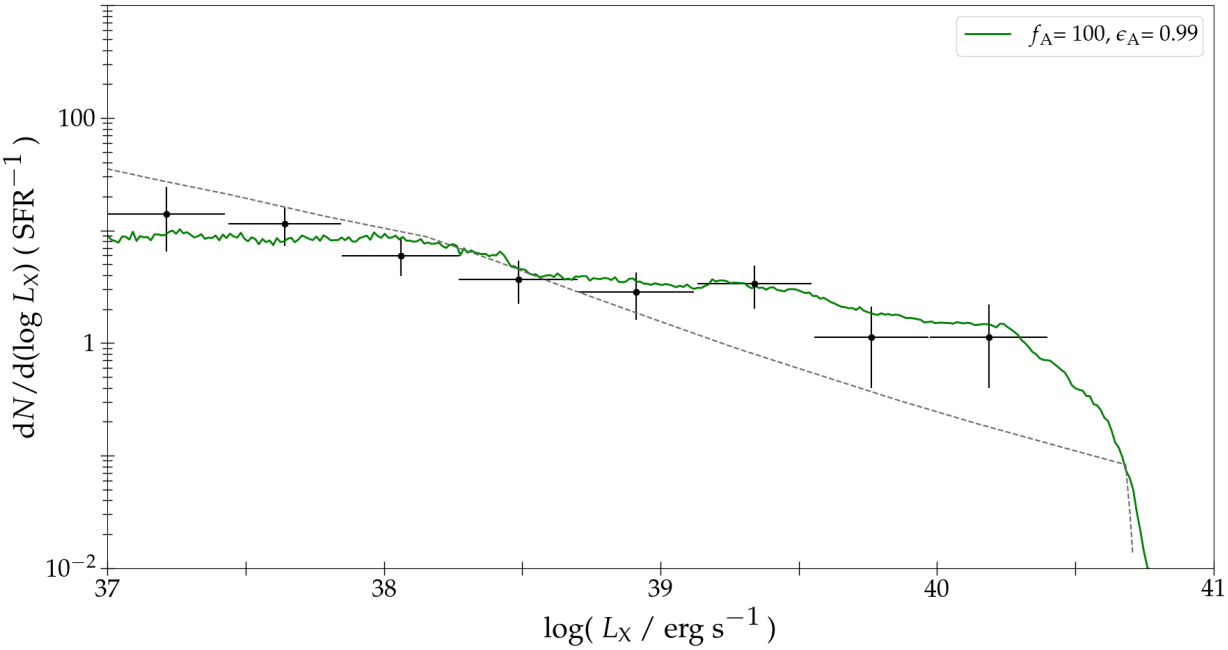

Figure 4.4: Optimised X-ray luminosity function (in the 0.5–8 keV energy band) of XRBs for a GALSEVN binary-star population of metallicity $Z = 0.008$ with binary fraction $f_{\rm bin} = 0.7$, assuming 100 Myr of constant star formation at the rate $\psi = 1 {\rm M}_\odot\,{\rm yr}^{-1}$. Accretion is assumed to proceed according to the two-phase model described by equation (4.5), with $f_{\rm A} = 100$ and $\epsilon_{\rm A} = 0.99$. Also shown for comparison is the average luminosity function derived from *Chandra* observations of the five most metal-poor star-forming galaxies in the sample studied by Lehmer et al. (2019, data points with error bars). The black dotted line shows an empirical model proposed by these authors (see text for details).

galaxies. The most extreme He II λ1640 emitters can be accounted for by invoking populations entirely dominated by massive stars (section 3.2.2). The model also allows us to compute, in a physically consistent way, the contribution by accretion discs of X-ray binaries to the ionizing radiation of a star-forming galaxy, as shown in section 4.1.1. Interestingly, we find that reproducing the observed luminosity function of X-ray binaries in nearby, metal-poor star-forming galaxies implies that XRB accretion discs must have, on average, a negligible impact on the predicted luminosities of high-ionization lines. While consistent with the results from several previous studies (e.g., Jaskot and Oey, 2013; Senchyna et al., 2017, 2020; Saxena et al., 2020), this finding contrasts with some recent claims (Schaerer et al., 2019; Umeda et al., 2022; Katz et al., 2023), which we now examine in more detail.

Schaerer et al. (2019) used an observed anti-correlation between X-ray luminosity per unit star formation rate ($L_{\rm X}^{\rm tot}$/SFR) and metallicity (Douna et al., 2015; Brorby et al., 2016), combined with an estimate of the rate of He II- ionizing photons ($\dot{N}_{\rm He\,II}$) per unit $L_{\rm X}^{\rm tot}$ in the metal-poor star-forming galaxy I Zw 18, to conclude that XRBs are likely to be the main source of He II emission in metal-poor star-forming galaxies. The founding assumption of this reasoning, that He II emission in I Zw 18 is produced by XRBs, has since been ruled out by Kehrig et al. (2021), who find that the high-mass binary dominating the X-ray emission lies about 200 pc away from the He II-emission peak. Also, the prediction by Schaerer et al. (2019) that the He II λ4686/Hβ line-luminosity ratio should correlate with $L_{\rm X}^{\rm tot}$/SFR does not appear to be confirmed observationally by the sample of 11 metal-poor star-forming galaxies with high-quality constraints on both X-ray and He II emission studied by Senchyna et al. (2020, see their figure 9).

In fact, by arbitrarily scaling ARES multicolour-disc models for a wide range of black hole masses (Mirocha, 2014) added to BPASS ionizing spectra of binary-star populations with constant star formation, Senchyna et al. (2020) find that $L_{\rm X}^{\rm tot}$/SFR in excess of $10^{42}\,{\rm erg\,s^{-1}/M_\odot\,yr^{-1}}$ is required for XRBs to significantly boost He II emission. This is 10–100 times larger than observed in the 11 metal-poor star-forming galaxies of their sample, suggesting that XRBs are not primarily responsible for

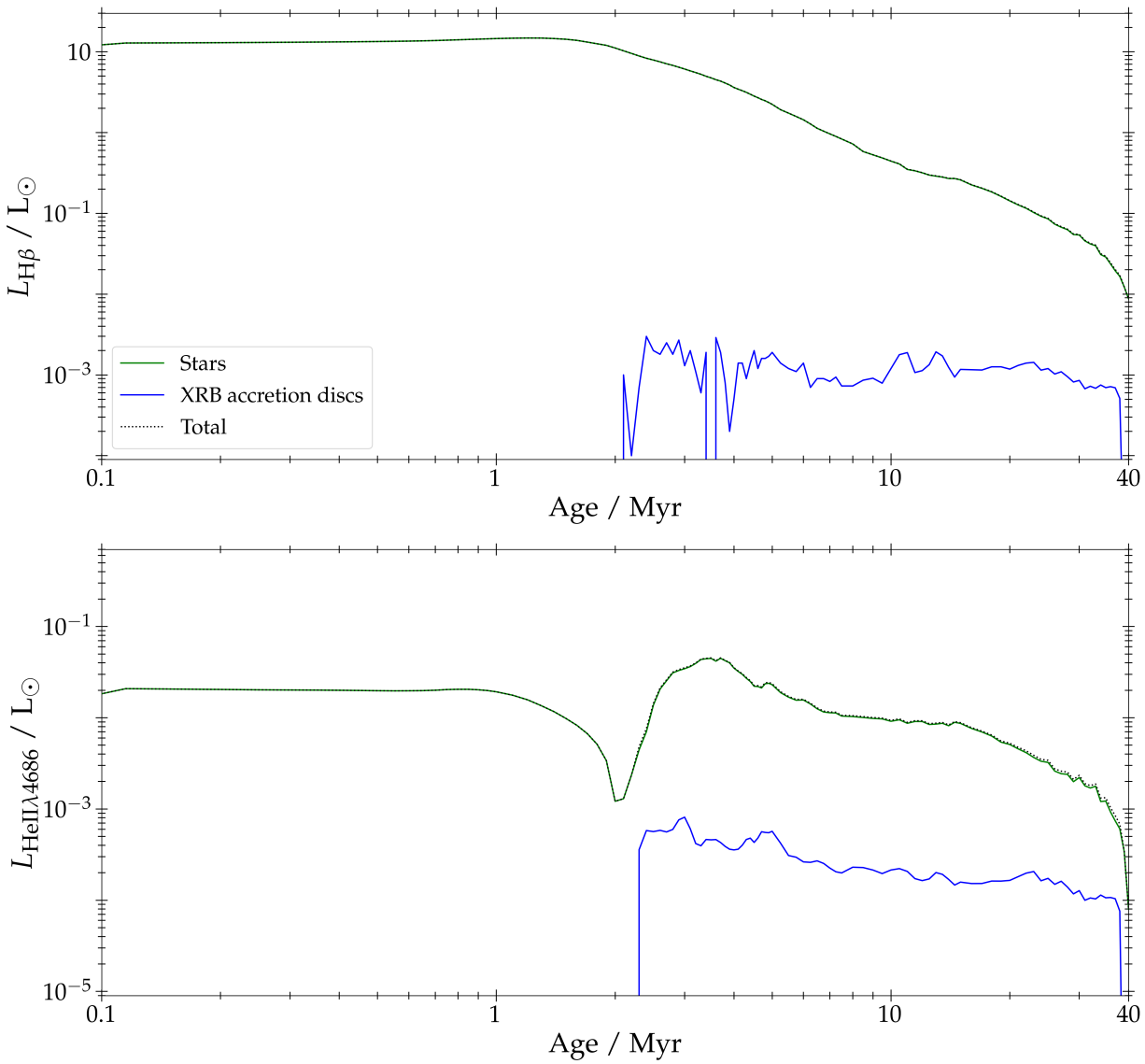

Figure 4.5: Contribution by XRB accretion discs (in blue), compared to the stellar contribution (in green), to the total luminosities (in black) of Hβ (top panel) and He II λ4686 (bottom panel) plotted against age, for a GALSEVN binary-star SSP with metallicity $Z = 0.001$. The model has the same zero-age Chabrier (2003) IMF normalized to a total initial stellar mass of $1\,\mathrm{M}_\odot$ integrated over 0.1–$300\,\mathrm{M}_\odot$ as in Figure 2.3.

He II emission in these galaxies. Similarly, Saxena et al. (2020) find no significant difference in the $L_\mathrm{X}^\mathrm{tot}$/SFR ratios of galaxies with and without He II emission at redshift $z \sim 3$ in the Chandra Deep Field South. These results are consistent with our finding that accretion discs of XRBs negligibly affect He II emission (Figure 4.5).

Katz et al. (2023) also explore the emission-line properties of gas photoionized by sources with different $L_\mathrm{X}^\mathrm{tot}$/SFR ratio by arbitrarily scaling an ARES multicolour-disc model, for a fixed black hole mass of $25\,\mathrm{M}_\odot$, added to the BPASS ionizing spectrum of a 5 Myr-old binary-star SSP.[5] They find that reproducing the surprisingly high [O III] λ4363/[O III] λ5007 ratio of 0.048 (0.055 when dust-corrected) in the *JWST*/NIRSpec spectrum of the metal-poor star-forming galaxy S04590 at redshift $z = 8.5$ requires $L_{\mathrm{X,2-10keV}}^\mathrm{tot}/\mathrm{SFR} > 10^{41}\,\mathrm{erg\,s^{-1}/M_\odot\,yr^{-1}}$, which translates into $L_\mathrm{X}^\mathrm{tot}/\mathrm{SFR} > 3 \times 10^{41}\,\mathrm{erg\,s^{-1}/M_\odot\,yr^{-1}}$ when adopting the energy band 0.5–8 keV used by Senchyna et al. (2020) and in Figure 4.3 of the present work. Again, this is much larger than observed in extremely metal-poor star-forming galaxies (Senchyna et al., 2017, 2020), and than predicted by our physically consistent model of the emission

[5] To compute $L_\mathrm{X}^\mathrm{tot}$/SFR, Katz et al. (2023) define an 'effective' star formation rate based on the rate of H-ionizing photons emitted by the 5 Myr-old BPASS SSP (H. Katz, private communication).

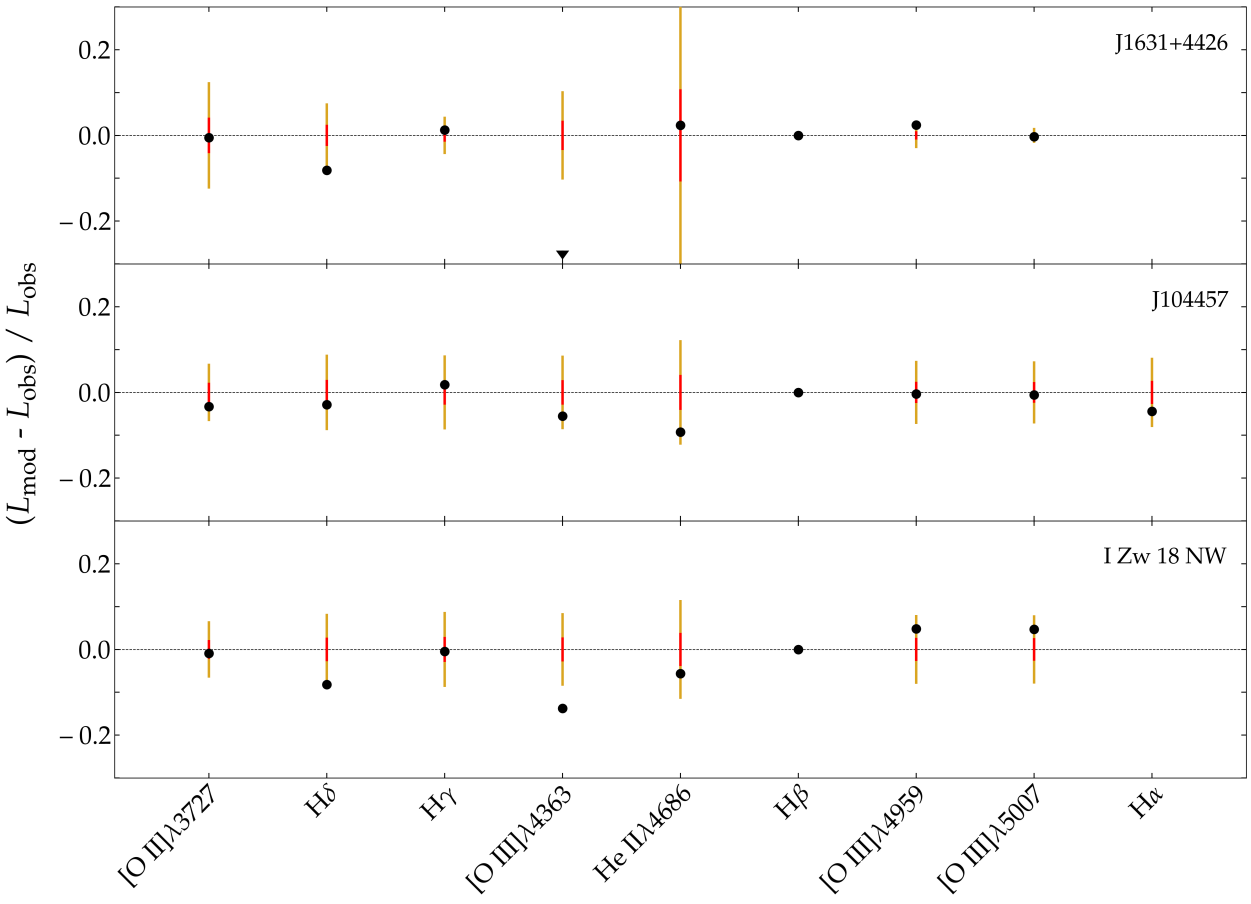

Figure 4.6: Relative offset between line luminosities of the best-fitting (i.e., minimum-χ^2) GALSEVN model among the limited library described in section 4.1.3, and observed line luminosities in the three metal-poor galaxies J1631+4426, J104457 and I Zw 18 NW (from top to bottom) studied by Umeda et al. (2022). All luminosities are normalized to that of Hβ. The 1-σ (3-σ) observational errors are shown in red (gold). For J1631+4426, the [O III] λ4363 point falls outside the plot, at $(L_{\rm mod} - L_{\rm obs})/L_{\rm obs} \approx -0.50$, as indicated by the down-pointing black triangle.

from stars and XRB accretion discs, anchored on the average observed XRB luminosity function of Figure 4.4.

It is important to bear in mind that the simple prescription presented in section 4.1.1 pertains to the average $\langle L_{\rm X}^{\rm tot}/{\rm SFR}\rangle \approx 2.1\times10^{40}\,{\rm erg\,s^{-1}/M_\odot\,yr^{-1}}$ produced by XRBs in the five metal-poor star-forming galaxies considered by Lehmer et al. (2019) to build the X-ray luminosity function of Figure 4.4, and that the associated standard deviation of $1.4\times10^{40}\,{\rm erg\,s^{-1}/M_\odot\,yr^{-1}}$ implies that this ratio can vary from galaxy to galaxy. The 10 star-forming galaxies with 12 + log(O/H) < 8.0 in the sample of Douna et al. (2015, see Figure 4.3 below) exhibit a very similar mean $\langle L_{\rm X}^{\rm tot}/{\rm SFR}\rangle \approx 2.7\times10^{40}\,{\rm erg\,s^{-1}/M_\odot\,yr^{-1}}$ with a standard deviation of $2.4\times10^{40}\,{\rm erg\,s^{-1}/M_\odot\,yr^{-1}}$. Yet, the X-ray luminosity per unit star formation rate required by Katz et al. (2023) to significantly impact the [O III] λ4363/[O III] λ5007 ratio of S04590 appears improbably high, as it is, respectively, 20 σ and 11 σ larger than the mean observed values for metal-poor galaxies in the samples of Lehmer et al. (2019) and Douna et al. (2015).

Using a slightly different approach, Umeda et al. (2022) appeal to Markov Chain Monte Carlo techniques to select the combination of a blackbody and power-law ionizing spectra and gas parameters providing the best fits to the emission-line properties of three extremely metal-poor galaxies with strong He II λ4686 emission (included in the sample of section 2.3.1): J1631+4426, J104457 and I Zw 18 NW. Umeda et al. (2022) then show that, for each galaxy, the best-fitting combination of blackbody+power-law ionizing spectra can be approached by a combination of the accretion-disc model spectrum of Gierliński et al. (2009) and the spectrum of a BPASS single-star SSP with an age between about 2 and

8 Myr (we note that the emission-line properties actually produced by these spectra are not compared to the observations in their paper). The $L_{\rm X}^{\rm tot}$/SFR ratios of these models are $5.0\times10^{40}\,{\rm erg\,s^{-1}/M_\odot\,yr^{-1}}$ (J1631+4426), $1.0\times10^{41}\,{\rm erg\,s^{-1}/M_\odot\,yr^{-1}}$ (J104457) and $3\times10^{41}\,{\rm erg\,s^{-1}/M_\odot\,yr^{-1}}$ (I Zw 18 NW), reaching again up to $11\,\sigma$ above the mean observed value in the Douna et al. (2015) sample of metal-poor star-forming galaxies.[6]

It is of interest to check how the emission-line and X-ray properties of the collection of models shown in Figure 3.5, which include self-consistent scaling of accretion-disc with stellar emission, compare with those of J1631+4426, J104457 and I Zw 18 NW. These 800 models, built using the star formation histories of 100 SPHINX galaxies (Rosdahl et al., 2022), are far from sampling the whole available space of stellar and gas parameters, as they have fixed $n_{\rm H} = 100\,{\rm cm^{-3}}$, $\log\langle U\rangle = -2$ and $\xi_{\rm d} = 0.3$, only two C/O abundance ratios (C/O =0.17 and 0.44) and four metallicities ($Z = Z_{\rm ISM} = 0.0005$, 0.001, 0.002 and 0.004), for ages between 2 and 10 Myr. Therefore, the use of sophisticated fitting algorithms (e.g., BEAGLE, Chevallard and Charlot, 2016) is not appropriate in this case, and we simply explore the properties of the models that, from this limited library, are best able to approximate the observed emission-line properties of the three galaxies considered by Umeda et al. (2022). After some experimentation and to better account for the physical and chemical conditions in these galaxies, it appeared opportune to probe higher ionization parameters, carbon-to-oxygen and dust-to-gas ratios, so we extended the library to include a few more values: $\log\langle U\rangle = -1.7$ and -1.4, C/O = 0.09 and $\xi_{\rm d} = 0.1$.

We present the results of this exercise in Figure 4.6, which shows the relative offset between luminosity of the best-fitting (i.e., minimum-χ^2) model and observed luminosity, for the lines in common between the two sets. Remarkably, among the restricted library of models at hand, those shown in Figure 4.6 appear to provide reasonable fits to all but one emission line. In particular, the models reproduce the strong observed He II λ4686 luminosities of these galaxies, corresponding to He II $\lambda4686/{\rm H}\beta$ ratios of 0.023 (J1631+4426), 0.018 (J104457) and 0.034 (I Zw 18 NW), i.e., totally out of reach of previous stellar population synthesis models (Figure 2.5b).

The only line that the limited set of models considered here does not seem to naturally reproduce is [O III] λ4363, whose observed luminosities in two of the three galaxies are higher than predicted by the best-fitting models, especially in the case of J1631+4426. The observed [O III] $\lambda4363/$[O III] λ5007 ratios are 0.048 (J1631+4426), 0.032 (J104457) and 0.036 (I Zw 18 NW). Intriguingly, the value for J1631+4426 is the same as that found in the high-redshift galaxy S04590 studied by Katz et al. (2023), for which no simple explanation, other than an improbably high contribution by XRBs (see above) or a high cosmic-ray background (not applicable to nearby galaxies), could be found. Exploring other potential causes of strong [O III] λ4363 emission, such as exceptional heating perhaps related to temperature inhomogeneities (e.g., Cameron et al., 2023a), is beyond the scope of the simple exercise considered here.

For reference, the $L_{\rm X}$/SFR ratios of the best-fitting models in Figure 4.6, computed by estimating the SFR from the 1500-Å luminosity by analogy with Umeda et al. (2022, see footnote 6), span the range 3.6–$7.2\times10^{40}\,{\rm erg\,s^{-1}/M_\odot\,yr^{-1}}$, compatible with the observations of Lehmer et al. (2019) and Douna et al. (2015). The best-fitting metallicities and volume-averaged ionization parameters are $(0.0005, -2.0)$, $(0.001, -1.4)$ and $(0.0005, -1.7)$ for J1631+4426, J104457 and I Zw 18 NW, respectively, close to the values $(0.0004, -1.6)$, $(0.001, -2.0)$ and $(0.0005, -1.7)$ derived by Umeda et al. (2022) using blackbody+power-law ionizing spectra. For reference, the best-fitting C/O and $\xi_{\rm d}$ values are $(0.09, 0.1)$, $(0.44, 0.3)$ and $(0.09, 0.1)$, respectively.

We therefore conclude, from the GALSEVN model predictions presented in this work, that XRB accretion discs have little influence on the high-ionization line properties of metal-poor star-forming galaxies, appears robust when confronted with observations of both the emission-line and X-ray properties of such galaxies.

[6] To compute $L_{\rm X}^{\rm tot}$/SFR, Umeda et al. (2022) define an 'effective' star formation rate based on the 1500 Å luminosity produced by the BPASS single-star SSP of their best-fitting model (using the conversion in Kennicutt, 1998).

4.2 Emission from fast radiative shocks

Radiative shocks, such as those expected from massive-star winds and SN blast waves, have spectral signatures characterized by strong high-ionization lines (e.g., Dopita and Sutherland, 1996; Alarie and Morisset, 2019), similar to those observed in some metal-poor star-forming galaxies (Izotov et al., 2012; Plat et al., 2019). As noted by Plat et al. (2019), the high gas densities ($n_{\rm H} \gtrsim 10^4\,{\rm cm^{-3}}$) measured from the [C III]λ1907+C III]λ1909 doublet in some metal-poor star-forming galaxies could be suggestive of the presence of radiative shocks from SNe. So far, however, no predictive phenomenological model has been proposed to link shocks to other galaxy properties.

In this section, we propose a simple prescription to compute the emission from radiative shocks generated by stellar winds and SN blast waves consistently with the emission from stars and photoionized H II regions in young star-forming galaxies. This prescription allows line luminosities to be computed from knowledge of the rates of energy injection into the ISM by stellar winds and SN explosions, based on line fluxes tabulated as a function of shock velocity ($V_{\rm s}$) and preshock density ($n_{\rm H}$) in grids of radiative-shock models (e.g., Dopita and Sutherland, 1996; Alarie and Morisset, 2019). We estimate the rate at which stellar winds inject energy into the ISM by summing the individual contributions of all stars – ignoring for simplicity the influence of binary-star processes on this rate. For energy injection by SNe, we consider the rate of SN explosions predicted by SEVN, including pair-instability, type-II and type-Ia SNe. We ignore non-exploding, 'failed' SNe leading to the formation of black holes (Spera et al., 2015; Spera and Mapelli, 2017). For reference, the rates of energy injection computed in this way are roughly consistent with those reported by Leitherer et al. (1992, see their figure 6) under slightly different assumptions.

4.2.1 Modelling and calibration of the emission of SN- and wind-driven shocks

The energy deposited into the ISM by stellar winds and supernova explosions (e.g., Leitherer et al., 1992; Leitherer and Heckman, 1995) can drive fast shocks contributing to line emission in star-forming galaxies (e.g., Shull and McKee, 1979; Izotov et al., 2012). We express the rate of total energy deposition into the ISM at SSP age t' (equation 2.1) as

$$\dot{E}_{\rm tot}(t') = \varepsilon_{\rm W}\,\dot{E}_{\rm W}(t') + \varepsilon_{\rm SN}\,r_{\rm SN}(t')\,E_{\rm SN}\,, \tag{4.6}$$

where $\dot{E}_{\rm W}$ is the rate of energy input by stellar winds, $E_{\rm SN} \approx 10^{51}\,{\rm erg}$ is the typical energy released by a SN explosion (e.g., Arnett, 1996),[7] $r_{\rm SN}(t')$ is the rate of SN explosions at time t', and $\varepsilon_{\rm W}$ and $\varepsilon_{\rm SN}$ are thermalization efficiency factors. This energy injection will generate shocks, whose radiative properties we wish to estimate.

Emission-line predictions for fast radiative shocks have been computed using the MAPPINGS photoionization code (e.g., Dopita and Sutherland, 1996; Allen et al., 2008; Alarie and Morisset, 2019). These usually pertain to high-velocity, steady-flow, fully radiative, plane-parallel magneto-hydrodynamic shocks and are traditionally expressed in flux per unit area ($\rm erg\,cm^{-2}\,s^{-1}$). We need to scale these predictions to the total energy deposition rate from equation (4.6) to obtain estimates of emission-line luminosities (in $\rm erg\,s^{-1}$). This can be achieved by considering the total radiative flux of a shock. Assuming that the entire flux of mechanical energy through the shock is radiated, Dopita and Sutherland (1996) express this quantity as (see their equation 3.3)

$$F_{\rm tot}^{\rm shock} = 2.28\times10^{-3}\left(\frac{V_{\rm s}}{100\,{\rm km\,s^{-1}}}\right)^{3.0}\left(\frac{n_{\rm H}}{\rm cm^{-3}}\right)\,{\rm erg\,cm^{-2}\,s^{-1}}\,, \tag{4.7}$$

where $V_{\rm s}$ denotes the shock velocity and $n_{\rm H}$ the hydrogen density. The fraction of this flux radiated in the Hβ recombination line in the plasma column behind the shock can be written (equation 3.4 of

[7] This is generally the case for type-II, type-Ia and low-mass pair-instability SNe, but the most massive PISNe can reach ~ 100 times this value (see Heger and Woosley, 2002). We show in this section that this has little effect on our conclusions.

Dopita and Sutherland, 1996)

$$F_{\mathrm{H}\beta}^{\mathrm{shock}} = 7.44 \times 10^{-6} \left(\frac{V_{\mathrm{s}}}{100\,\mathrm{km\,s^{-1}}}\right)^{2.41} \left(\frac{n_{\mathrm{H}}}{\mathrm{cm^{-3}}}\right) \mathrm{erg\,cm^{-2}\,s^{-1}}\,. \tag{4.8}$$

The photoionized region ahead of the shock also contributes to the total Hβ emission. The corresponding flux can be expressed as (equation 4.4 of Dopita and Sutherland, 1996)

$$F_{\mathrm{H}\beta}^{\mathrm{prec}} = 9.85 \times 10^{-6} \left(\frac{V_{\mathrm{s}}}{100\,\mathrm{km\,s^{-1}}}\right)^{2.28} \left(\frac{n_{\mathrm{H}}}{\mathrm{cm^{-3}}}\right) \mathrm{erg\,cm^{-2}\,s^{-1}}\,. \tag{4.9}$$

This is an upper limit to the contribution by the shock precursor, as the ISM can run out before the end of the H-Strömgren column ahead of the shock (especially for the fastest shocks).

Equations (4.7)–(4.9) allow one to express the ratio of total (shock+precursor) Hβ flux to total radiative flux generated by the shock in terms of the quantities V_{s} and n_{H}. This ratio can also be regarded as the ratio of total Hβ luminosity to total luminosity emitted by the shock, i.e., we write

$$\frac{F_{\mathrm{H}\beta}^{\mathrm{shock}} + F_{\mathrm{H}\beta}^{\mathrm{prec}}}{F_{\mathrm{tot}}^{\mathrm{shock}}} = \frac{L_{\mathrm{H}\beta}^{\mathrm{shock}} + L_{\mathrm{H}\beta}^{\mathrm{prec}}}{L_{\mathrm{tot}}^{\mathrm{shock}}}\,. \tag{4.10}$$

Since we have assumed that the entire flux of mechanical energy through the shock is radiated, we can replace $L_{\mathrm{tot}}^{\mathrm{shock}}$ by the power injected into the ISM (equation 4.6) and derive from this the total Hβ luminosity of the shock.

Unfortunately, analogues to equations (4.7)–(4.9) (derived by Dopita and Sutherland 1996 using MAPPINGS II) are not available for the more recent calculations of Alarie and Morisset (2019, based on MAPPINGS V). Instead, Alarie and Morisset (2019) provide tables of $F_{\mathrm{H}\beta}^{\mathrm{shock}}$ and $F_{\mathrm{H}\beta}^{\mathrm{prec}}$ versus shock velocity V_{s} and density n_{H}, while equation (4.7), which states that $F_{\mathrm{tot}}^{\mathrm{shock}}$ is equal to the flux of mechanical energy passing through the shock, can be assumed not to depend on the photoionization code. We therefore combine the results of Alarie and Morisset (2019) with the expression of F_{tot} as a function of V_{s} and n_{H} from equation (4.7) to compute the ratio on the left-hand side of equation (4.10). Then, we consider the luminosity $L_{\mathrm{H}\beta}^{\mathrm{shock}} + L_{\mathrm{H}\beta}^{\mathrm{prec}}$ separately for radiative shocks powered by stellar winds and SN explosions, as the ejection velocities associated with SN explosions ($\geq 10,000\,\mathrm{km\,s^{-1}}$; e.g., Draine and McKee, 1993) are higher than those associated with stellar winds ($\leq 3000\,\mathrm{km\,s^{-1}}$; e.g., Garcia et al., 2014; Gräfener et al., 2017). The implied radiative-shock velocities are therefore likely to differ on average.

We compute the total Hβ emission from radiative shocks driven by stellar winds as (dropping the dependence on t' for simplicity)

$$\begin{aligned} L_{\mathrm{H}\beta}^{\mathrm{shock}} + L_{\mathrm{H}\beta}^{\mathrm{prec}} = 4.39 \times 10^{2}\, \varepsilon_{\mathrm{W}}\, \dot{E}_{\mathrm{W}} \left(\frac{F_{\mathrm{H}\beta}^{\mathrm{shock}} + F_{\mathrm{H}\beta}^{\mathrm{prec}}}{\mathrm{erg\,cm^{-2}\,s^{-1}}}\right) \\ \times \left(\frac{V_{\mathrm{s}}}{100\,\mathrm{km\,s^{-1}}}\right)^{-3.0} \left(\frac{n_{\mathrm{H}}}{\mathrm{cm^{-3}}}\right)^{-1} \mathrm{erg\,s^{-1}}\,, \end{aligned} \tag{4.11}$$

where the total flux $F_{\mathrm{H}\beta}^{\mathrm{shock}} + F_{\mathrm{H}\beta}^{\mathrm{prec}}$ for shocks with velocity V_{s} propagating in a medium with density n_{H} is taken from Alarie and Morisset (2019). We obtain the rate $\dot{E}_{\mathrm{W}}$ of energy input from winds (equation 4.6) by summing the individual contributions $\frac{1}{2}\dot{m}v_{\infty}^{2}$ of all stars, where $\dot{m}$ is the stellar mass-loss rate and v_{∞} the terminal wind velocity.[8] For OB stars, we adopt the widely used relation $v_{\infty} = 2.65\,v_{\mathrm{esc}}$, where v_{esc} is the stellar escape velocity (e.g., Garcia et al., 2014). For WR stars, we take v_{∞} to be the minimum of $1.30\,v_{\mathrm{esc}}$ and $1800\,\mathrm{km\,s^{-1}}$ (e.g., Gräfener et al., 2017). For simplicity,

[8] For simplicity, we compute this estimate for a population of single stars and ignore the influence of binary-star processes on energy injection by stellar winds into the ISM.

we assume here that all of the kinetic energy injected by winds into the ISM is thermalized, i.e., we take $\varepsilon_{\rm W} = 1.0$ (e.g., Rosen, 2022).

Similarly, we express the total Hβ emission from radiative shocks driven by SN explosions as

$$L_{\rm H\beta}^{\rm shock} + L_{\rm H\beta}^{\rm prec} = 1.39 \times 10^{46}\, \varepsilon_{\rm SN} \left(\frac{r_{\rm SN}}{\rm yr^{-1}}\right) \left(\frac{F_{\rm H\beta}^{\rm shock} + F_{\rm H\beta}^{\rm prec}}{\rm erg\,cm^{-2}\,s^{-1}}\right) \times \left(\frac{V_{\rm s}}{100\,\rm km\,s^{-1}}\right)^{-3.0} \left(\frac{n_{\rm H}}{\rm cm^{-3}}\right)^{-1} \rm erg\,s^{-1}\,. \tag{4.12}$$

Constraints from the prototypical starburst galaxy M82 suggest $0.3 \lesssim \varepsilon_{\rm SN} \lesssim 1.0$ (Strickland and Heckman, 2009; Heckman and Thompson, 2017). Here, we adopt for simplicity $\varepsilon_{\rm SN} = 1.0$, which should provide an upper limit on the shock contribution to line emission.

Once the Hβ luminosity is known, whether for wind- or SN-driven shocks, the luminosity of any other line X can be computed as

$$L_{\rm X}^{\rm shock} + L_{\rm X}^{\rm prec} = L_{\rm H\beta}^{\rm shock}\, \frac{F_{\rm X}^{\rm shock}}{F_{\rm H\beta}^{\rm shock}} + L_{\rm H\beta}^{\rm prec}\, \frac{F_{\rm X}^{\rm prec}}{F_{\rm H\beta}^{\rm prec}}\,, \tag{4.13}$$

where the ratios $F_{\rm X}^{\rm shock}/F_{\rm H\beta}^{\rm shock}$ and $F_{\rm X}^{\rm prec}/F_{\rm H\beta}^{\rm prec}$ are available from the tables of Alarie and Morisset (2019).

4.2.2 Impact on emission lines

The top-two panels of Figure 4.7 show the resulting contributions of radiative shocks driven by stellar winds and SN explosions to the total Hβ and He II λ4686 luminosities of a GALSEVN binary-star population with standard metallicity $Z = 0.001$. These contributions, obtained by inserting line fluxes from the recent radiative-shock calculations of Alarie and Morisset (2019, based on MAPPINGS V) into equations (4.11)–(4.13), are shown for the full available range of shock velocities, $100 \leq V_{\rm s} \leq 1000\,\rm km\,s^{-1}$, and $n_{\rm H} = 100\,\rm cm^{-3}$ (Table 2.1). In each panel, the black dotted line shows the total line emission obtained by adding the maximum possible shock contribution (independently for stellar winds and SNe) to the emission from stars and XRB accretion discs (green solid line).

Figure 4.7 shows that radiative shocks in this model account at most for only a few per cent of the total Hβ and He II λ4686 line emission at ages below 10 Myr, with no significant impact on the global He II λ4686/Hβ ratio, except for an extremely brief period around 2 Myr, when shocks from stellar winds can produce around 40 per cent of the total He II λ1640 emission. At ages beyond 10 Myr, the shock contribution increases as the rates of ionizing photons produced by the stars begin to decrease, but it remains with no significant impact on the line luminosities and emission-line ratios. The two peaks in SN-shock contribution originate from PISNe at ages around 4 Myr, and type-II SNe at ages around 10 Myr, type-Ia SNe appearing only after about 30 Myr and in small number. We note that adopting energies greater than 10^{51} erg for the most massive PISNe (footnote 7) would increase the magnitude of the first peak, but only for a brief spike at the earliest ages.

It is instructive to also examine the predictions of our model for the luminosity of the [Ne V] λ3426 emission line, which has been suggested as a potential signature of radiative shocks in blue compact-dwarf galaxies (e.g., Izotov et al., 2012). The bottom panel of Figure 4.7 shows that, indeed, radiative shocks driven by stellar winds and SN explosions can significantly contribute to, and even dominate, [Ne V] λ3426 emission in metal-poor star-forming galaxies.

Overall, for what concerns the direct focus of the present study, we conclude from Figure 4.7 that radiative shocks driven by stellar winds and SN explosions are unlikely to contribute prominently to the strong He II emission observed in metal-poor star-forming galaxies in the sample of section 2.3.1.

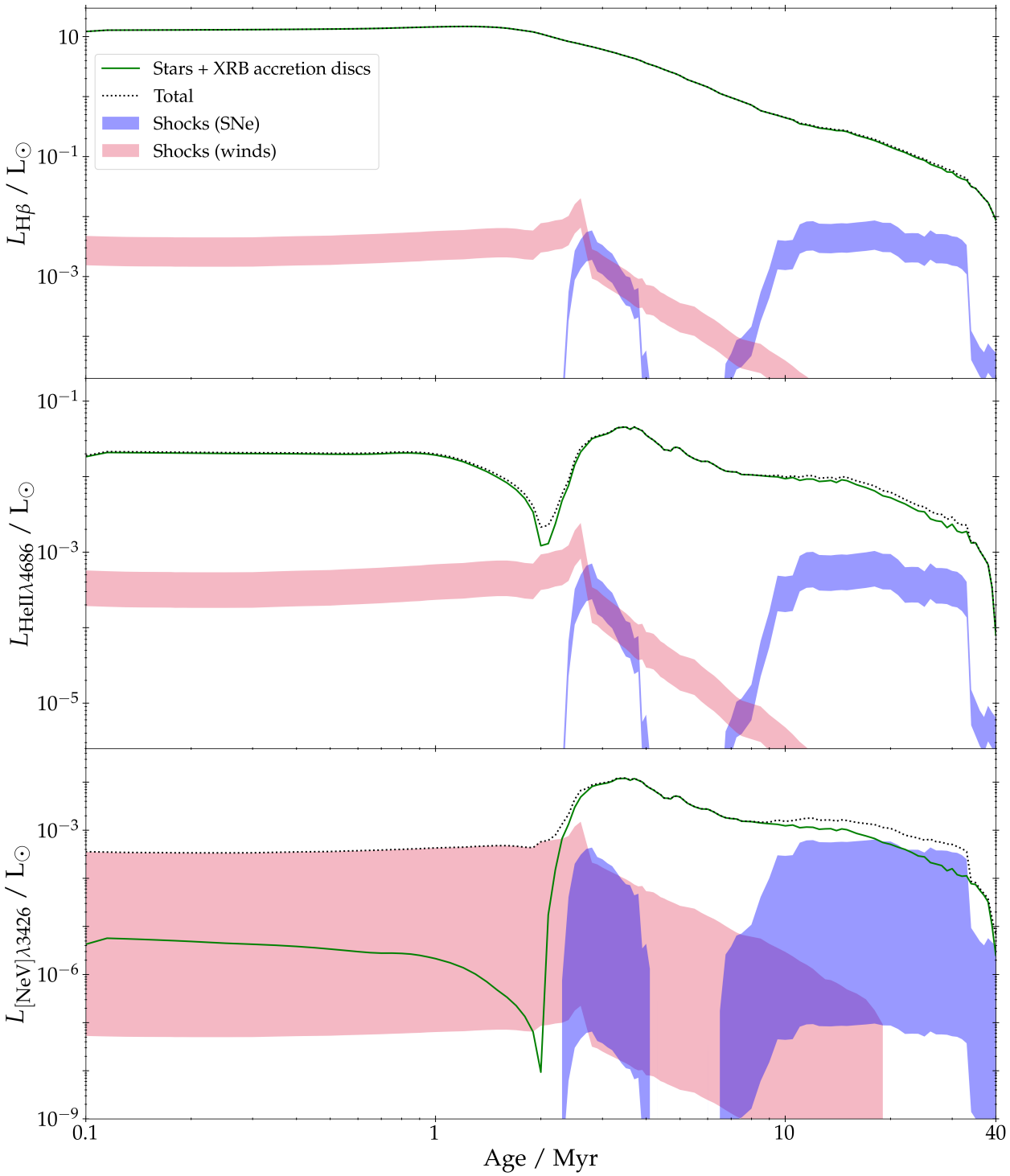

Figure 4.7: Contribution from shocks driven by stellar winds (in red) and SNe (in blue) to the total Hβ (top panel), He II λ4686 (middle panel) and [Ne V] λ3426 (bottom panel) luminosities of a GALSEVN binary-star SSP with metallicity $Z = 0.001$, plotted against age (see text section 4.2.1 for details). The contributions are shown for the range of shock velocities $100 \leq V_\mathrm{s} \leq 1000\,\mathrm{km\,s^{-1}}$ and the density $n_\mathrm{H} = 100\,\mathrm{cm^{-3}}$. In each panel, the black dotted line shows the total line emission obtained by adding the maximum possible shock contribution (independently for stellar winds and SNe) to the emission from stars and XRB accretion discs (green solid line). The model has the same zero-age Chabrier (2003) IMF normalized to a total initial stellar mass of $1\,\mathrm{M}_\odot$ integrated over 0.1–300 $\mathrm{M}_\odot$ as in Figure 2.3.

4.3 Conclusions on the GALSEVN parameter space exploration

We have explored, in the previous chapters, the emission-line properties of interstellar gas photoionized by young binary-star populations computed with the new GALSEVN model built by combining the SEVN (Iorio et al., 2023) and GALAXEV (Bruzual and Charlot, 2003) population-synthesis codes. This model allows us to compute in a physically consistent way, for the first time, the emission from stars, accretion discs of X-ray binaries and supernova-driven radiative shocks. We compared the predictions of this model with observed UV and optical emission-line properties of a sample of about 120 metal-poor star-forming galaxies in a wide redshift range. Our main results can be summarised as follows.

- We confirm that, as well known from previous work (e.g., Eldridge and Stanway, 2012; Eldridge et al., 2017; Götberg et al., 2020), the inclusion of binary-star processes (such as envelope stripping, quasi-homogeneous evolution, common-envelope ejection and star-star mergers) boosts and hardens the ionizing emission from young stellar populations. Such effect is achieved assuming even a relatively low fraction of binary stars, the rates of H-, He I- and He II-ionizing photons changing only little for stellar populations with $0.3 \leq f_{\rm bin} \leq 1.0$ (Figure 2.3).

- We find that the He II λ4686/Hβ ratios and Hβ equivalent widths of GALSEVN SSP models with metallicity $Z \sim 0.001$ reproduce remarkably well the observations of galaxies in our sample at all ages between 3 and 10 Myr, providing better agreement with the data than achievable with previous single-star and binary-star models (Figure 2.5b).

- The inclusion of bursty star formation histories, such as those predicted by the SPHINX simulations of young galaxies in the epoch of reionization (Rosdahl et al., 2022), allows broader sampling of the observational space than achievable with simpler models, and hence, should be encouraged when interpreting observations (Figures 3.4–3.5).

- We find that the most extreme He II λ1640 equivalent widths (and other high-ionization signatures) of galaxies in our sample can be reproduced by models with a top-heavy IMF with characteristic mass $\sim 50\,{\rm M}_\odot$, which could represent a transient phase in the evolution of a galaxy (Figure 3.7).

- Reproducing the average luminosity function of X-ray binaries per unit star formation rate in the most metal-poor star-forming galaxies observed by Lehmer et al. (2019) requires that the bulk of mass in such systems be accreted during episodes of X-ray outbursts, at a much higher rate than during the quiescent phase, the actual strength and duration of these outbursts being degenerate (section 4.1.1). This implies that XRBs contribute negligibly to the H- and He II-line emission from young star-forming galaxies at early population ages, in agreement with expectations from several previous studies (e.g., Jaskot and Oey, 2013; Senchyna et al., 2017, 2020; Saxena et al., 2020, see Figure 4.5). We find that the claims in some recent studies that XRB accretion discs might contribute significantly to the emission from high-ionization UV and optical lines (Schaerer et al., 2019; Umeda et al., 2022; Katz et al., 2023) are based on models predicting improbably high ratios of X-ray luminosity to star formation rate (section 4.1.3).

- Finally, by combining the rates of energy injection into the ISM by stellar winds and (pair-instability, type-II and type-Ia) SN explosions predicted by the GALSEVN model with the radiative-shock models of Alarie and Morisset (2019, see also Dopita and Sutherland 1996), we find that shocks are unlikely to contribute significantly to the H- and He II-line emission from young star-forming galaxies (Figure 4.7).

The work presented in these chapters provides only first examples of the properties of the new GALSEVN model of the emission from binary-star populations. The application of this model to interpret the spectral properties of young star-forming galaxies using Bayesian inference (e.g., with the BEAGLE tool) requires building a comprehensive library spanning full ranges of stellar and nebular parameters and the exploration of a comprehensive set of emission lines. This will be the subject of a chapter 6.

Chapter 5

On the properties of Reionization-Era galaxies

Contents

In the previous chapters, we tested GALSEVN SEDs against spectral observations of low- to intermediate-redshift galaxies. This comparison revealed a generally good agreement between GALSEVN predictions and most observed spectral features at metallicities down to a few per cent of solar. It is therefore interesting to focus now on other GALSEVN predictions at extremely low metallicities, to which there are no galaxy observations to be compared to date. These predictions could account for the physical properties of Pop III stars which might be present in such galaxies, and could be used as input data in cosmological simulations of the early Universe. In this context, the rate of ionizing photons produced by primordial stellar populations modelled using GALSEVN may be an important prediction for attempts to constrain reionization mechanisms and estimate the role played by extremely metal-poor stellar populations in young galaxies during the EoR. Accordingly, our goal in this chapter is to provide useful SEDs and associated quantities which could be of interest to characterize the contribution of Pop III stellar systems to reionization.

In this chapter, we explore the predictions of GALSEVN for stellar populations with extremely low metallicities, down to $Z = 10^{-11}$. Our preliminary exploration of the modelled SEDs includes the diagnostic diagrams highlighted as good probes for Pop III stellar emission by Nakajima and Maiolino (2022). We compare the predictions of the GALSEVN model with the widely used zero-metallicity models of Schaerer (2003), which do not include binary interactions – the important contribution of which has been discussed in detail in previous chapters. These models were among the first spectral-synthesis

models to incorporate zero-metallicity tracks,[1] and have remained the reference for Pop III modelling since their publication. Next, we complement this SED exploration with a detailed study of several observables useful to estimate physical properties in the EoR, and of specific stellar-population characteristics, to provide a comprehensive overview of how GALSEVN models can describe primeval star-forming regions. Finally, we examine the possibility of multi-messenger detection of these populations of very low-metallicity stars simulated with GALSEVN, and in particular their potential gravitational-wave counterparts.

5.1 Production of ionizing radiation by EoR galaxies

5.1.1 Extremely metal-poor stars as potential reionization drivers

As described in section 1.1.3, Cosmic Reionization refers to the complex phase transition between a mostly-neutral to a nearly fully-ionized state for intergalactic gas. This transition is expected to have involved complex interactions between stars and star-forming regions, the structure of the ISM in star-forming clusters and galaxies, the properties of the circumgalactic medium, the transmission efficiency of ionizing photons through the IGM and the background radiation from non-stellar sources. In simulations and models, reionization is studied by means of a global ionization parameter, representing the average volume-filling fraction of ionized gas, which reflects the balance between hydrogen photoionization and recombination and controls the global ionization state of the gas.

The approximate scenario of reionization is straightforward in principle: the first light-emitting objects ionize their immediate surroundings and create expanding ionized bubbles; as the number of sources increases, so does the number of ionization bubbles, until these bubbles fill the whole Universe. However, such a scenario suffers from important simplifications and neglected effects, such as the impact of stellar feedback, and yet unresolved issues. The current scenarios laid out by simulations still include many uncertainties, such as which mechanisms control the formation of the first light-emitting objects, the amount of ionizing radiation released by these objects, and how the ionized regions expand though the IGM. The main sources of ionizing photons in the EoR are believed to be stars in the first galaxies and high-redshift star-forming regions. The first galaxies presumably hosted extremely metal-poor, exotic Pop III stars, although due to their very short lifetimes and the small timescales of chemical enrichment, Pop II stars probably quickly took over control of the emission in most primeval galaxies (see section 1.1.4 for a more detailed discussion). Yet, recent studies have shown that Pop III-star formation could have persisted down to redshifts $z \sim 6$ in isolated mini-haloes (e.g., Mebane et al., 2018). AGNs in such galaxies and other non-stellar sources are also being investigated as potentially efficient sources of ionizing radiation (see section 1.1.3). Understanding the radiative properties of young, extremely metal-poor stellar populations in their primeval environment is therefore key to constraining the role played by primeval galaxies as drivers of reionization. We therefore consider here models with metallicities ranging from $Z = 10^{-11}$ to 0.001, to account for the variety of stellar populations which may be found in primeval galaxies.

Sections 1.1 and 1.2 introduced EoR galaxies and Pop III observations, as well as the predicted properties and evolution for such massive metal-poor stars. As observations of reionization tracers at such high redshifts ($z \gtrsim 10$) are very scarce, and only indirect constraints exist at present, cosmological and hydrodynamical simulations are at the heart of much current work on reionization. Our aim in the following section is therefore to present GALSEVN SED predictions for such stars, and to quantify observables which could be useful to characterize Reionization-era galaxies in such simulations.

These numerical approaches to reionization can be of two main types: fast, semi-analytical models, or full 3D N-body simulations. Semi-analytical models (e.g., Mesinger et al. 2011 and Murray et al. 2020; Santos et al. 2010; Cohen et al. 2017 and Reis et al. 2021) adopt approximations in their calculations of matter dynamics and radiative transfer, to optimise computation time. More precisely, such codes usually adopt the Zel'dovich (1970) perturbative approach, which considers only linear

[1] Other models, such as those developed by Tumlinson and Shull (2000); Tumlinson et al. (2001) and Bromm et al. (2001), had been published earlier, albeit with strong simplifying assumptions.

first-order terms for dynamics and dark-matter density estimates. On the other hand, full simulations (e.g., Ciardi and Madau 2003; Mellema et al. 2006; Baek et al. 2010, Semelin et al. 2017, Doussot and Semelin 2022, Meriot and Semelin 2024; Ocvirk et al. 2020 and Lewis et al. 2022), which are much more computationally expensive, are able to go to smaller scales, and resolve processes such as star formation, which is fundamental to reionization. The highest-resolution simulations are able to resolve individual star-forming haloes with their specific gas properties, and thus compute star formation in a self-consistent way. These contrasting approaches give similar results on large scales ($\gtrsim 1$ cMpc), but exhibit fundamental differences on smaller scales, as fast models only treat star formation and the related photon budgets based on halo statistics in the simulated region. The second key difference between these two approaches is the way in which radiative transfer is computed: while full simulations compute the exact radiative transfer equations in 3D, semi-analytical models often adopt approximations to speed up computation. Further diversity in the predictions of all these simulations is introduced by the differences in the physics implemented in these different codes to link gas properties, SF, and stellar emission. A detailed comparison between different radiative-transfer simulations can be found for instance by Iliev et al. (2009).

Given that the ionization state of the Universe in these simulations is globally governed by the competition between ionizing radiation and hydrogen recombination, the rate of ionizing photons produced by young stars and the fraction of photons escaping from star-forming regions are key parameters of the models. Spectral and photometric quantities commonly used to constrain these properties are presented in the next section.

In addition, other tracers of stellar populations can potentially greatly help to characterize primeval stars in high-redshift galaxies.

At extremely-low metallicities, gas cooling, although necessary for star formation, is very inefficient due to the absence of metals, which allow efficient collisional cooling. In this case, for low-mass star-forming haloes with virial temperatures below 10^4 K, cooling is thought to occur through vibrational deexcitation of small molecules – mostly H_2 in the pristine gas. However, H_2 molecules can easily be photodissociated by intermediate-energy photons, thus possibly quenching star formation in the irradiated gas, which can no longer cool sufficiently to form dense protostars. The photons capable of dissociating H_2 are called *Lyman-Werner* (LW) photons, and are generally considered to have energies in the range [912Å–1150Å]. As Pop III stars represent the main source of LW photons in the young Universe (see, e.g., Haiman et al., 2000; Agarwal et al., 2012; Incatasciato et al., 2023), it is important to compute the production rate of these photons to quantify the importance of their feedback on early star formation.

End-of-life events and stellar remnants can also provide interesting counterparts to primordial stellar-SED studies. Indeed, as well as introducing the possibility of multi-messenger signatures (e.g., gravitational waves from binary black hole systems), they trace stellar evolution – making it possible, for example, to follow the chemical enrichment of the ISM in various elements, through the rates of different types of SNe.

5.1.2 Production efficiency of ionizing photons

From a spectroscopic point of view, at the near-zero metallicities of interest here, the only detectable emission-line features are those of hydrogen and helium. We therefore focus on Pop III diagnostics based on H- and He-line ratios and equivalent widths.

With regard to photometry, a direct probe of the ionizing power of a stellar population is the production rate of H-ionizing photons (often used in a volume-averaged form in cosmological simulations) per unit non-ionizing ultraviolet luminosity, known as the ionizing-photon production efficiency. Three different definitions of this parameter can be found in the literature, which are more or less appropriate depending on whether one is interested in a theoretical or observational study:

– the stellar ionizing-photon production efficiency,

$$\xi^*_{\rm ion} = \dot{N}_{\rm ion}/L^*_{\rm UV}\,, \tag{5.1}$$

where $L^*_{\rm UV}$ is the intrinsic stellar monochromatic ultraviolet luminosity, that is, the UV luminosity that would be observed in the absence of gas and dust in the galaxy;

– the stellar+nebular ionizing-photon production efficiency,

$$\xi^{\rm H\,II}_{\rm ion} = \dot{N}_{\rm ion}/L^{\rm HII}_{\rm UV} \tag{5.2}$$

where $L^{\rm HII}$ is the UV luminosity accounting for the effects of dust absorption within H II regions and nebular recombination-continuum emission;

– and the observed ionizing-photon production efficiency,

$$\xi_{\rm ion} = \dot{N}_{\rm ion}/L_{\rm UV}\,, \tag{5.3}$$

where $L_{\rm UV}$ is the observed UV luminosity, corrected for all forms of nebular, galactic and extragalactic absorption and recombination.

These UV luminosities are computed respectively from the stellar spectrum, the stellar+nebular transmitted spectrum and the rest-frame observed spectrum, considering a 100Å window centred on 1500Å. In this work, we mainly focus on $\xi^{\rm H\,II}_{\rm ion}$ and $\xi^*_{\rm ion}$, the latter of which depends only on stellar-population properties, that is, mainly age, metallicity and IMF. Simulations often consider a fixed value of $\xi^*_{\rm ion}$, constant with age and chemical evolution. One of the goals of the present work is to provide an overview of $\xi^{\rm H\,II}_{\rm ion}$ and $\xi^*_{\rm ion}$ for GALSEVN SEDs, including how they evolve with these stellar-population parameters.

Another important parameter to constrain the amount of H-ionizing photons available for reionization is the Lyman-continuum escape fraction $f_{\rm esc}$, that is, the fraction of all ionizing photons produced which are actually able to escape through the ISM and IGM to ionize intergalactic neutral hydrogen. Recently, substantial efforts have been made to directly measure $f_{\rm esc}$ at redshifts up to $z \sim 4$. However, as the IGM opacity increases considerably at higher redshift (e.g., Inoue et al., 2014), the values reached by $f_{\rm esc}$ in the EoR can only be measured indirectly and from model-dependent inferences. Therefore, indicators need to be established from local observations, which can help to link more readily observable quantities, such as line emission (which traces the fraction of ionizing photons absorbed by the gas) and non-ionizing UV luminosity, which, combined with $\xi_{\rm ion}$, may provide new ways of measuring $f_{\rm esc}$ with greater confidence at high redshift. Other signatures, such as the impact of $f_{\rm esc}$ on the relation between H-Balmer line and UV-continuum luminosities (Zackrisson et al., 2013) and on the Lyα-line profile (Verhamme et al., 2015, 2017) have been proposed on the basis of local observations, but have not yet been applied to EoR galaxies. To avoid considering arbitrary values for $f_{\rm esc}$, and because of the CLOUDY partial treatment of this parameter, we do not vary $f_{\rm esc}$ in the present study. Instead, we focus on two limiting cases, studying both $\xi^*_{\rm ion}$– which corresponds to the case where $f_{\rm esc} = 1$, meaning that all ionizing photons escape from the surrounding H II region – and $\xi^{\rm H\,II}_{\rm ion}$– corresponding to $f_{\rm esc} = 0$, as we are considering an ionization-bounded H II region.

5.1.3 GALSEVN modelling

The GALSEVN models considered for Pop III stars in this work are, unless otherwise specified, pure-binary models at the lowest metallicities available in GALSEVN, which are $Z = 10^{-11}$ and $Z = 10^{-6}$. We also compute, for comparison, slightly more enriched Pop II models ($Z = 0.0001$, 0.0005 and 0.001). We explore different IMFs, similar to those presented in section 3.2.2: a classical Chabrier IMF, and three top-heavy IMFs (see equation 3.1 and Figure 3.6) with $m_{\rm char} = 50\,{\rm M}_\odot$, $100\,{\rm M}_\odot$ and $200\,{\rm M}_\odot$. We are not interested in the SFH over more than a massive-star lifetime and therefore only consider SSP models. The very slight impact of considering populations with a fraction of binaries more typical of nearby star-forming regions, e.g., around 70 per cent (Sana et al., 2012), instead of pure-binary models, has been discussed in chapter 2 and by Lecroq et al. (2024) and will not be considered further here.

The modelling procedure followed in this work is similar to that presented in previous chapters, with the GALSEVN SEDs being combined with the CLOUDY photoionization code. As the first aim of

this work is to compare GALSEVN predictions with the diagnostic diagrams and Pop III (single-stars) SEDs presented by Nakajima and Maiolino (2022), we adopt nebular parameters compatible with theirs, that is,

- $Z_{\rm ISM} = Z \in \{10^{-11}, 10^{-6}, 0.0001, 0.0005, 0.001\}$;
- $n_{\rm H} = 10^3\,{\rm cm}^{-3}$
- $\log\langle U\rangle = -2$, given that the values considered by Nakajima and Maiolino (2022) are between -3.5 to -0.5;
- no dust grains for the two metal-free models.

For the Pop II models with $0.0001 \leq Z \leq 0.001$, we adopt the same values of C/O = 0.17 and $\xi_{\rm d} = 0.3$ and the same abundance scaling as that presented in chapter 2.

Nakajima and Maiolino (2022) adopt a primordial He/H abundance of 0.0805, following Hsyu et al. (2020). They also consider a completely metal-free ISM.[2] We have tested these assumptions against Pop III models with metal abundances scaled for $Z = 10^{-11}$ and $Z = 10^{-6}$ following the method presented by Gutkin et al. (2016) and found that the two approaches give very similar results. We therefore choose to adopt the value of Hsyu et al. (2020) for the primordial He abundance, and to turn off metals as well as dust grains in CLOUDY, for the sake of consistency in our comparison with the work of Nakajima and Maiolino (2022). This choice should have very little impact on the predictions presented in the next sections.

We also choose to adopt a closed spherical geometry for CLOUDY calculations. As suggested by Schaerer (2002) and implemented by Nakajima and Maiolino (2022), we tested the impact of choosing a plane-parallel geometry instead. Once again, the results under the two assumptions give extremely similar results, so we choose not to investigate this aspect further.

We note that, with the assumptions presented here, the only emission-line features relevant to the metal-free models are those related to H and He. We also point out that, as our models do not follow the increase in gas-phase metallicity with stellar population evolution, strictly metal-free models should be considered only up to the time of the explosion of the first supernova. This limitation will be discussed further in the next section.

5.2 Emission properties of EoR galaxies

In recent work, the population synthesis models used to account for Pop III stars are generally those introduced by Schaerer (2002, 2003), based on Schaerer and Vacca (1998) spectral-synthesis code. These SPS models incorporate Padova evolutionary tracks (Marigo et al., 2001) for zero-metallicity stars with negligible mass loss, complemented with other models for stars with high mass loss (Lejeune and Schaerer, 2001; Meynet and Maeder, 2002), both sets covering the mass range from $1\,{\rm M}_\odot$ to $500\,{\rm M}_\odot$. These stellar tracks do not include binary interactions or the effects of rotation. Populations are generated based on a modified Salpeter (1955) IMF, with adjustable mass limits, as described by Raiter et al. (2010). It is therefore interesting to compare GALSEVN predictions to the results obtained using these models. We thus base our discussion in the next section on the results highlighted by Nakajima and Maiolino (2022), who combine the Schaerer (2003) SPS models with CLOUDY to predict the ultraviolet and optical spectral properties of populations of Pop III stars.

As Pop III stars are expected to be able to trigger intense He II-line emission (e.g., Inoue, 2011; Venditti et al., 2024), we first focus on He II-related spectral features and ionizing photons. After discussing GALSEVN predictions for UV-optical line emission and SEDs, we look into the predicted H-ionizing photon production rate and its dependence on time and metallicity. Finally, we complete the analysis of the predicted stellar populations by examining other important reionization tracers,

[2] CLOUDY offers a "no metals" option, as well as a "no dust grains" option.

such as the LW-band emission, which, as seen above, conditions the possibility of star formation in a circumstellar gas cloud, and the statistics of supernovæ, related to the chemical enrichment in pristine star-forming regions.

5.2.1 Ultraviolet and optical emission

We begin by examining the SEDs predicted by GALSEVN for populations of single and binary Pop III stars. Since stellar effective temperature generally increases with decreasing metallicity, we expect Pop III models to have higher rates of very high-energy photons than more metal-rich ones. This phenomenon, particularly present for extremely low metallicities ($Z \lesssim 10^{-10}$), is due to the absence of the trace amounts of C, N and O necessary to burn H through the CNO cycle in massive stars. For these extremely-low metallicity stars, the only channel for hydrogen fusion is the proton-proton (p-p) process, which is less efficient as a thermostat than the CNO cycle. Thus, gravitational contraction in the pre-main sequence phase cannot halt until the core reaches the very high temperature and density needed to initiate the p-p process and provide pressure support (Marigo et al., 2001; Costa et al., 2023). Moreover, as the emission is dominated by the most massive stars at early ages, single and binary models should coincide up to ages around 1 Myr, when the most massive stars leave the main sequence.

Figure 5.1 shows the production rates of He II- and He I-ionizing photons, normalized to that of H-ionizing photons, as a function of stellar-population age for different GALSEVN models. The models shown are Pop III ($Z = 10^{-11}$ and 10^{-6}) in orange and red respectively, with solid lines for pure binary- and dashed lines for single-star models. GALSEVN Pop II models with $Z = 0.0001$, 0.0005 and 0.001 are represented in dotted lines. All these models have the same zero-age Chabrier (2003) IMF as in Figure 2.3. As expected from the above argument, Pop III models, and especially the $Z = 10^{-11}$ model, have much higher $\dot{N}_{\mathrm{He\,II}}$ than models with metallicities of a few per cent of solar at early ages, due to their MS being shifted to much higher temperatures.[3] Figure 5.1 also confirms that the difference between single- and binary-star models appears after the first million years of evolution. This had already been highlighted in Figure 2.3. Then, around 2 Myr, both Pop III and Pop II binary-star models show a high $\dot{N}_{\mathrm{He\,II}}$ which is completely absent from single-star models, due to the formation of pure-He, WNE-like products of massive-star stripping. However, it is interesting to note that this increase in $\dot{N}_{\mathrm{He\,II}}$ is quite small for $Z = 10^{-11}$ and becomes much more pronounced as the metallicity increases. This is due to the more rapid evolution of extremely-low metallicity stars, because of their accelerated and hotter central-H burning: the WNE-like products of the evolution of the most massive stars begin to produce ionizing photons before most of the lower-mass stars leave the MS. Finally, another notable difference arises at ages greater than ~ 40 Myr, where the production-rate ratios of high-energy photons drops in Pop II models. This is due to the contribution from accretion discs of XRBs, which grows at earlier ages in Pop III models due to their faster evolution.[4] This is in agreement with the growing impact of XRB accretion discs with population age hinted in Figure 4.5.

These differences in behaviour between Pop III and Pop II models, as well as between single and binary stars, are less marked and appear later in the case of $\dot{N}_{\mathrm{He\,I}}$, because the conditions to produce photons capable of singly-ionizing He are less extreme – the first ionization energy of helium being equal to 24.6 eV, less than half the 54.4 eV required to doubly ionize it.

The green- and red-shaded regions show the areas covered by models with the three top-heavy IMFs with characteristic masses of 50 $\mathrm{M}_\odot$, 100 $\mathrm{M}_\odot$ and 200 $\mathrm{M}_\odot$ described in section 5.1.3, also with metallicities of $Z = 10^{-11}$ and 10^{-6} respectively. Their evolution is shown until their absolute UV magnitude reaches -14, where only few stars are left and the model becomes stochastically dependent on the seed used to draw their initial properties (as described in section 3.2.2). The $Z = 10^{-11}$ model

[3] While the MS of Pop II models roughly spans from 20,000 to 60,000 K, it is shifted to the 40,000-80,000 K range for $Z = 10^{-6}$ and 45,000-100,000 K for $Z = 10^{-11}$.

[4] Pop III models which do not take into account XRB accretion discs do not exhibit this feature. Instead, they show energetic-photon production rates which fall off more rapidly than in Pop II models, due to their faster evolution and their lack of WNE-type stars, present at late ages in Pop II models.

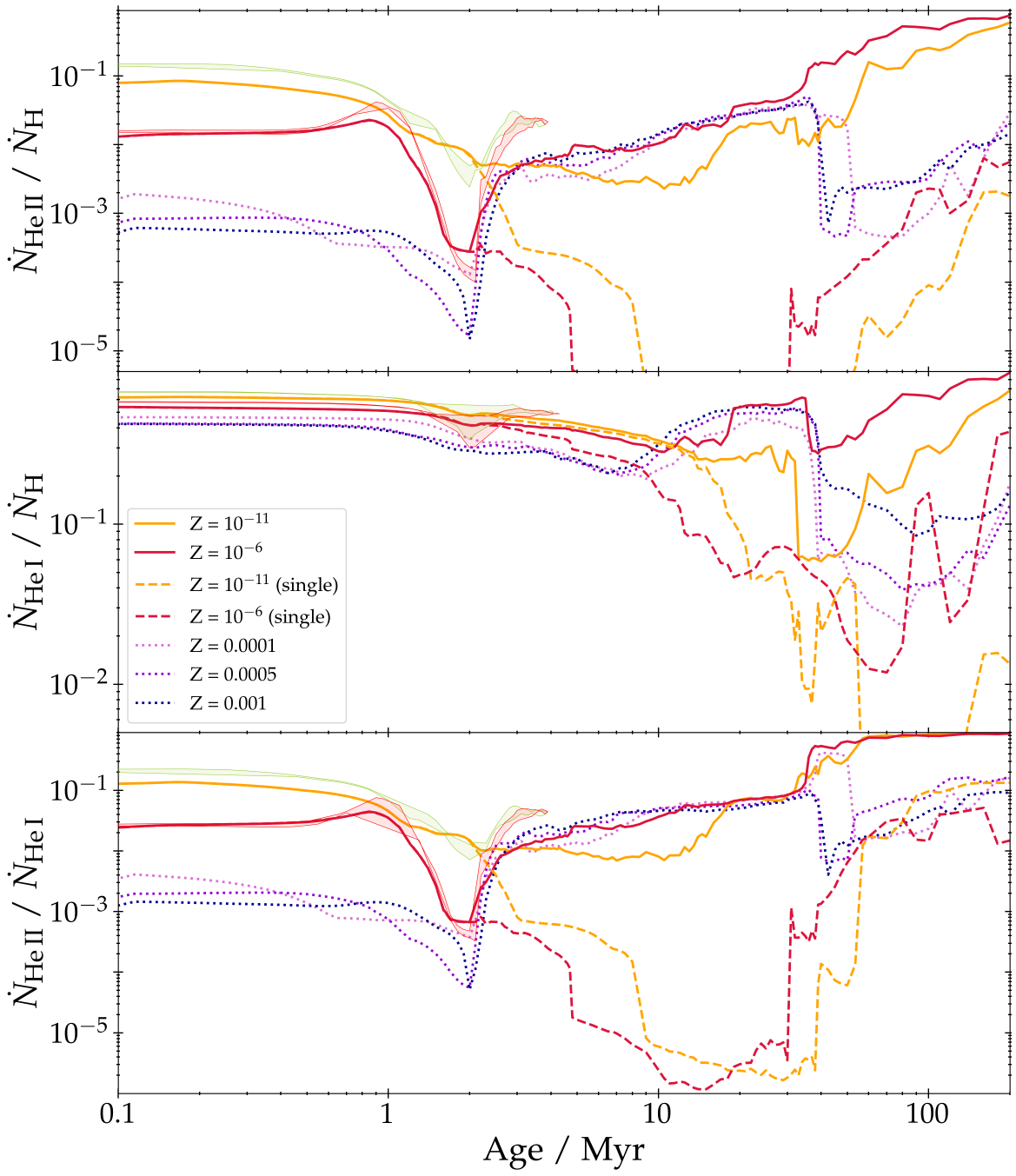

Figure 5.1: Production rates of He II- and He I-ionizing photons (normalized to that of H-ionizing photons in the upper two panels and relative to each other in the bottom panel) as a function of stellar-population age for different GALSEVN models. The solid orange and red lines denote GALSEVN Pop III pure-binary models. The dashed lines denote the Pop III single-stars models, for comparison. Pop II pure binary models are represented by dotted lines in shades of purple, for reference. All these models have the same zero-age Chabrier (2003) IMF as in Figure 2.3. The green- and red-shaded regions represent the areas covered by models with the three top-heavy IMFs with characteristic masses of 50 $M_\odot$, 100 $M_\odot$ and 200 $M_\odot$ described in section 5.1.3, for $Z = 10^{-11}$ and 10^{-6} respectively. As explained in section 3.2.2, these models are only considered up to the point where the stars are too few and the curve too noisy.

exhibits a globally higher $\dot{N}_{\mathrm{He\,II}}$ with this choice in IMF, resulting from a large fraction of extremely massive stars. This tendency is somewhat less strong for the slightly cooler $Z = 10^{-6}$. Once again, the evolution of $\dot{N}_{\mathrm{He\,I}}$ is very similar to that of models with a Chabrier (2003) IMF, since the difference in the fraction of very massive stars does not influence much the production rate of medium-energy ionizing photons.

We now consider the zero-metallicity stellar-population models of Schaerer (2003), based on an earlier version of the Padova evolutionary tracks for single zero-metallicity stars with negligible mass loss, complemented with other models for stars with high mass loss (Lejeune and Schaerer, 2001; Meynet and Maeder, 2002), both sets covering the mass range from $1\,\mathrm{M}_\odot$ to $500\,\mathrm{M}_\odot$. These stellar tracks do not include binary interactions or the effects of rotation. These models are provided for a range of modified Salpeter (1955) IMFs with different lower- and upper-mass cut-offs in the interval between 1 and $500\,\mathrm{M}_\odot$, as described by Raiter et al. (2010). We compare the predictions of these models with those of standard GALSEVN models with a Chabrier (2003) IMF truncated at 0.1 and $300\,\mathrm{M}_\odot$ for primary stars and a Sana et al. (2012) distribution of secondary-to-primary mass ratios at age zero (single stars being modelled as non-interacting binaries). As noted earlier, such an IMF can lead in binary-star populations to the presence of merged stars with masses up to $\sim 600\,\mathrm{M}_\odot$ (section 2). For completeness, we investigated the impact of adopting an upper mass cut-off of $100\,\mathrm{M}_\odot$ instead of $300\,\mathrm{M}_\odot$. We found the effect on $\dot{N}_{\mathrm{He\,II}}/\dot{N}_{\mathrm{H}}$ and $\dot{N}_{\mathrm{He\,I}}/\dot{N}_{\mathrm{H}}$ to be limited, due to the very small fraction of stars in the upper part of Chabrier (2003) distribution, and the extremely short lifetime of these very massive stars. Moreover, low-metallicity stars with masses up to $\sim 300\,\mathrm{M}_\odot$ have been observed in local environments (e.g., Crowther et al., 2016; Smith et al., 2016, see also Vink et al. 2011), and are expected to become more frequent at lower metallicities and higher redshift. Since in any case Pop III stars are expected to be very massive (up to $\sim 1000\,\mathrm{M}_\odot$ for Pop III stars), we choose not to investigate this aspect further here and fix the upper mass cut-off of GALSEVN models at $300\,\mathrm{M}_\odot$ for the remainder of this discussion.

Figure 5.2 compares Schaerer (2003) SEDs with different IMFs to the GALSEVN Pop III predictions presented in Figure 5.1. The evolution of $\dot{N}_{\mathrm{He\,II}}$ and $\dot{N}_{\mathrm{He\,I}}$ are quite similar between the standard model of Schaerer (2003), corresponding to a Salpeter (1955) IMF truncated at 1 and $500\,\mathrm{M}_\odot$, in dark purple, and the GALSEVN single-star $Z = 10^{-11}$ model, in dashed orange. Slight differences arise for $\dot{N}_{\mathrm{He\,II}}$ between 1 and 2 Myr, presumably due to differences in the stellar tracks and stellar spectral libraries.

The model of Schaerer (2003) with a Salpeter (1955) IMF truncated at 1 and $100\,\mathrm{M}_\odot$ exhibits a $\dot{N}_{\mathrm{He\,II}}/\dot{N}_{\mathrm{H}}$ ratio about 5 times lower than those with an IMF reaching $500\,\mathrm{M}_\odot$ at the earliest ages. This difference becomes less pronounced as the most massive stars leave the MS phase. In the Schaerer (2003) model with a Salpeter (1955) IMF truncated at 50 and $500\,\mathrm{M}_\odot$, the $\dot{N}_{\mathrm{He\,II}}/\dot{N}_{\mathrm{H}}$ and $\dot{N}_{\mathrm{He\,I}}/\dot{N}_{\mathrm{H}}$ ratios are initially slightly boosted relative to the other two models by the removal of the of the coolest ionizing stars, although they remain below the predictions of the GALSEVN models with top-heavy IMFs.

Based on these preliminary considerations regarding the Schaerer (2003) SEDs used by Nakajima and Maiolino (2022) to predict the properties of EoR galaxies, it is now interesting to compare GALSEVN predictions with the diagnostics these authors propose to differentiate ionization by Pop III stars from that by other high-energy sources in emission-line diagrams: pristine, direct-collapse black holes (DCBHs), evolved Pop II stars and metal-enriched AGNs. DCHBs are black holes with masses between 10^5 and 10^6 $\mathrm{M}_\odot$, which might have formed directly from the collapse of pristine gas clouds in the early Universe (see, e.g., Volonteri, 2012; Valiante et al., 2016; Beckmann et al., 2019; Inayoshi et al., 2020, for reference). Nakajima and Maiolino (2022) consider theoretical DCBH SEDs composed of a black-body-like spectrum peaking in the ultraviolet combined a power-law tail in the X-ray range, similar to AGN emission(Valiante et al., 2018), with adjustable black-body temperature and spectral index of the power law. They also consider Pop III stars and DCBHs evolving in an enriched medium of adjustable metallicity. Nakajima and Maiolino (2022) compute the ionizing spectra of Pop II galaxies using BPASS binary-star models with metallicities ranging from 10^{-5} to 10^{-3}, for 10 Myr-old stellar populations

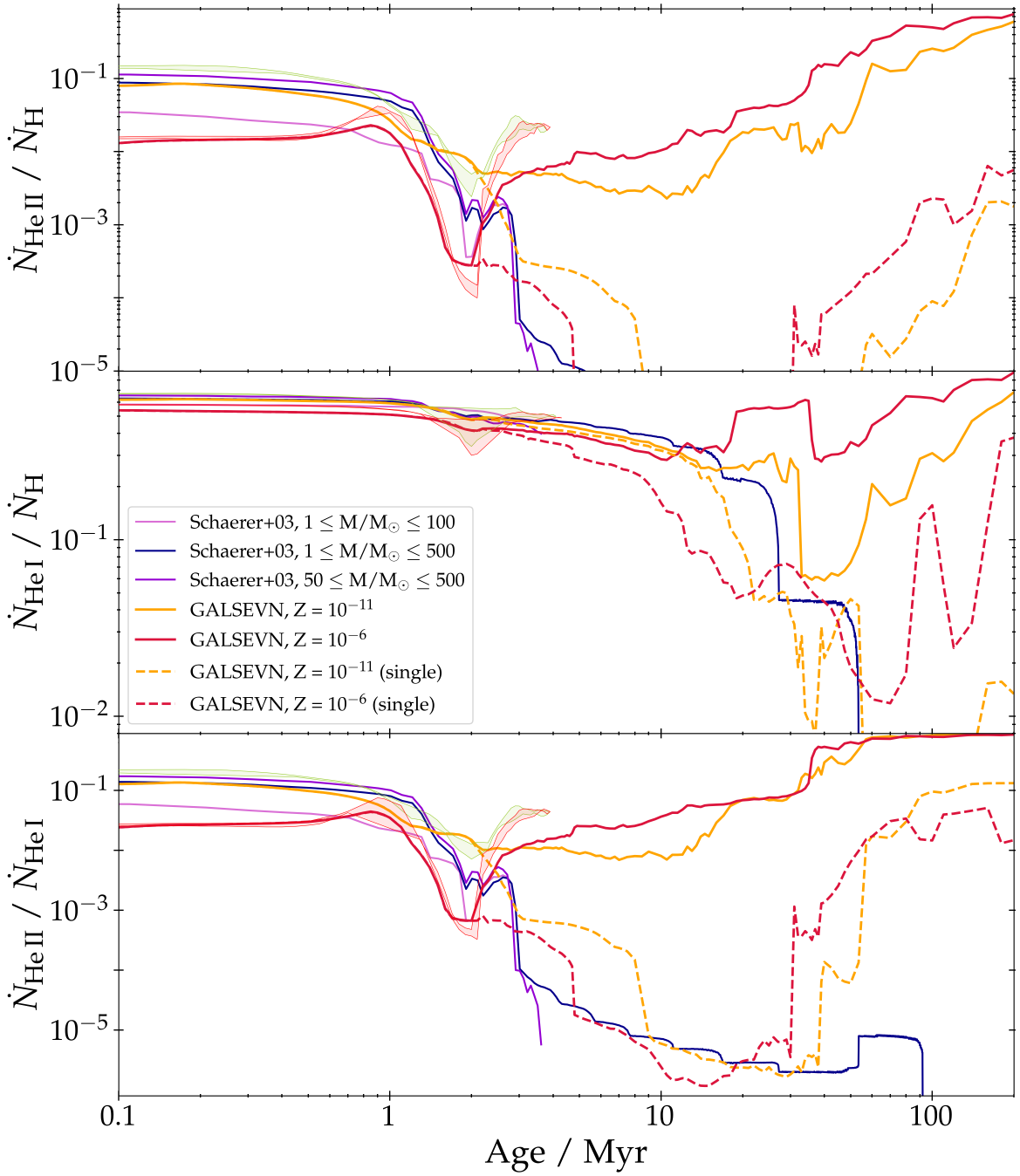

Figure 5.2: Same as Figure 5.1, but comparing the prediction of GALSEVN and Schaerer (2003) models. The solid- and dashed-orange and red curves represent the same GALSEVN Pop III models as in Figure 5.1, as well as the green- and red-shaded areas. The GALSEVN models have a Chabrier (2003) IMF truncated at 0.1 and 300 $\mathrm{M_\odot}$ for primary stars and a Sana et al. (2012) distribution of secondary-to-primary mass ratios at age zero (single stars being modelled as non-interacting binaries; see section 2). The curves in shades of purple show the zero-metallicity, single-star models of Schaerer (2003) for three Salpeter (1955) IMFs with different lower- and upper-mass cut-offs, as indicated.

with constant SFR. They model the ionizing radiation from AGNs using the same templates as for DCBHs but with higher metallicities. They then use the CLOUDY photoionization code to compute the nebular emission produced by these different sources, with adjustable parameters similar to those detailed in section 5.1.3.

In their paper, Nakajima and Maiolino (2022) investigate several emission-line diagrams able to isolate the signatures of either Pop III stellar populations or pristine DCBHs. They conclude that ionization by Pop III stars can be best discriminated based on the equivalent widths of He II λ4686 and, to a lesser extent, He II λ1640. Extreme values of these equivalent widths cannot be reproduced by any other source in their models, including primeval DCBHs. They also find the line ratios He II λ4686/Hβ and He II λ1640/Lyα useful to identify populations of Pop III stars with a top-heavy IMF, although these ratios do not discriminate between zero-metallicity stars and DCBHs. Nakajima and Maiolino (2022) also show that diagrams involving He I lines are not good indicators of metallicity, since the values for Pop II and Pop III stellar populations are similar for these ratios. They finally identify three criteria and tendencies based on these emission lines to identify Pop III stars in emission-line diagrams (see their figures 2, 3 and 6).

We plot these emission-line diagrams and the location of the Nakajima and Maiolino (2022) models in Figure 5.3, with the region corresponding to Pop III stars shown in shaded grey. Although the diagram represented in Figure 5.3b) is not strictly identified as a diagnostic diagram, it is also useful as it can be used to discriminate between several values of $n_{\rm H}$.The model predictions presented by Nakajima and Maiolino (2022) for DCBHs, evolved Pop II galaxies and AGNs – over their whole range of gas-phase metallicity, $\log\langle U\rangle$, $n_{\rm H}$, and IMFs – appear in this figure as colour-shaded regions (respectively in red, blue and green).

The coloured dots in Figure 5.3 show the locations of zero-age[5] GALSEVN SSP models with different metallicities and IMFs.

Figure 5.3 shows that the GALSEVN predictions strongly support the criteria proposed by Nakajima and Maiolino (2022) to identify signatures of Pop III stellar populations. These criteria appear strict enough for even models with $Z = 10^{-6}$ to be below the identified thresholds. This is not surprising, as Figure 5.2 shows a similarity in SEDs, especially at early ages, and we know that binaries are not decisive at such young ages. The best diagnostic diagram seems to be EW(He II λ4686) versus He II λ4686/Hβ, as the regions populated by evolved galaxies, AGNs/DCBHs and zero-metallicity models are well separated. The equivalent ultraviolet diagram of EW(He II λ1640) versus He II λ1640/Lyα also appears to separate the different sources well enough, although there is a small overlap in the lowest-EW(He II λ1640) part of the grey-shaded region. As for the pure line-ratio diagram representing He II λ4686/Hβ versus He Iλ5876/Hβ, it separates evolved galaxies from all other contributions quite well, but does not seem to discriminate AGNs/DCHBs from zero-metallicity stars. This diagram does, however, show a strong dependence on $n_{\rm H}$, as indicated by the horizontal arrows pointing to the locations of equivalent models with $n_{\rm H} = 10^2$ and $10^4\,{\rm cm}^{-3}$, for the lowest two metallicities. This diagram therefore provides useful complementary information to these Pop III diagnostics.

We note that the predictions of the GALSEVN model for evolved stellar populations with $Z = 0.0001$, 0.0005 and 0.001 are also in good agreement with those of Nakajima and Maiolino (2022). This is not surprising, given the agreement between GALSEVN and BPASS predictions at early ages (already shown in Figure 2.6).

We do not investigate predictions for Pop III stars evolving in a slightly enriched ISM, as do some of the models presented by Nakajima and Maiolino (2022). Although our approach allows such modelling (see section 3.1.3), we make this choice because of the short lifetimes of these stars, and because we focus in this study on the very first generations of Pop III stars.

It is of interest to examine the predicted signatures of primeval sources not only at zero age, but also in their evolution with time, to be able to estimate the probability of observing them in the areas

[5]In the Nakajima and Maiolino (2022) models, all stars begin their evolution on the zero-age main sequence. Instead, in the GALSEVN model, which includes pre-MS evolution, SSPs ignite when the most massive stars approach the MS. This difference in timing is minimal, as pre-MS evolution lasts only about 1 per cent of the MS duration, and does not impact the conclusions of this chapter.

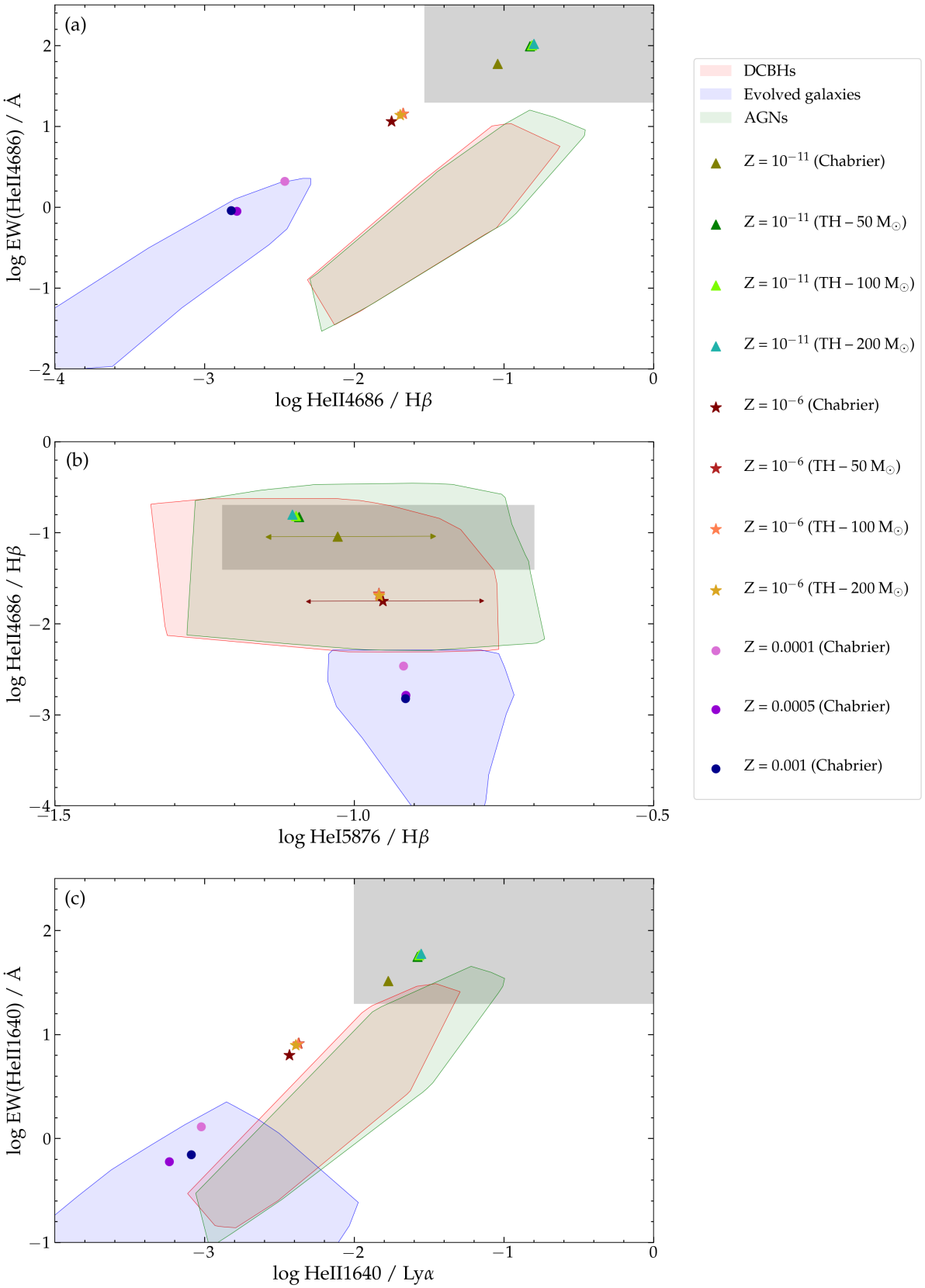

Figure 5.3: Diagnostic diagrams proposed by Nakajima and Maiolino (2022) to differentiate ionization by Pop III stars from that by other high-energy sources. The markers represent zero-age, pure binary-star GALSEVN models with different metallicities and IMFs, colour-coded as indicated on the right. The grey-shaded area corresponds to the region identified as populated by Pop III stars by Nakajima and Maiolino (2022). The other coloured regions correspond to the regions populated by primeval DCBHs, evolved (Pop II) galaxies and AGNs, as indicated. The horizontal arrows in panel (b) for $Z = 10^{-11}$ and 10^{-6} represent the positions of similar models with $n_{\rm H} = 10^2$ cm^{-3} (left-pointing) and 10^4 cm^{-3} (right-pointing).

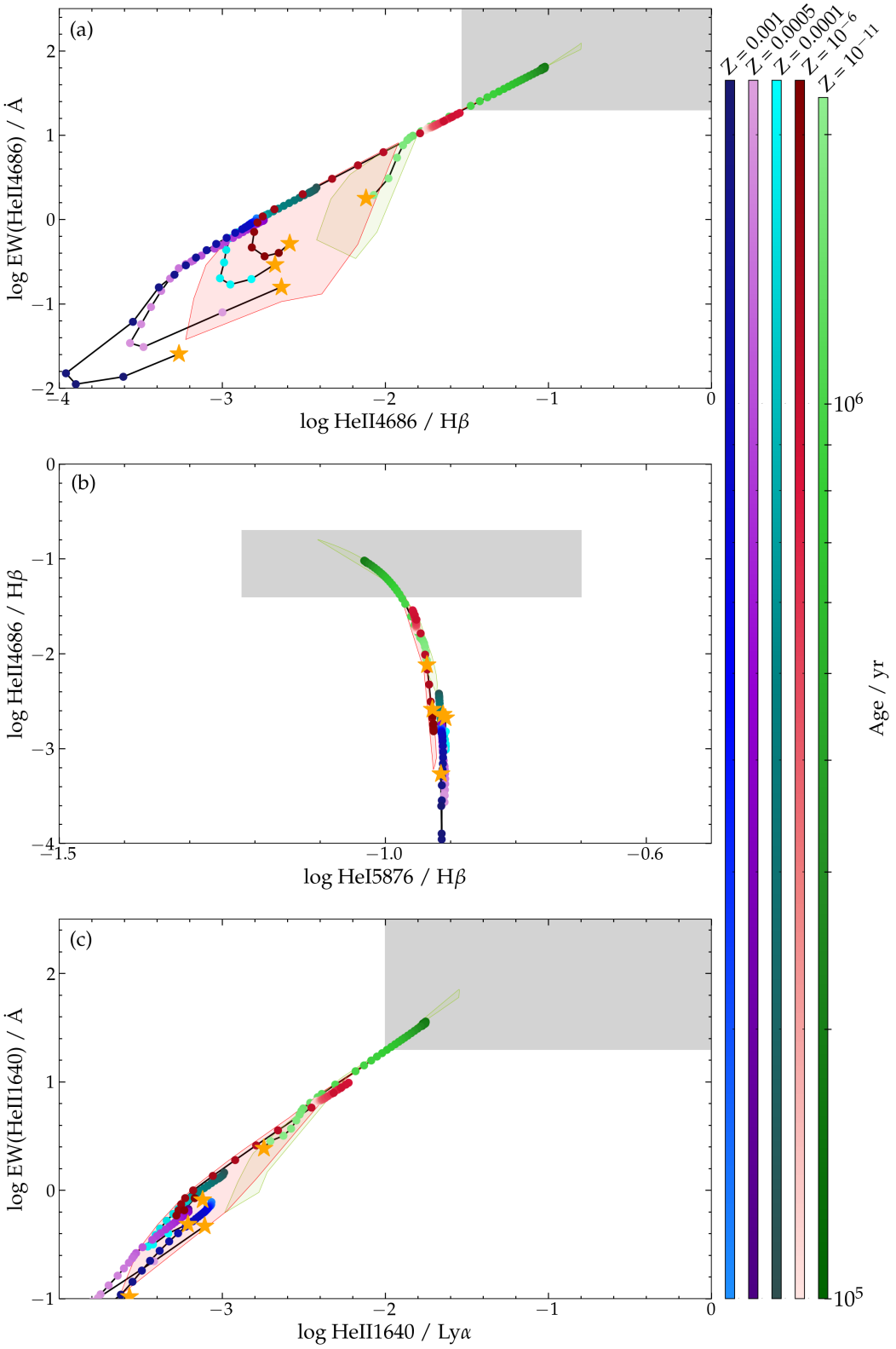

Figure 5.4: Same diagnostic diagrams as in Figure 5.3. As before, in each diagram, the grey-shaded zone shows the location of models powered by Pop III stars according to Nakajima and Maiolino (2022). The different curves with dots show the time evolution of the GALSEVN SSP models shown at zero age in Figure 5.3, as indicated by the colour bars on the right. For each model, the orange star marks the time of appearance of the first supernova, when the model is stopped in the present work. The red- and green-shaded regions have the same meaning as in Figures 5.1 and 5.2.

of diagnostic diagrams identified above. We therefore also discuss the time evolution of these spectral features for the GALSEVN models commented above.

The GALSEVN models presented here do not take into account the enrichment of the surrounding medium through stellar evolution, but assume a constant gas-phase metallicity. Such enrichment could considerably alter the values of $Z_{\rm ISM}$ for the lowest metallicities, which would be highly sensitive to the presence of even trace amounts of metals. We therefore stop here our calculations at the time when the first SN appears for each population, to ensure that the surrounding medium has not yet been polluted by new metals. This limitation was not raised in the previous chapters, as models with metallicities of a few per cent of solar are not expected to be as sensitive to chemical enrichment.

Figure 5.4 represents the time evolution of the same GALSEVN SSP models as shown at zero age in Figure 5.3. For clarity, the evolution has been detailed only for models with a Chabrier (2003) IMF, the areas sampled by models with top-heavy IMFs appearing as green- and red-shaded regions for the metallicities $Z = 10^{-11}$ and 10^{-6}, respectively. In each model, an orange star marks the time of appearance of the first supernova, when the model is stopped, corresponding to about 2.3 Myr for all models. Figure 5.4 reveals that the evolution of all considered spectral features is very rapid at these early ages. Indeed, models with $Z = 10^{-11}$ remain within the grey zones identified above to select ionization by Pop III stars only for ages up to ~ 1 Myr. This makes the probability of observing Pop III stars in this state quite low. Models with higher metallicities exhibit loops towards stronger He II λ1640 spectral features, around 1 Myr and later after 2 Myr. These loops, especially visible for the He II λ1640 equivalent widths predicted for $Z = 10^{-6}$, are due to the sudden increases in the production rate of He II-ionizing photons already discussed in Figure 5.1. However, these increases in EW(He II λ1640), EW(He II λ4686) and He II $\lambda4686/{\rm H}\beta$ are not intense enough to bring these models over the thresholds of the Pop III-diagnostic criteria.

Figures 5.3 and 5.4 overall highlight the fact that the GALSEVN models support the criteria presented by Nakajima and Maiolino (2022) to identify ionization by Pop III stellar populations. The figures also confirm that these criteria are strict enough to efficiently separate Pop III signatures from those from other possible sources of high-energy photons. However, the high thresholds of these criteria make them accurate for only a very short time, making the probability of actually observing stellar populations in this regime very low.

5.2.2 Production efficiency of ionizing photons

As direct measurements of the fraction of ionizing photons actually escaping from a galaxy are possible only once the Universe is reionized, it is difficult to establish observational signatures of the ionizing efficiency of young galaxies in early-Universe simulations. In this context, it is useful to investigate the values of the ionizing-photon production efficiencies $\xi^*_{\rm ion}$ and $\xi^{\rm H\,II}_{\rm ion}$ predicted by the GALSEVN model for extremely low-metallicity populations, which we can achieve self-consistently with the ultraviolet and optical spectral signatures mentioned above.

The nebular ionizing-photon production efficiency $\xi^{\rm H\,II}_{\rm ion}$, as defined in section 5.1.2, is a more direct observable than $\xi^*_{\rm ion}$, as it can be constrained by observations corrected for dust attenuation outside the ionized region. We therefore begin our analysis by looking at the evolution of $\xi^{\rm H\,II}_{\rm ion}$ with time and metallicity, for the SSP models discussed in the previous section. The quantity $\xi^{\rm H\,II}_{\rm ion}$ is calculated using the rate of H-ionizing photons predicted by the GALSEVN stellar-population models, and the UV luminosity computed from the spectrum output by CLOUDY, to account for the recombination continuum and dust absorption inside the ionized region.

Figure 5.5 shows the time evolution of $\xi^{\rm H\,II}_{\rm ion}$ for the same GALSEVN binary SSP models as in Figure 5.1. The time of appearance of the first SN in the lowest metallicity populations is marked by the vertical dashed line, to indicate the beginning of chemical enrichment. Estimates of $\xi_{\rm ion}$ have flourished in recent work, both from simulations and from observational constraints. Analytical reionization models often assume a canonical value in the range $\log \xi^*_{\rm ion}/{\rm erg^{-1}Hz} \approx 25.2$–$25.3$ (e.g., Robertson et al.,

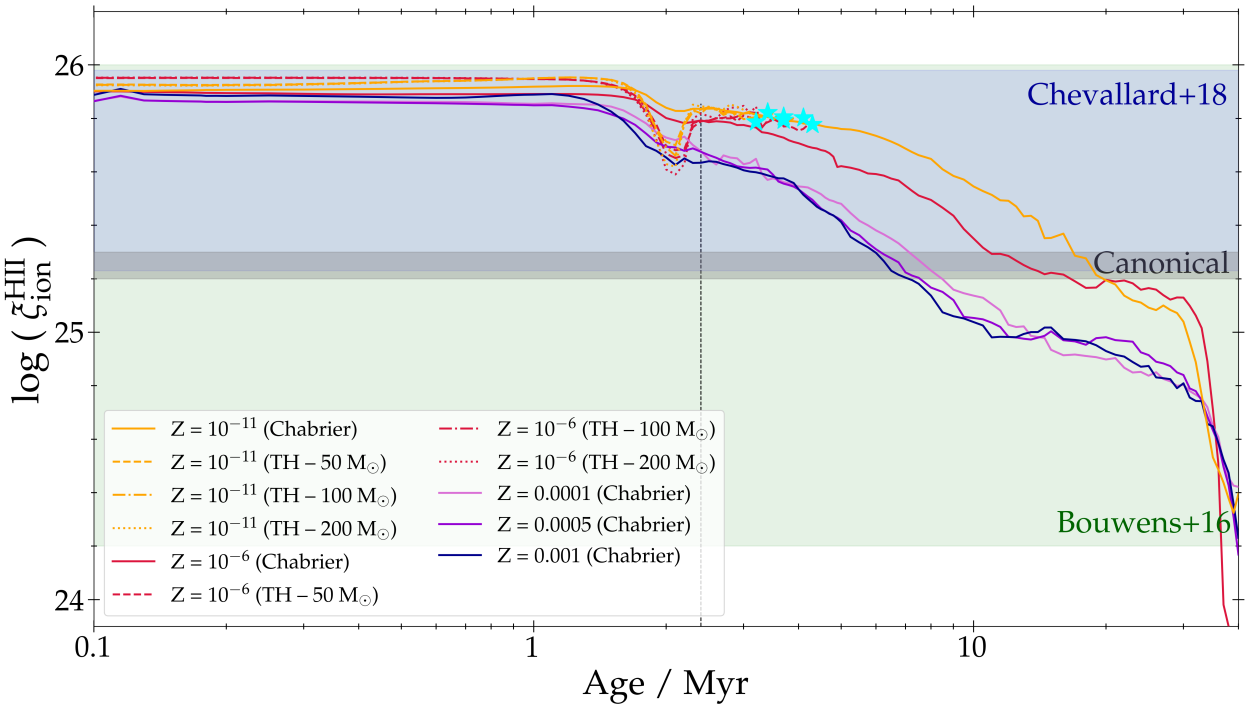

Figure 5.5: Nebular ionizing-photon production efficiency $\xi_{\rm ion}^{\rm H\,II}$ as a function of stellar-population age for the same GALSEVN binary models as in Figure 5.1. The time evolution is followed up to 40 Myr, but the H II regions surrounding the young stellar populations are expected to have been disrupted before at most 10 Myr, as discussed in chapter 2. The vertical dashed line marks the time of appearance the first SN in the lowest-metallicity models, corresponding to the beginning of chemical enrichment. The models with top-heavy IMFs are plotted until their absolute UV magnitude reaches $m_{\rm UV} = -14$, marked by cyan stars (as in section 3.2.2). The blue and green-shaded regions correspond to $\xi_{\rm ion}^{\rm H\,II}$ constraints derived from observations at low to intermediate redshifts, from different works. The grey-shaded region corresponds to the canonical values usually adopted for $\xi_{\rm ion}^{*}$ in simulations.

2013), shown by the grey-shaded region in Figure 5.5. We can also compare GALSEVN predictions to the $\xi_{\rm ion}$ ranges estimated in two recent observational studies. Bouwens et al. (2016) derive their values from observations of star-forming galaxies in the GOODS field, at redshifts $z \sim 3.8$–5.4, based on the measured UV-continuum slope and Hα intensities. Chevallard et al. (2018) obtain their values by fitting the SEDs of 10 nearby analogues of primeval galaxies from *HST*/*COS* observations, using the BEAGLE spectral-interpretation tool. The ranges of $\xi_{\rm ion}$ values in these two studies appear as green- and blue-shaded regions on Figure 5.5. These results are in general agreement with those derived in several other recent works, using different methods to retrieve the values of $\xi_{\rm ion}^{*}$ and $\xi_{\rm ion}^{\rm H\,II}$ from observations at various redshifts ($0.3 \lesssim z \lesssim 9$), and whose ranges of values have not been plotted in Figure 5.5 for the sake of clarity (e.g., Stark et al., 2015; Schaerer et al., 2016; Izotov et al., 2017a; Matthee et al., 2017; Stark et al., 2017; Shivaei et al., 2018, see section 5 of Chevallard et al. 2018 for a more detailed comparison).

Figure 5.5 shows that the GALSEVN predictions are very similar for all metallicities at early ages, with a relatively high estimated $\xi_{\rm ion}^{\rm H\,II}$ (still falling within the observed range), which remains almost constant at first, while most stars evolve on the MS. After ~ 1 Myr, the dependence of the evolution becomes more pronounced. The lowest-metallicity models generally keep a higher $\xi_{\rm ion}^{\rm H\,II}$, and the decrease in $\xi_{\rm ion}^{\rm H\,II}$ seems to be almost linear with slopes depending on metallicity until ~ 30 Myr. The slope seems to steepen with increasing metallicity. This is expected, due to the higher ionizing power of stars with extremely low metallicity, resulting from their specific properties (e.g., evolutionary tracks shifted towards higher temperatures), as discussed in the previous section.

Moreover, comparison of the models with a Chabrier (2003) and top-heavy IMFs reveals that the IMF does not appear to be a crucial parameter for the predicted $\xi_{\rm ion}^{\rm H\,II}$ values. While the predicted values for top-heavy IMFs are slightly higher at early ages, the main difference is a pronounced feature just before 2 Myr, when most massive stars reach the end of their H-burning phase, resulting in a

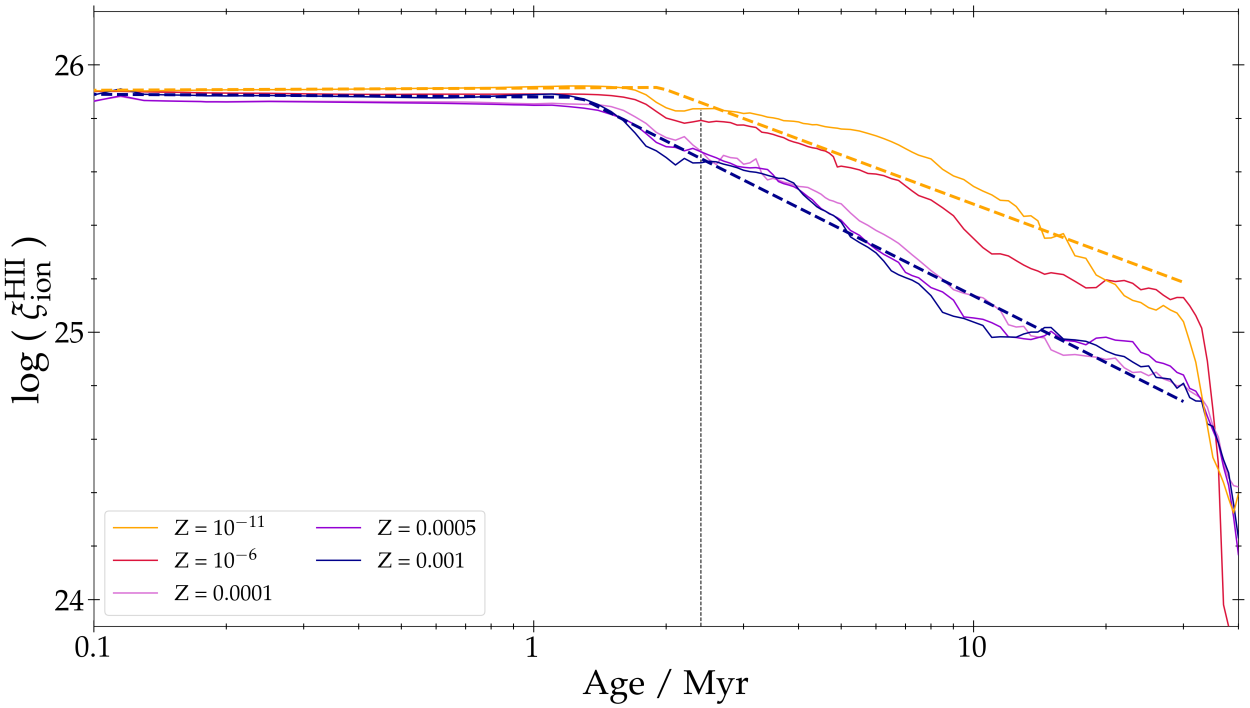

Figure 5.6: Bimodal linear fits adopted to represent $\xi_{\rm ion}^{\rm H\,II}$ as shown in the previous plot, for the two extreme metallicities $Z = 10^{-11}$ and 0.001.

drop in the production of ionizing photons until the appearance of hot, WNE-like products of binary evolution. As before, we stop the evolution of models with top-heavy IMFs when their absolute UV magnitude reaches −14.

Figure 5.5 shows overall good agreement between GALSEVN predictions for $\xi_{\rm ion}^{\rm H\,II}$ and recent observations. It also reveals a dependence of $\xi_{\rm ion}^{\rm H\,II}$ on time and metallicity, which is almost negligible for approximately the first million years, before becoming more pronounced.

According to simulations of early galaxy formation (e.g., Finkelstein et al., 2019) and recent observational constraints on the non-ionising UV luminosity density (e.g., Atek et al., 2024), with such high values of $\xi_{\rm ion}^{\rm H\,II}$, the escape of only a few per cent of ionizing photons from nascent galaxies would suffice to reionize the Universe. The fact that such high values of $\xi_{\rm ion}^{\rm H\,II}$ are naturally produced by GALSEVN models for metallicities up to a few per cent of solar supports the major role that early star-forming galaxies are likely to have played as reionization drivers.

For some applications to the modelling of early galaxy formation, it may be useful to have a simple analytical expression for estimates of $\xi_{\rm ion}^{\rm H\,II}$ as a function of time and metallicity. We derive such relations here for models with a Chabrier (2003) IMF (as Figure 5.5 shows, models with top-heavy IMFs have similar properties at early ages).

The general shape of the curves in Figure 5.5 suggests a fit with two linear regimes, before and after the breaks that occur between 1 and 2 Myr, depending on the metallicity. As the two extreme metallicities, $Z = 10^{-11}$ and 0.001, appear to bracket the intermediate ones, and as the slope after the break appears to decrease monotonically with metallicity, we present fits only for these two metallicities, assuming that the relations for the intermediate metallicities can then be interpolated. We find that

$$\log \xi_{\rm ion}^{\rm H\,II} = \begin{cases} 0.0082\log({\rm t/yr}) + 25.86 & \text{for } {\rm t} \leq 1.9\,{\rm Myr} \\ -0.61\log({\rm t/yr}) + 29.77 & \text{for } {\rm t} > 1.9\,{\rm Myr} \end{cases} \quad \text{for } Z = 10^{-11} \tag{5.4}$$

and

$$\log \xi_{\rm ion}^{\rm H\,II} = \begin{cases} -0.0094\log({\rm t/yr}) + 25.93 & \text{for } {\rm t} \leq 1.1\,{\rm Myr} \\ -0.82\log({\rm t/yr}) + 30.91 & \text{for } {\rm t} > 1.1\,{\rm Myr} \end{cases} \quad \text{for } Z = 0.001 \tag{5.5}$$

provide reasonable approximations to the actual models, as illustrated by Figure 5.6.

It is also of interest to provide a means of estimating the stellar ionizing-photon production rate $\xi^*_{\rm ion}$, which is often used (in combination with the $f_{\rm esc}$ parameter) in simulations of the reionization epoch. We can achieve this by combining the above expressions for $\xi^{\rm H\,II}_{\rm ion}$ with an estimate of the ratio between $\xi^*_{\rm ion}$ and $\xi^{\rm H\,II}_{\rm ion}$. For simplicity, we focus on the initial, bright phase with nearly constant $\xi^{\rm H\,II}_{\rm ion}$ at ages below 1 Myr (Figure 5.5), during which massive stars evolve on the main sequence. Figure 5.7 shows the evolution of the $\xi^*_{\rm ion}$-to-$\xi^{\rm H\,II}_{\rm ion}$ ratio during this phase, for the different metallicities, for the same GALSEVN binary SSP models with a Chabrier (2003) IMF as in Figure 5.1. The ratio is almost constant during this phase and decreases with increasing metallicity, reflecting the associated increasing absorption of stellar UV luminosity by dust in the H II region (at fixed dust-to-metal mass ratio $\xi_{\rm d}$). We compute the time-averaged value of this ratio for each metallicity (shown as a red horizontal line in each panel), which we report in Figure 5.8 with uncertainties reflecting the offset of the most extreme value from the time-averaged ratio. The dependence of this time-averaged value on metallicity can be well approximated by the relation

$$\xi^*_{\rm ion}/\xi^{\rm H\,II}_{\rm ion} = -0.35\log(Z) + 0.67\,, \tag{5.6}$$

obtained using weights inversely proportional to the uncertainties and shown as the red line in Figure 5.8.

5.2.3 Other properties

In this subsection, I present complementary quantities predicted by our GALSEVN models of EoR galaxies, which may offer additional probes of the stellar physics at play in the early Universe. These include the production rate of Lyman-Werner photons and the rates of different types of supernovæ, which can provide important information about chemical enrichment.

As mentioned in section 5.1.1, the rate of Lyman-Werner photons emerging from a star-forming region, that is, the rate of photons capable of photo-dissociating the H_2 molecules acting as the main coolants in the primordial Universe, is a key quantity to predict star formation in the environment of that population and in neighbouring haloes.

Unlike most high-energy photons, which are rapidly absorbed by neutral H in the IGM, LW photons have a very long mean free path due to their relatively low energies, just above the Lyman limit. It is therefore important to take self-consistent account of LW photons in simulations studying the formation of the first cosmological structures, as this has strong implications for star formation, and hence, for stellar properties and feedback, on chemical-enrichment timescales, and so on.

Incatasciato et al. (2023) present an in-depth study of the LW radiation field, its evolution with redshift and its consequences on H_2 photo-dissociation and star formation. They use SPS models to predict LW-photons emission for both Pop III and Pop II stellar populations. Their calculations are based on the Schaerer (2002) models with different IMFs for $Z = 0$, and on BPASS models with different IMFs for Pop II ($Z = 0.0005$) populations. They also compare their predictions with those obtained using SLUG[6] SPS calculations. Incatasciato et al. (2023) conclude that the mean LW intensity must have increased significantly from $z \sim 23$ to $z \sim 6$ – primarily due to massive star-forming galaxies – and highlight the importance of incorporating LW radiation into cosmological simulations for a realistic understanding of early galaxy formation. They examine the complexities of modelling the LW background radiation, comparing various models and noting the impacts of differing assumptions on the predictions. They also investigate the evolving minimum halo mass required for Pop III star formation under LW influence, advocating the high sensitivity of such predictions to model limitations. This, and the support by recent JWST observations of actively star-forming galaxies at high redshifts, indicates the crucial role of LW radiation in star formation within low-mass haloes in the early Universe.

[6]See section 2.1.1 for more details.

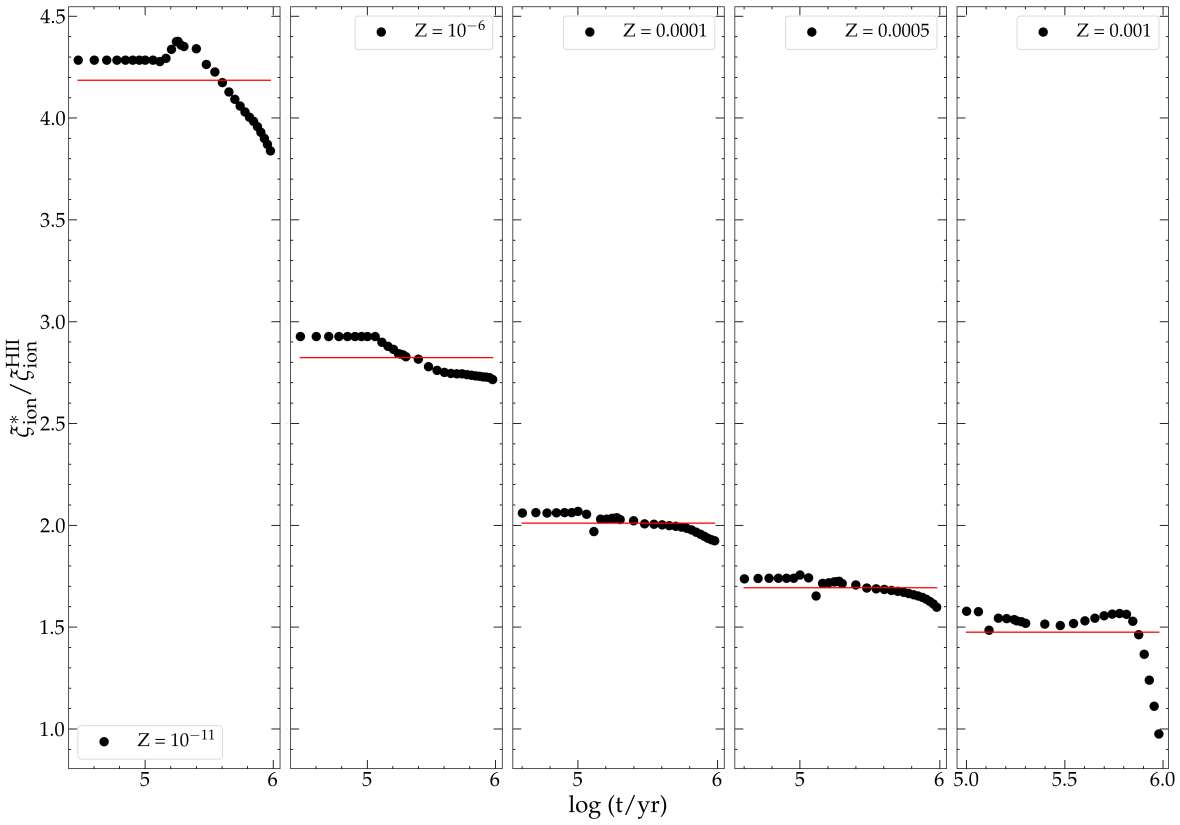

Figure 5.7: Time evolution of the $\xi^*_{\rm ion}/\xi^{\rm H\,II}_{\rm ion}$ ratio at ages below 1 Myr for the same GALSEVN binary SSP models with a Chabrier (2003) IMF as in Figure 5.1, for different metallicities, shown in different panels. In each panel, the red horizontal line shows the time-averaged value used to derive the expression of $\xi^*_{\rm ion}/\xi^{\rm H\,II}_{\rm ion}$ (Z) in equation (5.6).

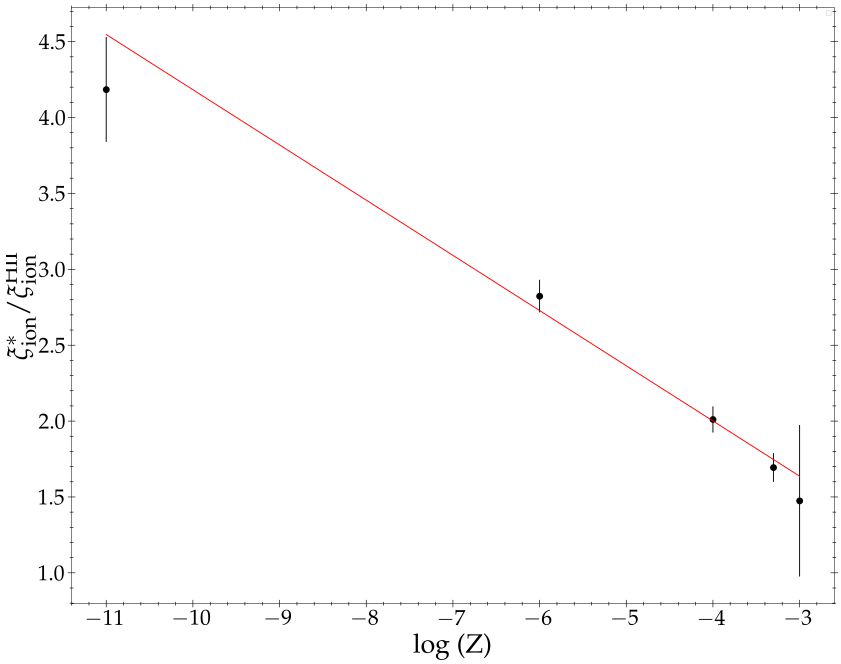

Figure 5.8: Illustration of the fit to time-average values of $\xi^*_{\rm ion}/\xi^{\rm H\,II}_{\rm ion}$ at ages less than 1 Myr as a function of metallicity provided by equation (5.6). The time-averaged values are estimated from Figure 5.7. Rough uncertainties are calculated as the distance between the most extreme point and the mean value at each metallicity (red line) in Figure 5.7, and are taken into account in the estimation of the best-fitting relation.

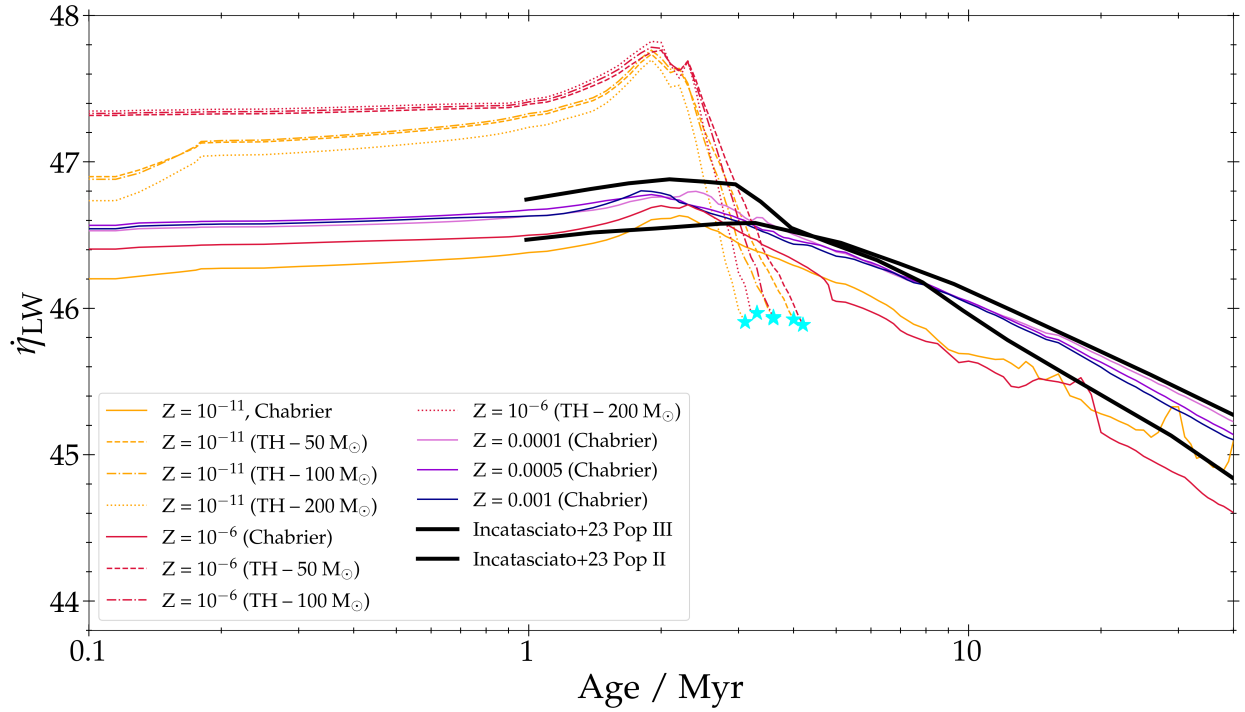

Figure 5.9: Lyman-Werner photon production rate (in the wavelength range 912 Å – 1150 Å) as a function of stellar-population age for the same GALSEVN binary models as in Figure 5.1 (normalized to a total initial stellar mass of 1 $M_\odot$ integrated over 0.1–300 $M_\odot$). For reference, the predictions of Incatasciato et al. (2023) for Pop II (using BPASS models for $Z = 0.0005$ with the IMF of Chabrier, 2003) and Pop III (using zero-metallicity models by Schaerer, 2003; Raiter et al., 2010, for stars with masses between 1 and 500 $M_\odot$) stellar populations are shown as dotted and solid black curves, respectively.

In Figure 5.9, we compare the fiducial model predictions of Incatasciato et al. (2023) for ages greater than 1 Myr, for Pop II (using BPASS models for $Z = 0.0005$ with the IMF of Chabrier, 2003)) and Pop III (using zero-metallicity models by Schaerer, 2003; Raiter et al., 2010, for stars with masses between 1 and 500 $M_\odot$) stellar populations with GALSEVN-model predictions. All production rates are normalized to a total initial stellar mass of 1 $M_\odot$. The production rates of LW photons computed by Incatasciato et al. (2023) are in general agreement with those obtained with the GALSEVN model for a Chabrier (2003) IMF. The main difference occurs before ~ 3 Myr: the Pop III models of Incatasciato et al. (2023) initially produce more LW photons than their Pop II models before the trend is reversed whereas Pop II stellar populations always produce more LW photons than Pop III ones in the GALSEVN model. The GALSEVN models show a global trend of increasing $\dot{\eta}_{\rm LW}$ with metallicity, at all ages, as the peak wavelength of the hot, near-black-body spectra of the most massive stars on the upper main sequence gradually shifts from the far-UV to the near-UV. Models with top-heavy IMFs initially exhibit much higher LW-production rates (per unit stellar mass), before falling with a much steeper slope shortly after 1 Myr as the most massive stars die out. This trend is also found for the Incatasciato et al. (2023) models and represented in their figure 2.

We find LW-photons production rates in general agreement with those presented by Incatasciato et al. (2023), therefore supporting their conclusions on the importance of including LW radiation in simulations of early galaxy formation and on the properties of star formation in low-mass haloes. Given the LW-photon production rates predicted here, it is likely that after the first generations of stars have evolved, most of the molecular H_2 in the ISM has been photo-dissociated. At this point, however, star-forming haloes are expected to have reached virial temperatures high enough for atomic cooling to take over, so that star formation is not quenched (e.g., Oh and Haiman, 2002), until the metallicity rises high enough for metals to become the most efficient coolants.

The study of the different types of SNe occurring in a stellar population provides useful information about the evolutionary paths followed by individual stars. As presented in section 1.2, the physical

conditions reached during the final core collapse of a star, which depend mainly on its mass and chemical composition, make it possible to distinguish between different types of explosive phenomena.

Type-Ia supernovæ arise at the surface of accreting white dwarfs – highly-degenerate remnants of progenitor stars initially less massive than $\sim 8\,M_\odot$– when their mass overcomes the Chandrasekhar limit for white dwarfs stability ($\sim 1.4\,M_\odot$). The remnant then becomes unstable and triggers a runaway fusion of oxygen and carbon all the way up to iron-peak elements, as the degenerate stellar interior is unable to stabilize the process, as MS stars could. This catastrophic fusion very rapidly releases large amounts of energy, of the order of 10^{51} erg, which disrupts the white dwarf and releases a relativistic ejecta composed mainly of iron-peak elements. They are therefore indicators of the proportion of accreting white dwarfs, and therefore of low-mass stars in binary systems, and are responsible for most of the Fe enrichment in the ISM.

On the other hand, type-II supernovæ are the product of the evolution of massive stars. They are therefore responsible for the enrichment of the ISM in α elements (O, Ne, Mg, Si, S, Ca), which are the products of the nuclear-fusion chain in massive stars. Pair-instability SNe (PISNe) are a particularly interesting indicator of mass distributions in a stellar population, as they arise only from extremely massive stars, with zero-age MS masses between typically 130 and $250\,M_\odot$.[7] As PISNe release enough energy to completely disrupt the stellar remnant, creating a mass gap in the mass spectrum of black holes (Spera et al., 2015; Belczynski et al., 2016; Woosley, 2017; Spera and Mapelli, 2017), a study of PISNe in a stellar population also gives indications of how many objects should have fallen into this mass gap. Stars slightly less massive than PISN progenitors, i.e., with zero-age MS masses typically between 60 and $130\,M_\odot$, can still reach He-core masses large enough to convert photons into electron-positron pairs. However, while the subsequent pair annihilation leads to core contraction and some explosive burning of oxygen and silicon, it does not generate enough energy to cause a complete disruption. These stars undergo Pulsational PISNe (PPISNe), experiencing multiple pulsations which release large amounts of kinetic energy through mass loss before ultimately collapsing to form a compact remnant (typically a black hole).

Due to the very high masses of their progenitors, and thus their very short lifetimes, PISNe and PPISNe are expected to arise only at early ages. Instead, due to the evolutionary timescale of low-mass stars and white dwarfs, type-Ia SNe are expected to occur after a few tens of million years. This radical difference in timescale is what makes the α-to-Fe element ratio in the ISM such a good indicator of the age of a stellar population.

Figure 5.10 shows the time evolution of the different types of SNe arising in the same binary-star GALSEVN SSP models as in Figure 5.1. We ignore non-exploding, 'failed' SNe leading to the formation of black holes (Spera et al., 2015; Spera and Mapelli, 2017). For clarity, only models with a Chabrier (2003) IMF are represented (predictions for top-heavy IMFs can be estimated from these models using mass-distribution arguments). The five different metallicities are represented in different colours, whereas the different line styles represent the different types of SNe.

As expected, the PISNe+PPISNe peak in Figure 5.10 arises between 2 and 6 Myr, for all metallicities. This rate is not strongly affected by metallicity, as the five metallicities represented here are all fairly low. It would decrease for higher metallicities, reducing to zero for metallicities above $Z = 0.01$ for PISNe and 0.018 for PPISNe (Spera and Mapelli, 2017). Other types of type-II SNe, for lower-mass progenitors, appear around 10 Myr and remain present for a few tens of Myr. Here again, the onset and duration of the peak are similar for all metallicities. This is not very surprising, as the IMF is the same for all models. Yet, the duration of the peak seems to be slightly shorter for the lowest metallicity, due to the faster evolution of the hotter stars at $Z = 10^{-11}$. The behaviour for type-Ia SNe, which appear for the first time around 30 Myr, is quite similar.

Finally, we note that chemical enrichment in Pop III models begins around 2 Myr, with the appearance of the first PISNe.

[7] The exact range depends on metallicity, which controls the efficiency of stellar winds and their influence on reaching the He-core mass required to form electron-positron pairs and activate the PISN mechanism (see, e.g., figure 2 of Spera and Mapelli, 2017).

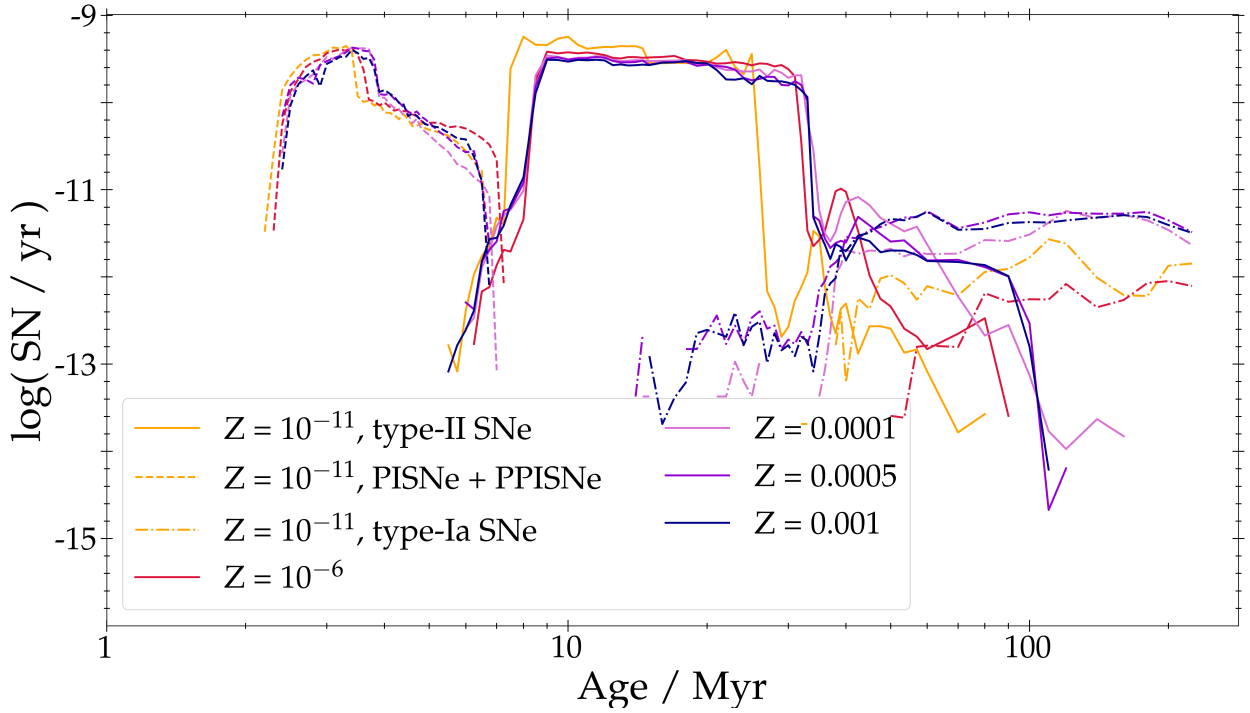

Figure 5.10: Supernova rate as a function of stellar-population age for the same binary-star GALSEVN models with a Chabrier (2003) IMF as in Figure 5.1 (normalized to a total initial stellar mass of $1\,M_\odot$ integrated over 0.1–300 $M_\odot$). Different metallicities are shown in different colours, and different types of supernovæ are shown in different line styles (short-dashed for pair-instability, solid for "classical" type-II, and dot-dashed for type-Ia SNe).

5.3 Gravitational-wave signal from Pop III binary black holes

As mentioned in section 1.1.5, direct optical observations of Pop III stars are extremely difficult. It is therefore useful to focus on indirect observations and multi-messenger emission, as these could provide valuable counterparts to the detection of Pop III stars at high redshift. Pair-instability and core-collapse SNe, which are expected to reach luminosities of up to 10^{12} $L_\odot$ (Whalen et al., 2013b,a), offer attractive opportunities for indirect detection up to $z \sim 15$ (Whalen et al., 2013b,a, 2014; Smidt et al., 2014, 2015) and can trigger gamma-ray bursts (Wang et al., 2012; **?**) potentially detectable up to $z \sim 20$ with near-future facilities (Amati et al., 2018). However, the short duration of such transients makes their detection probability still rather low. In this section, I therefore focus on another promising indirect probe of the properties of Pop III stellar populations: binary black holes, and in particular their mergers, which should produce potentially detectable gravitational-wave signatures – conveniently exempt from foreground contamination and line-of-sight absorption, unlike electromagnetic messengers. In this section, we adopt Planck Collaboration et al. (2020a) values for all cosmological parameters (see section 1.1.1).

5.3.1 Gravitational signal of binary black hole mergers

The theory of General Relativity published by Einstein (1915, 1916), which describes the structure of the spacetime continuum under the effect of gravitation, predicts the existence of gravitational waves (GW) as the propagation of a perturbation of the spacetime metric. These waves appear as slight contractions and dilations of spacetime resulting from a catastrophic gravitational event. The tensor formalism of general relativity describes gravitational waves as a perturbation term $h_{\mu\nu}$ to the Minkowski flat-spacetime metric $\eta_{\mu\nu}$, with $|h_{\mu\nu}| \ll 1$, such that the general metric describing spacetime can be written as $g_{\mu\nu} = \eta_{\mu\nu} + h_{\mu\nu}$. The spacetime structure becomes increasingly Minkowskian as the distance to the gravitational waves increases. With suitable choices of gauge and coordinates, Einstein

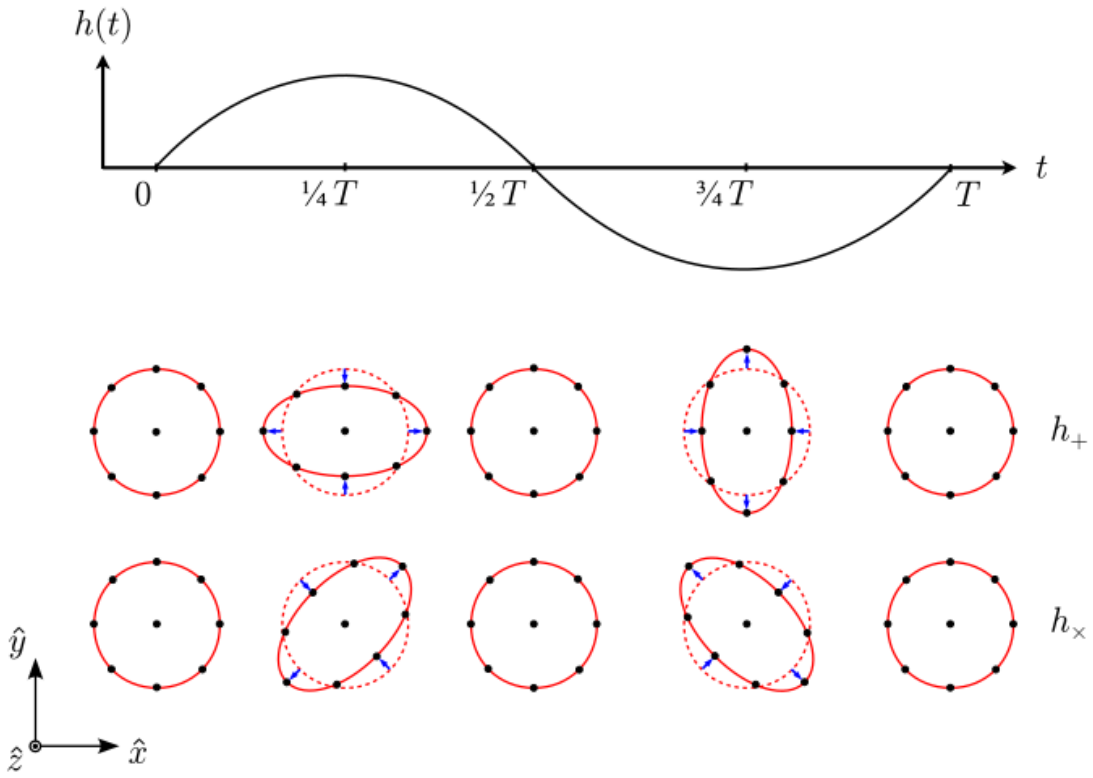

Figure 5.11: Diagram showing the propagation of a monochromatic gravitational wave along the $\hat{z}$ axis. The wave has a pulsation $2\pi/T$ and a period T. The effect of the + and × polarisations on a ring of free particles, shown in dashed red when at rest, is represented by solid red curves. *Credit: A. Le Tiec & J. Novak, by Auger and Plagnol (2017)*

(1916) derived the wave equation satisfied by GW,

$$\Box h_{\mu\nu} = -\frac{16\pi G}{c^4} T_{\mu\nu} \,, \tag{5.7}$$

where $\Box$ is the usual d'Alembertian operator ($\Box \equiv \eta^{\mu\nu}\partial_\mu\partial_\nu$ in a Minkowski spacetime) and T is the stress-energy tensor, which describes the flux and density of energy and momentum in spacetime. More detail on the GW formalism and detailed calculations can be found by Auger and Plagnol (2017, e.g., chap. 1 from). In the next paragraphs, I discuss only a few expressions providing physical insight into GW emission and interaction with matter, without detailing general-relativity calculations.

The gravitational waves that are solution to equation (5.7) are created by the motion of accelerated masses. In the context of general relativity, GW are transverse, non dispersive waves propagating at the speed of light. In a vacuum ($T = 0$), they are a superposition of monochromatic plane waves with two possible transverse polarisations, separated by a angle of $\frac{\pi}{4}$, denoted + and ×. As transverse waves, GWs only affect matter in directions orthogonal to their direction of propagation (denoted $\overrightarrow{n_+}$ for +-polarised and $\overrightarrow{n_\times}$ for ×-polarised waves) through successive contractions and dilations, characterized for a rest-length L by the *strain*

$$\frac{\Delta L}{L} = \frac{1}{2} h_{ij} n^i n^j \,, \tag{5.8}$$

using Ricci tensor-index notation. The time evolution of spacetime distortions caused by both polarisations are represented in Figure 5.11.

The amplitude of a GW and the energy it carries away from the source can be determined from the mass distribution and mass of the source, using the *quadrupole formula* (Einstein, 1918), which directly relates the GW amplitude $h_{ij}(\vec{x}, t)$ to the second time derivative of the Newtonian quadrupole moment of the source of density ρ,

$$Q_{ij}(t) = \int_{source} \mathrm{d}^3\vec{x}\,\rho(\vec{x},t)\left(x_i x_j - \frac{1}{2}||x||^2\delta_{ij}\right). \tag{5.9}$$

The dependence of h on the second time derivative of $Q_{ij}(t)$ highlights that GWs originate from the acceleration of massive objects.

As the energy flux carried by a GW of amplitude h is

$$F_{\mathrm{GW}} = \frac{c^3}{16\pi G}h^2(\vec{x},t)\,, \tag{5.10}$$

the GW luminosity of a source can be written as

$$L_{\mathrm{GW}} = \frac{G}{5c^5}\langle \dddot{Q}_{ij}\dddot{Q}^{ij}\rangle \approx L^0_{\mathrm{GW}}\, s^2\,\Xi^2\,\beta^6 \tag{5.11}$$

where $\Xi = Gm/Rc^2$ is the compactness of the source, β the dimensionless velocity and s a factor representing the symmetry of the source ($s = 0$ for a spherically-symmetric source). The quantity $L^0_{\mathrm{GW}} = c^5/5G$ is the fundamental GW luminosity, which is equal to $2 \times 10^{25}\,\mathrm{L}_\odot$.

The detailed derivation of these expressions from the quadrupole formula can be found in sections I.6 and I.7 of Auger and Plagnol (2017) for more details.

Equation (5.11) shows that for a source to emit GWs efficiently, it must be at the same time:

– highly compact ($\Xi \to 1$), that is, general-relativistic;

– special-relativistic ($\beta \to 1$);

– highly non-symmetric ($s > 0$).

Under these conditions, binaries of compact objects (that is, neutron stars and black holes), and especially binary black holes (BBHs), appear as excellent candidates for the emission of gravitational waves. These systems form as remnants of stellar binaries, whose stars have undergone explosive end-of-life events and whose binary parameters allow the system to remain bound despite the colossal amount of energy released by these explosive events. After their formation, these compact binary objects orbit the system barycentre, radiating energy and angular momentum through the emission of GWs. As they lose momentum, the two compact objects move closer together, until they finally collide and merge in a catastrophic gravitational event. The orbital phase when the systems gradually move closer together before coalescing is usually called *inspiraling*, and its duration depends mainly on the masses of the objects and their initial separation.

The evolution of orbital parameters, that is, the semi-major axis a and the eccentricity e of the system, during the inspirals, for a binary system composed of two compact objects of masses m_1 and m_2, is given by the formulæ established by Peters (1964):

$$\begin{cases} \dot{a} = -\dfrac{64G^3 m_1 m_2(m_1+m_2)}{5c^5 a^3(1-e^2)^{7/2}}\left(1 + \dfrac{73}{24}e^2 + \dfrac{37}{96}e^4\right) \\ \dot{e} = -\dfrac{304G^3 m_1 m_2(m_1+m_2)}{15c^5 a^4(1-e^2)^{5/2}}\left(1 + \dfrac{121}{304}e^2\right)e\,. \end{cases} \tag{5.12}$$

It is important to note that, in most cases, the orbit tends to rapidly circularize due to the loss of energy and angular momentum (implying $e = 0$ close to the merger event).

As mentioned earlier, the duration of this inspiraling phase is dictated by the orbital parameters of the system and the masses of the compact objects. Iorio et al. (2023) derive an expression for this

duration, which is accurate (with a relative error of less than 0.6 per cent) for the whole range of eccentricities:

$$t_{\rm delay} = \frac{1}{1+f_{\rm corr}(e)}\,\frac{5c^5}{256G^3}\,\frac{a^4}{m_1m_2(m_1+m_2)}(1-e^2)^{7/2}\,, \tag{5.13}$$

with $f_{\rm corr}(e) = e^2\left[-0.443 + 0.580(1-e^3.074)^{1.105-0.807e+0.193e^2}\right]$ (see their Appendix D for a detailed study of accuracy).

In the case of a quasi-circular orbit ($e \sim 0$), that is, for orbits close to the merger event (which are often those detected), the waveform of the GW emitted during the inspiraling phase of a BBH system can be derived from equation (5.7) and gives, along the two polarisation axes mentioned above,

$$\begin{cases} h_+(t) = h(t)\,\dfrac{1+\cos^2\iota}{2}\cos(2\omega(t-D_{\rm L}/c) \\ h_\times(t) = h(t)\,\cos\iota\sin(2\omega(t-D_{\rm L}/c)\,, \end{cases} \tag{5.14}$$

where ι is the viewing angle between the angular momentum of the system and the line of sight from the observer to the source, and ω the orbital frequency of the system.

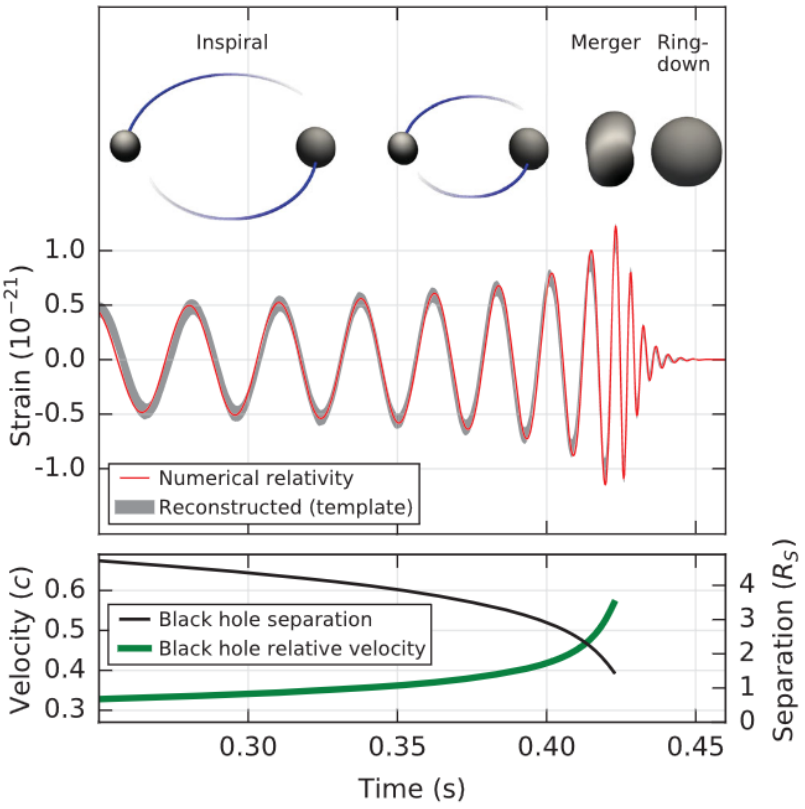

Figure 5.12: Gravitational-wave signal calculated for GW 150914 – the first BBH merger detected with LIGO – as recorded at Hanford. The strain of the signal is defined as in equation (5.8). The bottom panel shows the evolution of the separation and relative velocity between the black holes along the three steps of the merger. *Credit: Abbott et al. (2016)*

These gravitational waves therefore exhibit a quasi-monochromatic signal at a rest-frame time-dependent frequency which is twice that of the orbiting system,

$$\nu_{em}(t) = \frac{1}{\pi}\sqrt{\frac{G(m_1+m_2)}{a(t)^3}}\,, \tag{5.15}$$

and with an amplitude $h(t)$ such that

$$h(t) = \frac{64^{1/3} G^{5/3}}{c^4} \frac{\mathcal{M}_{\rm chirp}^{5/3} \omega(t)^{2/3}}{D_{\rm L}} \,, \tag{5.16}$$

where $\mathcal{M}_{\rm chirp} = (m_1 m_2)^{3/5}/(m_1+m_2)^{1/5}$. In the case of a source emitting at high redshift, the redshift dependence appears not only through the luminosity distance $D_{\rm L}$ but also through its impact on the GW frequency, which is observed with a frequency $\nu_{obs} = \nu_{em}/(1+z)$. This double dependence on redshift makes it difficult to observe gravitational waves emitted at high redshift with current facilities. Moreover, GWs exhibit a mass-redshift degeneracy which, in the absence of complementary electromagnetic data to measure the source redshift, limits mass measurements to the so-called redshifted mass $\mathcal{M}_z = \mathcal{M}(1+z)$. Equation (5.15) also indicates that the frequency of the signal diverges at the time of merger ($a \to 0$): the frequency rapidly increases in the last seconds before the collision (*chirp*[8]). The coalescence regime, and the subsequent relaxation regime (*ringdown*) therefore require a completely different approach and the recourse to numerical-relativity simulations to describe the GW emitted at the time of merger. The shape of the GW signal created by the merger of two black holes and the three steps of the merger (inspiraling, merger and ringdown) are represented in Figure 5.12, along with the evolution of the separation between the two objects.

As the passage of a gravitational wave manifests through contractions and dilations of space, the detection of GWs is based on strain measurements (see equation 5.8). The amplitudes involved are extremely small because of the weakness of the signal: a variation of the size of an atom over a distance of 10^6 km. Such a small variation in distance can only be measured reliably by laser interferometry, using extraordinarily precise, noise-free detectors. Although such an unlikely and precise detection was long thought impossible, at 09:51 UTC on 14 September 2015, the two Laser Interferometer Gravitational-Wave Observatory (LIGO) interferometers, based in Livingston (Louisiana) and Hanford (Washington), detected quasi-simultaneously what was officially confirmed as the first observation of the gravitational signature of the merger of two black holes with masses around $30\,M_\odot$ (GW 151409). Figure 5.13 shows a schematic diagram of the LIGO detectors.

In practice, real waveforms are more complex than those described above and must take into account additional effects, such as tidal forces between compact objects. Precise computation of waveforms during the inspiraling phase can be carried out using post-Newtonian developments around the wave equation presented in equation (5.7), as long as the separation between the two compact objects remains large enough (see e.g., Blanchet, 2014, for a review of these methods). For automatic detections, waveforms banks are constituted for the different regimes (inspiraling, merger and ringdown) and a real-time fitting of the observed signal is carried out using these banks, to trigger a detection if a matching waveform is detected. This method, known as the *matched filtering* technique, allows GWs to be detected on the fly from continuous observations (see e.g. Dal Canton et al., 2014, for more details on matched filtering).

The observed signal is analysed in Fourier space, to allow the direct subtraction of instrumental noise. The detectors are characterized by a sensitivity curve $S_n(f)$, which corresponds to the frequency power spectrum of the overall instrumental noise. For reference, the sensitivity curve of LIGO is represented in the upper-right diagram of Figure 5.13. If it is to be described roughly, data analysis therefore consists of taking the Fourier transform of the signal over well-chosen time series, dividing by the power spectrum of the noise, and analyzing the cleaned signal in the time domain after an inverse Fourier transform.[9] As a result of this process, the signal-to-noise ratio (SNR) of a detection can be expressed as

$$\mathrm{SNR}^2 = \int_0^\infty \mathrm{d}f \frac{4|\tilde{h}(f)|^2}{S_n(f)} \,. \tag{5.17}$$

[8]This name originates from the actual frequency of this phase which is in the acoustic range and with an increase in frequency similar to a bird chirping.

[9]The frequency signal undergoes additional scaling and cleaning processes which are beyond the scope of this manuscript.

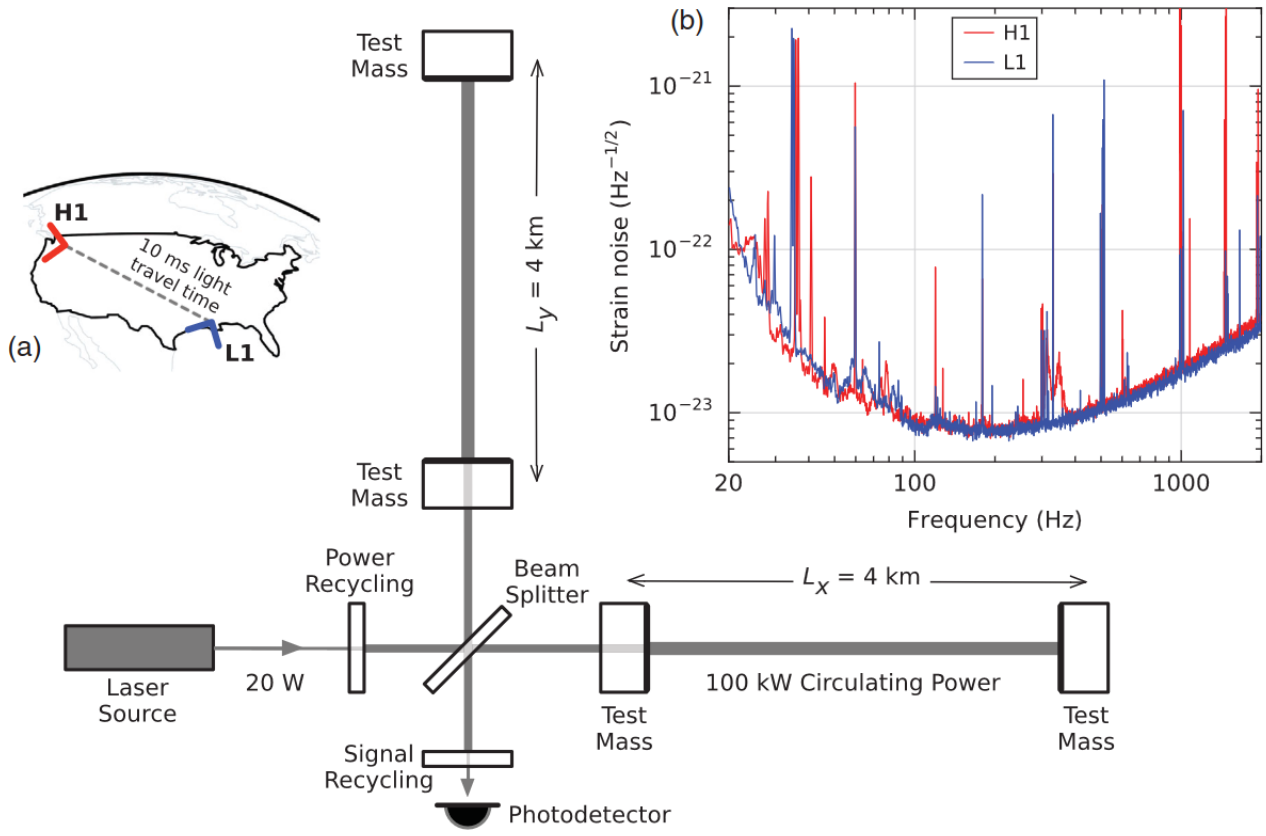

Figure 5.13: Simplified diagram of one of the Advanced LIGO interferometers. A GW propagating in the plane orthogonal to the detector and polarised parallel to one of the arms will dilate the cavity in that given arm and contract the other during the first half of its period, and vice-versa during the second half. The changes in cavity length result in changes in the interference pattern of the laser, which are recorded by the photodetector. The plot on the upper right shows the sensitivities (that is, the noise spectral densities) of the Hanford (H1) and Livingston (L1) detectors as a function of detected frequency. *Credit: Abbott et al. (2016)*

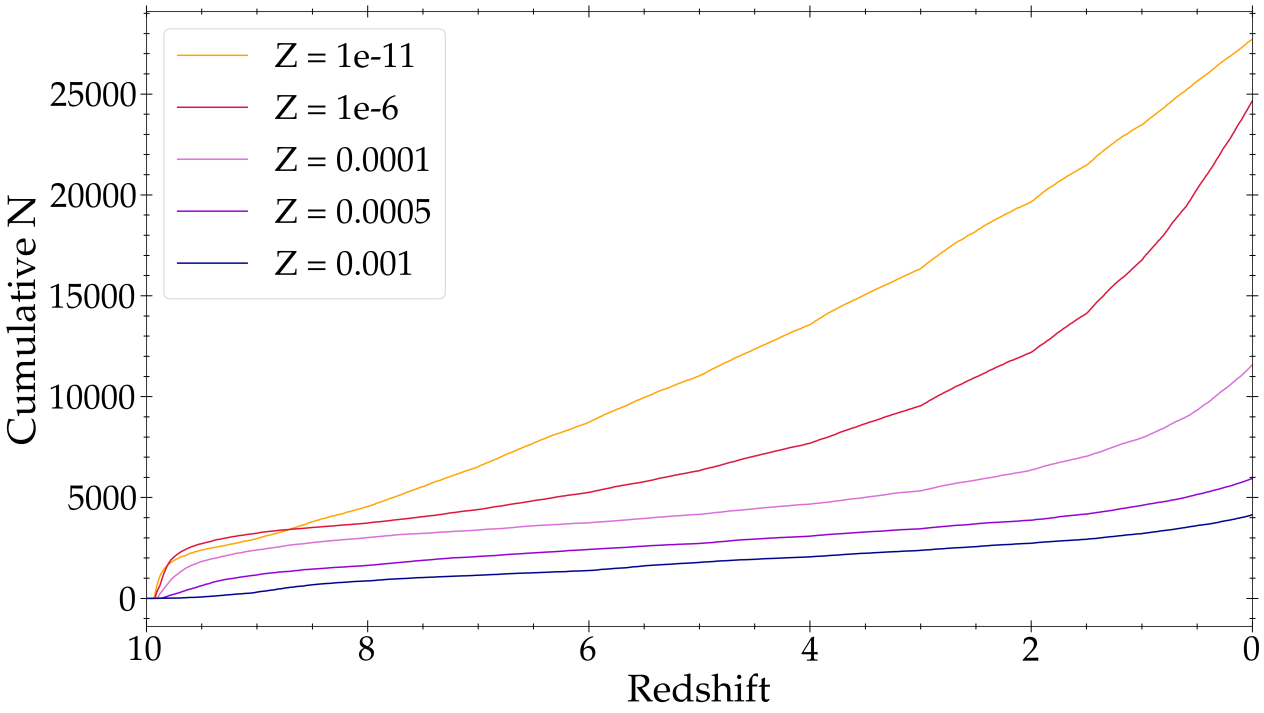

Figure 5.14: Cumulative number of binary black hole mergers as a function of redshift in GALSEVN populations of pure-binary stars (of 1 million pairs each) for different metallicities, as indicated.

A thorough review on GWs and more details about the characteristics and detection of the gravitational signal emitted by merging BBHs can be found e.g. in the works of Maggiore (2007, 2018).

Since September 2015, more than 90 detections of merging compact-object binaries have been realised by the LIGO (USA) – Virgo (Italy) collaboration. New runs have recently been launched with additional interferometers, such as KAGRA (Japan), promising further detections of GWs from different sources. Promising perspectives are also offered by the Einstein Telescope, currently under study by the European Union, which should make it possible to achieve sensitivities an order of magnitude higher than those of Virgo, over a wider range of frequencies. I discuss the capabilities and prospects of these two detectors in more detail in section 5.3.3.

5.3.2 Binary black hole mergers in GALSEVN models of EoR galaxies

The GALSEVN runs that I used in this work follow the evolution of binary stars only up to 200 Myr after the initial burst of star formation. A very low fraction of the BBH systems formed in these models merge in this time interval, which limits their statistical significance. Moreover, if we consider an initial SF burst at a redshift around $z = 10$, this would mean that we focus only on mergers occuring at redshifts higher than 7.7.

We therefore seek to extend the timescale over which we follow BBHs in our stellar population. We can achieve this while keeping the same runs up to 200 Myr as before by estimating, for each BBH, the time at which it will merge.

We follow pure-binary SSPs with a Chabrier (2003) IMF for the five metallicities considered before. For each BBH system formed, we estimate the merger time based on the BH masses, separation (semi-major axis) and eccentricity at the time of formation, according to equation (5.13). We assume that the black hole masses do not change after the BBH has formed, since accretion is no longer possible. For the systems that we actually observe merging within 200 Myr of the SF burst, we check the validity of this approach.

The expected cumulative number of merging BBHs in the GALSEVN models is shown as a function of redshift in Figure 5.14. For the Pop III models, approximately a third of the total BBH population

merges between $z = 10$ and $z = 0$ and contributes to this plot. The number of merging BBHs increases significantly with decreasing metallicity. This results from the less efficient mass loss at such low metallicities, which allows stars to retain more mass, making them larger and less compact, increasing the likelihood of interactions, such as mass-transfer or common-envelope phases, and leading to tighter BBHs able to merge within a Hubble time (e.g., Iorio et al., 2023). The number of mergers initially rises rapidly at high redshift, particularly in Pop III models. This is due to the most massive and tightest binaries very rapidly becoming close BBHs and merging, all within a few Myr. Finally, although the total number of merging BBHs is largest for $Z = 10^{-11}$, it is below that for $Z = 10^{-6}$ during the first Myr. This arises from the larger masses of progenitor stars at $Z = 10^{-11}$, which increase the probability of unstable mass transfer resulting in premature mergers and common envelope configurations, hence reducing the formation of very tight BBHs. The surviving, looser BBHs exhibit longer delay times before merging.

We now focus on the masses of BBHs that merge before $z = 0$ according to Figure 5.14. We show this distribution for black holes forming from the the primary (m_1) and secondary (m_2) stars in Figure 5.15, for the metallicities $Z = 10^{-11}$, $Z = 10^{-6}$, $Z = 0.0001$ and $Z = 0.001$.

Figure 5.15 exhibits two notable features: in each panel, the objects tend to be distributed primarily either along the identity relation, or in the upper-left corner of the diagram. This second, increasingly prominent sequence toward low metallicities, reveals that in systems where the black-hole masses are not similar, the remnant of the secondary star tends to be the most massive. This is primarily due to the inclusion of quasi-homogeneous evolution in the binary-star models, which results in compact, pure-helium secondary stars immediately after the main sequence following Roche-lobe mass transfer from the primary star. These helium stars lead to the formation of more massive black holes, almost as massive as the pure helium stars, than in models without QHE. To illustrate this, we show in Figure 5.16 the analog of Figure 5.15, but for binary-star models not including QHE. The sequence of BBHs with $m_2 > m_1$ is largely absent from these diagrams. At the lowest metallicities, the significantly smaller number of merging BBHs in models without QHE is mainly due to premature mergers before the secondary can form a black hole, and partly to greater mass loss from less compact secondaries, giving rise to neutron stars rather than black holes in SNe. At the highest metallicities, instead, the significantly larger number of BBHs merging by $z = 0$ in models without QHE results from more efficient mass loss leading to less massive secondaries and tighter systems. Hence, the inclusion of QHE in binary-star models can strongly influence the population of early BBHs that are expected to merge within a Hubble time.

5.3.3 Detectability of binary black hole mergers from EoR galaxies

Having highlighted the variety in orbital and mass parameters of BBHs expected to merge between $z = 10$ and now in the GALSEVN models, it is interesting to investigate what fraction of mergers from Pop III precursors could actually be observed by current or near-future GW detectors. I provide in this section an estimate of the percentage of sources from the GALSEVN populations whose signal-to-noise ratio would be sufficiently high to be detected with the upcoming LIGO-Virgo-KAGRA O5 run and with the Einstein Telescope.

Virgo is a laser interferometer, located near Pisa (Italy), composed of two orthogonal arms of 3 km each (similar to the LIGO interferometers schematised in Figure 5.13). The Advanced Virgo program increased its sensitivity by a factor 10 in 2017. Since then, it has gone through several observation campaigns, each preceded by several upgrades, the fifth of which (O5) is scheduled for 2027 with a sensitivity never before achieved. In this study, we consider Virgo as a single detector, without considering that its observations could be coupled with the two LIGO detectors for a better signal-to-noise ratio.

For the Einstein Telescope (ET), we assume the ET-D configuration, composed of three nested triangular detectors with arms of 10 km each (e.g., Hild et al., 2008; Maggiore et al., 2020; Branchesi et al., 2023). For simplicity, we assume the three detectors to be identical and independent.

Furthermore, for simplicity, and given their sensitivities and optimal frequency ranges for detecting merging black holes with masses around $30\,M_\odot$, we focus on these two experiments only, considering

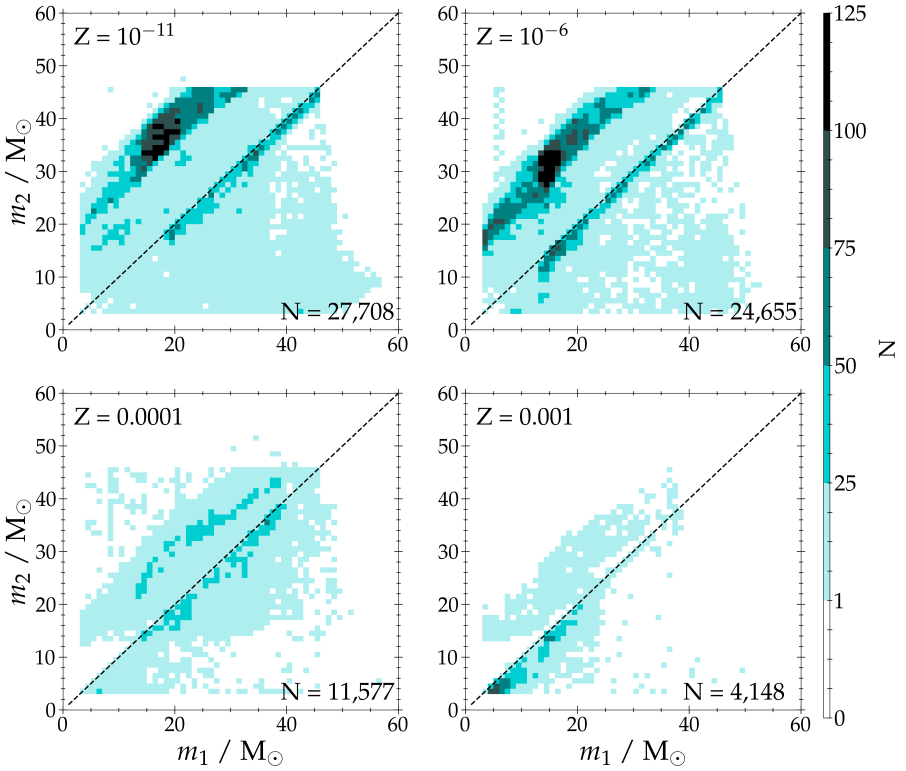

Figure 5.15: Two-dimensional histograms of the masses of black holes in merging BBH systems, for the same GALSEVN models as in Figure 5.14, for the metallicities $Z = 10^{-11}$, $Z = 10^{-6}$, $Z = 0.0001$ and $Z = 0.001$ (in different panels, as indicated). m_1 refers to the BH forming from the primary star, whereas m_2 refers to the remnant of the secondary. The total number of BBH mergers is indicated in the lower-right corner of each panel. The identity relation is shown as a dashed line.

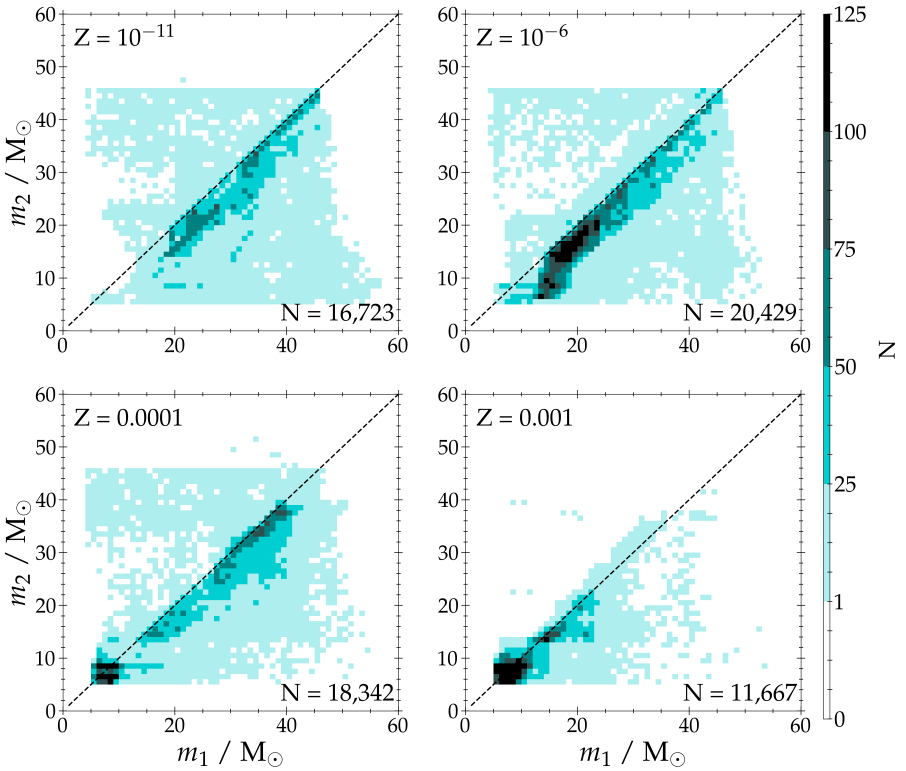

Figure 5.16: Same as Figure 5.15, but for binary-star models not including QHE.

the O5 run for Virgo and the predicted specifications for ET (expected first light in 2036, Branchesi et al., 2023). We use sensitivity curves from recent publications (Abbott et al., 2020; Maggiore et al., 2020).

For this study, we consider the population of BBHs emerging from a stellar population formed during a single burst at $z = 10$, which merge before $z = 0$ (using equation 5.13, as in the previous section, for this selection).

We make the conventional assumption that a merger is detectable if it gives a signal-to-noise ratio greater than 9 for a given detector. We estimate the SNR of an individual signal following the approach outlined by Santoliquido et al. (2023). For each merging BBH, we evaluatee the SNR based on equation (5.17), by computing the amplitude of the GW in the frequency domain, $|\tilde{h}(f)|^2$, using the PYCBC library. Following several recent works (e.g., Dominik et al., 2015; Taylor and Gerosa, 2018; Bouffanais et al., 2019; Chen et al., 2021; Santoliquido et al., 2023), we adopt the phenomenological waveform IMRPHENOMXAS (García-Quirós et al., 2020) for compact binary mergers. We take care of combining all three detectors of ET in the SNR calculation.

To account for the impact of the position of the objects in the sky, we randomly draw the position of each merger, considering isotropically distributed sources. We also randomly sample the inclination angle ι of each system. More details on the exact formulæ implemented in this method, in particular for the different wave polarisations, can be found in section 2.5 of Santoliquido et al. (2023). To avoid any bias resulting from the stochastic sampling of these angles over a relatively small number of sources, we compute the number of detectable sources a hundred times for each population, from which we derive a mean value and standard deviation.

For both Pop III models, corresponding to $Z = 10^{-11}$ and $Z = 10^{-6}$, we obtain very similar results. We find that Virgo-O5 should be able to detect at most a few per cent of the sources in the simulated populations – more precisely, 6.7 ± 1.9 per cent for $Z = 10^{-11}$, and 10.2 ± 2.0 per cent for $Z = 10^{-6}$. The BBH mergers that could be detected by Virgo-O5 occur at low redshift ($z \lesssim 1$), and involve mainly systems with BH masses greater than $20\,\mathrm{M}_\odot$. This is in line with the larger fraction of merging BBHs at low redshift shown in Figure 5.14 for $Z = 10^{-6}$, compared to $Z = 10^{-11}$.

On the other hand, ET-D is predicted to be able to detect 90.2 ± 4.3 per cent of the merging BBHs for $Z = 10^{-11}$, and 90.2 ± 4.0 per cent for $Z = 10^{-6}$. This finding supports the importance of studying the population characteristics of such Pop III predictions, as a substantial amount of observational gravitational-wave constraints may soon be available to put these predictions to the test (e.g., Santoliquido et al., 2024). However, even if most of these objects become detectable in the near future, it will likely remain challenging to conclusively identify them as signatures of Pop III stars.

5.4 Summary of GALSEVN Pop III models

In this chapter, we have used the GALSEVN model, discussed in detail in the previous chapters, to compute the emission properties of extremely metal-poor populations with $Z = 10^{-11}$ and $Z = 10^{-6}$. We compared these to GALSEVN models of metal-poor populations with higher metallicities ($Z = 0.0001$, 0.0005 and 0.001), and to the predictions of Nakajima and Maiolino (2022). We confirm that the emission-line diagrams highlighted by Nakajima and Maiolino (2022) offer accurate diagnostics of ionization by zero-age Pop III stars, with the GALSEVN models providing additional information that these criteria can isolate Pop III stellar populations at ages $\lesssim$ 1 Myr, as shown by Figures 5.3 and 5.4. We also provided predictions for the production efficiency of ionizing photons by these metal-poor stellar population, to investigate their potential role in the reionization of the Universe, as well as simple approximate analytical expressions to relate this quantity directly to age and metallicity. We presented predictions for the production rate of Lyman-Werner photons, which are essential to understand the mechanisms of pristine-gas cooling and early star formation, and for supernova rates, which provide insight into the timescales of chemical enrichment. Finally, we discussed the properties of binary black holes in these GALSEVN models, and the probability of detecting their mergers through gravitational waves, which could prove to be essential counterparts to the difficult direct detection of

Pop III stars.

The main preliminary conclusions of this study in progress can be summarised as follows.

- We confirm that the ultraviolet and optical H and He emission-line diagrams introduced by Nakajima and Maiolino (2022) (Figure 5.3) are effective to discriminate between ionization by very young ($\lesssim$ 1 Myr) Pop III stellar populations and other primordial or later sources (Figure 5.4). We also confirm, as already shown in previous chapters, that the production of ionizing photons after the first million years is dominated by processes originating from binary interactions (Figures 5.1–5.2).

- We find that GALSEVN models of Pop III and metal-poor Pop II stellar populations predict high production efficiencies of ionizing photons. We find high values of $\xi_{\rm ion}^{\rm H\,II}$ relative to standard predictions, in agreement with recent observational studies of galaxies in a wide range of redshifts (Figure 5.5). We also provide analytical expressions to describe the evolution of $\xi_{\rm ion}^{\rm H\,II}$ as a function of age and metallicity, and to relate $\xi_{\rm ion}^{\rm H\,II}$ and $\xi_{\rm ion}^{*}$, the latter being often used in simulations (Figures 5.6–5.8). Comparison of our predictions with recent theoretical and observational work suggests that the escape of only a few per cent of the ionizing photons from nascent galaxies with such properties would be sufficient to reionize the primordial Universe.

- We find production rates of Lyman-Werner photon in agreement with recent simulations (e.g., Incatasciato et al., 2023), which are expected to play a crucial role in the mechanisms and timescales of early star formation (Figure 5.9).

- We analyse the supernova rates and find relatively consistent behaviour across metallicities ranging from 10^{-11} to 0.001. This study allows us to set the onset of chemical enrichment in GALSEVN Pop III stellar populations at approximately 2 Myr.

- We discuss properties of BBHs born from GALSEVN Pop III stellar populations. The expected merger rates and mass properties of such systems depend critically on the inclusion of QHE in the models. Our results suggest that most BBH mergers occurring in such Pop III stellar populations, even at high redshift, should be observable with the Einstein Telescope. This high detectability could make BBH mergers an important complement to direct observations in the characterisation of Pop III stellar populations in the EoR.

Chapter 6

SED fitting using BEAGLE

Contents

The previous chapters presented GALSEVN models with selected sets of parameters, in an attempt to reproduce several spectral features under observational or simulation constraints. This approach, while allowing conclusions to be drawn about the suitability of the models,[1] is somewhat rudimentary when it comes to accurately estimating physical parameters of observed galaxies, especially because of the degeneracies introduced in the spectral features by the large number of adjustable parameters. To accurately estimate the physical conditions in an observed metal-poor star-forming region while accounting for spectral degeneracies, it is therefore necessary to resort to statistical methods to fit the total SED of the star-forming region. To this end, it is necessary to build a model grid covering a wide range of nebular and stellar-population parameters, from which the physical parameters of the observed galaxy can be recovered. This is achievable through Bayesian inference, performed with the BayEsian Analysis of GaLaxy sEds (BEAGLE) tool developed by Chevallard and Charlot (2016). In this chapter, I first present the basics of Bayesian inference (section 6.1.1) and the main features of BEAGLE (section 6.1.2), before focusing in section 6.2 on the production of the GALSEVN model grid that will allow us to interpret *JWST*/NIRSpec observations of high-redshift galaxies with BEAGLE.

6.1 Statistical tools for SED fitting

Fitting the different features present in high-redshift galaxy SED, whether in terms of emission lines or continuum emission, has proved challenging to achieve in a physically-consistent way (e.g., Walcher et al., 2011; Pacifici et al., 2023). The large number of nebular and stellar parameters involved in SPS models, combined with the scarcity and limited quality (at least prior to the advent of *JWST*) of high-redshift spectroscopic data, makes spectral interpretation an intricate problem. In this section, I present some statistical tools which can be used to derive probability distributions of physical parameters from such observed SEDs.

[1] See, e.g., Figure 4.6.

6.1.1 Bayesian inference

Bayesian inference is a statistical method which evaluates the probability of a hypothesis given a set of evidence or information. It is therefore extremely valuable for testing the hypotheses of a physical model, and for giving an estimate of the most probable values of the model parameters, given empirical constraints.

More precisely, Bayesian inference gives access to the probability distribution of a set of model parameters (also called *posterior distribution*) by combining information obtained from a given set of data (through the *likelihood function*) with prior knowledge about these parameters (through the *prior distribution*). It is mathematically based on the Bayes theorem, which states:

$$P(\Theta|D,H) = \frac{P(\Theta|H)\ P(D|\Theta,H)}{P(D|H)} = \frac{P(\Theta|H)\ P(D|\Theta,H)}{\int P(\Theta|H)P(D|\Theta,H)\mathrm{d}\Theta}\,, \tag{6.1}$$

where the different probabilities represented are

- $P(\Theta|D,H)$: the probability distribution of the set of parameters Θ given a model H and observations D (posterior);
- $P(\Theta|H)$: the prior distribution, i.e., theoretical predictions of model H;
- $P(D|\Theta,H)$: the likelihood function, i.e., the ability of model H to fit the observations D for a given set of parameters Θ;
- $P(D|H) = \int P(\Theta|H)P(D|\Theta,H)\mathrm{d}\Theta$: the *evidence*, or the probability without a priori that the data can be generated by model H.

In most cases, the evidence (or marginalisation) integral is very expensive to compute analytically, making it difficult to compute the posterior distribution. However, the development of *Markov Chain Monte Carlo* (MCMC) algorithms made it possible to overcome computational limitations and apply Bayesian inference to increasingly complex models. In practice, given a prior distribution and a likelihood function, MCMC algorithms stochastically explore the parameter space through random walks, constituting a Markov chain which can be constructed so that the equilibrium distribution of the random walk is the posterior probability distribution. This equilibrium distribution is then sampled by the Markov-chain steps, which can be recorded to construct the probability distribution; the greater the number of steps observed, the more this distribution will correspond to the actual probability distribution of the parameters. This method, based on random-walk exploration, allows the algorithm to converge efficiently – and much faster than the classical approach for a large number of free parameters – towards the desired solution.

One of the most widely used algorithms to sample the parameter space and build the posterior distribution is the *Metropolis-Hastings algorithm* (Metropolis et al., 1953; Hastings, 1970). This algorithm consists in a stochastic exploration of the parameter space, in which the parameter values at step $n+1$ of the random walk depend only on those at step n. At each iteration, the algorithm chooses values for step $n+1$, which are then either chosen or discarded according to the probability – that is, the values of the prior and likelihood, through $P(\Theta|H)P(D|\Theta,H)$ – of this point.[2] The Metropolis-Hastings algorithm therefore tends to stay longer in regions of higher probability, intuitively returning samples of points which follow the parameter distribution. Although such algorithms make it possible to explore a high-dimensional multi-parameter space while converging much faster than more basic algorithms generating independent Markov Chains from a given distribution, they suffer from serious limitations. For example, such a process converges to a distribution which may be very different from the initial behaviour of the Markov Chain, creating a "burn-in" period during which samples much be rejected to

[2]To adequately sample regions of low probability, the next point is accepted if its probability is greater than that of the current point, but is not systematically rejected if it is lower. The probability of it being rejected in this case is proportional to the probability ratio between the current and the next points.

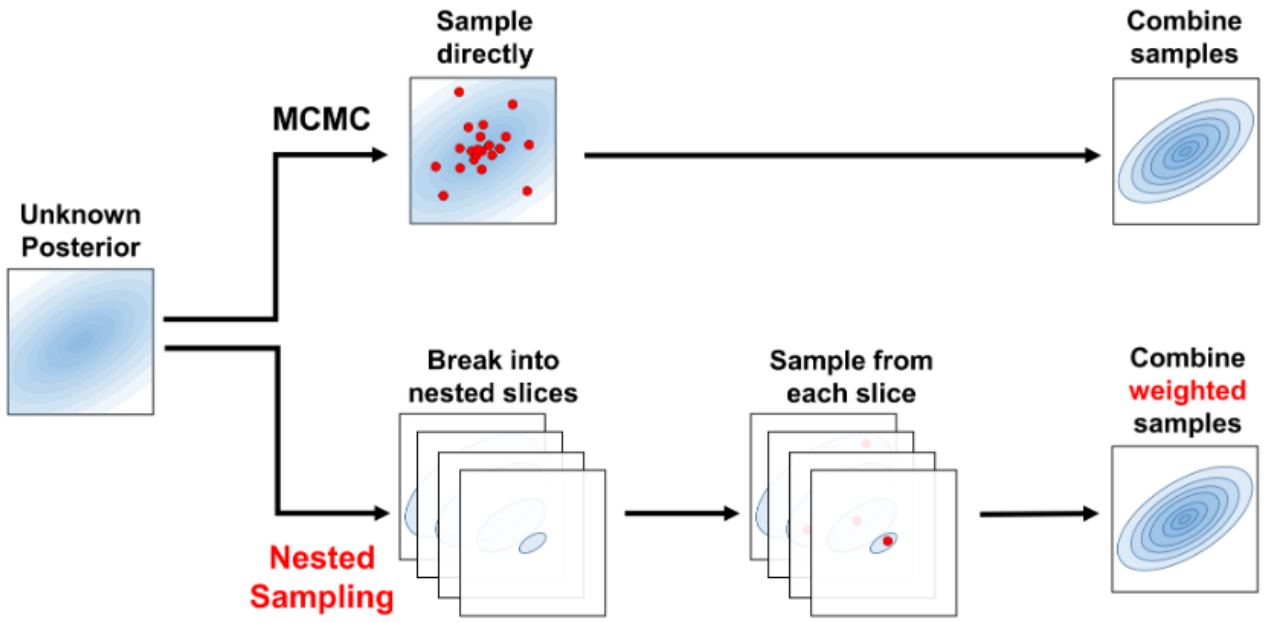

Figure 6.1: Schematic comparison of MCMC and Nested-Sampling algorithms. Whereas MCMC algorithms directly sample the posterior distribution, Nested-Sampling algorithms divide the parameter space into iso-likelihood surfaces, sample each of them and use well-chosen weights to reconstruct the posterior distribution. *Credit: Speagle (2020).*

avoid inducing errors in the final distribution. It also induces correlations between successive samples, which are not independent. This auto-correlation could bias the final distribution. However, they often remain the best choice of algorithm given the complexity and dimensionality of the problems to be solved.

An alternative algorithm called *Nested Sampling* was developed by Skilling (2006) to overcome these limitations. This algorithm is useful to discriminate between two competing models and has therefore been widely used in astrophysics and cosmology. The idea of Nested Sampling is to constrain the posterior probability distribution by drawing iso-likelihood surfaces in parameter space, that is, surfaces composed of every point with a given likelihood. Computations are much easier when restricted to given iso-likelihood surface in parameter space, as integrals become one-dimensional. This is effectively achieved by considering "active points", which are sets of parameters with given likelihoods. At each iteration, the sample with the lowest likelihood is deleted, stored in a set of discarded samples, and replaced by the set of parameters (or point) with the highest likelihood. Increasing the number of iterations therefore exponentially reduces the prior volume, as the set of parameters converges towards the highest-likelihood point. Evidence and posterior distributions can then be computed from the discarded and highest-likelihood points.

Figure 6.1 shows a comparison between MCMC algorithms which directly sample the parameter space, and Nested-Sampling algorithms which reduce the parameter space to iso-likelihood surfaces, sample these surfaces and then reconstruct the probability distributions of the parameters.

6.1.2 BEAGLE how-to

In this work, I use the BEAGLE[3] tool developed by Chevallard and Charlot (2016) to gain a first insight into how well the GALSEVN model can fit observed SEDs of distant galaxies.

BEAGLE is a statistical spectral-analysis tool, which, in its fitting mode, uses Nested Sampling to perform Bayesian inference on an input set of observed data to interpret the observed spectral energy

[3] www.iap.fr/beagle/

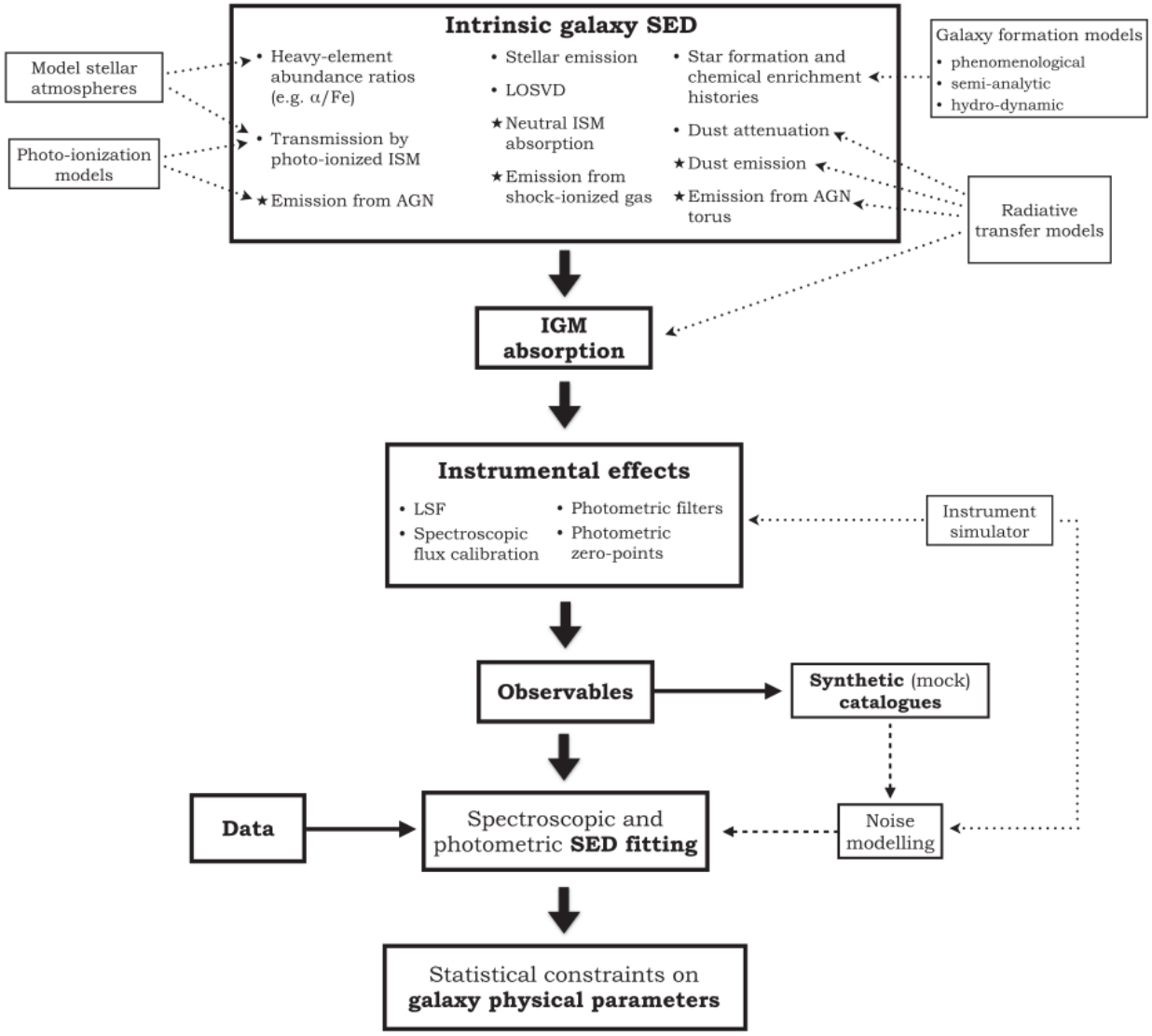

Figure 6.2: Workflow diagram showing the BEAGLE operating system. The different building blocks encompass various astrophysical ingredients. The dotted arrows indicate where external models are required for complementary ingredients. *Credit: Chevallard and Charlot (2016).*

distribution in terms of statistical constraints on physical parameters. BEAGLE also has a mock mode, which can be used to generate catalogues of galaxy SEDs from a collection of input physical parameters.

BEAGLE is a highly modular tool, allowing constraints to be derived not only on model stellar and ISM parameters, but also on redshift and the predicted strengths of spectral features. Its flexibility allows the contributions of a wide variety of phenomena to be explored, such as attenuation by dust, contribution to the emission by an AGN, kinematics along the line of sight and instrumental biases, while self-consistently treating stellar and nebular emission thanks to the incorporation of the GALSEVN model. A number of versatile modules also allow SPS models to be combined with complex star-formation and chemical-enrichment histories.

The Bayesian approach adopted in BEAGLE is based on the MULTINEST Nested-Sampling tool (Feroz et al., 2009). This algorithm allows correlations between model parameters to be taken into account, while rigorously estimating uncertainties and propagating observational errors. Figure 6.2 provides a summary of all the building blocks involved in fitting galaxy SEDs, which is the main focus of this work. The top block represents the main ingredients of galaxy modelling, where the dotted arrows show where the use of external models is needed. This diagram then shows how the light emerging from the mock galaxy is transmitted through the ISM and subjected to instrumental effects, before being submitted to statistical regression to interpret the observational data.

BEAGLE allows the user to define the different model parameters as free – in which case they will be sampled directly from the prior, fixed at given standard values, or dependent – in which case they are estimated from the values of other parameters to which they are physically linked. The different adjustable parameters are summarized in table 2 of Chevallard and Charlot (2016). These parameters can be related to:

- flexible arbitrary star-formation histories: duration and delay between star-formation episodes, mass formed during a given episode, etc.;
- chemical enrichment histories: metallicity, α-to-Fe abundance ratio, metallicity of a given set of stars, chemical enrichment timescale, etc.;
- redshifts of formation or observation of the galaxy;
- optical properties of the dust, distribution in different ISM components and galaxy orientation to characterize dust attenuation;
- galactic morphology and amount of stars in the disc and bulge;
- nebular parameters described in chapter 3;
- kinematics for stellar and nebular emission and interstellar absorption.

The IMF chosen for the stellar population can be adjusted by providing different sets of SPS-generated spectra for the stellar emission.

In this work, I focus mainly on quantities related to star formation and nebular emission, which I explore in more detail in the next section. The most probable values and posterior probability density functions computed by BEAGLE for these quantities will be output by BEAGLE. This output is organised in FITS files with multiple extensions containing information about the different physical modules. The detailed structure of the BEAGLE output files can be found in the user manual, at www.iap.fr/beagle/.

6.2 Spectral analysis of primeval galaxies with BEAGLE

6.2.1 Model grid

To fit galaxy SEDs without a priori knowledge of their physical properties, it is necessary to construct a model grid which spans as wide a range of parameters as possible.

We build such a grid by sampling the parameters over the ranges presented in Table 6.1.

The stellar and gas-phase metallicities are taken to be equal in this first grid, but may be set to be different. Future calculations may explore this possibility to mimic super-solar ratios of α to iron-peak elements in young star-forming regions, as was done in section 3.1.3.

The C/O and N/O abundance ratios are set independently, which represents an improvement over the more restrictive approach of Gutkin et al. (2016). After each alteration, the abundances and depletions of all elements are rescaled to maintain a fixed gas-phase metallicity, following Gutkin et al. (2016).

All the models in this first grid have a Chabrier (2003) IMF. This choice will later be completed with additional models for different IMFs.

The CLOUDY calculations of the models in this grid assume ionization-bounded H II regions in closed, spherical geometry, and the fraction of escaping Lyman-continuum photons is set to zero ($f_{\rm esc} = 0$).

We compute the spectral evolution of individual star clusters (SSPs), which will be convolved by BEAGLE to compute the evolution of galaxies with any star formation history.

Table 6.1: Grid parameters and the ranges they span.

Parameter	Range	Description
$Z_{\rm ISM}$	[0.0001, 0.0005, 0.001, 0.002, 0.004, 0.006, 0.008, 0.01, 0.014, 0.017, 0.02, 0.03, 0.04]	Gas-phase metallicity
Z_*	[0.0001, 0.0005, 0.001, 0.002, 0.004, 0.006, 0.008, 0.01, 0.014, 0.017, 0.02, 0.03, 0.04]	Stellar metallicity
$n_{\rm H}$	[10, 100, 1000, 10,000] cm^{-3}	Hydrogen density
C/O	[0.04, 0.17, 0.44, 1.41]	Carbon-to-oxygen abundance ratio
N/O	[0.006, 0.022, 0.071, 0.316, 1.000]	Nitrogen-to-oxygen abundance ratio[a]
$\log\langle U\rangle$	[−3.5, −3.0, −2.5, −2.0, −1.5, −1.0, −0.5]	Volume-averaged ionization parameter at age $t' = 0$
$\xi_{\rm d}$	[0.1, 0.3, 0.5]	Dust-to-metal mass ratio

[a]For reference, Gutkin et al. (2016) adopt $(\mathrm{N/O})_\odot = 0.071$.

We also choose to run this grid using the latest C23.01 version of CLOUDY (Chatzikos et al., 2023; Gunasekera et al., 2023), which includes updated atomic and molecular data, notably for H- and He-collisional rates and several chemical-reaction rates, compared to the C17.00 version used in chapters 2–5. This latest version also fixes a coding error which affected Lyα optical-depth calculations in dusty environments, especially at high ionization parameters. This version change has allowed us to improve the code management and the amount of information retained for spectral analysis thanks to a major rewrite of the interface for producing BEAGLE-compatible files compared to Gutkin et al. (2016).

6.2.2 BEAGLE fitting of *JWST*/NIRSpec spectra of distant galaxies

The content of this section represents ongoing research and is currently under development.

Chapter 7

Conclusions and perspectives

In this thesis, I have used the novel code GALSEVN, which combines the population-synthesis code SEVN (Iorio et al., 2023) with the spectral-evolution code GALAXEV (Bruzual and Charlot, 2003), to explore the emission properties of young metal-poor star-forming galaxies. I coupled these spectral-synthesis predictions with the photoionization code CLOUDY (Ferland et al., 2017) to compute in a self-consistent way the global spectral energy distribution out of the H II regions ionized by the light emitted by stars, accretion discs of X-ray binaries, and wind- and supernova-driven radiative shocks in such galaxies. I paid particular attention to reproducing the challenging high-ionization ultraviolet and optical emission lines observed in local galaxies with properties similar to those of primeval galaxies. As expected from previous work (e.g., Eldridge and Stanway, 2012; Eldridge et al., 2017; Götberg et al., 2020), I confirmed that modelling the interactions between stars in binary systems, and more precisely of their mass transfers, has a significant impact on the hardness of the radiation field produced by these stellar populations, and therefore on the intensity of the highest-energy emission lines arising from their surrounding ionized region. I also found that the challenging He II λ4686/Hβ ratio and Hβ equivalent width observed in local analogues of primeval galaxies were remarkably well reproduced by GALSEVN SSP models at metallicities of a few per cent of solar, at all ages between 3 and 10 Myr – after which we stop photoionization computations due to the disruption of star-forming clouds. Such good agreement had never been achieved with stellar emission only from previous single- and binary-star models.

I then explored the GALSEVN parameter space, to investigate the agreement with emission lines arising from ionized metals (e.g., carbon and oxygen) and with the most extreme observed values of high-ionization spectral features. In addition to adjusting metallicity and nebular parameters to match the observed properties of these galaxies, I investigated the effect of changing the formation history and initial mass function of the modelled stellar population. This study notably highlighted that the inclusion of bursty SFHs, such as those predicted by the SPHINX simulation (Rosdahl et al., 2022), could broaden the agreement with most observations in our sample of local analogues of primeval galaxies, and should be encouraged when interpreting spectroscopic data. I also found that some of the most extreme high-ionization spectral features, such as the He II λ1640 equivalent width, can be accounted for by populations dominated by very massive stars – that is, with an IMF which is more top-heavy than the standard Chabrier (2003) IMF.

I also complemented the stellar predictions of GALSEVN with self-consistent approaches to model other processes at work in metal-poor star-forming regions, which could produce large amounts of ionizing photons, namely accretion onto X-ray-binary discs and radiation from fast radiative shocks due to winds and supernovæ. I carefully calibrated the prescription for the emission arising from accretion discs of XRBs, computed from GALSEVN-population predictions, to agree with the average luminosity function of X-ray binaries per unit star formation rate in local metal-poor star-forming galaxies. I also combined GALSEVN predictions of energy injection rates from stellar winds and different types of

supernovæ(PISN, type-II and type-Ia) with the radiative-shock models of Alarie and Morisset (2019) to obtain accurate and self-consistent computations of their contribution to nebular emission lines. Both of these prescriptions revealed that XRBs and radiative shocks are unlikely to contribute significantly to the H- and He II-line emission from young, metal-poor star-forming galaxies. I examined claims of recent studies that XRB accretion discs may contribute significantly to this emission (e.g., Schaerer et al., 2019; Umeda et al., 2022; Katz et al., 2023), only to find that such predictions are based on prescriptions which overestimate the ratio of X-ray luminosity to star-formation rate compared to local observations.

Based on this successful interpretation of the observed properties of local analogues of primeval galaxies, I applied a similar approach to predict the properties of Reionization-Era galaxies, and more precisely the population-III stellar populations ($Z = 10^{-11}$ and $Z = 10^{-6}$) they may have contained. I first focused on investigating the agreement between GALSEVN predictions and the diagnostic diagrams introduced by Nakajima and Maiolino (2022) to separate the signatures of ionization by Pop III stars from those of other sources, and found that these diagrams were indeed good indicators of the emission from very young ($\lesssim 1$ Myr) Pop III stellar populations. I also found that the ionizing power of metal-poor populations computed using GALSEVN (considering stars with metallicities up to $Z = 0.001$), traced by the ionizing-photon production efficiency $\xi_{\rm ion}$, is such that the escape of only a few per cent of ionizing photons would be sufficient, in light of recent theoretical and observational studies, to reionize the early Universe. I then explored and presented various properties of these populations, such as their production rate of Lyman-Werner photons – which is a key element for understanding early star formation in low-mass haloes – and their supernova rates, distinguishing between different SN types, to follow the chemical enrichment of their surrounding medium. Finally, I focused on predictions concerning the detectability of the gravitational-wave counterparts to direct observations of such populations, which mainly arises from mergers of binary black holes. The results of this study highlight the importance of constraining the properties of such systems in Pop III stellar populations, as most of them should be detectable with the forthcoming Einstein Telescope.

After this extensive study of GALSEVN predictions for widely different stellar populations with a broad range of parameters and modelling choices, I finally aimed to enable a more generic approach to accurately interpreting spectroscopic data with the GALSEVN model. To this end, it is necessary to resort to statistical methods such as Bayesian Inference to fit the combined SEDs of observed star-forming regions and interpret this fit in terms of physical parameters; such statistical regression can be performed using the BEAGLE tool (Chevallard and Charlot, 2016). Bayesian Inference requires the construction of an extensive model grid with varied parameters, which I finally presented for the GALSEVN model.

This Bayesian approach using BEAGLE should enable more in-depth interpretation of the spectra of high-redshift galaxies, as a growing amount of spectroscopic data are being collected by increasingly powerful instruments such as those on board the *JWST*. This approach will allow constraints to be derived from a much broader range of spectral features than the few investigated in this thesis. Spectral interpretation of the galaxies with the more extreme properties will provide a better understanding of the emergence of star formation at Cosmic Dawn, and invaluable insight into the physical conditions of the early Universe at the time of Reionization.

The wide variety of observables predicted by GALSEVN will also, when combined with simulations of galaxy formation, make it possible to interpret the statistics of gravitational-wave detections in terms of population properties, providing the keys to appealing multi-messenger detections of early stellar populations. This prospect paves the way for exciting future explorations using the next generation of astronomical facilities.

Appendix A

Chemical abundances and depletions

This appendix summarises the chemical abundances and depletion coefficients adopted in this work. All values are adopted from the work of Gutkin et al. (2016).

Table A.1 presents the abundances of the 30 lightest elements by number relative to hydrogen, for $Z_{\rm ISM} = {\rm Z}_{\odot}$ and $\xi_{\rm d} = \xi_{{\rm d}\odot} = 0.36$. For non-solar metallicities, these depletions are rescaled linearly with $Z_{\rm ISM}$ for all metals except carbon and nitrogen, which require specific prescriptions, as described in Gutkin et al. (2016, see also Groves et al. 2004 for the formula adopted for nitrogen scaling). Carbon abundance is rescaled based on the C/O parameter described in section 2.3.2. Finally, the helium abundance by mass is scaled based on the prescription from Bressan et al. (2012).

Gutkin et al. (2016) adopt the default ISM depletion factors of CLOUDY for most elements, with updates from Groves et al. (2004), notably for C, Na, Al, Si, Cl, Ca and Ni. They apply an additional rescaling of the O depletion factor, based on a comparison between models and SDSS observations. These depletion factors correspond to $\xi_{{\rm d}\odot} = 0.36$. Depletion factors for other dust-to-metal mass ratios are interpolated linearly as a function of $\xi_{\rm d}$ with the boundary conditions that they be equal to 0 and 1 for $\xi_{\rm d} = 0$ and 1, respectively.

Table A.2 presents the values of $12 + \log({\rm O/H})_{\rm gas}$ corresponding to the different model gas-phase metallicities represented in the spectral diagrams of chapters 2–4.

Table A.1: Interstellar abundances and depletions adopted for the photoionization calculations, as presented in section 2.2. These values are presented for $Z_{\rm ISM} = {\rm Z}_{\odot}$ and $\xi_{\rm d} = \xi_{{\rm d}\odot} = 0.36$.

Element	$\log(n_i/n_{\rm H})$	$(1 - f^i_{\rm dpl})$
He	− 1.01	1
Li	− 10.99	0.16
Be	− 10.63	0.6
B	− 9.47	0.13
C	− 3.53	0.5
N	− 4.32	1
O	− 3.17	0.7
F	− 7.47	0.3
Ne	− 4.01	1
Na	− 5.70	0.25
Mg	− 4.45	0.2
Al	− 5.56	0.02
Si	− 4.48	0.1
P	− 6.57	0.25
S	− 4.87	1
Cl	− 6.53	0.5
Ar	− 5.63	1
K	− 6.92	0.3
Ca	− 5.67	0.003
Sc	− 8.86	0.005
Ti	− 7.01	0.008
V	− 8.03	0.006
Cr	− 6.36	0.006
Mn	− 6.64	0.05
Fe	− 4.51	0.01
Co	− 7.11	0.01
Ni	− 5.78	0.04
Cu	− 7.82	0.1
Zn	− 7.43	0.25

Table A.2: Oxygen abundances corresponding to the different gas-phase metallicities $Z_{\rm ISM}$ of the models presented in chapter 2, for the standard $\xi_{\rm d} = 0.3$ value adopted in this work.

Z	$12 + \log({\rm O/H})$	$12 + \log({\rm O/H})_{\rm gas}$
0.0001	6.64	6.53
0.0005	7.34	7.23
0.001	7.64	7.53
0.002	7.94	7.83
0.004	8.24	8.14
0.006	8.42	8.31
0.008	8.55	8.44
0.010	8.65	8.54
0.014	8.80	8.69
0.01524 ($\rm Z_{\odot}$)	8.83	8.71
0.017	8.88	8.77
0.020	8.96	8.85
0.030	9.14	9.03
0.040	9.28	9.16

Bibliography

B. P. Abbott et al. Observation of Gravitational Waves from a Binary Black Hole Merger. *Phys. Rev. Let.*, 116(6):061102, February 2016. doi: 10.1103/PhysRevLett.116.061102.

B. P. Abbott et al. Prospects for observing and localizing gravitational-wave transients with advanced ligo, advanced virgo and kagra. *Living Reviews in Relativity*, 23(1):3, Sep 2020. ISSN 1433-8351. doi: 10.1007/s41114-020-00026-9.

B. Agarwal et al. Ubiquitous seeding of supermassive black holes by direct collapse. *MNRAS* , 425(4): 2854–2871, October 2012. doi: 10.1111/j.1365-2966.2012.21651.x.

A. Alarie and C. Morisset. Extensive Online Shock Model Database. *Revista Mexicana de Astronomía y Astrofísica*, 55:377–394, October 2019. doi: 10.22201/ia.01851101p.2019.55.02.21.

M. G. Allen, B. A. Groves, M. A. Dopita, R. S. Sutherland, and L. J. Kewley. The MAPPINGS III Library of Fast Radiative Shock Models. *Ap. J. Suppl.* , 178(1):20–55, September 2008. doi: 10.1086/589652.

L. Amati et al. The THESEUS space mission concept: science case, design and expected performances. *Advances in Space Research*, 62(1):191–244, July 2018. doi: 10.1016/j.asr.2018.03.010.

R. Amorín et al. Analogues of primeval galaxies two billion years after the Big Bang. *Nature Astronomy*, 1:0052, March 2017. doi: 10.1038/s41550-017-0052.

D. Arnett. *Supernovae and Nucleosynthesis: An Investigation of the History of Matter from the Big Bang to the Present*. 1996.

H. Atek et al. Most of the photons that reionized the Universe came from dwarf galaxies. *Nature*, 626 (8001):975–978, February 2024. doi: 10.1038/s41586-024-07043-6.

G. Auger and E. Plagnol. *An Overview of Gravitational Waves : Theory, Sources and Detection*. 2017. doi: 10.1142/10082.

M. Bachetti et al. An ultraluminous X-ray source powered by an accreting neutron star. *Nature*, 514 (7521):202–204, October 2014. doi: 10.1038/nature13791.

S. Baek, B. Semelin, P. Di Matteo, Y. Revaz, and F. Combes. Reionization by UV or X-ray sources. *Astron. Astrophys.* , 523:A4, November 2010. doi: 10.1051/0004-6361/201014347.

J. A. Baldwin, M. M. Phillips, and R. Terlevich. Classification parameters for the emission-line spectra of extragalactic objects. *Pub. Astron. Soc. Pac.* , 93:5–19, February 1981. doi: 10.1086/130766.

C. S. Beals. On the nature of Wolf-Rayet emission. *MNRAS* , 90:202–212, December 1929. doi: 10.1093/mnras/90.2.202.

R. S. Beckmann et al. Dense gas formation and destruction in a simulated Perseus-like galaxy cluster with spin-driven black hole feedback. *Astron. Astrophys.* , 631:A60, November 2019. doi: 10.1051/0004-6361/201936188.

M. C. Begelman. Super-Eddington Fluxes from Thin Accretion Disks? *Ap. J. Lett.* , 568(2):L97–L100, April 2002. doi: 10.1086/340457.

M. C. Begelman, A. R. King, and J. E. Pringle. The nature of SS433 and the ultraluminous X-ray sources. *MNRAS* , 370(1):399–404, July 2006a. doi: 10.1111/j.1365-2966.2006.10469.x.

M. C. Begelman, M. Volonteri, and M. J. Rees. Formation of supermassive black holes by direct collapse in pre-galactic haloes. *MNRAS* , 370(1):289–298, July 2006b. doi: 10.1111/j.1365-2966.2006.10467.x.

K. Belczynski, D. E. Holz, T. Bulik, and R. O'Shaughnessy. The first gravitational-wave source from the isolated evolution of two stars in the 40-100 solar mass range. *Nature*, 534(7608):512–515, June 2016. doi: 10.1038/nature18322.

D. A. Berg, E. D. Skillman, R. B. C. Henry, D. K. Erb, and L. Carigi. Carbon and Oxygen Abundances in Low Metallicity Dwarf Galaxies. *Ap. J.* , 827(2):126, August 2016. doi: 10.3847/0004-637X/827/2/126.

D. A. Berg, D. K. Erb, M. W. Auger, M. Pettini, and G. B. Brammer. A Window on the Earliest Star Formation: Extreme Photoionization Conditions of a High-ionization, Low-metallicity Lensed Galaxy at z $\sim$ 2*. *Ap. J.* , 859(2):164, June 2018. doi: 10.3847/1538-4357/aab7fa.

D. A. Berg, D. K. Erb, R. B. C. Henry, E. D. Skillman, and K. B. W. McQuinn. The Chemical Evolution of Carbon, Nitrogen, and Oxygen in Metal-poor Dwarf Galaxies. *Ap. J.* , 874(1):93, March 2019. doi: 10.3847/1538-4357/ab020a.

D. A. Berg et al. The COS Legacy Archive Spectroscopy Survey (CLASSY) Treasury Atlas. *Ap. J. Suppl.* , 261(2):31, August 2022. doi: 10.3847/1538-4365/ac6c03.

L. Blanchet. Gravitational Radiation from Post-Newtonian Sources and Inspiralling Compact Binaries. *Living Reviews in Relativity*, 17(1):2, December 2014. doi: 10.12942/lrr-2014-2.

T. C. N. Boekholt et al. Formation of massive seed black holes via collisions and accretion. *MNRAS* , 476(1):366–380, May 2018. doi: 10.1093/mnras/sty208.

H. Bondi and F. Hoyle. On the mechanism of accretion by stars. *MNRAS* , 104:273, January 1944. doi: 10.1093/mnras/104.5.273.

Y. Bouffanais et al. Constraining the Fraction of Binary Black Holes Formed in Isolation and Young Star Clusters with Gravitational-wave Data. *Ap. J.* , 886(1):25, November 2019. doi: 10.3847/1538-4357/ab4a79.

R. J. Bouwens et al. Reionization After Planck: The Derived Growth of the Cosmic Ionizing Emissivity Now Matches the Growth of the Galaxy UV Luminosity Density. *Ap. J.* , 811(2):140, October 2015. doi: 10.1088/0004-637X/811/2/140.

R. J. Bouwens et al. The Lyman-Continuum Photon Production Efficiency ξ_{ion} of z $\sim$ 4-5 Galaxies from IRAC-based Hα Measurements: Implications for the Escape Fraction and Cosmic Reionization. *Ap. J.* , 831(2):176, November 2016. doi: 10.3847/0004-637X/831/2/176.

M. Branchesi et al. Science with the Einstein Telescope: a comparison of different designs. *JCAP*, 2023(7):068, July 2023. doi: 10.1088/1475-7516/2023/07/068.

A. Bressan et al. PARSEC: stellar tracks and isochrones with the PAdova and TRieste Stellar Evolution Code. *MNRAS* , 427(1):127–145, November 2012. doi: 10.1111/j.1365-2966.2012.21948.x.

V. Bromm. The first stars and galaxies - Basic principles. *Asociacion Argentina de Astronomia La Plata Argentina Book Series*, 4:3, January 2013. doi: 10.48550/arXiv.1203.3824.

V. Bromm, R. P. Kudritzki, and A. Loeb. Generic Spectrum and Ionization Efficiency of a Heavy Initial Mass Function for the First Stars. *Ap. J.* , 552(2):464–472, May 2001. doi: 10.1086/320549.

M. Brorby, P. Kaaret, and A. Prestwich. X-ray binary formation in low-metallicity blue compact dwarf galaxies. *MNRAS* , 441(3):2346–2353, July 2014. doi: 10.1093/mnras/stu736.

M. Brorby, P. Kaaret, A. Prestwich, and I. F. Mirabel. Enhanced X-ray emission from Lyman break analogues and a possible L_X-SFR-metallicity plane. *MNRAS* , 457(4):4081–4088, April 2016. doi: 10.1093/mnras/stw284.

G. Bruzual and S. Charlot. Stellar population synthesis at the resolution of 2003. *MNRAS* , 344: 1000–1028, October 2003. doi: 10.1046/j.1365-8711.2003.06897.x.

N. Byler et al. Stellar and Nebular Diagnostics in the Ultraviolet for Star-forming Galaxies. *Ap. J.* , 863(1):14, August 2018. doi: 10.3847/1538-4357/aacd50.

D. Calzetti. The Dust Opacity of Star-forming Galaxies. *Pub. Astron. Soc. Pac.* , 113(790):1449–1485, December 2001. doi: 10.1086/324269.

A. G. W. Cameron and M. Mock. Stellar Accretion and X-ray Emission. *Nature*, 215(5100):464–466, July 1967. doi: 10.1038/215464a0.

A. J. Cameron, H. Katz, and M. P. Rey. A novel approach to correcting T_e-based mass-metallicity relations. *MNRAS* , 522(1):L89–L94, June 2023a. doi: 10.1093/mnrasl/slad046.

A. J. Cameron et al. JADES: Probing interstellar medium conditions at $z \sim 5.5 - 9.5$ with ultra-deep JWST/NIRSpec spectroscopy. *arXiv e-prints*, art. arXiv:2302.04298, February 2023b. doi: 10.48550/arXiv.2302.04298.

A. C. Carnall. SpectRes: A Fast Spectral Resampling Tool in Python. *arXiv e-prints*, art. arXiv:1705.05165, May 2017. doi: 10.48550/arXiv.1705.05165.

S. Carniani et al. Ionised outflows in z ~2.4 quasar host galaxies. *Astron. Astrophys.* , 580:A102, August 2015. doi: 10.1051/0004-6361/201526557.

G. Chabrier. Galactic Stellar and Substellar Initial Mass Function. *Pub. Astron. Soc. Pac.* , 115(809): 763–795, July 2003. doi: 10.1086/376392.

S. Charlot and G. Bruzual. Stellar Population Synthesis Revisited. *Ap. J.* , 367:126, January 1991. doi: 10.1086/169608.

S. Charlot and S. M. Fall. A Simple Model for the Absorption of Starlight by Dust in Galaxies. *Ap. J.* , 539:718–731, August 2000. doi: 10.1086/309250.

S. Charlot and M. Longhetti. Nebular emission from star-forming galaxies. *MNRAS* , 323:887–903, May 2001. doi: 10.1046/j.1365-8711.2001.04260.x.

M. Chatzikos et al. The 2023 Release of Cloudy. *Revista Mexicana de Astronomía y Astrofísica*, 59: 327–343, October 2023. doi: 10.22201/ia.01851101p.2023.59.02.12.

H.-Y. Chen et al. Distance measures in gravitational-wave astrophysics and cosmology. *Classical and Quantum Gravity*, 38(5):055010, March 2021. doi: 10.1088/1361-6382/abd594.

W. Chen, C. R. Shrader, and M. Livio. The Properties of X-Ray and Optical Light Curves of X-Ray Novae. *Ap. J.* , 491(1):312–338, December 1997. doi: 10.1086/304921.

Y. Chen et al. PARSEC evolutionary tracks of massive stars up to 350 $M_\odot$ at metallicities $0.0001 \leq Z \leq 0.04$. *MNRAS* , 452(1):1068–1080, September 2015. doi: 10.1093/mnras/stv1281.

J. Chevallard and S. Charlot. Modelling and interpreting spectral energy distributions of galaxies with BEAGLE. *MNRAS* , 462(2):1415–1443, October 2016. doi: 10.1093/mnras/stw1756.

J. Chevallard et al. Physical properties and H-ionizing-photon production rates of extreme nearby star-forming regions. *MNRAS* , 479(3):3264–3273, September 2018. doi: 10.1093/mnras/sty1461.

J. Chisholm et al. Do galaxies that leak ionizing photons have extreme outflows? *Astron. Astrophys.* , 605:A67, September 2017. doi: 10.1051/0004-6361/201730610.

B. Ciardi and P. Madau. Probing beyond the Epoch of Hydrogen Reionization with 21 Centimeter Radiation. *Ap. J.* , 596(1):1–8, October 2003. doi: 10.1086/377634.

A. Cohen, A. Fialkov, R. Barkana, and M. Lotem. Charting the parameter space of the global 21-cm signal. *MNRAS* , 472(2):1915–1931, December 2017. doi: 10.1093/mnras/stx2065.

C. Conroy and J. E. Gunn. The Propagation of Uncertainties in Stellar Population Synthesis Modeling. III. Model Calibration, Comparison, and Evaluation. *Ap. J.* , 712(2):833–857, April 2010. doi: 10.1088/0004-637X/712/2/833.

C. Conroy, J. E. Gunn, and M. White. The Propagation of Uncertainties in Stellar Population Synthesis Modeling. I. The Relevance of Uncertain Aspects of Stellar Evolution and the Initial Mass Function to the Derived Physical Properties of Galaxies. *Ap. J.* , 699(1):486–506, July 2009. doi: 10.1088/0004-637X/699/1/486.

G. Costa et al. Mixing by overshooting and rotation in intermediate-mass stars. *MNRAS* , 485(4): 4641–4657, Jun 2019. doi: 10.1093/mnras/stz728.

G. Costa et al. Formation of GW190521 from stellar evolution: the impact of the hydrogen-rich envelope, dredge-up, and $^{12}C(\alpha, \gamma)^{16}O$ rate on the pair-instability black hole mass gap. *MNRAS* , 501(3):4514–4533, March 2021. doi: 10.1093/mnras/staa3916.

G. Costa et al. Massive binary black holes from Population II and III stars. *arXiv e-prints*, art. arXiv:2303.15511, March 2023. doi: 10.48550/arXiv.2303.15511.

P. A. Crowther et al. The R136 star cluster dissected with Hubble Space Telescope/STIS. I. Far-ultraviolet spectroscopic census and the origin of He II λ1640 in young star clusters. *MNRAS* , 458 (1):624–659, May 2016. doi: 10.1093/mnras/stw273.

F. Cullen et al. The NIRVANDELS Survey: a robust detection of α-enhancement in star-forming galaxies at z $\simeq$ 3.4. *MNRAS* , 505(1):903–920, July 2021. doi: 10.1093/mnras/stab1340.

E. Curtis-Lake et al. Spectroscopic confirmation of four metal-poor galaxies at z = 10.3-13.2. *Nature Astronomy*, 7:622–632, May 2023. doi: 10.1038/s41550-023-01918-w.

E. da Cunha, S. Charlot, and D. Elbaz. A simple model to interpret the ultraviolet, optical and infrared emission from galaxies. *MNRAS* , 388(4):1595–1617, August 2008. doi: 10.1111/j.1365-2966.2008.13535.x.

R. L. da Silva, M. Fumagalli, and M. Krumholz. SLUG—Stochastically Lighting Up Galaxies. I. Methods and Validating Tests. *Ap. J.* , 745(2):145, February 2012. doi: 10.1088/0004-637X/745/2/145.

R. L. da Silva, M. Fumagalli, and M. R. Krumholz. SLUG - Stochastically Lighting Up Galaxies - II. Quantifying the effects of stochasticity on star formation rate indicators. *MNRAS* , 444(4): 3275–3287, November 2014. doi: 10.1093/mnras/stu1688.

T. Dal Canton et al. Implementing a search for aligned-spin neutron star-black hole systems with advanced ground based gravitational wave detectors. *Phys. Rev. D*, 90:082004, Oct 2014. doi: 10.1103/PhysRevD.90.082004.

A. De Cia et al. Dust-depletion sequences in damped Lyman-α absorbers. A unified picture from low-metallicity systems to the Galaxy. *Astron. Astrophys.* , 596:A97, December 2016. doi: 10.1051/0004-6361/201527895.

F. D'Eugenio et al. JADES: Carbon enrichment 350 Myr after the Big Bang in a gas-rich galaxy. *arXiv e-prints*, art. arXiv:2311.09908, November 2023. doi: 10.48550/arXiv.2311.09908.

A. I. Diaz, M. A. Prieto, and W. Wamsteker. The optical and UV spectrum of the Seyfert type 2 galaxy NGC 3393. *Astron. Astrophys.* , 195:53–59, April 1988.

M. Dominik et al. Double Compact Objects III: Gravitational-wave Detection Rates. *Ap. J.* , 806(2): 263, June 2015. doi: 10.1088/0004-637X/806/2/263.

M. A. Dopita and R. S. Sutherland. Spectral Signatures of Fast Shocks. I. Low-Density Model Grid. *Ap. J. Suppl.* , 102:161, January 1996. doi: 10.1086/192255.

O. L. Dors, M. V. Cardaci, G. F. Hägele, and Â. C. Krabbe. Metallicity evolution of AGNs from UV emission lines based on a new index. *MNRAS* , 443(2):1291–1300, September 2014. doi: 10.1093/mnras/stu1218.

V. M. Douna, L. J. Pellizza, I. F. Mirabel, and S. E. Pedrosa. Metallicity dependence of high-mass X-ray binary populations. *Astron. Astrophys.* , 579:A44, July 2015. doi: 10.1051/0004-6361/201525617.

A. Doussot and B. Semelin. A bubble size distribution model for the Epoch of Reionization. *Astron. Astrophys.* , 667:A118, November 2022. doi: 10.1051/0004-6361/202244108.

B. T. Draine. Interstellar Dust Grains. *Annu.Rev.Astron.Astrophys.*, 41:241–289, January 2003. doi: 10.1146/annurev.astro.41.011802.094840.

B. T. Draine. On Radiation Pressure in Static, Dusty H II Regions. *Ap. J.* , 732(2):100, May 2011a. doi: 10.1088/0004-637X/732/2/100.

B. T. Draine and C. F. McKee. Theory of interstellar shocks. *Annu.Rev.Astron.Astrophys.*, 31:373–432, January 1993. doi: 10.1146/annurev.aa.31.090193.002105.

B. T. Draine. *Physics of the Interstellar and Intergalactic Medium*. 2011b.

L. M. Dray. On the metallicity dependence of high-mass X-ray binaries. *MNRAS* , 370(4):2079–2090, August 2006. doi: 10.1111/j.1365-2966.2006.10635.x.

P. P. Eggleton. The evolution of low mass stars. *MNRAS* , 151:351, January 1971. doi: 10.1093/mnras/151.3.351.

A. Einstein. Die Feldgleichungen der Gravitation. *Sitzungsberichte der Königlich Preussischen Akademie der Wissenschaften*, pages 844–847, January 1915.

A. Einstein. Die Grundlage der allgemeinen Relativitätstheorie. *Annalen der Physik*, 354(7):769–822, January 1916. doi: 10.1002/andp.19163540702.

A. Einstein. Über Gravitationswellen. *Sitzungsberichte der Königlich Preussischen Akademie der Wissenschaften*, pages 154–167, January 1918.

S. Ekström et al. Grids of stellar models with rotation. I. Models from 0.8 to 120 $M_{\odot}$ at solar metallicity (Z = 0.014). *Astron. Astrophys.* , 537:A146, January 2012. doi: 10.1051/0004-6361/201117751.

J. J. Eldridge and E. R. Stanway. The effect of stellar evolution uncertainties on the rest-frame ultraviolet stellar lines of C IV and He II in high-redshift Lyman-break galaxies. *MNRAS* , 419(1): 479–489, January 2012. doi: 10.1111/j.1365-2966.2011.19713.x.

J. J. Eldridge, R. G. Izzard, and C. A. Tout. The effect of massive binaries on stellar populations and supernova progenitors. *MNRAS* , 384(3):1109–1118, March 2008. doi: 10.1111/j.1365-2966.2007.12738.x.

J. J. Eldridge, N. Langer, and C. A. Tout. Runaway stars as progenitors of supernovae and gamma-ray bursts. *MNRAS* , 414(4):3501–3520, July 2011. doi: 10.1111/j.1365-2966.2011.18650.x.

J. J. Eldridge et al. Binary Population and Spectral Synthesis Version 2.1: Construction, Observational Verification, and New Results. *Publications of the Astronomical Society of Australia*, 34:e058, November 2017. doi: 10.1017/pasa.2017.51.

J. J. Eldridge and E. R. Stanway. Spectral population synthesis including massive binaries. *MNRAS* , 400(2):1019–1028, December 2009. doi: 10.1111/j.1365-2966.2009.15514.x.

D. K. Erb et al. Physical Conditions in a Young, Unreddened, Low-metallicity Galaxy at High Redshift. *Ap. J.* , 719(2):1168–1190, August 2010. doi: 10.1088/0004-637X/719/2/1168.

J. Faulkner, D. N. C. Lin, and J. Papaloizou. On the evolution of accretion disc flow in cataclysmic variables- I.The prospect of a limit cycle in dwarf nova systems. *MNRAS* , 205:359–375, October 1983. doi: 10.1093/mnras/205.2.359.

A. Feltre, S. Charlot, and J. Gutkin. Nuclear activity versus star formation: emission-line diagnostics at ultraviolet and optical wavelengths. *MNRAS* , 456(3):3354–3374, March 2016. doi: 10.1093/mnras/stv2794.

G. J. Ferland et al. The 2013 Release of Cloudy. *Revista Mexicana de Astronomía y Astrofísica*, 49: 137–163, April 2013. doi: 10.48550/arXiv.1302.4485.

G. J. Ferland et al. The 2017 Release Cloudy. *Revista Mexicana de Astronomía y Astrofísica*, 53: 385–438, October 2017. doi: 10.48550/arXiv.1705.10877.

F. Feroz, M. P. Hobson, and M. Bridges. MULTINEST: an efficient and robust Bayesian inference tool for cosmology and particle physics. *MNRAS* , 398(4):1601–1614, October 2009. doi: 10.1111/j.1365-2966.2009.14548.x.

S. L. Finkelstein et al. Conditions for Reionizing the Universe with a Low Galaxy Ionizing Photon Escape Fraction. *Ap. J.* , 879(1):36, July 2019. doi: 10.3847/1538-4357/ab1ea8.

R. A. E. Fosbury et al. Massive Star Formation in a Gravitationally Lensed H II Galaxy at z = 3.357. *Ap. J.* , 596(2):797–809, October 2003. doi: 10.1086/378228.

T. Fragos et al. X-Ray Binary Evolution Across Cosmic Time. *Ap. J.* , 764(1):41, February 2013. doi: 10.1088/0004-637X/764/1/41.

T. Fragos et al. POSYDON: A General-purpose Population Synthesis Code with Detailed Binary-evolution Simulations. *Ap. J. Suppl.* , 264(2):45, February 2023. doi: 10.3847/1538-4365/ac90c1.

J. Frank, A. King, and D. J. Raine. *Accretion Power in Astrophysics: Third Edition*. 2002.

C. L. Fryer et al. Compact Remnant Mass Function: Dependence on the Explosion Mechanism and Metallicity. *Ap. J.* , 749:91, April 2012. doi: 10.1088/0004-637X/749/1/91.

F. Fürst et al. X-ray variation statistics and wind clumping in Vela X-1. *Astron. Astrophys.* , 519: A37, September 2010. doi: 10.1051/0004-6361/200913981.

M. Garcia, A. Herrero, F. Najarro, D. J. Lennon, and M. Alejandro Urbaneja. Winds of Low-metallicity OB-type Stars: HST-COS Spectroscopy in IC 1613. *Ap. J.* , 788(1):64, June 2014. doi: 10.1088/0004-637X/788/1/64.

C. García-Quirós et al. Multimode frequency-domain model for the gravitational wave signal from nonprecessing black-hole binaries. *Phys. Rev. D* , 102(6):064002, September 2020. doi: 10.1103/PhysRevD.102.064002.

C. Georgy et al. Grids of stellar models with rotation. III. Models from 0.8 to 120 $M_\odot$ at a metallicity Z = 0.002. *Astron. Astrophys.* , 558:A103, October 2013. doi: 10.1051/0004-6361/201322178.

N. Giacobbo and M. Mapelli. The impact of electron-capture supernovae on merging double neutron stars. *MNRAS* , 482(2):2234–2243, January 2019. doi: 10.1093/mnras/sty2848.

N. Giacobbo and M. Mapelli. Revising Natal Kick Prescriptions in Population Synthesis Simulations. *Ap. J.* , 891(2):141, March 2020. doi: 10.3847/1538-4357/ab7335.

M. Gierliński, C. Done, and K. Page. Reprocessing of X-rays in the outer accretion disc of the black hole binary XTE J1817-330. *MNRAS* , 392(3):1106–1114, January 2009. doi: 10.1111/j.1365-2966.2008.14166.x.

S. Goswami et al. Impact of very massive stars on the chemical evolution of extremely metal-poor galaxies. *Astron. Astrophys.* , 663:A1, July 2022. doi: 10.1051/0004-6361/202142031.

Y. Götberg et al. Spectral models for binary products: Unifying subdwarfs and Wolf-Rayet stars as a sequence of stripped-envelope stars. *Astron. Astrophys.* , 615:A78, July 2018. doi: 10.1051/0004-6361/201732274.

Y. Götberg et al. Contribution from stars stripped in binaries to cosmic reionization of hydrogen and helium. *Astron. Astrophys.* , 634:A134, February 2020. doi: 10.1051/0004-6361/201936669.

G. Gräfener, S. P. Owocki, L. Grassitelli, and N. Langer. On the optically thick winds of Wolf-Rayet stars. *Astron. Astrophys.* , 608:A34, December 2017. doi: 10.1051/0004-6361/201731590.

P. C. Gregory and J. J. Condon. The 87GB Catalog of Radio Sources Covering 0 degrees $<$ delta $<$ +75 degrees at 4.85 GHz. *Ap. J. Suppl.* , 75:1011, April 1991. doi: 10.1086/191559.

T. H. Greif, S. C. O. Glover, V. Bromm, and R. S. Klessen. The First Galaxies: Chemical Enrichment, Mixing, and Star Formation. *Ap. J.* , 716(1):510–520, June 2010. doi: 10.1088/0004-637X/716/1/510.

H.-J. Grimm. *X-ray binaries in the Milky Way and other galaxies*. PhD thesis, Ludwig-Maximilians University of Munich, Germany, January 2003.

B. A. Groves, M. A. Dopita, and R. S. Sutherland. Dusty, Radiation Pressure-Dominated Photoionization. II. Multiwavelength Emission Line Diagnostics for Narrow-Line Regions. *Ap. J. Suppl.* , 153 (1):75–91, July 2004. doi: 10.1086/421114.

C. M. Gunasekera, P. A. M. van Hoof, M. Chatzikos, and G. J. Ferland. The 23.01 Release of Cloudy. *Research Notes of the American Astronomical Society*, 7(11):246, November 2023. doi: 10.3847/2515-5172/ad0e75.

J. Gutkin, S. Charlot, and G. Bruzual. Modelling the nebular emission from primeval to present-day star-forming galaxies. *MNRAS* , 462(2):1757–1774, October 2016. doi: 10.1093/mnras/stw1716.

Z. Haiman, T. Abel, and M. J. Rees. The Radiative Feedback of the First Cosmological Objects. *Ap. J.* , 534(1):11–24, May 2000. doi: 10.1086/308723.

R. Hainich et al. PoWR grids of non-LTE model atmospheres for OB-type stars of various metallicities. *Astron. Astrophys.* , 621:A85, January 2019. doi: 10.1051/0004-6361/201833787.

W. R. Hamann and G. Gräfener. Grids of model spectra for WN stars, ready for use. *Astron. Astrophys.* , 427:697–704, November 2004. doi: 10.1051/0004-6361:20040506.

J. M. Hameury. A review of the disc instability model for dwarf novae, soft X-ray transients and related objects. *Advances in Space Research*, 66(5):1004–1024, September 2020. doi: 10.1016/j.asr.2019.10.022.

J. M. Hameury and J. P. Lasota. Models of ultraluminous X-ray transient sources. *Astron. Astrophys.* , 643:A171, November 2020. doi: 10.1051/0004-6361/202038857.

T. Hashimoto et al. The onset of star formation 250 million years after the Big Bang. *Nature*, 557: 392–395, 2018. doi: 10.1038/s41586-018-0117-z.

S. Hassan et al. Constraining the contribution of active galactic nuclei to reionization. *Monthly Notices of the Royal Astronomical Society*, 473(1):227–240, 08 2017. ISSN 0035-8711. doi: 10.1093/mnras/stx2194.

W. K. Hastings. Monte Carlo Sampling Methods using Markov Chains and their Applications. *Biometrika*, 57(1):97–109, April 1970. doi: 10.1093/biomet/57.1.97.

T. M. Heckman and T. A. Thompson. Galactic Winds and the Role Played by Massive Stars. In A. W. Alsabti and P. Murdin, editors, *Handbook of Supernovae*, page 2431. 2017. doi: 10.1007/978-3-319-21846-5_23.

A. Heger and S. E. Woosley. The Nucleosynthetic Signature of Population III. *Ap. J.* , 567(1):532–543, March 2002. doi: 10.1086/338487.

P. Hertz et al. X-Ray Variability of Scorpius X-1 during a Multiwavelength Campaign. *Ap. J.* , 396: 201, September 1992. doi: 10.1086/171710.

S. Hild, S. Chelkowski, and A. Freise. Pushing towards the ET sensitivity using 'conventional' technology. *arXiv e-prints*, art. arXiv:0810.0604, October 2008. doi: 10.48550/arXiv.0810.0604.

D. J. Hillier and T. Lanz. CMFGEN: A non-LTE Line-Blanketed Radiative Transfer Code for Modeling Hot Stars with Stellar Winds. In G. Ferland and D. W. Savin, editors, *Spectroscopic Challenges of Photoionized Plasmas*, volume 247 of *Astronomical Society of the Pacific Conference Series*, page 343, January 2001.

G. Hobbs, D. R. Lorimer, A. G. Lyne, and M. Kramer. A statistical study of 233 pulsar proper motions. *MNRAS* , 360(3):974–992, July 2005. doi: 10.1111/j.1365-2966.2005.09087.x.

T. Hsyu, R. J. Cooke, J. X. Prochaska, and M. Bolte. The PHLEK Survey: A New Determination of the Primordial Helium Abundance. *Ap. J.* , 896(1):77, June 2020. doi: 10.3847/1538-4357/ab91af.

E. Hubble. A relation between distance and radial velocity among extra-galactic nebulae. *Proceedings of the National Academy of Sciences*, 15(3):168–173, 1929. doi: 10.1073/pnas.15.3.168.

J. R. Hurley, C. A. Tout, and O. R. Pols. Evolution of binary stars and the effect of tides on binary populations. *MNRAS* , 329(4):897–928, February 2002. doi: 10.1046/j.1365-8711.2002.05038.x.

R. I. Hynes et al. The remarkable rapid X-ray, ultraviolet, optical and infrared variability in the black hole XTE J1118+480. *MNRAS* , 345(1):292–310, October 2003. doi: 10.1046/j.1365-8711.2003.06938.x.

I. T. Iliev et al. Cosmological radiative transfer comparison project - II. The radiation-hydrodynamic tests. *MNRAS* , 400(3):1283–1316, December 2009. doi: 10.1111/j.1365-2966.2009.15558.x.

K. Inayoshi, E. Visbal, and Z. Haiman. The Assembly of the First Massive Black Holes. *Annu.Rev.Astron.Astrophys.*, 58:27–97, August 2020. doi: 10.1146/annurev-astro-120419-014455.

A. Incatasciato, S. Khochfar, and J. Oñorbe. Modelling the cosmological Lyman-Werner background radiation field in the early Universe. *MNRAS* , 522(1):330–349, June 2023. doi: 10.1093/mnras/stad1008.

A. K. Inoue. Rest-frame ultraviolet-to-optical spectral characteristics of extremely metal-poor and metal-free galaxies. *MNRAS* , 415(3):2920–2931, August 2011. doi: 10.1111/j.1365-2966.2011.18906.x.

A. K. Inoue, I. Shimizu, I. Iwata, and M. Tanaka. An updated analytic model for attenuation by the intergalactic medium. *MNRAS* , 442(2):1805–1820, August 2014. doi: 10.1093/mnras/stu936.

G. Iorio et al. Compact object mergers: exploring uncertainties from stellar and binary evolution with SEVN. *MNRAS* , 524(1):426–470, September 2023. doi: 10.1093/mnras/stad1630.

Y. I. Izotov and T. X. Thuan. Deep Hubble Space Telescope ACS Observations of I Zw 18: a Young Galaxy in Formation. *Ap. J.* , 616(2):768–782, December 2004. doi: 10.1086/424990.

Y. I. Izotov, T. X. Thuan, and G. Privon. The detection of [Ne V] emission in five blue compact dwarf galaxies. *MNRAS* , 427(2):1229–1237, December 2012. doi: 10.1111/j.1365-2966.2012.22051.x.

Y. I. Izotov et al. Eight per cent leakage of Lyman continuum photons from a compact, star-forming dwarf galaxy. *Nature*, 529(7585):178–180, January 2016a. doi: 10.1038/nature16456.

Y. I. Izotov et al. Detection of high Lyman continuum leakage from four low-redshift compact star-forming galaxies. *MNRAS* , 461(4):3683–3701, October 2016b. doi: 10.1093/mnras/stw1205.

Y. I. Izotov, N. G. Guseva, K. J. Fricke, C. Henkel, and D. Schaerer. The efficiency of ionizing photon production and the radiation energy balance in compact star-forming galaxies. *MNRAS* , 467:4118–4130, January 2017a. doi: 10.1093/mnras/stx347.

Y. I. Izotov, T. X. Thuan, and N. G. Guseva. LBT observations of compact star-forming galaxies with extremely high [O III]/[O II] flux ratios: He I emission-line ratios as diagnostics of Lyman continuum leakage. *MNRAS* , 471(1):548–561, October 2017b. doi: 10.1093/mnras/stx1629.

Y. I. Izotov et al. J1154+2443: a low-redshift compact star-forming galaxy with a 46 per cent leakage of Lyman continuum photons. *MNRAS* , 474(4):4514–4527, March 2018a. doi: 10.1093/mnras/stx3115.

Y. I. Izotov et al. Low-redshift Lyman continuum leaking galaxies with high [O III]/[O II] ratios. *MNRAS* , 478(4):4851–4865, August 2018b. doi: 10.1093/mnras/sty1378.

Y. I. Izotov et al. Abundances of CNO elements in z 0.3-0.4 Lyman continuum leaking galaxies. *MNRAS* , 522(1):1228–1246, June 2023. doi: 10.1093/mnras/stad1036.

A. E. Jaskot and M. S. Oey. The Origin and Optical Depth of Ionizing Radiation in the "Green Pea" Galaxies. *Ap. J.* , 766(2):91, April 2013. doi: 10.1088/0004-637X/766/2/91.

V. Kalogera and R. F. Webbink. Formation of Low-Mass X-Ray Binaries. II. Common Envelope Evolution of Primordial Binaries with Extreme Mass Ratios. *Ap. J.* , 493(1):351–367, January 1998. doi: 10.1086/305085.

H. Katz et al. First insights into the ISM at z $>$ 8 with JWST: possible physical implications of a high [O III] λ4363/[O III] λ5007. *MNRAS* , 518(1):592–603, January 2023. doi: 10.1093/mnras/stac2657.

G. Kauffmann et al. The host galaxies of active galactic nuclei. *MNRAS* , 346(4):1055–1077, December 2003. doi: 10.1111/j.1365-2966.2003.07154.x.

A. A. Kaurov, D. Hooper, and N. Y. Gnedin. The effects of dark matter annihilation on cosmic reionization. *Ap. J.* , 833(2):162, dec 2016. doi: 10.3847/1538-4357/833/2/162.

C. Kehrig, M. A. Guerrero, J. M. Vílchez, and G. Ramos-Larios. On the Contribution of the X-Ray Source to the Extended Nebular He II Emission in IZW18. *Ap. J. Lett.* , 908(2):L54, February 2021. doi: 10.3847/2041-8213/abe41b.

J. Kennicutt, R. C. Star Formation in Galaxies Along the Hubble Sequence. *Annu.Rev.Astron.Astrophys.*, 36:189–232, January 1998. doi: 10.1146/annurev.astro.36.1.189.

R. C. Kennicutt and N. J. Evans. Star Formation in the Milky Way and Nearby Galaxies. *Annu.Rev.Astron.Astrophys.*, 50:531–608, September 2012. doi: 10.1146/annurev-astro-081811-125610.

L. J. Kewley and M. A. Dopita. Using Strong Lines to Estimate Abundances in Extragalactic H II Regions and Starburst Galaxies. *Ap. J. Suppl.* , 142(1):35–52, September 2002. doi: 10.1086/341326.

L. J. Kewley, M. A. Dopita, R. S. Sutherland, C. A. Heisler, and J. Trevena. Theoretical Modeling of Starburst Galaxies. *Ap. J.* , 556(1):121–140, July 2001. doi: 10.1086/321545.

R. Kippenhahn, A. Weigert, and A. Weiss. *Stellar Structure and Evolution*. 2013. doi: 10.1007/978-3-642-30304-3.

T. Kitayama and N. Yoshida. Supernova Explosions in the Early Universe: Evolution of Radiative Remnants and the Halo Destruction Efficiency. *Ap. J.* , 630(2):675–688, September 2005. doi: 10.1086/432114.

R. S. Klessen and S. C. Glover. The first stars: Formation, properties, and impact. *Annual Review of Astronomy and Astrophysics*, 61(1):65–130, 2023. doi: 10.1146/annurev-astro-071221-053453.

T. Kojima et al. EMPRESS. II. Highly Fe-enriched Metal-poor Galaxies with $\sim$1.0 $(\mathrm{Fe/O})_{\odot}$ and 0.02 $(\mathrm{O/H})_{\odot}$: Possible Traces of Supermassive ($>$300 $\mathrm{M}_{\odot}$) Stars in Early Galaxies. *Ap. J.* , 913(1):22, May 2021. doi: 10.3847/1538-4357/abec3d.

S. B. Kraemer, C.-C. Wu, D. M. Crenshaw, and J. P. Harrington. IUE Spectra and Photoionization Models of the Seyfert 2 Galaxies NGC 7674 and I ZW 92. *Ap. J.* , 435:171, November 1994. doi: 10.1086/174803.

P. Kroupa. On the variation of the initial mass function. *MNRAS* , 322(2):231–246, April 2001. doi: 10.1046/j.1365-8711.2001.04022.x.

A. Lapi et al. The Coevolution of Supermassive Black Holes and Massive Galaxies at High Redshift. *Ap. J.* , 782(2):69, February 2014. doi: 10.1088/0004-637X/782/2/69.

N. Laporte et al. Probing cosmic dawn: Ages and star formation histories of candidate z $\geq$ 9 galaxies. *MNRAS* , 505(3):3336–3346, August 2021. doi: 10.1093/mnras/stab1239.

J. P. Lasota. The disc instability model of dwarf novae and low-mass X-ray binary transients. *New Astronomy Reviews*, 45(7):449–508, June 2001. doi: 10.1016/S1387-6473(01)00112-9.

M. Lecroq et al. Nebular emission from young stellar populations including binary stars. *MNRAS* , 527(3):9480–9504, January 2024. doi: 10.1093/mnras/stad3838.

B. D. Lehmer et al. X-Ray Binary Luminosity Function Scaling Relations for Local Galaxies Based on Subgalactic Modeling. *Ap. J. Suppl.* , 243(1):3, July 2019. doi: 10.3847/1538-4365/ab22a8.

C. Leitherer and T. M. Heckman. Synthetic Properties of Starburst Galaxies. *Ap. J. Suppl.* , 96:9, January 1995. doi: 10.1086/192112.

C. Leitherer, C. Robert, and L. Drissen. Deposition of Mass, Momentum, and Energy by Massive Stars into the Interstellar Medium. *Ap. J.* , 401:596, December 1992. doi: 10.1086/172089.

C. Leitherer et al. Starburst99: Synthesis Models for Galaxies with Active Star Formation. *Ap. J. Suppl.* , 123(1):3–40, July 1999. doi: 10.1086/313233.

C. Leitherer et al. The Effects of Stellar Rotation. II. A Comprehensive Set of Starburst99 Models. *Ap. J. Suppl.* , 212(1):14, May 2014. doi: 10.1088/0067-0049/212/1/14.

T. Lejeune and D. Schaerer. Database of Geneva stellar evolution tracks and isochrones for $(\mathrm{UBV})_J(\mathrm{RI})_C$ JHKLL'M, HST-WFPC2, Geneva and Washington photometric systems. *Astron. Astrophys.* , 366:538–546, February 2001. doi: 10.1051/0004-6361:20000214.

G. Lemaître. Un Univers homogène de masse constante et de rayon croissant rendant compte de la vitesse radiale des nébuleuses extra-galactiques. *Annales de la Société Scientifique de Bruxelles*, 47: 49–59, January 1927.

J. S. W. Lewis et al. The short ionizing photon mean free path at z = 6 in Cosmic Dawn III, a new fully coupled radiation-hydrodynamical simulation of the Epoch of Reionization. *MNRAS* , 516(3): 3389–3397, November 2022. doi: 10.1093/mnras/stac2383.

L.-X. Li. Accretion, growth of supermassive black holes, and feedback in galaxy mergers. *MNRAS* , 424(2):1461–1470, August 2012. doi: 10.1111/j.1365-2966.2012.21336.x.

E. López-Navas, N. Degenaar, A. S. Parikh, J. V. Hernández Santisteban, and J. van den Eijnden. The connection between the UV/optical and X-ray emission in the neutron star low-mass X-ray binary Aql X-1. *MNRAS* , 493(1):940–951, March 2020. doi: 10.1093/mnras/staa275.

X. Ma et al. The difficulty of getting high escape fractions of ionizing photons from high-redshift galaxies: a view from the FIRE cosmological simulations. *MNRAS* , 453(1):960–975, October 2015. doi: 10.1093/mnras/stv1679.

S. J. Maddox, W. J. Sutherland, G. Efstathiou, and J. Loveday. The APM galaxy survey - I. APM measurements and star-galaxy separation. *MNRAS* , 243:692–712, April 1990.

M. Maggiore. *Gravitational Waves: Volume 1: Theory and Experiments*. Oxford University Press, 10 2007. ISBN 9780198570745. doi: 10.1093/acprof:oso/9780198570745.001.0001.

M. Maggiore. *Gravitational Waves: Volume 2: Astrophysics and Cosmology*. Oxford University Press, 03 2018. ISBN 9780198570899. doi: 10.1093/oso/9780198570899.001.0001.

M. Maggiore et al. Science case for the Einstein telescope. *JCAP*, 2020(3):050, March 2020. doi: 10.1088/1475-7516/2020/03/050.

M. Mapelli, L. Zampieri, E. Ripamonti, and A. Bressan. Dynamics of stellar black holes in young star clusters with different metallicities - I. Implications for X-ray binaries. *MNRAS* , 429(3):2298–2314, March 2013. doi: 10.1093/mnras/sts500.

M. Mapelli et al. Impact of the Rotation and Compactness of Progenitors on the Mass of Black Holes. *Ap. J.* , 888(2):76, January 2020. doi: 10.3847/1538-4357/ab584d.

P. Marigo, L. Girardi, C. Chiosi, and P. R. Wood. Zero-metallicity stars. I. Evolution at constant mass. *Astron. Astrophys.* , 371:152–173, May 2001. doi: 10.1051/0004-6361:20010309.

R. G. Martin, C. Nixon, P. J. Armitage, S. H. Lubow, and D. J. Price. Giant Outbursts in Be/X-Ray Binaries. *Ap. J. Lett.* , 790(2):L34, August 2014. doi: 10.1088/2041-8205/790/2/L34.

J. Matthee et al. The production and escape of Lyman-Continuum radiation from star-forming galaxies at z $\sim$ 2 and their redshift evolution. *MNRAS* , 465(3):3637–3655, March 2017. doi: 10.1093/mnras/stw2973.

C. F. McKee and E. C. Ostriker. Theory of Star Formation. *Annu.Rev.Astron.Astrophys.*, 45(1): 565–687, September 2007. doi: 10.1146/annurev.astro.45.051806.110602.

R. H. Mebane, J. Mirocha, and S. R. Furlanetto. The Persistence of Population III Star Formation. *MNRAS* , 479(4):4544–4559, October 2018. doi: 10.1093/mnras/sty1833.

G. Mellema, I. T. Iliev, U.-L. Pen, and P. R. Shapiro. Simulating cosmic reionization at large scales - II. The 21-cm emission features and statistical signals. *MNRAS* , 372(2):679–692, October 2006. doi: 10.1111/j.1365-2966.2006.10919.x.

R. Meriot and B. Semelin. The LORELI database: 21 cm signal inference with 3D radiative hydrodynamics simulations. *Astron. Astrophys.* , 683:A24, March 2024. doi: 10.1051/0004-6361/202347591.

A. Mesinger, S. Furlanetto, and R. Cen. 21CMFAST: a fast, seminumerical simulation of the high-redshift 21-cm signal. *MNRAS* , 411(2):955–972, February 2011. doi: 10.1111/j.1365-2966.2010.17731.x.

N. Metropolis, A. W. Rosenbluth, M. N. Rosenbluth, A. H. Teller, and E. Teller. Equation of State Calculations by Fast Computing Machines. *The Journal of Chemical Physics*, 21(6):1087, June 1953. doi: 10.1063/1.1699114.

G. R. Meurer, T. M. Heckman, and D. Calzetti. Dust Absorption and the Ultraviolet Luminosity Density at z ~3 as Calibrated by Local Starburst Galaxies. *Ap. J.* , 521(1):64–80, August 1999. doi: 10.1086/307523.

F. Meyer and E. Meyer-Hofmeister. On the elusive cause of cataclysmic variable outbursts. *Astron. Astrophys.* , 104:L10–L12, January 1981.

G. Meynet and A. Maeder. Stellar evolution with rotation. VIII. Models at Z = 10^{-5} and CNO yields for early galactic evolution. *Astron. Astrophys.* , 390:561–583, August 2002. doi: 10.1051/0004-6361:20020755.

M. Mingozzi et al. CLASSY IV. Exploring UV Diagnostics of the Interstellar Medium in Local High-z Analogs at the Dawn of the JWST Era. *Ap. J.* , 939(2):110, November 2022. doi: 10.3847/1538-4357/ac952c.

D. J. Mink and W. F. Wyatt. EMSAO: Radial Velocities from Emission Lines in Spectra. In R. A. Shaw, H. E. Payne, and J. J. E. Hayes, editors, *Astronomical Data Analysis Software and Systems IV*, volume 77 of *Astronomical Society of the Pacific Conference Series*, page 496, January 1995.

J. Mirocha. Decoding the X-ray properties of pre-reionization era sources. *MNRAS* , 443(2):1211–1223, September 2014. doi: 10.1093/mnras/stu1193.

K. Mitsuda et al. Energy spectra of low-mass binary X-ray sources observed from Tenma. *Publications of the Astronomical Society of Japan*, 36:741–759, January 1984.

M. Moe and R. Di Stefano. Mind Your Ps and Qs: The Interrelation between Period (P) and Mass-ratio (Q) Distributions of Binary Stars. *Ap. J. Suppl.* , 230(2):15, June 2017. doi: 10.3847/1538-4365/aa6fb6.

N. Murray. Star Formation Efficiencies and Lifetimes of Giant Molecular Clouds in the Milky Way. *Ap. J.* , 729(2):133, March 2011. doi: 10.1088/0004-637X/729/2/133.

N. Murray, E. Quataert, and T. A. Thompson. The Disruption of Giant Molecular Clouds by Radiation Pressure & the Efficiency of Star Formation in Galaxies. *Ap. J.* , 709:191–209, January 2010. doi: 10.1088/0004-637X/709/1/191.

S. Murray et al. 21cmFAST v3: A Python-integrated C code for generating 3D realizations of the cosmic 21cm signal. *The Journal of Open Source Software*, 5(54):2582, October 2020. doi: 10.21105/joss.02582.

K. Nakajima and R. Maiolino. Diagnostics for PopIII galaxies and direct collapse black holes in the early universe. *MNRAS* , 513(4):5134–5147, July 2022. doi: 10.1093/mnras/stac1242.

K. Nakajima et al. A Hard Ionizing Spectrum in z = 3-4 Lyα Emitters with Intense [O III] Emission: Analogs of Galaxies in the Reionization Era? *Ap. J. Lett.* , 831(1):L9, November 2016. doi: 10.3847/2041-8205/831/1/L9.

K. Nakajima et al. The VIMOS Ultra Deep Survey: Nature, ISM properties, and ionizing spectra of CIII]λ1909 emitters at z = 2-4. *Astron. Astrophys.* , 612:A94, May 2018. doi: 10.1051/0004-6361/201731935.

T. Nanayakkara et al. Exploring He II λ1640 emission line properties at z ∼2-4. *Astron. Astrophys.* , 624:A89, April 2019. doi: 10.1051/0004-6361/201834565.

C. T. Nguyen et al. PARSEC V2.0: Stellar tracks and isochrones of low- and intermediate-mass stars with rotation. *Astron. Astrophys.* , 665:A126, September 2022. doi: 10.1051/0004-6361/202244166.

P. Ocvirk et al. Cosmic Dawn II (CoDa II): a new radiation-hydrodynamics simulation of the self-consistent coupling of galaxy formation and reionization. *MNRAS* , 496(4):4087–4107, August 2020. doi: 10.1093/mnras/staa1266.

P. A. Oesch et al. A remarkably luminous galaxy at z=11.1 measured with Hubble Space Telescope grism spectroscopy. *Ap. J.* , 819(2):129, March 2016. doi: 10.3847/0004-637X/819/2/129.

S. P. Oh and Z. Haiman. Second-Generation Objects in the Universe: Radiative Cooling and Collapse of Halos with Virial Temperatures above 10^4 K. *Ap. J.* , 569(2):558–572, April 2002. doi: 10.1086/339393.

G. M. Olivier et al. Characterizing Extreme Emission Line Galaxies. II. A Self-consistent Model of Their Ionizing Spectrum. *Ap. J.* , 938(1):16, October 2022. doi: 10.3847/1538-4357/ac8f2c.

D. E. Osterbrock and G. J. Ferland. *Astrophysics of gaseous nebulae and active galactic nuclei*. 2006.

C. Pacifici et al. The Art of Measuring Physical Parameters in Galaxies: A Critical Assessment of Spectral Energy Distribution Fitting Techniques. *Ap. J.* , 944(2):141, February 2023. doi: 10.3847/1538-4357/acacff.

B. E. J. Pagel, M. G. Edmunds, D. E. Blackwell, M. S. Chun, and G. Smith. On the composition of H II regions in southern galaxies - I. NGC 300 and 1365. *MNRAS* , 189:95–113, October 1979. doi: 10.1093/mnras/189.1.95.

P. Panuzzo, A. Bressan, G. L. Granato, L. Silva, and L. Danese. Dust and nebular emission. I. Models for normal galaxies. *Astron. Astrophys.* , 409:99–114, October 2003. doi: 10.1051/0004-6361:20031094.

S. Parsa, J. S. Dunlop, and R. J. McLure. No evidence for a significant AGN contribution to cosmic hydrogen reionization. *MNRAS* , 474(3):2904–2923, March 2018. doi: 10.1093/mnras/stx2887.

R. B. Partridge and P. J. E. Peebles. Are Young Galaxies Visible? *Ap. J.* , 147:868, March 1967. doi: 10.1086/149079.

A. W. A. Pauldrach, T. L. Hoffmann, and M. Lennon. Radiation-driven winds of hot luminous stars. XIII. A description of NLTE line blocking and blanketing towards realistic models for expanding atmospheres. *Astron. Astrophys.* , 375:161–195, August 2001. doi: 10.1051/0004-6361:20010805.

B. Paxton et al. Modules for Experiments in Stellar Astrophysics (MESA): Binaries, Pulsations, and Explosions. *Ap. J. Suppl.* , 220(1):15, September 2015. doi: 10.1088/0067-0049/220/1/15.

P. C. Peters. Gravitational Radiation and the Motion of Two Point Masses. *Physical Review*, 136(4B): 1224–1232, November 1964. doi: 10.1103/PhysRev.136.B1224.

V. Petrosian, J. Silk, and G. B. Field. A Simple Analytic Approximation for Dusty STRÖMGREN Spheres. *Ap. J. Lett.* , 177:L69, October 1972. doi: 10.1086/181054.

C. Pinto, M. J. Middleton, and A. C. Fabian. Resolved atomic lines reveal outflows in two ultraluminous X-ray sources. *Nature*, 533(7601):64–67, May 2016. doi: 10.1038/nature17417.

Planck Collaboration et al. Planck intermediate results - XLVII. Planck constraints on reionization history. *A&A*, 596:A108, 2016. doi: 10.1051/0004-6361/201628897.

Planck Collaboration et al. Planck 2018 results - VI. Cosmological parameters. *A&A*, 641:A6, 2020a. doi: 10.1051/0004-6361/201833910.

Planck Collaboration et al. Planck 2018 results - VII. Isotropy and statistics of the CMB. *A&A*, 641: A7, 2020b. doi: 10.1051/0004-6361/201935201.

A. Plat et al. Constraints on the production and escape of ionizing radiation from the emission-line spectra of metal-poor star-forming galaxies. *MNRAS* , 490(1):978–1009, November 2019. doi: 10.1093/mnras/stz2616.

K. Pottschmidt et al. Long term variability of Cygnus X-1. I. X-ray spectral-temporal correlations in the hard state. *Astron. Astrophys.* , 407:1039–1058, September 2003. doi: 10.1051/0004-6361:20030906.

R. K. Prinja, S. R. Rosen, and K. Supelli. Time-resolved ultraviolet spectroscopy of the cataclysmic variable PG 1711+336. *MNRAS* , 248:40, January 1991. doi: 10.1093/mnras/248.1.40.

A. Raiter, D. Schaerer, and R. A. E. Fosbury. Predicted UV properties of very metal-poor starburst galaxies. *Astron. Astrophys.* , 523:A64, November 2010. doi: 10.1051/0004-6361/201015236.

M. J. Rees. Tidal disruption of stars by black holes of 10^6-10^8 solar masses in nearby galaxies. *Nature*, 333(6173):523–528, June 1988. doi: 10.1038/333523a0.

I. Reis, A. Fialkov, and R. Barkana. The subtlety of Ly α photons: changing the expected range of the 21-cm signal. *MNRAS* , 506(4):5479–5493, October 2021. doi: 10.1093/mnras/stab2089.

R. A. Remillard and J. E. McClintock. X-Ray Properties of Black-Hole Binaries. *Annu.Rev.Astron.Astrophys.*, 44(1):49–92, September 2006. doi: 10.1146/annurev.astro.44.051905.092532.

B. E. Robertson et al. New Constraints on Cosmic Reionization from the 2012 Hubble Ultra Deep Field Campaign. *Ap. J.* , 768(1):71, May 2013. doi: 10.1088/0004-637X/768/1/71.

G. A. Rodríguez Castillo et al. Discovery of a 2.8 s Pulsar in a 2 Day Orbit High-mass X-Ray Binary Powering the Ultraluminous X-Ray Source ULX-7 in M51. *Ap. J.* , 895(1):60, May 2020. doi: 10.3847/1538-4357/ab8a44.

J. Rosdahl et al. LyC escape from SPHINX galaxies in the Epoch of Reionization. *MNRAS* , 515(2):2386–2414, September 2022. doi: 10.1093/mnras/stac1942.

A. L. Rosen. A Massive Star Is Born: How Feedback from Stellar Winds, Radiation Pressure, and Collimated Outflows Limits Accretion onto Massive Stars. *Ap. J.* , 941(2):202, December 2022. doi: 10.3847/1538-4357/ac9f3d.

V. C. Rubin, J. Ford, W. K., and N. Thonnard. Rotational properties of 21 SC galaxies with a large range of luminosities and radii, from NGC 4605 (R=4kpc) to UGC 2885 (R=122kpc). *Ap. J.* , 238:471–487, June 1980. doi: 10.1086/158003.

E. E. Salpeter. The Luminosity Function and Stellar Evolution. *Ap. J.* , 121:161, January 1955. doi: 10.1086/145971.

H. Sana et al. Binary Interaction Dominates the Evolution of Massive Stars. *Science*, 337(6093):444, July 2012. doi: 10.1126/science.1223344.

S. F. Sánchez et al. SDSS-IV MaNGA: pyPipe3D Analysis Release for 10,000 Galaxies. *Ap. J. Suppl.* , 262(2):36, October 2022. doi: 10.3847/1538-4365/ac7b8f.

A. Sander, W. R. Hamann, and H. Todt. The Galactic WC stars. Stellar parameters from spectral analyses indicate a new evolutionary sequence. *Astron. Astrophys.* , 540:A144, April 2012. doi: 10.1051/0004-6361/201117830.

F. Santoliquido et al. Binary black hole mergers from population III stars: uncertainties from star formation and binary star properties. *MNRAS* , 524(1):307–324, September 2023. doi: 10.1093/mnras/stad1860.

F. Santoliquido et al. Classifying binary black holes from Population III stars with the Einstein Telescope: a machine-learning approach. *arXiv e-prints*, art. arXiv:2404.10048, April 2024. doi: 10.48550/arXiv.2404.10048.

M. G. Santos, L. Ferramacho, M. B. Silva, A. Amblard, and A. Cooray. Fast large volume simulations of the 21-cm signal from the reionization and pre-reionization epochs. *MNRAS* , 406(4):2421–2432, August 2010. doi: 10.1111/j.1365-2966.2010.16898.x.

A. Saxena et al. X-ray properties of He II λ 1640 emitting galaxies in VANDELS. *MNRAS* , 496(3): 3796–3807, August 2020. doi: 10.1093/mnras/staa1805.

D. Schaerer. On the properties of massive Population III stars and metal-free stellar populations. *Astron. Astrophys.* , 382:28–42, January 2002. doi: 10.1051/0004-6361:20011619.

D. Schaerer. The transition from Population III to normal galaxies: Lyalpha and He II emission and the ionising properties of high redshift starburst galaxies. *Astron. Astrophys.* , 397:527–538, January 2003. doi: 10.1051/0004-6361:20021525.

D. Schaerer et al. The ionizing photon production efficiency of compact z ~0.3 Lyman continuum leakers and comparison with high-redshift galaxies. *Astron. Astrophys.* , 591:L8, June 2016. doi: 10.1051/0004-6361/201628943.

D. Schaerer, T. Fragos, and Y. I. Izotov. X-ray binaries as the origin of nebular He II emission in low-metallicity star-forming galaxies. *Astron. Astrophys.* , 622:L10, February 2019. doi: 10.1051/0004-6361/201935005.

D. Schaerer and W. Vacca. New Models for Wolf-Rayet and O Star Populations in Young Starbursts. *Ap. J.* , 497(2):618–644, April 1998. doi: 10.1086/305487.

A. T. P. Schauer, N. Drory, and V. Bromm. The Ultimately Large Telescope: What Kind of Facility Do We Need to Detect Population III Stars? *Ap. J.* , 904(2):145, December 2020. doi: 10.3847/1538-4357/abbc0b.

K. B. Schmidt et al. The Grism Lens-Amplified Survey from Space (GLASS). XI. Detection of C IV in Multiple Images of the z = 6.11 Lyα Emitter behind RXC J2248.7-4431. *Ap. J.* , 839(1):17, April 2017. doi: 10.3847/1538-4357/aa68a3.

B. Semelin, E. Eames, F. Bolgar, and M. Caillat. 21SSD: a public data base of simulated 21-cm signals from the epoch of reionization. *MNRAS* , 472(4):4508–4520, December 2017. doi: 10.1093/mnras/stx2274.

P. Senchyna et al. Ultraviolet spectra of extreme nearby star-forming regions - approaching a local reference sample for JWST. *MNRAS* , 472(3):2608–2632, December 2017. doi: 10.1093/mnras/stx2059.

P. Senchyna et al. Extremely metal-poor galaxies with HST/COS: laboratories for models of low-metallicity massive stars and high-redshift galaxies. *MNRAS* , 488(3):3492–3506, September 2019. doi: 10.1093/mnras/stz1907.

P. Senchyna et al. High-mass X-ray binaries in nearby metal-poor galaxies: on the contribution to nebular He II emission. *MNRAS* , 494(1):941–957, May 2020. doi: 10.1093/mnras/staa586.

P. Senchyna et al. Direct Constraints on the Extremely Metal-poor Massive Stars Underlying Nebular C IV Emission from Ultra-deep HST/COS Ultraviolet Spectroscopy. *Ap. J.* , 930(2):105, May 2022. doi: 10.3847/1538-4357/ac5d38.

N. I. Shakura and R. A. Sunyaev. Black holes in binary systems. Observational appearance. *Astron. Astrophys.* , 24:337–355, January 1973.

M. Shirazi and J. Brinchmann. Strongly star forming galaxies in the local Universe with nebular He IIλ4686 emission. *MNRAS* , 421(2):1043–1063, April 2012. doi: 10.1111/j.1365-2966.2012.20439.x.

I. Shivaei et al. The MOSDEF Survey: Direct Observational Constraints on the Ionizing Photon Production Efficiency, ξ_{ion}, at z $\sim$ 2. *Ap. J.* , 855(1):42, March 2018. doi: 10.3847/1538-4357/aaad62.

J. M. Shull and C. F. McKee. Theoretical models of interstellar shocks. I. *Ap. J.* , 227:131–149, January 1979. doi: 10.1086/156712.

J. Skilling. Nested sampling for general Bayesian computation. *Bayesian Analysis*, 1(4):833 – 859, 2006. doi: 10.1214/06-BA127.

J. Smidt et al. Population III Hypernovae. *Ap. J.* , 797(2):97, December 2014. doi: 10.1088/0004-637X/797/2/97.

J. Smidt et al. Finding the First Cosmic Explosions. IV. 90 - 140 $M_{\odot}$ Pair-instability Supernovae. *Ap. J.* , 805(1):44, May 2015. doi: 10.1088/0004-637X/805/1/44.

L. J. Smith, P. A. Crowther, D. Calzetti, and F. Sidoli. The Very Massive Star Content of the Nuclear Star Clusters in NGC 5253. *Ap. J.* , 823(1):38, May 2016. doi: 10.3847/0004-637X/823/1/38.

E. Sonbas, K. S. Dhuga, and E. Göğüş. Evidence of an X-Ray-Ultraviolet Spectral Correlation in Ultraluminous X-Ray Sources. *Ap. J. Lett.* , 873(2):L12, March 2019. doi: 10.3847/2041-8213/ab0a75.

J. S. Speagle. DYNESTY: a dynamic nested sampling package for estimating Bayesian posteriors and evidences. *MNRAS* , 493(3):3132–3158, April 2020. doi: 10.1093/mnras/staa278.

M. Spera and M. Mapelli. Very massive stars, pair-instability supernovae and intermediate-mass black holes with the sevn code. *MNRAS* , 470(4):4739–4749, October 2017. doi: 10.1093/mnras/stx1576.

M. Spera, M. Mapelli, and A. Bressan. The mass spectrum of compact remnants from the PARSEC stellar evolution tracks. *MNRAS* , 451(4):4086–4103, August 2015. doi: 10.1093/mnras/stv1161.

M. Spera et al. Merging black hole binaries with the SEVN code. *MNRAS* , 485(1):889–907, May 2019. doi: 10.1093/mnras/stz359.

E. R. Stanway and J. J. Eldridge. Re-evaluating old stellar populations. *MNRAS* , 479(1):75–93, September 2018. doi: 10.1093/mnras/sty1353.

E. R. Stanway and J. J. Eldridge. Initial mass function variations cannot explain the ionizing spectrum of low metallicity starbursts. *Astron. Astrophys.* , 621:A105, January 2019. doi: 10.1051/0004-6361/201834359.

D. P. Stark. Galaxies in the first billion years after the Big Bang. *Annual Review of Astronomy and Astrophysics*, 54(1):761–803, 2016. doi: 10.1146/annurev-astro-081915-023417.

D. P. Stark et al. Ultraviolet emission lines in young low-mass galaxies at z $\simeq$ 2: physical properties and implications for studies at z $>$ 7. *MNRAS* , 445(3):3200–3220, December 2014. doi: 10.1093/mnras/stu1618.

D. P. Stark et al. Spectroscopic detection of C IV λ1548 in a galaxy at z = 7.045: implications for the ionizing spectra of reionization-era galaxies. *MNRAS* , 454(2):1393–1403, December 2015. doi: 10.1093/mnras/stv1907.

D. P. Stark et al. Lyα and C III] emission in z = 7-9 Galaxies: accelerated reionization around luminous star-forming systems? *MNRAS* , 464(1):469–479, January 2017. doi: 10.1093/mnras/stw2233.

C. C. Steidel et al. Reconciling the Stellar and Nebular Spectra of High-redshift Galaxies. *Ap. J.* , 826 (2):159, August 2016. doi: 10.3847/0004-637X/826/2/159.

C. C. Steidel et al. The Structure and Kinematics of the Circumgalactic Medium from Far-ultraviolet Spectra of z ~= 2-3 Galaxies. *Ap. J.* , 717(1):289–322, July 2010. doi: 10.1088/0004-637X/717/1/289.

J. F. Steiner, R. Narayan, J. E. McClintock, and K. Ebisawa. A Simple Comptonization Model. *Pub. Astron. Soc. Pac.* , 121(885):1279, November 2009. doi: 10.1086/648535.

D. K. Strickland and T. M. Heckman. Supernova Feedback Efficiency and Mass Loading in the Starburst and Galactic Superwind Exemplar M82. *Ap. J.* , 697(2):2030–2056, June 2009. doi: 10.1088/0004-637X/697/2/2030.

A. L. Strom, C. C. Steidel, G. C. Rudie, R. F. Trainor, and M. Pettini. Measuring the Physical Conditions in High-redshift Star-forming Galaxies: Insights from KBSS-MOSFIRE. *Ap. J.* , 868(2): 117, December 2018. doi: 10.3847/1538-4357/aae1a5.

B. Strömgren. The Physical State of Interstellar Hydrogen. *Ap. J.* , 89:526, May 1939. doi: 10.1086/144074.

R. Sunyaev and M. Revnivtsev. Fourier power spectra at high frequencies: a way to distinguish a neutron star from a black hole. *Astron. Astrophys.* , 358:617–623, June 2000. doi: 10.48550/arXiv.astro-ph/0003308.

A. D. Sutton, T. P. Roberts, and M. J. Middleton. The ultraluminous state revisited: fractional variability and spectral shape as diagnostics of super-Eddington accretion. *MNRAS* , 435(2):1758–1775, October 2013. doi: 10.1093/mnras/stt1419.

Y. Tanaka and N. Shibazaki. X-ray Novae. *Annu.Rev.Astron.Astrophys.*, 34:607–644, January 1996. doi: 10.1146/annurev.astro.34.1.607.

T. M. Tauris et al. Formation of Double Neutron Star Systems. *Ap. J.* , 846:170, September 2017. doi: 10.3847/1538-4357/aa7e89.

S. R. Taylor and D. Gerosa. Mining gravitational-wave catalogs to understand binary stellar evolution: A new hierarchical Bayesian framework. *Phys. Rev. D* , 98(8):083017, October 2018. doi: 10.1103/PhysRevD.98.083017.

H. O. Tekin, T. Manici, E. Altunsoy Guclu, K. Yılancıoğlu, and B. Yilmaz. An artificial neural network-based estimation of bremsstarahlung photon flux calculated by mcnpx. *Acta Physica Polonica A*, 132:967–969, 09 2017. doi: 10.12693/APhysPolA.132.967.

B. M. Tinsley and J. E. Gunn. Evolutionary synthesis of the stellar population in elliptical galaxies. I. Ingredients, broad-band colors, and infrared features. *Ap. J.* , 203:52–62, January 1976. doi: 10.1086/154046.

H. Todt et al. Potsdam Wolf-Rayet model atmosphere grids for WN stars. *Astron. Astrophys.* , 579: A75, July 2015. doi: 10.1051/0004-6361/201526253.

E. Tolstoy, V. Hill, and M. Tosi. Star-Formation Histories, Abundances, and Kinematics of Dwarf Galaxies in the Local Group. *Annu.Rev.Astron.Astrophys.*, 47(1):371–425, September 2009. doi: 10.1146/annurev-astro-082708-101650.

M. W. Topping et al. The MOSDEF-LRIS Survey: The connection between massive stars and ionized gas in individual galaxies at z $\sim$ 2. *MNRAS* , 499(2):1652–1665, December 2020. doi: 10.1093/mnras/staa2941.

N. Torres-Albà, V. Bosch-Ramon, and K. Iwasawa. AGN jets versus accretion as reionization sources. *Astron. Astrophys.* , 635:A57, March 2020. doi: 10.1051/0004-6361/201936047.

J. Tumlinson and J. M. Shull. Zero-Metallicity Stars and the Effects of the First Stars on Reionization. *Ap. J. Lett.* , 528(2):L65–L68, January 2000. doi: 10.1086/312432.

J. Tumlinson, M. L. Giroux, and J. M. Shull. Probing the First Stars with Hydrogen and Helium Recombination Emission. *Ap. J. Lett.* , 550(1):L1–L5, March 2001. doi: 10.1086/319477.

H. Übler et al. GA-NIFS: A massive black hole in a low-metallicity AGN at z $\sim$ 5.55 revealed by JWST/NIRSpec IFS. *Astron. Astrophys.* , 677:A145, September 2023. doi: 10.1051/0004-6361/202346137.

H. Umeda et al. EMPRESS. VII. Ionizing Spectrum Shapes of Extremely Metal-poor Galaxies: Uncovering the Origins of Strong He II and the Impact on Cosmic Reionization. *Ap. J.* , 930(1):37, May 2022. doi: 10.3847/1538-4357/ac602d.

R. Valiante, R. Schneider, M. Volonteri, and K. Omukai. From the first stars to the first black holes. *MNRAS* , 457(3):3356–3371, April 2016. doi: 10.1093/mnras/stw225.

R. Valiante et al. Chasing the observational signatures of seed black holes at z $>$ 7: candidate observability. *MNRAS* , 476(1):407–420, May 2018. doi: 10.1093/mnras/sty213.

J. van den Eijnden et al. Radio monitoring of transient Be/X-ray binaries and the inflow-outflow coupling of strongly magnetized accreting neutron stars. *MNRAS* , 516(4):4844–4861, November 2022. doi: 10.1093/mnras/stac2518.

J. van Paradijs. On the Accretion Instability in Soft X-Ray Transients. *Ap. J. Lett.* , 464:L139, June 1996. doi: 10.1086/310100.

E. Vanzella et al. Hubble Imaging of the Ionizing Radiation from a Star-forming Galaxy at Z=3.2 with fesc$>$50%. *Ap. J.* , 825(1):41, July 2016. doi: 10.3847/0004-637X/825/1/41.

E. Vanzella et al. Magnifying the Early Episodes of Star Formation: Super Star Clusters at Cosmological Distances. *Ap. J.* , 842(1):47, June 2017. doi: 10.3847/1538-4357/aa74ae.

A. Venditti et al. A hide-and-seek game: Looking for Population III stars during the Epoch of Reionization through the HeIIλ1640 line. *arXiv e-prints*, art. arXiv:2405.10940, May 2024. doi: 10.48550/arXiv.2405.10940.

A. Verhamme, I. Orlitová, D. Schaerer, and M. Hayes. Using Lyman-α to detect galaxies that leak Lyman continuum. *Astron. Astrophys.* , 578:A7, June 2015. doi: 10.1051/0004-6361/201423978.

A. Verhamme et al. Lyman-α spectral properties of five newly discovered Lyman continuum emitters. *Astron. Astrophys.* , 597:A13, January 2017. doi: 10.1051/0004-6361/201629264.

A. Vidal-García, S. Charlot, G. Bruzual, and I. Hubeny. Modelling ultraviolet-line diagnostics of stars, the ionized and the neutral interstellar medium in star-forming galaxies. *MNRAS* , 470(3):3532–3556, September 2017. doi: 10.1093/mnras/stx1324.

J. Vink. Supernova remnants: the X-ray perspective. *The Astronomy and Astrophysics Review*, 20:49, December 2012. doi: 10.1007/s00159-011-0049-1.

J. S. Vink. Theory and diagnostics of hot star mass loss. *Annual Review of Astronomy and Astrophysics*, 60(1):203–246, 2022. doi: 10.1146/annurev-astro-052920-094949.

J. S. Vink et al. Wind modelling of very massive stars up to 300 solar masses. *Astron. Astrophys.* , 531:A132, July 2011. doi: 10.1051/0004-6361/201116614.

M. Volonteri. The Formation and Evolution of Massive Black Holes. *Science*, 337(6094):544, August 2012. doi: 10.1126/science.1220843.

J. Walcher, B. Groves, T. Budavári, and D. Dale. Fitting the integrated spectral energy distributions of galaxies. *Astrophysics and Space Science*, 331:1–52, January 2011. doi: 10.1007/s10509-010-0458-z.

F. Y. Wang et al. Probing Pre-galactic Metal Enrichment with High-redshift Gamma-Ray Bursts. *Ap. J.* , 760(1):27, November 2012. doi: 10.1088/0004-637X/760/1/27.

Y.-Y. Wang et al. The mini-QSO's contribution to cosmic reionization. *Research in Astronomy and Astrophysics*, 10(3):199, mar 2010. doi: 10.1088/1674-4527/10/3/001.

K. Watarai. New Analytical Formulae for Supercritical Accretion Flows. *Ap. J.* , 648(1):523–533, September 2006. doi: 10.1086/505854.

D. J. Whalen et al. Finding the First Cosmic Explosions. II. Core-collapse Supernovae. *Ap. J.* , 768 (1):95, May 2013a. doi: 10.1088/0004-637X/768/1/95.

D. J. Whalen et al. Finding the First Cosmic Explosions. III. Pulsational Pair-instability Supernovae. *Ap. J.* , 781(2):106, February 2014. doi: 10.1088/0004-637X/781/2/106.

D. Whalen et al. Finding the First Cosmic Explosions. I. Pair-instability Supernovae. *Ap. J.* , 777(2): 110, November 2013b. doi: 10.1088/0004-637X/777/2/110.

T. Wiklind, B. Mobasher, and V. Bromm. *The First Galaxies: Theoretical Predictions and Observational Clues*. 01 2013. ISBN 978-3-642-32361-4. doi: 10.1007/978-3-642-32362-1.

J. H. Wise, T. Abel, M. J. Turk, M. L. Norman, and B. D. Smith. The birth of a galaxy - II. The role of radiation pressure. *MNRAS* , 427(1):311–326, November 2012. doi: 10.1111/j.1365-2966.2012.21809.x.

A. Wofford et al. Stars and gas in the most metal-poor galaxies - I. COS and MUSE observations of SBS 0335-052E. *MNRAS* , 500(3):2908–2927, January 2021. doi: 10.1093/mnras/staa3365.

S. E. Woosley. Pulsational Pair-instability Supernovae. *Ap. J.* , 836(2):244, February 2017. doi: 10.3847/1538-4357/836/2/244.

Z. Yan and W. Yu. X-Ray Outbursts of Low-mass X-Ray Binary Transients Observed in the RXTE Era. *Ap. J.* , 805(2):87, June 2015. doi: 10.1088/0004-637X/805/2/87.

P. Yang et al. The origin of UV/optical emission in the black hole low-mass X-ray binary Swift J1753.5-0127. *MNRAS* , 514(1):234–248, July 2022. doi: 10.1093/mnras/stac1120.

E. Zackrisson, A. K. Inoue, and H. Jensen. The Spectral Evolution of the First Galaxies. II. Spectral Signatures of Lyman Continuum Leakage from Galaxies in the Reionization Epoch. *Ap. J.* , 777(1): 39, November 2013. doi: 10.1088/0004-637X/777/1/39.

E. Zackrisson et al. The detection and characterization of highly magnified stars with JWST: Prospects of finding Population III. *arXiv e-prints*, art. arXiv:2312.09289, December 2023. doi: 10.48550/arXiv.2312.09289.

Y. B. Zel'dovich. Gravitational instability: An approximate theory for large density perturbations. *Astron. Astrophys.* , 5:84–89, March 1970.

H. Zinnecker and H. W. Yorke. Toward Understanding Massive Star Formation. *Annu.Rev.Astron.Astrophys.*, 45(1):481–563, September 2007. doi: 10.1146/annurev.astro.44.051905.092549.